Regulation of intestinal T cell homeostasis by autophagy

Cristina Dumitru

Lincoln College, University of Oxford

A thesis submitted for the degree of

Doctor of Philosophy,

Hilary Term 2021

Table of Contents

List of Tables **4**

List of Figures **5**

Declaration of Authorship **9**

CHAPTER 1. INTRODUCTION 10

1.1 Systems of cellular degradation **10**
1.1.1 Introduction to the autophagy pathways 10
1.1.2 Mechanism of autophagy machinery 11
1.1.3 Regulation of the autophagy pathway 15
1.1.4 Autophagy in T cells 17
1.1.5 Proteasomal degradation pathways 18
1.1.6 Regulation of proteasomal function 21
1.1.7 Cross talk between autophagy and proteasome 22
1.1.8 The proteasome in T cell responses 23

1.2 The development and functioning of $CD4^+$ Th subsets **24**
1.2.1 Thymic selection and development of CD4+ T cells 24
1.2.2 Metabolic reprogramming during $CD4^+$ T cell activation 26
1.2.3 Th1 cells 31
1.2.4 Th17 cells 32
1.2.5 Th2 cells and type 2 responses 33
1.2.6 T follicular helper (Tfh) cells and other non-regulatory $CD4^+$ T cell subsets 35
1.2.7 Treg cells 36

1.3 The pathogenies of inflammatory bowel disease (IBD) **37**
1.3.1 ATG16L1 T300A variant and intestinal immune homeostasis 40

1.4 Rationale and summary of thesis aims **41**

CHAPTER 2. MATERIALS AND METHODS 43

2.1 Mouse strains **43**

2.2 Genotyping of mouse strains **44**
2.2.1 Genomic DNA isolation 44
2.2.2 Polymerase chain reaction (PCR) 44
2.2.3 Gel electrophoresis 46

2.3 Cell isolation, enrichment and depletion **46**
2.3.1 Isolation of spleen and lymph node cells 46
2.3.2 Isolation of leukocytes from the blood 46
2.3.3 Isolation of leukocytes from the colonic lamina propria 46
2.3.4 Isolation of cells from fat tissue 47
2.3.5 T cell enrichment 47
2.3.6 $CD3^+$ T cell depletion 47

2.4 Flow cytometry and cell sorting **47**
2.4.1 Flow cytometry antibodies 47

2.4.2 Re-stimulation of lymphocytes for intracellular cytokine staining 48
2.4.3 Surface staining 48
2.4.4 Intracellular staining for transcription factors and/or cytokines 49
2.4.5 Flow cytometric analysis 49
2.4.6 Fluorescence-activated cell sorting (FACS) 49

2.5 In vivo experiments 49
2.5.1 Generation of bone marrow chimaeras 49
2.5.2 Tamoxifen injection 50
2.5.3 Sampling blood from mouse tail vein 50
2.5.4 Histological assessment 50

2.6 In vitro experiments 50
2.6.1 Induced Treg (iTreg) cultures 50
2.6.2 Colon explant cultures 51
2.6.3 Proteasomal activity measurement 51

2.7 Analysis of gene expression 51
2.7.1 Droplet based single-cell RNA sequencing 51
2.7.2 Real-time quantitative polymerase chain reaction (RT-qPCR) analysis 52

2.8 Analysis of protein levels 52
2.8.1 Enzyme linked immunosorbent assays (ELISAs) 52
2.8.2 Western blot (WB) 53

2.9 Statistical analysis 53

2.10 Experimental design and power analysis 54

CHAPTER 3. AUTOPHAGY REGULATES INTESTINAL TH2 CELLS THROUGH CELL INTRINSIC AND CELL EXTRINSIC MECHANISMS 55

3.1 Introduction and aims of chapter 55

3.2 Experimental results 57
3.2.1 Validation of tamoxifen meditated Atg16l1-excision and tdTomato reporter expression 57
3.2.2 Autophagy-deficient Th2 cells compete well with WT counterparts whilst autophagy deficient Treg cells are outcompeted by WT counterparts in $Rag^{-/-}$ mixed BM chimeras 61
3.2.2 C57BL/6 mixed BM chimeras corroborate the differential competitiveness of Atg16l1-deficient Th subsets 70

3.2.5 Summary and conclusions 81

CHAPTER 4. INVESTIGATING THE ROLE OF TYPE 2 RESPONSES IN THE DEVELOPMENT OF THE PATHOLOGY SEEN IN ATG16L1$^{\Delta CD4}$ MICE 82

4.1 Introduction and aims of chapter 82

4.2 Experimental results 84
4.2.1 Characterization and validation of Atg16l1$^{\Delta CD4}$ IL13 reporter mice 84
4.2.2 Atg16l1$^{\Delta CD4}$ IL-13KO mice phenocopy the disease pathology and immune dysregulation seen in Atg16l1$^{\Delta CD4}$ mice 88
4.2.3 The exacerbated Th2 response in Atg16l1$^{\Delta CD4}$ mice does affect clearance of a helminth parasite 95
4.2.4 Investigating adipose tissues in Atg16l1$^{\Delta CD4}$ mice 98
4.2.5 High fat diet does not rescue Treg cells in Atg16l1$^{\Delta CD4}$ mice 104

4.3. Summary and conclusions 109

CHAPTER 5. CHARACTERISATION OF THE TRANSCRIPTIONAL CHANGES IN AUTOPHAGY DEFICIENT CD4$^+$ T CELLS 112

5.1 Introduction and aims of chapter **112**

5.2 Experimental results **116**
5.2.1 Filtering cells by quality control metrics 116
5.2.2 Dimensionality reduction and feature selection 120
5.2.3 Samples integration using shared HVG 123
5.2.4 Cell clustering and identification by known cell type markers 123
5.2.5 Differential expression and over-representation analysis 131
5.2.6 Successful validation of some of the sc-RNAseq findings 142

5.3 Summary and conclusions **149**

CHAPTER 6. GENERAL DISCUSSION 153
The role of the microenvironment in number, function and metabolism of Treg cells 153
The complementary roles of the proteasome and autophagy pathways 155

APPENDIX 157

REFERENCES 159

List of Tables

Table 1. List of abbreviations 7

Table 2. Primer sequences used to screen transgenic mice 44

Table 3. PCR programmes used for genotyping 45

Table 4. Antibodies used for Flow cytometry 48

Table 5. Top upregulated genes from each cluster. 136

Table 6. Top downregulated genes from each cluster. 137

Table 7. Upregulated genes part of an enriched GO categories for the named clusters. 157

Table 8. Upregulated genes part of an enriched KEGG pathway for the named clusters. 158

List of Figures

Figure 1. Schematic representation of the autophagy machinery. 14

Figure 2. Schematic representation of possible combinations of 20S (A) and immuno-20S (B) proteasome cores with regulatory particles. 20

Figure 3. Main metabolic pathways in T cells. 28

Figure 4. $CD4^+$ T cell differentiation schematic. 30

Figure 5. Validation of $Atg16l1^{fl/fl}$ Rosa26-$tdTomato^{fl/fl}$ $Rosa26^{CreERT2}$ genetic construct. 59

Figure 6. Validation of tamoxifen dosing regimen for triggering Atg16l1 deletion in the $Atg16l1^{fl/fl}$ Rosa26-$tdTomato^{fl/fl}$ $Rosa26^{CreERT2}$ mouse model. 60

Figure 7. Setup of mixed BM chimeras in $Rag^{-/-}$ hosts. 63

Figure 8. Analysis of Th cells in peripheral blood of $Rag^{-/-}$ mixed BM chimeras. 65

Figure 9. Analysis of Th cells in different tissues of $Rag^{-/-}$ mixed BM chimeras. 67

Figure 10. Analysis of Th cells at different tissues of $Rag^{-/-}$ mixed BM chimeras. 68

Figure 11. Set up of mixed BM chimeras with C57BL/6 hosts. 72

Figure 12. Analysis of Th cells in peripheral blood of mixed BM chimeras (C57BL/6 hosts) 74

Figure 13. Analysis of Th cells intracellular markers across different tissues from mixed BM chimera (C57BL/6 hosts) mice. 76

Figure 14. Analysis of Th cells cytokines expression across different tissues from mixed BM chimera (C57BL/6 hosts) mice. 78

Figure 15. Systemic measurements of the C57BL/6 chimeras and control mice. 80

Figure 16. $Atg16l1^{\Delta CD4}$IL-13 heterozygous reporter mice reproduce the immunopathology of $Atg16l1^{\Delta CD4}$ mice. 86

Figure 17. $Atg16l1^{\Delta CD4}$IL-13 heterozygous reporter mice provide a good equivalent to IL-13 antibody staining through GFP fluorescence. 87

Figure 18. IL-13 is not required for the weight and intestinal pathology seen in $Atg16l1^{\Delta CD4}$ mice. 89

Figure 19. IL-13 is not required for the systemic pathology seen in $Atg16l1^{\Delta CD4}$ mice. 91

Figure 20. Elevated levels of IL-5, but not IL-4, in the colon of aged (> 5 months old) $Atg16l1^{\Delta CD4}IL13^{gfp/+}$, $Atg16l1^{fl/fl}$ IL-$13^{gfp/gfp}$ and littermate controls mice. 93

Figure 21. $Atg16l1^{\Delta CD4}$ mice show comparable clearance of the intestinal parasite, H. polygyrus, as littermate controls. 96

Figure 22. Aged $Atg16l1^{\Delta CD4}$ mice show evidence of fat remodelling as compared to littermate controls. 100

Figure 23. Young $Atg16l1^{\Delta CD4}$ mice (~9 weeks old) exhibit selective expansion of Th2 cells and loss of Treg cells in the epididymal WAT compartment. 102

Figure 24. Systemic effects of HFD on $Atg16l1^{\Delta CD4}$ mice and littermate controls. 105

Figure 25. HFD treatment does not rescue autophagy deficient Treg cells. 106

Figure 26. Autophagy-sufficient Treg and Th2 cells in the cLP show increased lipid uptake after HFD exposure, as measured by BODIPY staining. 108

Figure 27. Quality control summary metrics of dataset comprising single-cell transcriptome analysis of $CD4^+$ T cells isolated from the colonic lamina propria of $Atg16l1^{\Delta CD4}$ mice (KO) and $Atg16l1^{fl/fl}$ littermate (WT) controls. 118

Figure 28. Percentage of counts accounted for by the top 50 most highly expressed genes of dataset comprising single-cell transcriptome analysis of $CD4^+$ T cells isolated from the colonic lamina propria of $Atg16l1^{\Delta CD4}$ mice (KO) and $Atg16l1^{fl/fl}$ littermate (WT) controls. 119

Figure 29. Principal Components selection of dataset comprising single-cell transcriptome analysis $CD4^+$ T cells isolated from the colonic lamina propria of $Atg16l1^{\Delta CD4}$ mice (KO) and $Atg16l1^{fl/fl}$ littermate (WT) controls. 122

Figure 30. Clustering tree of dataset comprising single-cell transcriptome analysis $CD4^+$ T cells isolated from the colonic lamina propria of $Atg16l1^{\Delta CD4}$ mice (KO) and $Atg16l1^{fl/fl}$ littermate (WT) controls. 126

Figure 31. UMAP visualisation of clustering analysis and identification of cell populations of dataset comprising single-cell transcriptome analysis $CD4^+$ T cells isolated from the colonic lamina propria of $Atg16l1^{\Delta CD4}$ mice (KO) and $Atg16l1^{fl/fl}$ littermate (WT) controls. 127

Figure 32. Heatmap displaying the expression patters of the top 10 marker genes across all cells with the 11 clusters resulting from clustering analysis. 129

Figure 33. Clustering composition breakdown of dataset comprising single-cell transcriptome analysis of $CD4^+$ T cells isolated from the colonic lamina propria of $Atg16l1^{\Delta CD4}$ mice (KO) and $Atg16l1^{fl/fl}$ littermate (WT) controls. 130

Figure 34. Volcano plots of differentially expressed (DE) genes across clusters. 135

Figure 35. Summary of the number of differentially expressed genes (DEG) per cluster. 138

Figure 36. Visualisation of upregulated genes relating to the mTOR (A) and proteasome (B) pathways by autophagy-deficient pTreg $IL10^+$ cells using "Pathview" R package. 140

Figure 37. Summary of enriched GO categories (A) and KEGG pathways (B) following over-representation analysis. 141

Figure 38. Validation of $IL\text{-}10^+$ expression by Treg cells in $Atg16l1^{\Delta CD4}$ mice and $Atg16l1^{fl/fl}$ littermate controls. 144

Figure 39. Validation of mTOR and activity expression by Treg cells in $Atg16l1^{\Delta CD4}$ mice and $Atg16l1^{fl/fl}$ littermate controls. 145

Figure 40. Validation of proteasome activity in in-vitro differentiated Treg cells derived from $Atg16l1^{\Delta CD4}$ mice and $Atg16l1^{fl/fl}$ littermate controls. 146

Figure 41. Proteasome inhibitor treatment of in vitro differentiated Treg cells, isolated from splenocytes of $Atg16l1^{\Delta CD4}$ or $Atg16l1^{fl/fl}$ mice. 147

Figure 42. Potential mechanistic implications of autophagy deficiency in Treg cells. 152

Table 1. List of abbreviations

Abbreviation	Description
ACK	Ammonium chloride potassium
AF	Alexa Fluor
ANOVA	Analysis of variance
APC	Allophycocyanin
Atg	Autophagy related gene
Bcl-6	B cell lymphoma 6
BM	Bone marrow
BMCh	Bone marrow chimera
bp	Base pair
BSA	Bovine serum albumin
BV	Brilliant Violet
cLP	Colonic lamina propria
DEG	Differentially expressed genes
DNA	Deoxyribonucleic acid
EDTA	Ethylenediaminetetraacetic acid
ELISA	Enzyme-linked immunosorbent assay
EtOH	Ethanol
FACS	Fluorescence-activated cell sorting
FCS/FBS	Foetal calf serum/ Foetal bovine serum
FDR	False discovery rate
FITC	Fluorescein isothiocyanate
fl/fl	Flanked by LoxP
Foxp3	Forkhead box P3
FSC	Forward scatter
Gata3	GATA binding protein 3
GFP	Green fluorescent protein
GM-CSF	Granulocyte macrophage colony-stimulating factor
GWAS	Genome-wide association study
H&E	Haematoxylin and eosin
HPRT	Hypoxanthine phosphoribosyl transferase
i.p.	Intraperitoneal
i.v.	Intravenous
IBD	Inflammatory Bowel disease
IFN	Interferon
Ig	Immunoglobulin
IL	Interleukin
IMDM	Iscove's Modified Dulbecco's Medium
iTreg	Induced regulatory T cell
min	Minute
mRNA	Messenger ribonucleic acid
OD	Optical density
ON	Overnight
OXPHOS	Oxidative phosphorylation
P/S	Penicillin-streptomycin

PBMC	Peripheral blood mononuclear cell
PBS	Phosphate-buffered saline
PCA	Principal Component Analysis
PCR	Polymerase chain reaction
PE	Phycoerythrin
Rag	Recombinase activating gene
RPMI	Roswell Park Memorial Institute Medium
RT	Room temperature
scRNA-seq	Single cell RNA sequencing
SSC	Side scatter
STAT	Signal transducer and activator of transcription
tdTomato	Tandem dimer Tomato
TF	Transcription factor
TNF	Tumour necrosis factor
Treg	Regulatory T cell
UMAP	Uniform Manifold Approximation and Projection
UMI	Unique molecular identifier
WT	Wild type

Declaration of Authorship

Data presented in the thesis are from the author's own experiments, other than data present in *section 4.2.3*, which were performed by the group of Prof. Rick Maizels at Glasgow University as indicated.

Parts of *section 1.2.2* are reproduced from one of the author's own publications *(Dumitru et al., 2018).* Co-authors, Dr. Agnieszka Kabat and Prof. Kevin Maloy, were notified and agreed with the reproduction of the mentioned published material in this thesis.

Chapter 1. Introduction

1.1 Systems of cellular degradation

The capacity to maintain protein homeostasis (proteostasis) is a critical requirement for the long-term viability and wellbeing of any cell type *(Dikic, 2017).* Two major degradation systems have evolved to handle the degradation of cellular constituents: the autophagy-lysosome pathway and the ubiquitin-proteasome system (UPS). It is generally considered that proteasomal degradation targets small, short-lived, abnormally folded proteins, while the autophagy pathway degrades large cytoplasmic components, like organelles, protein aggregates and intracellular pathogens *(Dikic, 2017).* The workings of these two processes are detailed in the chapters below.

1.1.1 Introduction to the autophagy pathways

Autophagy is an evolutionary conserved, nutrient recycling pathway essential for cellular survival during periods of low nutrient availability *(Clarke and Simon, 2019).* Autophagy occurs at low basal levels and performs homeostatic functions in virtually all cells and defective autophagy has been associated with a broad range of pathologies. The importance of autophagy is also highlighted by the observation that mice lacking essential autophagy genes are unable to survive the neonatal starvation period and die shortly after birth *(Kuma et al., 2004; Saitoh et al., 2008)*. Autophagy has two main roles: it maintains cellular homeostasis, by removing unwanted cytoplasmic content (pathogens, protein aggregates, damaged organelles, reactive oxygen species); and it provides biomolecules for cellular metabolism through the catabolism of proteins and complex lipids *(Simon et al., 2019)*. In recent years more complex and cell type specific functions of autophagy have emerged, including roles in innate and adaptive immune responses *(Kabat et al., 2016a; Riffelmacher T. et al., 2017; Simon et al., 2019)*.

There are three major types of autophagy pathways, that differ in their method of delivering cargo to the lysosome, these are: chaperone-mediated autophagy, microautophagy and macroautophagy.

Chaperone-mediated autophagy (CMA) involves the delivery of soluble proteins directly across the lysosomal membrane. A complex composed of heat shock 70 kDa protein 8 (HSPA8/HSC70) selects proteins that expose to a pentapeptide signature motif (KFERQ), this complex in turn binds to lysosomal-associated membrane protein 2A (LAMP2A) *(Cuervo and Wong, 2014).* The target proteins are then unfolded and translocated into the lysosomal lumen where they are degraded.

During microautophagy, cytosolic content that is in close proximity to the lysosome becomes sequestered by the direct invagination of the lysosomal membrane that pinches off into the lumen *(Li et al., 2012).* The importance of microautophagy is unclear for mammalian cells as this process has been mainly studied in yeast cells.

The best-characterized form of autophagy is macroautophagy (hereafter referred to as autophagy). Its hallmark is the sequestration of non-selective areas of the cytoplasm or specific organelles by a double-membrane vesicle which closes to form the autophagosome *(Dikic and Elazar, 2018).* Autophagosomes subsequently fuse with lysosomes to form the autolysosome, where the contents are exposed to the low pH and proteases of the lysosome degraded and recycled back to the cytoplasm *(Dikic and Elazar, 2018).*

1.1.2 Mechanism of autophagy machinery

The nearly 40 autophagy related proteins (ATGs) are crucial for autophagosome formation and are referred to as the core autophagy machinery. Induction of autophagy starts with recruitment of ATGs to a specific subcellular location called the phagophore assembly site (PAS) and formation of the isolation membrane that forms the cup- shaped structure termed the phagophore *(Dikic and Elazar, 2018)*.

The core autophagy machinery in mammalian cells can be grouped by their functional and physical interactions into five complexes (Figure 1):

(1) the ULK1 (unc-51-like kinase-1) - Atg13 - FIP200 - Atg101 kinase complex involved in autophagy initiation;

One of the most characterised triggers for induction of autophagy is nutrient deprivation, which results in inhibition of the master cell growth regulator serine/threonine kinase mTORC1 (mechanistic target of rapamycin complex1) and activation of AMP-activated protein kinase (AMPK) *(Gonzalez and Hall, 2017; Tripathi et al., 2013).* Please see *section 1.1.3* for a more detail description on autophagy regulators.

Briefly, in high nutrient conditions, ATG13 and ULK1 are bound by mTORC1 and remain inactive in this form. Upon starvation, ULK1 dissociates from mTORC1, undergoes autophosphorylation, followed by activation of ATG13 and FIP200 *(Gonzalez and Hall, 2017).* Once activated, the Ulk1 complex translocate to the site of autophagosome formation and activates the second functional complex.

(2) the class III phosphatidylinositol 3-kinase (PI3K) complex which mediates the nucleation step of the phagophore;

Nucleation of the phagophore membrane is a complex process, and its molecular details are still not completely elucidated. According to current understanding this step involves a cascade of events for which VPS34 (the catalytic subunit vacuolar protein sorting 34) that converts PI into PI-3-phosphate (PI3P), Beclin-1 and general vesicular transport factor p115, joined by ATG14 in PI3KC3 complex I (PI3KC3–C1) or UVRAG (UV radiation resistance-associated gene protein) (UVRAG) in complex II (PI3KC3–C2) are important for the promotion of autophagy *(Dikic and Elazar, 2018).* Once activated, this complex triggers local phosphatidylinositol-3-phosphate (PI3P) production at a subdomain of the endoplasmic reticulum ER called the omegasome. PI3P then recruits the PI3P-binding effector proteins to the phagophore membrane, including WIPI1/2 (WD repeat domain phosphoinositide-interacting proteins). WIPI1/2 was recently shown to bind ATG16L1, a member of an E3-like protein complex involved in one of two ubiquitin-like conjugation systems essential for autophagosome formation, required for elongation of the autophagosome membrane *(Bakula et al., 2018).*

(3) Atg9 (the only known transmembrane Atg protein) and its cycling system, involving Atg2 and WIPI1/2;

This complex is thought to be involved in the supply of required membranes for phagophore and autophagosome formation. The components provided by Atg9 are thought to originate from various sources, including mitochondria, the Golgi apparatus, the plasma membrane and the ER *(Dikic and Elazar, 2018)*. Once initiated, elongation of the isolation membrane requires the subsequent action of two ubiquitin – like (UBL) conjugation systems (4) and (5).

(4) the Atg12–Atg5–Atg16l1 complex, which is assembled through the action of Atg7 (E1-like enzyme) and Atg10 (E2-like enzyme)

The Atg12-Atg5-Atg16L1 complex is recruited to the PAS though the interaction of Atg16l1 with WIPI1/2, where it is thought to be important for regulating the curvature and growth of the nascent autophagosome. The Atg12-Atg5-Atg16L1 complex dissociates from the autophagosome vesicle upon closure*(Mizushima et al., 1998; Shaid et al., 2013).*

(5) the LC3 complex, containing LC3A/B/C, GABARAP, GABARAPL1/2, Atg7 (E1-like enzyme), Atg3 (E2-like enzyme)

In the second conjugation system, microtubule-associated protein 1 light chain 3 (LC3, also known as mammalian Atg8) is conjugated to the membrane lipid phosphatidylethanolamine (PE). This happens through a series of steps. First, newly synthesised LC3 is proteolytically cleaved by the cysteine protease Atg4. The exposed glycine resulting from this reaction facilitates the binding of LC3 to Atg7. Activated LC3 is then transferred to Atg3,with the assistance of the Atg12-Atg5-Atg16L1 complex, which enables the conjugation of LC3 to PE to create its lipidated soluble form, known as LC3-II *(Geng and Klionsky, 2008)*. Once formed,

LC3-II is incorporated into the autophagosome membrane where it is needed for autophagosome closure and proposed to play a scaffolding role in membrane growth. LC3-II is also important for the binding of autophagy adaptors and thus in mediating selective types of autophagy *(Geng and Klionsky, 2008).* LC3-II is distributed symmetrically on both sides of the isolation membrane. Upon closure of the autophagosome the LC3-II located on the outer facing membrane dissociates the fully formed autophagosome by a second Atg4-dependent cleavage, whilst the LC3-II found on the inner facing membrane remains inside the vesicle and will eventually be degraded after fusion with the lysosome *(Shaid et al., 2013) .*

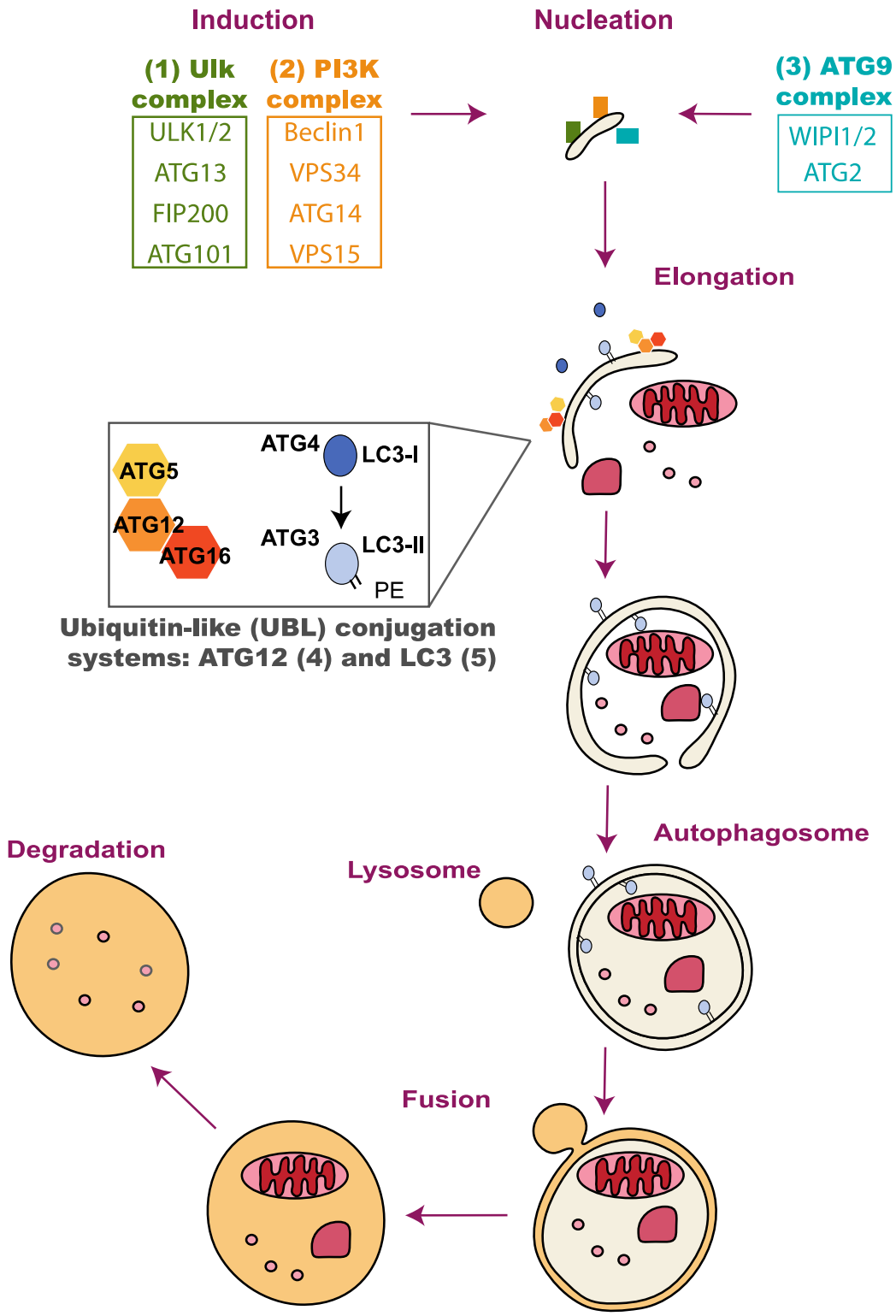


Figure 1. Schematic representation of the autophagy machinery.
The ULK (1) and PI3K (2) complexes initiate nucleation of the autophagosome. The ATG9 complex (3) provides membranes for the growing autophagosome. Two UBL conjugates systems (4 and 5) contribute to the formation of the isolation membrane. Once the autophagosome is complete it fuses with lysosomes and the internal cargo is degraded along with the autophagosome inner membrane.

1.1.3 Regulation of the autophagy pathway

As previously mentioned, autophagy can be directly regulated by both mTOR and AMPK in response to cellular starvation *(Dikic and Elazar, 2018).* In mammals, mTOR forms two functionally distinct complexes, mTORC1 and mTORC2, each with specific downstream targets and functions. mTORC1 is characterized by the presence of the scaffolding protein Raptor (regulatory-associated protein of mTOR), while mTORC2 is characterized by the presence of the Rictor (Rapamycin-insensitive companion of mTOR) protein *(Saxton and Sabatini, 2017).* Both of these complexes take part in regulating autophagy, although the role for mTORC1 is more direct *(Mehrpour et al., 2010).*

mTORC1 integrates a wide spectrum of signals: from detecting the presence of extracellular growth factors and cytokines, to detecting local cellular signals, like amino acid, glucose or oxygen levels *(Saxton and Sabatini, 2017).* Activation of mTORC1 leads to increased protein synthesis through its downstream targets: the eukaryotic initiation factor 4E (eIF4E)-binding proteins (4E-BP) and the ribosomal S6 kinases (S6K) *(Saxton and Sabatini, 2017)*. mTOR plays a pivotal role in coordinating anabolic responses and cell growth, and in regulating cellular metabolic pathways such as glycolysis, lipid synthesis or amino acid metabolism.

The autophagy pathway is regulated by mTORC1 in several ways. When nutrients are abundant, mTORC1 is active, promotes cell growth and suppresses autophagy through inhibitory phosphorylation of Ulk1/2 complex *(Saxton and Sabatini, 2017)*. mTORC1 also indirectly regulates autophagy by inhibiting TFEB (transcription factor EB), a master transcription factor controlling cellular clearance. mTORC1 mediated phosphorylation of TFEB leading to its sequestration in the cytoplasm, whilst upon starvation TFEB is released to regulate the expression of genes involved in lysosomal biogenesis and lipid catabolism *(Dikic and Elazar, 2018)*.

In nutrient starvation, mTORC1 is inhibited and Ulk1 dissociates from mTORC1 making it available to trigger autophagosome formation. Once activated, autophagy can further inhibit mTORC1 activity by promoting a negative feedback loop involving S6K, or through Ulk1-mediated inhibitory phosphorylation of Raptor *(Mehrpour et al., 2010).* Autophagy activity eventually leads to increased nutrient levels, which in turn reactivates mTORC1 and terminates autophagy.

Regulation of autophagy by the mTORC2 network is less well understood. So far, there is no evidence that mTORC2 interacts with components of the autophagy machinery directly. However, mTORC2 can modulate autophagy indirectly through phosphorylation of Akt (also known as protein kinase B; PKB), which in turn activates mTORC1 and inhibits autophagy *(Shimobayashi and Hall, 2014).* Additionally, activation of Akt results in nuclear exclusion and transcriptional inactivation of Foxo3 (Forkhead box O3), a transcription factor known to

promote autophagy by increasing the expression of several autophagy genes, including *Ulk2*, *Beclin 1*, *Vps34*, *Atg12*, *Atg4b* and *Lc3)* *(Fullgrabe et al., 2014)*.

Along with mTORC1 AMPK is the other key signalling hub for autophagy regulation. *(Mihaylova and Shaw, 2011)*. AMPK senses decreased cellular energy levels by detecting changes in cytoplasmic AMP-to-ATP concentrations. Additionally, three upstream kinases can also activate AMPK by phosphorylation of the α subunit: LKB1 (liver kinase B1), CAMKKβ ($Ca2^+$/calmodulin-activated protein kinase kinase-β) and TAK1 (TGF (transforming growth factor-β activated kinase-1) *(Blagih et al., 2015)*. When activated, AMPK initiates metabolic reprogramming by switching on ATP-producing pathways and switching off ATP-consuming anabolic pathways.

AMPK can activate autophagy, directly or indirectly, to initiate metabolic reprogramming toward catabolic reactions *(Mihaylova and Shaw, 2011)*. In direct regulation, AMPK phosphorylates the Ulk1/2 complex at multiple sites to trigger autophagosome formation. However, inhibitory phosphorylation of Ulk1 on Ser758 by active mTORC1 prevents association with AMPK and thereby prevents autophagy from happening *(Mihaylova and Shaw, 2011)*. In addition to direct interactions, AMPK can indirectly activate autophagy by inhibiting mTORC1 through at least two mechanisms: by activating the TSC1-TSC2 (tuberous sclerosis 1) complex - a critical upstream inhibitor of mTORC1, or by inhibitory phosphorylation of the Raptor subunit *(Andris and Leo, 2015)*. Interestingly, AMPK activity is not indispensable for autophagy induction, as starvation still induces autophagy in AMPK-deficient cells, suggesting a fine-tuning role for this kinase in autophagy modulation *(Andris and Leo, 2015).*

Some of the other important regulators of autophagy include anti-apoptotic protein family members (Bcl-2, Bcl-XL, and Mcl-1), which inhibit autophagy through interaction with Beclin1 (Kroemer *et al.*, 2010). The key tumour suppressor p53 is able to activate or inhibit autophagy, depending on its cellular localization *(Fullgrabe et al., 2014)*. The transcription factor NF-κB (nuclear factor-κB) can promote autophagy through increasing expression of some of the autophagy genes (including *Beclin1*) and NF-κB is in turn regulated by the autophagy pathway, although NF-κB can also downregulate autophagy, for instance after TNF stimulation *(Andris and Leo, 2015)*.

In summary, multiple intersecting systems regulate autophagy on many levels, reflecting the importance of this complex homeostatic pathway in cellular homeostasis and in facilitating adaptations to environmental factors.

1.1.4 Autophagy in T cells

The importance of the autophagy pathway in T cells homeostasis was first underscored by a study of *Atg5*$^{-/-}$ foetal liver chimeric mice which were described to harbour decreased numbers of thymic and splenic autophagy deficient CD4$^+$ and CD8$^+$ T cells *(Pua et al., 2007).*

Subsequently, several targeted genetic models with T cell-specific deletion of *Atg3, Atg5, Atg7, Vps34* or *Beclin1* focused on investigating T cells within the thymus and in secondary lymphoid organs, including the spleen and lymph nodes. These studies consistently showed decreased frequencies and numbers of CD4$^+$ and CD8$^+$ T in secondary lymphoid organs, whereas thymic development was largely unperturbed *(Parekh et al., 2013; Pua et al., 2009; Puleston et al., 2014; Willinger and Flavell, 2012)*.

Whilst decreased numbers of peripheral CD4$^+$ and CD8$^+$ T cells in the absence of T cell-specific autophagy were consistently observed, the mechanistic explanations for these findings differ between reports. Some studies pointed towards defective organelle turnover as the main cause of decreased fitness of autophagy-deficient T cells. For example, increased mitochondrial mass in naïve autophagy-deficient T cells, resulted in increased ROS production, which was suggested to lead to increased cell apoptosis *(Parekh et al., 2013; Pua et al., 2009; Willinger and Flavell, 2012).* In addition, increases in ER mass and changes in intracellular calcium signalling were also linked to impaired fitness and survival *(Jia et al., 2011)*. Moreover, *Beclin-1*-deficient T cells, showed similar decreases in peripheral T cell populations but did not have increased mitochondrial mass *(Kovacs et al., 2012).* However, the direct mechanism between the effects described above and cell survival was not formally proven in any of these studies.

A role for autophagy in the formation of memory CD8$^+$ T cells during viral infections was also described *(Puleston et al., 2014; Schlie et al., 2015).* These studies, which focused on *in vivo* responses of autophagy-deficient CD8$^+$ T cells to influenza or lymphocytic choriomeningitis virus infections, revealed new aspects of autophagic regulation of T cells. Both studies observed that autophagy was dispensable for the highly proliferative expansion phase of antigen activated CD8$^+$ T cells during early viral infections and that autophagy-deficient T cells did not show defects in effector cytokine production *(Puleston et al., 2014; Schlie et al., 2015)*. However, mice with autophagy-deficient CD8$^+$ T cells did not mount proper memory CD8$^+$ T cell responses during secondary challenge. Thus, activation of the autophagy pathway is crucial during the transition phase between late effector to memory T cells *(Puleston et al., 2014; Schlie et al., 2015)*. While the mechanisms behind these observations remains to be elucidated, comparison of metabolic profiles between WT and *Atg7*-deficient memory CD8$^+$ T cells suggest that metabolic adaptation might be involved *(Puleston et al., 2014).*

It is also worth considering that inhibition of a catabolic process, such as autophagy, can alter the availability of nutrients thus leading to dysregulations in cell metabolism *(Riffelmacher et*

al., 2018). A study from the Maloy lab in which the essential autophagy gene *Atg16l1* was selectively deleted in Foxp3$^+$ Treg cells found that these animals developed severe spontaneous multiorgan inflammation by 5 months of age *(Kabat et al., 2016a)*. This was characterized by an accumulation of Th effector subsets and a drastic depletion of Foxp3$^+$ Treg *(Kabat et al., 2016a).* Further analyses revealed that *Atg16l1*-deficient Treg cells had higher expression of glycolytic genes than Treg cells from control mice, whereas genes involved in FAS/FAO were markedly decreased *(Kabat et al., 2016a).* These metabolic differences were much more pronounced in Treg cells originating from the colonic lamina propria than from the spleen. Consistent with these findings, a parallel study reported that mice with seflective deletion of the essential autophagy genes Atg7 or Atg5 in FoxP3$^+$ Treg cells developed severe multiorgan inflammation by 5 months of age *(Wei et al., 2016). Atg7*-deficient Treg cells from these animals had aberrant mTORC1 activity, associated with increased c-Myc expression and heightened glycolytic metabolism *(Wei et al., 2016).*

All in all, while it is clear that autophagy plays a crucial role in the maintenance of peripheral CD4$^+$ and CD8$^+$ T cells and memory CD8$^+$ T cells, the way in which autophagy influences different aspects of T cell physiology in naïve vs activated T cells is still not completely understood. However, autophagy most likely performs many distinct functions in T cells and these roles could be highly context-dependent and might differ between distinct subsets of T cells.

1.1.5 Proteasomal degradation pathways

Whereas autophagy is the preferred degradative route for bulky cytosolic materials such as proteins aggregates, organelles or invading bacteria, the proteasome is in charge of degrading small, short-lived proteins. Proteasomes are cylindrical, cytoplasmic organelles that function primarily to degrade proteins that have been modified by the attachment of the small protein ubiquitin *(Dikic, 2017).*

The most common form of the proteasome in eukaryotes is the 26S proteasome - a multi-catalytic, ATP-dependent protease made up of two subcomplexes: the proteolytically active core particle (CP) 20S and a regulatory particle (RP) 19S subunit (also known as PA700) that can attach to one (26S proteasome) or both ends of the core particle (19S-20S-19S complex – Figure 2A) *(Finley, 2009; Murata et al., 2009).*

The 20S complex consists of two outer α-rings, which control the entrance of the substrate into the catalytic cavity, and of two inner β-rings that enable proteolytic breakdown of proteins into smaller peptides (Figure 2A). Each ring is comprised of seven distinct subunits, with the outer α-rings operating as a “gate”, which is often closed in the absence of activators *(Murata et al., 2009)*. The inner β-rings contain the proteolytic active sites β1, β2 and β5 which possess caspase-like, trypsin-like and chymotrypsin- like activities, respectively *(Finley, 2009;*

Murata et al., 2009). These active sites provide an essential source of amino-acids for the cells by digesting proteins entering the 20S complex into peptides of 2-24 amino-acids *(Finley, 2009; Murata et al., 2009)*. Indeed, increased cell lethality due to severe shortage of amino-acids is a major consequence of proteasome inhibition *(Suraweera et al., 2012).*

The 19S complex recognises polyubiquitylated substrate proteins and prepares them for degradation by the 20S *(Finley, 2009; Murata et al., 2009)*. The 19S RP consist of 19 different subunits and can be divided into two subcomplexes: the base and the lid, plus an additional subunit known as Rpn10, which is assumed to sit at the interface of the lid and the base (Figure 2A). The base of 19S is composed of six AAA^+ ATPase subunits (Rpt1- Rpt6) that form a hexameric ring and three non-ATPases proteins (Rpn1, Rpn2, Rpn13) *(Dikic, 2017).* Rpn10 and Rpn13 possess ubiquitin biding domain and are the established ubiquitin receptors. The ATPase subunits are required for substrate unfolding and opening of the α-ring, prerequisites for substrate entering into the CP *(Murata et al., 2009).* Rpn1, Rpn10, Rpn13 and Rpt5 capture ubiquitylated proteins either directly or through proteins that contain both ubiquitin-like (UBL) domains and ubiquitin-associated (UBA) domains The lid of 19S is composed of nine non-ATPase subunits: Rpn3, Rpn5-9, Rpn11, Rpn12, and Rpn15 (Sem1) *(Murata et al., 2009)*. Although the function of most of these subunits is unknown, one of the defined activities of the lid is the de-ubiquitylation of capture substrates, a process for which Rpn11, the deubiquinating enzyme, is essential.

In addition to the 26 proteasome, mammalian cells express a specialized form of the 20S proteasome, known as the immunoproteasome because of its prevalence in cells of hematopoietic origin and role in generating peptides for major histocompatibility complex (MHC) class I molecules *(Ferrington and Gregerson, 2012).* The benefit conferred by the immunoproteasome is attributed to structural changes in substrate binding pockets and an altered cleavage pattern, thus optimizing the quality and quantity of the peptides generated for presentation on MCH class I molecules *(Basler et al., 2013).* Of note, the immunoproteasome is also present in many non-immune cells where it is thought to be involved in regulation of protein homeostasis during inflammation and aging *(Lundh et al., 2017; Wagner et al., 2017).*

Three genes *PSMB8*, *PSMB9,* and *PSMB10* encode proteasome components that subtly modify the range of peptides produced by proteasomes *(Ferrington and Gregerson, 2012).* The expression of these genes is induced by pro-inflammatory cytokines like IFN-γ or TNF-α, and ultimately lead to the substitution of the constitutive catalytic subunits β1, β2 and β5 of the 20S proteasome with inducible catalytic subunits termed: β1i (LMP2), β2i (MEC-L) and β5i (LMP7) (Figure 2B). The 20S immunoproteasome (i20S) can bind at its two ends to the 19S RP proteasome, to on interferon inducible subunit called proteasome activator-28 α/β (PA28 or 11S proteasome), or to a combination of both proteasome subunits. to form different types of immunoproteasomes *(Ferrington and Gregerson, 2012)*.

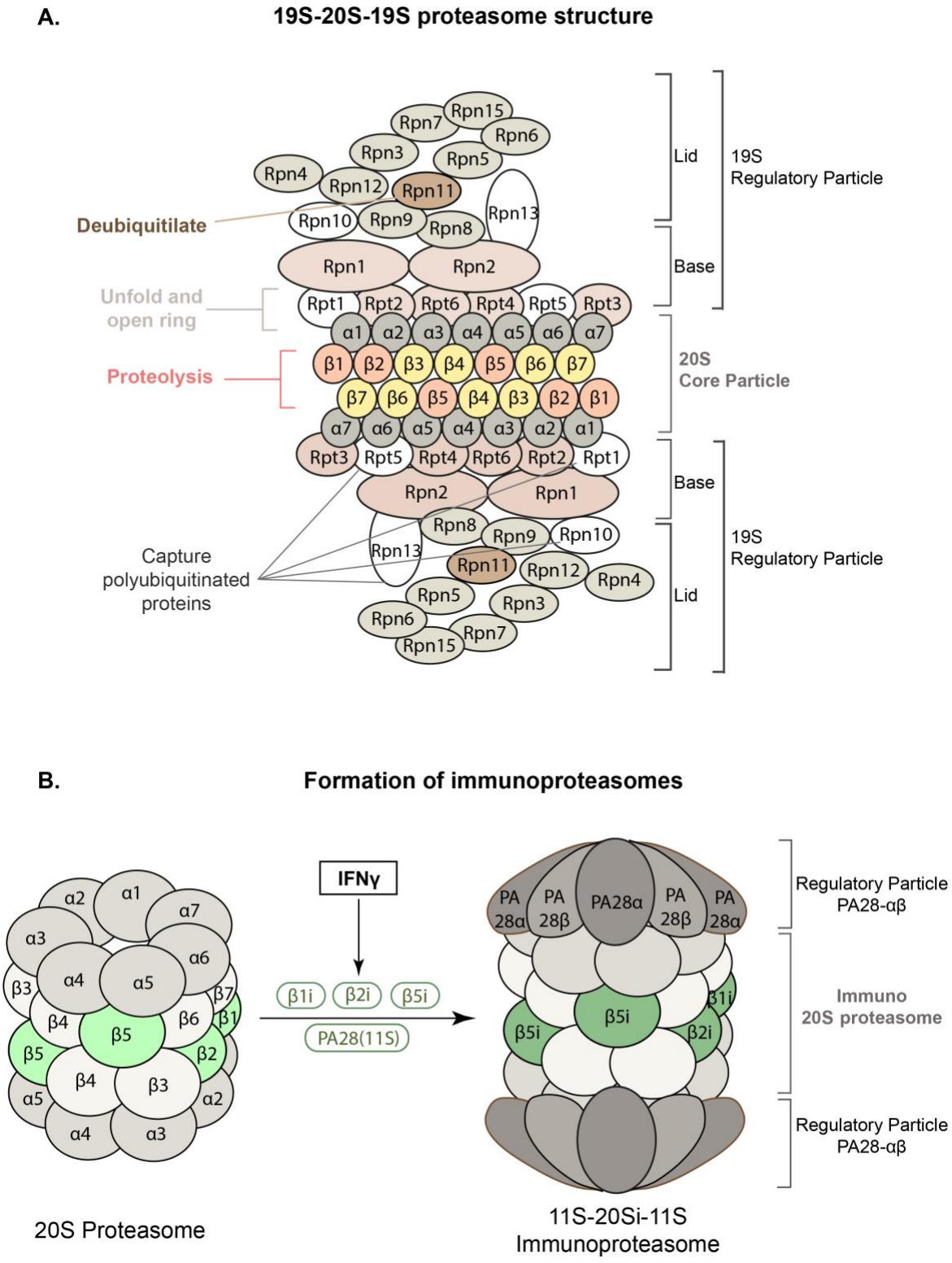


Figure 2. Schematic representation of possible combinations of 20S (A) and immuno-20S (B) proteasome cores with regulatory particles.

1.1.6 Regulation of proteasomal function

The proteasome pathway if tightly controlled by (*1*) transcription of genes encoding proteasomal subunits and assembly factors, (*2*) posttranslational modifications and (3) factors triggering degradation of proteasomes *(Dikic, 2017)*.

Under nutrient-rich conditions mammalian cells increase the expression of proteasome subunits in response to proteasome inhibition *(Dikic, 2017)*. Two mammalian transcription factors have been proposed to increase the expression of proteasome subunits in response to proteasome inhibition: Nrf1 and Nrf2 (nuclear factor erythroid 2-related factor 1 and 2 respectively) *(Rousseau and Bertolotti, 2018).* Nrf1 is an integral ER membrane protein that, under normal conditions, is constantly retrotranslocated from the ER to the cytosol, where it is rapidly ubiquitylated and degraded by the proteasome *(Dikic, 2017)*. When proteasomal function is compromised, NRF1 escapes proteasomal degradation, undergoes cleavage and becomes activated. Active NRF1 then translocate from the cytosol into the nucleus to induce expression of proteasome subunits *(Dikic, 2017)*.

Interestingly, translocation of active Nrf1 only happens when proteasomal capacity needs to be enhanced or proteasomal activity is inhibited. This “bounce back” mechanism has a significant medical relevance for therapeutic proteasome inhibitors, like bortezomib, which promptly triggers the upregulation of proteasome genes in malignant cells *(Mitsiades et al., 2002)*. This compensatory response likely promotes tumour survival and hampers therapeutic efficiency, as such proteasome inhibitors are usually one component of combination chemotherapy *(Mitsiades et al., 2002)*.

In addition, in nutrient-rich conditions, Nrf1 transcription is also upregulated by active mTORC1. mTORC1 induces Nrf1 through the posttranslational activation of SREBP1 (Sterol regulatory element-binding transcription factor 1), which in turn switches on the transcription of the *Nrf1* gene along with genes involved in lipid synthesis (Zhang et al., 2014). As previously mentioned, mTORC1 also functions as a master regulator of autophagy. Thus, active mTORC1 in nutrient-rich conditions, induces the production of new proteasomes and simultaneously suppresses the autophagy pathway *(Dikic, 2017)*.

However, this regulation process changes under stress conditions, such as starvation, oxidative stress, or growth factor deprivation. Here, mTORC1 is inhibited, thus biosynthetic processes are halted, autophagy is induced and the transcription factor Nrf2 is activated. *(Dikic, 2017)*. Nrf2 not only regulated the transcription of proteasomal subunits but also activates the expression of factors that maintain proteasome assembly *(Kwak et al., 2003).* Proteasome assembly is a highly complex process, for which the exact mechanistic details have not yet been identified in mammalian cells *(Dikic, 2017)*.

Nrf2 not only regulates the transcription of proteasomal subunits but also activates a general stress response that includes oxidative and heat stress response pathways and an increase in cellular protein folding capacity *(Kwak et al., 2003)*. Unlike Nrf1, Nrf2 is not tethered to the ER but is localised in the cytosol and the mitochondrial surface *(Dikic, 2017)*.

Post-translational modifications of the proteasome offer additional possibilities to regulate assembly, localisation and the degradation capacity of the proteasome. Large-scale analyses of the proteasome have revealed more than 110 post-translational modifications on the 26S proteasome, however, the functional consequences of most of these modifications remain unknown *(Rousseau and Bertolotti, 2018)*. Those modifications that have been functionally characterized are beyond the scope of this thesis.

Selective proteasome degradation by autophagy (proteaphagy) is a highly regulated process mediated through distinct mechanisms depending on the physiological context *(Marshall et al., 2015)*. Proteaphagy has been described in mammalian cells in response to amino acid starvation, which triggers autophagy activation and the ubiquitination multiple RP proteasomal subunits including the ubiquitin receptors Rpn1, Rpn10, and Rpn13 *(Marshall et al., 2015)*. The ubiquitin-tagged proteasome is recognized by the autophagy receptor sequestosome 1 (SQSTM1 or p62), which is also implicated in several types of selective autophagy *(Kirkin and Rogov, 2019).* p62 functions as selective autophagy receptor that specifically links the polyubiquitinated proteasomes to the growing autophagosome membrane via interactions with Atg8/LC3 *(Kirkin and Rogov, 2019)*. After complete engulfment of the proteasome, the autophagosome fuses with the lysosome, where the proteasome gets digested.

1.1.7 Cross talk between autophagy and proteasome

Several studies have shown that impairment of proteasomal degradation induces autophagy *(Tanaka and Matsuda, 2014).* However, it remains unclear whether autophagy inhibition can induce compensatory proteasome activation. Given the popular dogma that autophagy degrades larger cellular structures and that the proteasome degrades small proteins, proteasomal degradation is unlikely to functionally replace autophagy.

Nevertheless, molecular connections between these two degradation systems occur at multiple levels *(Dikic, 2017)*. For example, the proteasome is responsible for the degradation of misfolded proteins in an attempt to prevent them from forming large aggregates. When the proteasome is defective or overwhelmed, misfolded proteins accumulate and form large aggregates, which are degraded by autophagy *(Dikic, 2017)*. Thus, both degradative machineries collaborate to clear misfolded proteins and maintain the proteostasis *(Dikic, 2017)*.

Another connection is provided by ubiquitin which serves as a signal to target proteins for degradation by both systems *(Shaid et al., 2013).* Selective autophagy employs autophagy receptors, such as p62, to target cargo to autophagosomes. These are modular proteins that bind onto the ubiquitin attached to the cargo on one side and to autophagosome-bound proteins (members of the LC3 family) on the other side. As described above, the proteasome is itself a substrate that undergoes ubiquitination and selective degradation by autophagy *(Shaid et al., 2013; Waite et al., 2016)*.

From the perspective of this thesis, the most interesting connection is that these two degradative systems are under the control of one central regulator, mTORC1. As previously mentioned, under nutrient-rich conditions, mTORC1 is activated to promote anabolic processes, which induces production of new proteasomes (through Nrf1) presumably to maintain proteastasis as active mTOR turns on protein synthesis whilst simultaneously suppressing autophagy *(Dikic, 2017)*. Under cellular stress, like nutrient scarcity, mTORC1 is inhibited in order to decrease cellular anabolism and favour catabolic processes, including autophagy and the proteasome (through Nrf2) *(Dikic, 2017)*.

1.1.8 The proteasome in T cell responses

As previously mentioned, specialised proteasome structures termed immunoproteasomes can be involved in producing peptides for presentation on MHC class I molecules. Thus, the immunoproteasome plays a pivotal role in shaping naïve $CD8^+$ T cell repertoire in the thymus and cytotoxic T cell responses in the periphery in order to avoid generation of auto-reactive T cells *(Basler et al., 2006; Chen et al., 2001).* The immunoproteasome has been proposed to also play a role in T cell expansion, Th cell differentiation, metabolism and cytokine production *(Basler et al., 2013).*

Muchamuel *et al*. showed that selective inhibition of β5i (LMP7) blocked the production of IL-23 by activated monocytes and the production of IFNγ and IL-2 by T cells, whereas the inhibition of β5 did not substantially affect cytokine release in an experimental model of arthritis *(Muchamuel et al., 2009).* In another study, selective inhibition or genetic ablation of β5i resulted in diminished Th1 and Th17 differentiation, enhanced development of Treg cells but showed no effect on Th2 differentation *(Kalim et al., 2012).*

Recently, the asymmetrical division of the proteasome was shown to impact $CD8^+$ T cell fate *(Widjaja et al., 2017)*. Daughter cells with an effector phenotype showed low proteasome activity, whereas memory-fated daughter cells exhibited higher activity. Proteasome-activators such as cyclosporine were found to tip the balance of dividing $CD8^+$ T cell progeny toward memory T cells *(Widjaja et al., 2017)*.

1.2 The development and functioning of CD4+ Th subsets

CD4+ T cells are the main focus of the work presented in this thesis. The sections below detail their development, activation and functions.

1.2.1 Thymic selection and development of CD4+ T cells

CD4+ T cells derive from lymphoid progenitor cells that migrate from the bone marrow into the thymus, where they undergo multiple developmental stages on the way to maturation and antigen specificity *(Koch and Radtke, 2011)*.

The thymus is morphologically divided into two regions that support distinct phases of T cell development: the cortex and the medulla *(DeFranco et al., 2007)*. Early stage development of T cell precursors (also called thymocytes) are characterized by their movement toward the outer cortex and their expansion there. As maturation proceeds, thymocytes move into the medulla where the more mature cells are located prior to their exit into the periphery. This development process, from the arrival of an early lymphoid progenitor into the thymus to the export of a mature CD4+ or CD8+ T cell takes about 12 days *(DeFranco et al., 2007).*

The stages of T cell development in the thymus are largely defined by the expression of the CD4 and CD8 co-receptors. Early lymphoid progenitors express neither of these co-receptors, that is, they are double negative (DN) for CD4 and CD8 *(Koch and Radtke, 2011)*. To progress past this stage thymocytes need to undergo Rag-dependent rearrangement of their TCRβ locus *(DeFranco et al., 2007)*. In order to produce mature T cells able to recognise a wide variety of foreign antigens, a diverse array of T cell receptors (TCR) is generated at this stage by a process of somatic gene rearrangement termed V(D)J recombination. The TCR is made up of a series of alternative gene fragments: variable (V), joining (J) and, in the case of TCRβ, diversity (D) gene segments are joined together to form a completed variable region gene *(DeFranco et al., 2007)*. This process leads to the enormous amount of variability of the TCR repertoire. The recombination activating genes 1 and 2 (*Rag1* and *Rag2*) are crucial for rearrangement process, as *Rag1*- and *Rag2*-deficient mice have no lymphocytes *(Mombaerts et al., 1992; Shinkai et al., 1993)*.

Thymocytes that have successfully rearranged their TCRβ chains and produce a functional pre-TCR complex proceed to the double positive (DP) developmental stage in which the co-receptors CD4 and CD8 are upregulated and V(D)J recombination shifts from the TCRβ locus to the TCRα locus *(Schatz and Swanson, 2011).* Cells that fail to produce a functional pre-TCR are eliminated by apoptosis. This process is referred to as the beta-selection checkpoint *(DeFranco et al., 2007)*.

Once a TCRα chain has been rearranged it can combine with the pre-TCR complex to produce the αβ-TCR that can react with self-peptides MHC (major histocompatibility complex) class I

or class II in the thymic cortex *(DeFranco et al., 2007)*. Those cells that engage antigen presented on MHC I or MHC II with appropriate affinity are positively selected toward the CD8 and CD4 lineages respectively, whereas cells those cells that interact with a weaker affinity die by apoptosis *(Stritesky et al., 2012).*

Thymocytes then migrate into the medulla to undergo negative selection, which ensures deletion of thymocytes with potentially pathogenic reactivity (central tolerance). Thymocytes are presented with peptides expressed by thymic medullary epithelial cells (mTEC) and thymic antigen presenting cells (APC) *(Derbinski et al., 2001)*. The affinity of peptide-MHC–TCR binding dictates the fate of the thymocytes. Intermediate affinity to self-peptide-MHC complexes promotes selection, whereas high affinity leads to the removal of such self-reactive clones by induction of apoptosis *(DeFranco et al., 2007)*.

Foxp3$^+$ Treg cells are thought to originate from clones whose TCR receptor exhibits affinity at the threshold between intermediate and high, which enables generation of Treg cells with relatively high self-reactivity, that are able to enforce dominant peripheral tolerance *(Stritesky et al., 2012; Xing and Hogquist, 2012)*.

The negative selection process is controlled by the transcription factor autoimmune regulator (AIRE) *(Anderson et al., 2002)*, which endows mTEC with the capacity to present peptides derived from peripheral tissue antigens that would not otherwise be present in the thymus *(Mathis and Benoist, 2009)*. The importance of AIRE is illustrated in patients that carry a mutated *AIRE* variant and develop a severe autoimmune disease known as Autoimmune Polyendocrinopathy-Candidiasis-Ectodermal Dystrophy (APECED) *(Finnish-German, 1997)*.

Finally, the thymocytes that successfully complete beta, positive and negative selection give rise to two distinct populations of immunocompetent T cells: MHCII-restricted CD4$^+$ T cells and MHCI-restricted CD8$^+$ T cells. These leave the thymus and migrate into the blood, lymphoid tissues and organs throughout the body.

These recirculating naïve T cells can be activated in secondary lymphoid organs by antigen-driven TCR signalling and co-stimulatory signals provided by activated APCs *(Chen and Flies, 2013)*.

1.2.2 Metabolic reprogramming during CD4⁺ T cell activation

Activation of CD4⁺ T cells on encounter with antigens in the periphery initiates a dynamic network of transcriptional and translational changes which go hand in hand with metabolic adaptations to match the bioenergetic demands of proliferating cells *(MacIver et al., 2013)*. Naïve, quiescent CD4⁺ T cells are characterized by a metabolic program that favours energy production over biosynthesis and generally rely on mitochondrial oxidative pathways. During the initial phase after activation, oxidative metabolism is downregulated, while biosynthetic pathways are increased *(Wang and Green, 2012).*

CD28 is one of the best characterized costimulatory receptors on naïve T cells, it promotes cell proliferation by activating different signalling pathways that sustain the bioenergetic demands associated with T cell activation *(Smith-Garvin et al., 2009)*. For example, CD28 co-stimulation has been described to upregulate glucose utilization allowing T cells to meet the biosynthetic demands associated with activation *(Frauwirth et al., 2002; Jacobs et al., 2008).*

One critical signalling pathway for the transduction of the TCR/CD28 signal in activated T cells is the PI3K–Akt pathway, which promotes entry into the cell cycle and resistance to apoptosis; however, its role in the metabolic reprogramming of T cells is debated, since the requirement for Akt activation in promoting glycolytic metabolism in activated T cells is unclear *(Finlay and Cantrell, 2011)*. T cell activation also leads to the induction of the mechanistic target of rapamycin (mTOR) pathway, either through the PI3K–Akt pathway or independently. As described in a previous chapter, mTOR plays a pivotal role in regulating cellular metabolic pathways such as glycolysis, lipid synthesis, and amino acid metabolism (Figure3).

During T cell activation, the glycolytic program is activated by transcription factors, such as c-Myc and HIF-1α, which orchestrate the expression of glycolytic enzymes and glucose transporters that facilitate increased uptake and catabolism of glucose (Figure 3) *(Yang and Chi, 2012)*. Once in the cytoplasm, glucose can be metabolized to yield two units of pyruvate, which are further processed according to the availability of oxygen. In aerobic conditions, pyruvate is further degraded to the acetyl group of acetyl-CoA and fed into the citric acid cycle, also known as the tricarboxylic acid (TCA) or Krebs cycle, which occurs in the inner layer of the mitochondria *(Nelson et al., 2013)*. The NADH and $FADH_2$ produced at each turn of the cycle donate electrons to the ETC, a series of membrane-bound carriers, called complexes I–IV, located in the inner mitochondrial membrane (Figure 3). The large amount of energy released during the course of the electron transfer fuels the production of over 30 molecules of ATP through OXPHOS *(Gerriets and Rathmell, 2012; Nelson et al., 2013)*. By contrast, under low oxygen conditions, glucose is reduced to lactate *via* anaerobic glycolysis, generating only two molecules of ATP per one unit of glucose (Figure 3) *(Fracchia and Walsh, 2015)*.

Some cells, like tumour cells and proliferating T cells, adopt an unusual metabolic profile in which they preferentially utilise glycolysis to generate ATP, even when oxygen is not limiting. This so called "aerobic glycolysis" was first described by the German biochemist Otto Warburg for tumour cells, and it is thus known as the "Warburg effect" *(Warburg et al., 1927)*. Quiescent T cells generate most of their energy through OXPHOS, but T cell activation induces metabolic remodelling toward a program of anabolic growth and enhanced protein synthesis, necessitating greater uptake of nutrients. Since ATP production *via* glycolysis is much less efficient than *via* OXPHOS, it seems counterintuitive that this pathway would dominate in proliferating T cells *(Fracchia and Walsh, 2015)*. One potential explanation is that proliferating cells prefer reducing pyruvate to lactate in order to generate NAD^+, which allows glycolysis to continue to convert glucose metabolites into nucleotides via the pentose phosphate pathway (PPP) (Figure 3). Proliferating cells require an extensive supply of nucleotides to support rapid replication.

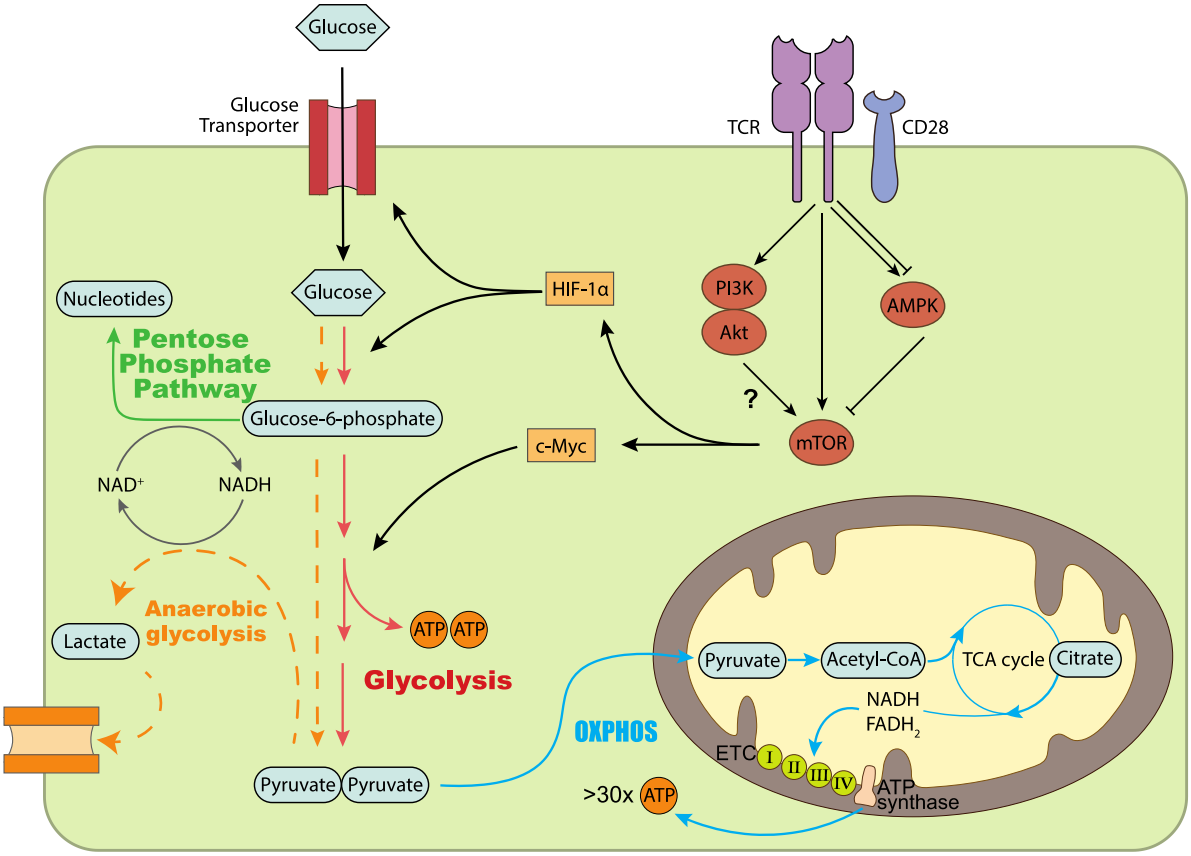


Figure 3. Main metabolic pathways in T cells.

Glycolysis (red arrows) begins with the uptake of extracellular glucose from the environment surroundings the cells. The glycolysis pathway then processes the glucose in the cytosol to yield two units of pyruvate and other by-products. Under low oxygen conditions, glucose can be metabolised into lactate via anaerobic glycolysis (orange arrows), with the final step in this pathway involving the conversion of pyruvate to lactate. In aerobic conditions pyruvate is further degraded to the acetyl group of acetyl-CoA and fed into the tricarboxylic acid (TCA) cycle to generate ATP via the process of oxidative phosphorylation (OXPHOS) (blue arrows). Glucose breakdown intermediates produced during glycolysis (glucose-6-phosphate) can be metabolised via the pentose phosphate pathway (green arrow) donating important building-blocks for nucleotides synthesis. TCR stimulation induces the expression of several genes involved in glucose transport and metabolism by recruiting the transcription factors c-Myc and HIF-1a via activation of the PI3K-Akt- mTORC1 axis.

The balance between protective immunity and chronic inflammation requires that $CD4^+$ T cells appropriately differentiate into the effector or regulatory lineages. Initially, two subsets of $CD4^+$ T cells were characterised: T-helper 1 (Th1) that specialised in immune responses against intracellular bacteria and T-helper 2 (Th2) cells specialised in responses against viruses and parasites *(Mosmann et al., 1986).* Since that time, the breadth of $CD4^+$ T cell subsets have broadened to a more expansive collection including: Th17, T follicular helper (Tfh), Th9 as well as thymically derived and peripherally induced regulatory T cells (tTreg cells and pTreg cells, respectively) *(Rich, 2013).* Each T cell subset can be characterized by its ability to sense different inductive cytokines, program the expression of distinct transcription factors, produce select cytokines as well as utilise distinct metabolic programmes to support their functioning (Figure 4). While polarised immune responses are critical for fighting specific pathogens, it is important to emphasize that Th lineages are not definitive and exhibit a range of plasticity, meaning that a single $CD4^+$ T cell can take on characteristics of many T cell subsets simultaneously or at different times during the course of its life cycle *(DuPage and Bluestone, 2016).*

Here, the major Th cell subsets will be briefly described, using the framework of polarized T cell subsets, with a more comprehensive literature presented on Th2 and Treg cells functions.

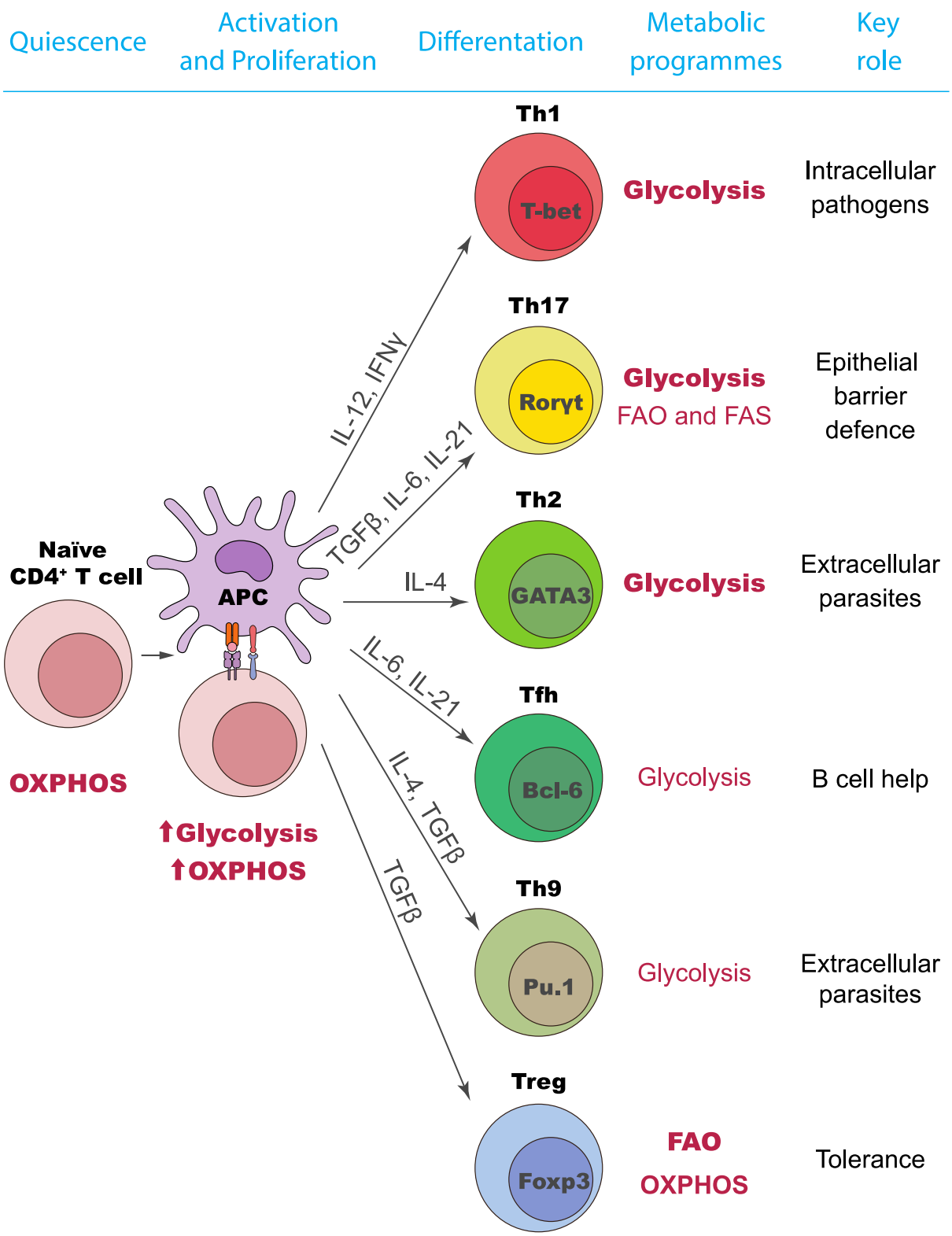


Figure 4. CD4⁺ T cell differentiation schematic.

APCs prime naïve CD4⁺ T cells and in the presence of polarising cytokines promote differentiation of distinct Th cell subsets via activation of lineage defining transcription factors. These transcriptional and translational changes go hand in hand with metabolic programmes to match the bioenergetic requirement for the effector function of each subset. While T cell differentiation is presented here in a linear fashion, these processes are not as straightforward and exhibit a range of plasticity.

1.2.3 Th1 cells

Th1 cells are characterised by the expression of the master transcription factor T-bet and production of high amounts of IFNγ, but can also secrete TNF-α, GM-CSF, lymphotoxin and also IL-2 *(Szabo et al., 2003)*.

The strength of TCR signalling during antigen-MHC interactions is thought to influence the fate of naïve CD4 T cells with stronger signalling leading to Th1 differentiation while weak signalling is thought to favour Th2 differentiation *(Tao et al., 1997).*

Thus, strong TCR activation of naïve $CD4^+$ T cells activates T-bet in a STAT1 (signal transducer and activator of transcription 1)-dependent manner *(Lighvani et al., 2001)*. As Th1 differentiation proceeds, secreted IFNγ binds to its receptor, leading to STAT1 activation, which further increases T-bet and leads to reinforcement of Th1 commitment through an autocrine feedback loop *(Lighvani et al., 2001)*. In addition, T-bet acts in conjunction with IRF1 (IFN-γ-inducible transcription factor 1) to up-regulate expression of the IL-12 receptor which can further enhance and maintain Th1 differentiation through the activity of STAT4 *(Kano et al., 2008; Mullen et al., 2001; Schulz et al., 2009).* IL-18 can further synergise with IL-12 to promote IFN-γ production independent of TCR activation *(Yoshimoto et al., 1998)*. Additionally, another STAT1-activating cytokine, IL-27, can also induce T-bet and IL-12R expression in $CD4^+$ T cells *(Takeda et al., 2003).*

Metabolic sensors that favour differentiation towards the Th1 lineage include signalling through mTORC1. Rheb-deficient mice have impaired mTORC1 function and fail to generate Th1 and Th17 cells but are able to differentiate Th2 cells *(Delgoffe et al., 2011)* .Conversley, T cells from Rictor-deficient mice, in which mTORC2 activation is impaired, fail to differentiate into Th2 cells but are able to generate Th1 and Th17 cells *(Delgoffe et al., 2011).* Recently, glucose uptake and aerobic glycolysis through lactate dehydrogenase A (LDHA) have been described as essential in order to support Th1 differentiation and IFNγ production*(Peng et al., 2016)*. The importance of this pathway for Th1 responses *in vivo* was shown by conditional deletion of LDHA in T cells which protected susceptible mice from Th1-mediated lethal auto-inflammatory disease *(Peng et al., 2016)*. This may suggest that when Th1 cells migrate to a glucose-deprived inflammatory environment, the reduced glucose availability will lead to a drop-in glycolysis and decreased IFNγ production, possibly representing intrinsic negative feedback mechanisms to inhibit excessive Th1-mediated immune pathology *(Peng et al., 2016)*.

1.2.4 Th17 cells

Th17 cells are largely confined to barrier sites such as the intestine, lungs, or skin, where they play a key role in defence from opportunistic pathogens and maintenance of epithelial barrier function *(Ishigame et al., 2009; Ivanov et al., 2008).* However, it is also evident that their aberrant production of inflammatory cytokines is important in driving a number of autoimmune diseases *(Park et al., 2005).* Th17 cells are defined by expression of Rorγt and production of signature cytokines IL-17A, IL-17F, IL-21 and IL-22 *(Ivanov et al., 2008)*.

While Rorγt expression is necessary for Th17 differentiation, it is not sufficient, and interactions with multiple other transcription factors are involved, including STAT3, IRF4, Runx1, and Ahr *(Ciofani et al., 2012; Gaffen et al., 2014)*. The differentiation into Th17 cells requires TGF-β together with IL-1β and STAT3-activating cytokines, like IL-6 or IL-21, which promote induction of Rorγt *(Korn et al., 2009)*. IL-23 was originally thought to be essential for Th17 cell differentiation, however, now it is well established that IL-23 is dispensable for Th17 cell differentiation, and instead promotes their survival and acquisition of pathogenic effector potential *(Ghoreschi et al., 2010; McGeachy et al., 2007).* Th17 cells can also express IL-10: while Rorγt$^+$IL-17A$^+$IFN-γ$^+$ Th17 cells can drive pathogenic responses, Rorγt$^+$IL-17A$^+$IL-10$^+$ Th17 cells likely represent a non-pathogenic subtype *(Zielinski et al., 2012).*

Recent evidence suggests that lipid metabolic pathways play a role in regulating the dichotomous function of Th17 cells under normal and pathogenic conditions *(Berod et al., 2014; Gaublomme et al., 2015; Wang et al., 2015)*. Lipogenic pathways are a crucial part of T cell metabolic reprogramming, as proliferating T cells require fatty acids for membrane synthesis and also for a plethora of other cellular processes, such as signalling and energy production. Activated T cells rapidly augment fatty acid synthesis (FAS) while concomitantly decreasing FAO (*93*). FAS takes place in the cytosol and commences with ATP consumption through the carboxylation of acetyl-CoA to malonyl-CoA, a reaction catalysed by acetyl-CoA carboxylase 1 (ACC1) *(Lochner et al., 2015).* By contrast, FAO occurs mainly in the mitochondria and involves generation of acetyl-CoA, which can be directly shuttled into the TCA cycle and further oxidized to generate ATP *via* OXPHOS. The enzyme acetyl-CoA carboxylase 2 is located in the inner mitochondrial membrane and promotes mitochondrial FAO (*111*). These fatty acid metabolic pathways have emerged as important regulators of Th17 function. ACC1 can regulate the balance between Th17 and Treg cells, as pharmacological or genetic blockade of ACC1 impaired differentiation of human and mouse Th17 cells but favoured the induction of Foxp3$^+$ Treg cells *(Berod et al., 2014; Gaublomme et al., 2015; Wang et al., 2015)*.

Another cell-intrinsic metabolic pathway that has been associated with a pathogenic Th17 phenotype is mTORC1. Similarly to Th1 cells, Th17 cells require mTORC1 activation during differentiation, but are additionally dependent on HIF-1α which promotes glycolysis and

increases the expression of RORγt while targeting Foxp3 for proteasomal degradation *(Dang et al., 2011; Shi et al., 2011).* Deletion of HIF-1α in $CD4^+$ T cells abrogated Th17 development and promoted Treg cell differentiation, even under Th17 culture conditions *(Dang et al., 2011; Shi et al., 2011)*. Moreover, deletion of *p70S6KI* (which encodes a serine/threonine kinase that is downstream from mTORC1) resulted in decreased expression of Th17-associated genes, including *il17a, il17f*, and *il23r* *(Sasaki et al., 2016*). By contrast, differentiation into Treg, Th1, or Th2 cells was not altered in the absence of *p70S6KI*, suggesting that it plays a selective role in the differentiation of Th17 cells *(Sasaki et al., 2016*).

1.2.5 Th2 cells and type 2 responses

Type 2 immunity, typified by the secretion of IL-4, IL-5 and IL-13 cytokines, is critical for protection against metazoan parasites, however, these cytokines also underlay the pathologic inflammation associated with allergic diseases *(Pulendran and Artis, 2012)*. Additional functions, like resistance against toxins and venoms *(Tsai et al., 2015)*, promoting tissue repair pathway *(Gause et al., 2013)*, and regulation of glucose homeostasis, adiposity and thermogenesis *(Wu and Qiu, 2019)* have also been assigned to type 2 immune responses.

The cell lineages that interact to coordinate an effective type 2 immune response involve an ever-expanding list of innate immune cells: basophils, eosinophils, mast cells, M2 macrophages (also known as alternatively activated macrophages), dendritic cells and group 2 innate lymphoid cells (ILCs); as well as adaptive immune cells, of which Th2 cells function as the central mediators of the type 2 immune response by promoting B cells to secrete immunoglobulin E (IgE) *(Gause and Artis, 2016)*. IgE further binds to high-affinity IgE receptors (FceR1) on basophils and mast cells, encouraging the secretion of several cytokines and inflammatory mediators such as histamine, heparin, and serotonin *(Pulendran and Artis, 2012)*.

Th2 lineage commitment is orchestrated by the transcription factor Gata3, induced in response to IL-4 driven activation of STAT6 *(Zheng and Flavell, 1997).* Gata3 can positively regulate its own expression by binding to its regulatory elements and also to *Il5* and *Il13* promoters to induce their expression *(Gause and Artis, 2016)*. Gata3 deficiency in T cells abrogates Th2 differentiation and Th2 cytokine production *(Pai et al., 2004; Zhu et al., 2004)*. Additionally, multiple studies support a role for mTORC2 as a preferential signalling pathway in the differentiation, function, and metabolism of Th2 cells although mTORC1 signalling is also needed *(Delgoffe et al., 2011)*. For example, *Rheb*-deficient mice have impaired mTORC1 function and fail to generate Th1 and Th17 cells but are able to differentiate Th2 cells *(Delgoffe et al., 2011)*. Conversely, T cells from *Rictor*-deficient mice, in which mTORC2

activation is impaired, fail to differentiate into Th2 cells but are able to generate Th1 and Th17 cells *(Delgoffe et al., 2011)*.

When the Th1/Th2 "division of labour" paradigm was originally described by Mosmann and Coffman, Th2 responses were considered to represent a regulatory arm of adaptive immunity that counteracted the detrimental inflammatory consequences of Th1 mediated immunity *(Mosmann et al., 1986).* Although today it is well appreciated that there is a more complex network that regulates the differentiation and function of Th subsets, there is still a close relationship between Th1 and Th2 cells. Gata3 prevents the production of IFNγ, while T-bet directly inhibits Gata3 *(Usui et al., 2003; Yagi et al., 2010).* Also, *T-bet* deficient mice are known to develop severe airway inflammation *(Finotto et al., 2002).*

Initiation of type 2 immune responses is believed to predominantly result from the production of danger-associated molecular patterns (DAMPs), endogenous signals that alert neighbouring cells about potential damage, by host immune and non-immune cells *(Patel et al., 2014; Wills-Karp et al., 2012).* DAMPs further trigger the release of alarmins, most notably IL-33, IL-25 and thymic stromal lymphopoietin (TSLP), that attract and activate various innate immune cells to the site of tissue injury and together with these promote Th2 cell activation *(Kitajima et al., 2011; Wills-Karp et al., 2012; Wynn, 2015)*.

Given that helminths are large pathogens that cause significant tissue damage, by either eating host tissue for food or by setting up a niche for reproduction *(Allen and Wynn, 2011)*, it is perhaps not surprising that helminthic infections trigger a wound healing response to repair the resulting damage. The study of helminth infection has provided valuable insight into understanding how Th2 cytokines mediate wound healing. However, if not appropriately regulated, Th2 responses can drive fibrosis, a pathologic condition where excess scar tissue is formed to fill the wound instead of newly regenerated tissue *(Gause and Artis, 2016)*. One of the first stages of wound healing involves the creation of a type 2 cytokine milieu that mediates the generation of alternatively activated macrophages (AAM). These macrophages contribute to the wound repair process through the generation of a battery of molecules, including: antimicrobial peptides (resistin-like molecule-α - RELMα), growth factors (vascular endothelial growth factor - VEGF, insulin-like growth factor 1 - IGF1), enzymes (matrix metalloproteinases – MMP) and collagens (α1 type 1 collagen) *(Lloyd and Snelgrove, 2018)*. Finally, in response to Th2 cytokines and AAM-derived factors, non-immune cells, like fibroblasts and epithelial cells, migrate to the wound site to generate newly formed functional tissue *(Gause and Artis, 2016)*.

1.2.6 T follicular helper (Tfh) cells and other non-regulatory $CD4^+$ T cell subsets

T follicular helper became recognized as a separated lineage of $CD4^+$ T cells that specialize in providing help to B cell in order to produce antibodies in response to protein antigens *(Linterman et al., 2009)*.

T follicular helper cells are characterized by the expression of the chemokine receptor CXCR5, the inducible T cell co-stimulator ICOS, the transcription factor Bcl-6, and the production of IL-21 *(Crotty, 2011)*. They have a critical role in the formation and maintenance of germinal centres (GCs) that promote the generation of affinity matured B cells and as such are essential for the production of most types of antibodies *(Crotty, 2011)*. The transcriptional repressor Bcl-6 orchestrates Tfh lineage commitment and is both necessary and sufficient to drive Tfh differentiation *(Nurieva et al., 2009).* Bcl-6 was shown to repress T-bet, Gata3 and Rorγt, thereby blocking the Th1, Th2 and Th17 transcriptional programmes. Tfh cell lineage specification was shown to be promoted by the presence of IL- 6 and IL-21 *(Crotty, 2011)*.

Not much is known about specific metabolic requirements of Tfh cells, however some studies suggest that these cells have decreased mTORC1 activity which seem to favour their differentiation at the expense of Th1 and T-bet expression *(Ray et al., 2015)*. In addition, Tfh cells are thought to be less glycolytic than Th1 cells and instead to relay mainly on mitochondrial respiration. This might be driven by Bcl-6, as overexpression of Bcl-6 in naïve $CD4^+$ T cells recapitulates the metabolic characteristics observed in Tfh cells *(Ray et al., 2015).*

The collection of $CD4^+$ Th cell subsets has broadened in the last years, and new subsets dependent on different combinations of cytokines and distinct transcription factors for their development have been described. These include Th9 and Th22 cells, named according to the most abundant cytokine they produce, IL-9 and IL-22, respectively.

Th9 effector cells develop from naïve $CD4^+$ T cells in the presence TGF-β and IL-4, secrete IL-9 in large amounts, are also known to produce IL-10 and IL-21, and have been implicated in some inflammatory allergic processes, such as asthma *(Veldhoen et al., 2008).* Th9 cells are closely related to Th2 cells and are similarly specialised in the defence against extracellular parasites. Their differentiation results in the induction of STAT6 and the transcription factor Pu.1 *(Kaplan et al., 2015)*.

$CD4^+$T cells, which express IL-22 but no IFNγ, IL-4 or IL-17α are termed Th22 cells. They can be differentiated in the presence of IL-6 and tumour necrosis factor (TNF)-α. They also express AHR (aryl hydrocarbon receptor) transcription factor, which likely maintains IL-22 production. Th22 cells express the CCR4 and CCR10 chemokine receptors, and are thus thought to play a central role in the skin, contributing to host defence against pathogens and in promoting skin repair *(Sonnenberg et al., 2011)*.

1.2.7 Treg cells

$CD4^+Foxp3^+$ Treg cells produce immunosuppressive cytokines such as IL-10 and TGF-β and are critical for maintaining immune tolerance and preventing deleterious inflammatory responses *(Savage et al., 2020).* However, the same immunosuppressive functions of Treg cells may have negative consequences in other contexts. For example, Treg cells may contribute to establishing chronic infections and promoting tumour progression. Thus, tight regulation of Treg development and function is critical.

The master transactional regulator, Foxp3, endows Treg cells with their immunosuppressive phenotype and is indispensable for their development and function. Patients with loss of function mutations in the *FOXP3* gene develop IPEX syndrome (immunodeficiency, polyendocrinopathy, and enteropathy, X- linked syndrome), which manifests with multiorgan inflammation *(Wildin et al., 2001)*. Likewise, scurfy mice, which also carry a mutation in the *Foxp3* gene, develop a lymphoproliferative disease that parallels the symptoms seen in IPEX patients *(Wildin et al., 2001)*.

The majority of $Foxp3^+$ Treg cells develop in the thymus (tTregs) but Foxp3 expression can also be induced in naïve $CD4^+$ T cells in the periphery (pTregs). Treg development is discussed in more depth in *section 3.1*.

Multiple mechanisms of Treg suppression have been described. These can occur in both cell-dependent and cell-independent fashions and range from production of regulatory cytokines (IL-10, TGF-β), suppression by metabolic disruption, direct modulation of dendritic cell (DC) function, and cytolysis *(Savage et al., 2020)*.

Treg cells inhibit effector immune responses in a cell-contact dependent way by increased expression of inhibitory molecules on their surface. CTLA-4, GITR, ICOS, PD-1 and OX-40 are among the surface markers enriched on $Foxp3^+$ Treg that have been shown to promote their regulatory function and survival *(Savage et al., 2020)*. Engagement of these molecules can directly modulate the effector cells or alternatively induce an immunosuppressive phenotype in antigen-presenting-cells (APCs) *(Savage et al., 2020)*.

$Foxp3^+$ Tregs are a rich source of immunosuppressive cytokines, such as IL- 10 and TGF-β. In the context of intestinal homeostasis, IL-10 and TGF-β are of particular importance in enforcing tolerance and genetic deletion of IL-10 or IL-10R results in spontaneous intestinal inflammation *(Izcue et al., 2009; Maloy and Powrie, 2011)*. TGF-β is another immunosuppressive cytokine, which is enriched in the intestines. TGF-β -deficient mice suffer from a lymphoproliferative autoimmune disorder resulting in death within the first few weeks of life *(Shull et al., 1992).* The ability of T effector cells to respond to TGF-β is critical for Treg-mediated prevention of inflammation *(Fahlen et al., 2005)*. However, Treg cells expressing a

dominant-negative form of the TGF-βRII, also prevented colitis, suggesting that TGF-β is dispensable for Treg cell function *(Fahlen et al., 2005)*.

Interestingly, Foxp3$^+$ Treg cells appear to display some functional specialisations that match the effector responses that they antagonize. This specialisation has been mostly described on the level of transcription modules. For example, expression of T-bet by Treg cells was shown to be necessary to inhibit Th1 cells and this was attributed to increased expression of CXCR3 that allowed more efficient homing of T-bet$^+$ Treg cells to sites of Th1 driven inflammation *(Koch et al., 2009).* Similarly, expression of STAT3, important for Th17 lineage specification, has been described to facilitate Treg cell control over Th17 cells *(Chaudhry et al., 2009)*. However, expression of IRF4 and Gata3, transcription factors that are typically expressed in Th2 cells, are increased in peripheral and activated Treg cells and appear to play broad roles in Treg cell homeostasis *(Wohlfert et al., 2011).* Thus, the concept of mirrored expression of effector T cell transcriptional modules by Treg cells may not be as straightforward.

Treg cells have distinct metabolic requirements and have been described to preferentially rely on OXPHOS driven by lipid oxidation, rather than glucose, for ATP production *(Buck et al., 2015; Howie et al., 2017)*. However, recently it has been suggested that metabolic adaptations of Treg cells are context dependent and are influenced by factors such as Treg cell origin or anatomical distribution *(Newton et al., 2016),* although, it still remains largely undetermined how distinct subpopulations of Tregs, i.e., tTregs, pTregs, and *in vitro* generated iTregs, differ metabolically.

1.3 The pathogenies of inflammatory bowel disease (IBD)

Inflammatory bowel disease (IBD) incorporates a spectrum of chronic, relapsing and debilitating inflammatory disorders of the gastrointestinal tract. There are two major types of IBD: Crohn's disease (CD) and ulcerative colitis (UC), both of these have peak age of onset in the second to third decades of life *(Jairath and Feagan, 2020).*

IBD is most prevalent in developed countries of the Northern hemisphere, including the USA, UK and Scandinavia. Estimates during the 2000s for the UK suggest that UC has a prevalence of approximately 240 per 100,000 people whilst the prevalence for CD was about 157 per 100,000 people, although these figures most likely underestimate true prevalence *(Rubin et al., 2000; Steed et al., 2010)*. Although, in recent years, newly industrialised nations have seen a rising incidence of IBD that parallels with the westernisation of diet - increased exposure to processed food, refined sugars, dairy, and less plant-based fibres *(Jairath and Feagan, 2020)*. Moreover, epidemiological studies of migrant populations have shown that children of immigrants from regions with low IBD prevalence like Asia to the developed world, have a similar incidence of IBD as the children of non-immigrants *(Jairath and Feagan, 2020)*. Thus,

these studies suggest that risk might be mediated by earlier life exposure to environmental antigens.

Although both CD and UC are characterised by chronic inflammation, they differ in the way the inflammation manifests itself *(Baumgart and Sandborn, 2007)*. CD can affect most of the gastrointestinal (GI) tract from the mouth to the anus, although it is usually restricted to the ileum and colon. UC, in contrast typically only affects the rectum or the colon. CD inflammation is also described as 'patchy' with inflamed regions neighbouring areas of unaffected tissue, while inflammation in UC is more continuous *(Baumgart and Sandborn, 2007)*. CD inflammation often spreads throughout several layers of the gastrointestinal wall. Common complications involve narrowing of the bowel, known as strictures – where the bowel wall is thickened by inflammation and the accompanying submucosal fibrosis, and also the development of fistulas – channels that extend the inflammation into adjoining tissues *(DeFranco et al., 2007)*. Inflammation in UC is mostly restricted to the top most layer of the colonic mucosa, which becomes eroded by lymphocytes and neutrophil infiltration, which can lead to the formation of crypt abscess, that destroy sites involved in epithelial stem cell renewal *(DeFranco et al., 2007)*.

There is currently no cure for these conditions and treatments typically involve long-term intake of immunosuppressive agents and in many cases, surgical interventions. Anti-TNF mAb treatment has improved treatment outcomes for many IBD patients, however, this is associated with many side-effects including increased risk of secondary infections (*Targan et al., 1997)*. Additionally, approximately a third of IBD patients are refractory to anti-TNF therapy *(Peyrin-Biroulet, 2010).* Anti-TNF antibody treatment is believed to not only target TNF-mediated inflammation but also to induce apoptosis of Th1 and Th17 cells that express membrane TNF *(Peyrin-Biroulet, 2010)*. More recent treatments include the anti-IL-12 antibody which is believed to block both IL-12 and IL-23 through recognition of their shared p40 subunit and appears to be effective in CD patients with refractory disease for whom other TNF treatment has failed *(Peyrin-Biroulet, 2010)*.

While both CD and UC are chronic inflammatory disorders, the adaptive immune responses in these diseases show marked differences. Analysis of lesions and biopsies from CD patients suggest a strong Th1 and Th17 component, highlighted by increased expression of T-bet, IFN-γ, IL-12, IL-18, IL-17A and IL-22 *(Geremia et al., 2014)*. Analysis of lesions from patients with UC suggest that dysregulated Th2 immune response may contribute to the underlying pathogenesis, however, experimental and clinical evidence do not unequivocally support this hypothesis *(Geremia et al., 2014).* Although IL-4 is not typically present in UC, IL-5 and IL-13 are increased along with elevated serum IgG_4 which is consistent with immunoglobulin isotype switching mediated by Th2 cytokine *(Geremia et al., 2014)*. Nevertheless, UC and CD classifications are most likely made up of heterogeneous sub-phenotypes and it is likely that some forms of IBD may manifest through increased type 2 responses.

Although the exact aetiology of CD and UC is unknow, it is now well accepted that both of these forms of IBD develop in genetically predispose individuals as a result of an exaggerated mucosal immune response directed against the commensal microbiota combined with the possible involvement of external environmental triggers *(Kaser et al., 2010; Maloy and Powrie, 2011).*

Genome-wide association studies (GWAS) have identified over 200 genetic loci linked to IBD, unequivocally showing the biological complexity of the disease *(Jostins et al., 2012; Liu et al., 2015a).* The majority of these loci influence the genetic susceptibility of both CD and UC, it is thus likely that many of the underlying risk pathways are shared between these conditions. However, identification of susceptibility loci provides only correlative evidence for the involvement of specific genes and pathways. An understanding of the functional consequences of the majority of genetic polymorphisms identified by GWAS is still lacking.

A large proportion of the IBD-susceptibility genes uncovered by GWAS studies are involved in adaptive and innate immune responses, promotion of epithelial barrier integrity and also bacteria handling *(Van Limbergen et al., 2014)*. Specifically, the IL-23-Th17 axis appears to represent a major driver of pathology in IBD. GWAS identified multiple polymorphisms in the *IL23R* locus associated with higher risks of both forms of IBD, and subsequently, other variants in genes associated with Th17 type of responses were identified (*JAK2*, *STAT3*, *RORC*, *IL17A*, *IL21*) *(de Lange and Barrett, 2015; Duerr et al., 2006)*. Additionally, defects in negative regulatory pathways have also been highlighted as a risk for IBD development. Mutations in *IL10R* have been associated with severe early-onset IBD, suggesting that a breakdown of intestinal homeostasis due to defective immunosuppressive mechanisms might underlie IBD pathogenesis *(Glocker et al., 2009).*

Dysfunctional autophagy was also described as a contributing factor for IBD. A single missense nucleotide polymorphism (T300A) in the essential autophagy gene *ATG16L1* was identified as a strongly associated risk locus for CD. Along with polymorphisms in other autophagy genes, this suggested for the first time a role for the autophagy pathway in IBD pathogenesis *(Hampe et al., 2007; Rioux et al., 2007)*. Although GWAS studies pinpointed towards the autophagy pathway as a genetic key in understanding IBD pathogenesis they did not provide information regarding the cell types in which autophagy is important during chronic intestinal inflammation or the functional consequences of altered autophagy. This has prompted mucosal immunologists to investigate the functional roles of autophagy in different cell types in the gut in order to address two key questions: "*What are the cell types for which autophagy deficiency is most detrimental*?" and "*What is the functional role of autophagy in those cells?*".

1.3.1 *ATG16L1* T300A variant and intestinal immune homeostasis

Despite the discovery of the T300A *ATG16L1* variant over a decade ago *(Hampe et al., 2007),* research is still ongoing to understand the underlying molecular mechanism resulting in the association of this variant with increased susceptibility to CD. To understand the effect of the T300A polymorphism on ATG16L1 protein function, a study by *Murthy et al* used human cells homozygous for the T300A variant, as well as mice with the corresponding T316A knock-in mutation that recapitulates the CD susceptibility SNP *(Murthy et al., 2014)*. This study identified a caspase cleavage site at amino acids 296–299 of the ATG16L1 protein, showing that the CD-associated SNP further sensitises ATG16L1 to caspase 3 cleavage and degradation, ultimately resulting in decreased autophagy *(Murthy et al., 2014).* Moreover, the enhanced caspase 3 cleavage was observed when subjecting cells to stress conditions (apoptosis induction, starvation or *Yersina enterocolitica* infection), but not in unstimulated cells *(Murthy et al., 2014)*. Thus, this study supports the idea that the CD-associated T300A variant leads to defective autophagy during stress conditions.

Several other studies have highlighted different immune cell types through which the CD-associated polymorphism in *ATG16L1* might impact on intestinal immune homeostasis. Although not *bona fide* immune cells, IECs (intestinal epithelial cells) form a single barrier layer on the surface of the intestinal mucosa and, through their interactions with the intestinal microbiota and host leukocytes, play a crucial role in maintaining immune homeostasis *(Pott and Hornef, 2012).* Studies on IECs have concentrated on trying to understand how the polymorphisms in *ATG16L1* may impact on epithelial homeostasis. For example, Paneth cells (a type of specialised secretory IEC) from CD patients homozygous for the *ATG16L1* T300A variant allele, or from mice with a hypomorphic mutation of *Atg16l1*, exhibit abnormal granule structure and reduced secretion of antimicrobial peptides *(Cadwell et al., 2008; Cadwell et al., 2010).* However, the Paneth cell abnormalities in the *Atg16l1* hypomorphic mice were only observed when the mice harbored a commensal microbiota that contained an enteric norovirus *(Cadwell et al., 2008; Cadwell et al., 2010).* This suggests that decreased autophagy levels drive Paneth cell abnormalities only when additional triggering factors are present. Consistent with the notion, a subsequent study using T316A knock-in mice reported decreased autophagy and compromised xenophagy in IEC with the CD-associated SNP after *Shigella flexineri* infection *(Lassen et al., 2014).* Furthermore, three recent studies uncovered that deficiency of autophagy in IECs renders the cells susceptible to TNF-α induced cell death and exacerbated infection-driven pathology *(Burger et al., 2018; Matsuzawa-Ishimoto et al., 2017; Pott et al., 2018).*

The *ATG16L1* T300A variant has also been implicated in the function of macrophages and dendritic cells. As professional phagocytic cells, these cells are particularly well equipped to handle bacteria and autophagy is thought to play an important role in intracellular bacterial killing (xenophagy). Autophagy can be triggered in macrophages and DCs upon activation of pattern recognition receptors (PRR), such as TLR (Toll-like receptors) and NLR (NOD-like

receptors) *(Kabat et al., 2016b)*. Activation of autophagy in DCs by the NOD2 ligand MDP (muramyldipeptide) was shown to be reduced when these cells harbour the *ATG16L1* T300A allele variant *(Cooney et al., 2010; Travassos et al., 2010)*. Activation of NOD1 and NOD2 was reported to recruit ATG16L1 to the site of bacterial entry (*Travassos et al., 2010*) and variants of NOD2 have also been associated with increased suceptibility to CD, highlighting a potential mechansitic link between these two pathways. Another study reported that macrophages isolated from subjects homozygous for the T300A risk allele exhibited significantly reduced autophagy upon infection with *S. typhimurium,* but not under basal conditions *(Zhang et al., 2017)*. Moreover, ATG16L1 function in macrophages was also associated with the ability to regulate the balance between pro-inflammatory M1 macrophages and regulatory M2 macrophages *(Zhang et al., 2017)*.

Taken together, these studies suggest that a functional autophagy pathway is important for both epithelial and immune homeostasis in the gut and it intersects with other pathogen sensing and cellular stress responses to regulate intestinal homeostasis during infection and inflammation.

1.4 Rationale and summary of thesis aims

Previous work done in the Maloy lab showed that mice in which the autophagy protein ATG16L1 was selectively ablated in T cells ($Atg16l1^{\Delta CD4}$) develop spontaneous intestinal inflammation, characterized by loss of $Foxp3^+$ Treg cells and a selective expansion of $Gata3^+$ Th2 cells. This phenotype was most pronounced in the colonic lamina propria (cLP) *(Kabat et al., 2016a)*. Thus, a lack of autophagy simultaneously reduces anti-inflammatory Treg cells and increases pro-inflammatory Th2 effector cells in the intestine. This discrepancy could be partly attributed to an altered metabolic programme employed by *Atg16l1*-deficient Treg cells, with increased glycolysis and impaired fatty acid metabolism. In contrast, the metabolic profile of *in vitro* polarized Th2 cells seemed to be independent of autophagy *(Kabat et al., 2016a)*.

As described in the sections above, immune cells have a clear requirement for functioning autophagy in order to maintain normal immune homeostasis. Work building up to this thesis emphasised that Treg and Th2 cells have differing intrinsic requirements for autophagy, however, the true mechanistic basis for this is not well understood.

We hypothesised that autophagy would be required for Treg cell survival and functional competency in the intestinal mucosa. Additionally, we hypothesised that Th2 cells may be more resistant to autophagy defects and that autophagy may act as a brake on their expansion in the intestine. Thus, the aims of this thesis are to investigate the mechanistic consequences of altered autophagy in different T cell subsets and also to explore the link

between the dominant type 2 immune responses and the observed intestinal pathology. This work has been guided by the following research questions:

- What is the link between the decrease in Treg cells and the increase in Th2 cells? Is the Th2 increase dependent on defective Treg control in the intestine (*Chapter 3*)
- What are the pathogenic consequences of the Th2 bias in Atg16l1$^{\Delta CD4}$ mice? (*Chapter 4*)
- How does autophagy-deficiency affect the transcriptional program in different T cell subsets? In particular, why is autophagy dispensable for Th2 cells but absolutely required for Treg cell survival in the gut? (*Chapter 5*)

Many of the tools required to answer the questions above have been developed in the course of this research. Finally, this thesis hopes to elucidate the correlation between autophagy defects in CD4^{+} T cells and altered intestinal T cell homeostasis and to better define how autophagy regulates intestinal immunity.

Chapter 2. Materials and Methods

2.1 Mouse strains

Atg16l1$^{fl/fl}$ mice were obtained from H. Virgin (Washington University) and were generated as previously described *(Hwang et al., 2012)*. Atg16l1$^{fl/fl}$ mice were crossed by the Maloy lab with B6.Cg-Tg (Cd4-cre)1Cwi/BfluJ (CD4-Cre mice) obtained from Jackson Laboratory (Bar Harbor, ME) to generate Atg16l1$^{\Delta CD4}$ mice as described *(Kabat et al., 2016a)*. Additionally, Atg16l1$^{fl/fl}$ mice were crossed by the Maloy lab with Gt(ROSA)26Sor$^{tm2(cre/ERT2)Brn}$ (Rosa$^{Cre\text{-}ERT2}$ mice), obtained from E.Bikoff at the Dunn School (University of Oxford), to generate Atg16l1$^{\Delta RosaCre\text{-}ERT2}$ mice. Atg16l1$^{\Delta CD4}$ mice were crossed by the Maloy lab with B6.Cg-Gt(ROSA)26Sor$^{tm14(CAG\text{-}tdTomato)Hze/J}$ (Jackson Laboratory, Bar Harbor, Maine, USA) to introduce the Cre-tdTomato excision reporter and generate the Atg16l1$^{\Delta CD4\text{-}tdTomato}$ line.

During the course of this thesis, I crossed Atg16l1$^{\Delta RosaCre\text{-}ERT2}$ and Atg16l1$^{\Delta CD4\text{-}tdTomato}$ mice to generate a line in which Atg16l1 excision is triggered by tamoxifen administration and tdTomato expression acts as a marker of excision, denoted as Atg16l1^{flfl}Rosa26-tdTomato$^{fl/fl}$Rosa26^{CreERT2}.

B6.IL13-eGFP and B6.IL13-tdTomato reporter mice, generated as described *(Neill et al., 2010)*, were obtained from A. McKenzie (University of Cambridge). During the course of this thesis, I crossed these IL-13 reporter lines with Atg16l1$^{\Delta CD4}$ mice to obtain Atg16l1$^{\Delta CD4}$IL13-eGFP and Atg16l1$^{\Delta CD4}$IL13-tdTomato mice, respectively.

All of the above strains were bred and maintained under specific pathogen-free (SPF) conditions at the University of Oxford and all experimental procedures were conducted in accordance with the UK Scientific Procedures Act of 1986 by a Personal Licence holder (I376FB0D9) under a Project License (30/3423) authorized by the UK Home office. If not otherwise stated, both females and males were used in experiments, age and sex matched whenever possible. Most animals were analysed at 8-12 weeks (young mice) or at 5 months or more of age (aged mice). Mice were either littermates or co-housed throughout the experiment.

The background strain of the above-mentioned mouse lines was C57BL/6 (also denoted as B6), sub-strain B6/J. It is accepted that a number of different sub-strains of C57BL/6 have arisen over time as a result of accumulated spontaneous mutations, such as C57BL/6NJ (B6N), which differs genetically from B6/J *(Bryant, 2011)*. We did not perform additional genotyping to check for genetic drift of the B6/J sub-strain used. However, in order to mitigate any potential confounding effects of mispairing different sub-strains of B6 mice, we used littermate controls whenever possible, as indicated throughout the results chapters.

2.2 Genotyping of mouse strains

2.2.1 Genomic DNA isolation

DNA from Atg16l1$^{\Delta Foxp3}$ mice, was extracted using the Proteinase K extraction method, as a higher DNA purity is required for the accurate genotyping of this strain. DNA from all other mouse strains was extracted using the HotSHOT extraction method *(Truett et al., 2000)*.

Proteinase K method:

Ear tissue samples were digested overnight at 55°C in 200µL lysis buffer (5mM EDTA, 100mM Tris-HCl, 0.2% SDS, 200mM NaCl) and 0.2mg/mL proteinase K (Bioline). DNA was isolated from the digested supernatants by precipitation with isopropanol (1:1 volume). Following centrifugation at 13,000rpm for 3-4min, DNA pellets were washed with 70% ethanol and dried for 10 min at 37^{o}C. The DNA was then resuspended in 80µL of MiliQ water and used for PCR.

HotSHOT method:

HotSHOT buffer (25mM NaOH /0.2 mM EDTA) was added to ear punches, which were incubated on a heat block at 95^{o}C for 1h. An equal amount of neutralisation buffer (40 mM Tris HCl, pH 5.5) was further added to the ear punches. The tubes were vortexed and centrifuged at 4000g for 3 minutes for debris to settle at the bottom of the tube, before the DNA was used for PCR.

2.2.2 Polymerase chain reaction (PCR)

The presence of transgenes in mice was assessed by genotyping of DNA isolated from mouse ear punch biopsies through PCR. PCR reactions were carried either:

- In a total volume of 15µL using Taq polymerase (0.7 U/µL, Invitrogen), PCR buffer (1x, Bioline), MgCl2 solution (2mM, Bioline), dNTP mix (0.2mM, Sigma), primers (0.5 µM), UltraPure DNase/RNase-Free Distilled Water (Fisher Scientific) and 1µL of DNA samples.
- Or a total volume of 20µL using MyTaq RedMix 2x (Bioline), primers (0.5 µM), UltraPure DNase/RNase-Free Distilled Water (Fisher Scientific) and 1.5µL of DNA samples.

Table 2. Primer sequences used to screen transgenic mice

Transgene	Primers
Atg16l1-fl/fl	Primer F: CTTTCTCAACAGAACCAGCAGTAC Primer R: GTAGAAAGACTGGTGATGGTAAACC
CD4-Cre or Rosa-Cre and WT control	Mutant Primer F: AGGTTCGTTCACTCATGGA Mutant Primer R: TCGACCAGTTTAGTTACCC Control Primer F: CCTCCGGAGAGCAGCGATTAAAAGTGTCAG Control Primer R: TAGAGCTTTGCCACATCACAGGTCATTCAG
tdTomato and WT control	Mutant Primer F: CTGTTCCTGTACGGCATGG Mutant Primer R: GGCATTAAAGCAGCGTATCC

	Control Primer F: AAGGGAGCTGCAGTGGAGTA Control Primer R: CCGAAAATCTGTGGGAAGTC
IL13-eGFP and WT control	Forward Primer: GCTTCGTCTGTCACTCACACAGG Reverse Control Primer: TCAACAGGCTAAGGCCACAAGCC Reverse Mutant Primer: CATGGTCCTGCTGGAGTTCGTG
IL13-tdTomato and WT control	Forward Primer: TCAACAGGCTAAGGCCACAAGCC Reverse Control Primer: GCTTCGTCTGTCACTCACACAGG Reverse Mutant Primer: ACCTCCTCGCCCTTGCTCACCAT

DNA was amplified under the following conditions:

Table 3. PCR programmes used for genotyping

Transgene	PCR conditions
Atg16l1-flox/flox CD4-Cre (250bp) and WT control (480bp) Rosa-Cre (250bp) and WT control (480bp) *(one PCR reaction)*	1. 94°C, 4 min 2. 94°C, 30 sec 3. 60°C, 30 sec 4. 72°C, 1 min 5. 30 cycles from step 2 6. 72°C, 5 min 7. Hold at 4°C
tdTomato (196bp) and WT control (297bp) *(one PCR reaction)*	1. 94°C, 3 min 2. 94°C, 20 sec 3. 61°C, 30 sec 4. 72°C, 30 sec 5. 35 cycles from step 2 6. 72°C, 2 min 7. Hold at 4°C
IL13-eGFP (522bp) and WT control (300bp) *(one PCR reaction)*	1. 94°C, 2 min 2. 94°C, 30 sec 3. 60°C, 30 sec 4. 72°C, 45 sec 5. 31 cycles from step 2 6. Hold at 4°C
IL13-tdTomato (100bp) and WT control (270bp) *(one PCR reaction)*	1. 94°C, 2 min 2. 94°C, 30 sec 3. 62°C, 30 sec 4. 72°C, 45 sec 5. 31 cycles from step 2 6. Hold at 4°C

2.2.3 Gel electrophoresis

PCR products were visualised by gel electrophoresis. UltraPure Agarose (Invitrogen, 16500) was dissolved in 0.5M TAE buffer (45mM Tris-borate and 1mM EDTA) at a concentration of 1.5%-2% (w/v) by boiling in a microwave for 2 minutes. The agarose solution was cooled briefly under running cold water and 2µg/ml of SYBR Safe Gel Stain (Thermo Fisher) was added. The solution was poured in a casting chamber to set. 10µL of PCR sample was loaded into individual wells and the gel was run at 110V (PowerPac, Bio-Rad) for 25-30 minutes and visualised by UV transillumination using a Syngene bioimaging system.

2.3 Cell isolation, enrichment and depletion

2.3.1 Isolation of spleen and lymph node cells

Spleens and mesenteric lymph nodes were harvested following the sacrifice of the mice. Organs were mashed through a 70-100µm cell strainer (Falcon, BD Biosciences) or 70µm pore nylon mesh (Plastok Associates) and washed with PBS/0.1% BSA/5mM EDTA followed by centrifugation at 1500 rpm for 5 minutes. Splenic cells were additionally incubated with 500µL ACK lysis buffer (10mM $KHCO_3$, 150mM NH_4Cl, 0.1mM Na_2.EDTA, pH 7.2-7.4) for 3 minutes at room temperature to remove red blood cells. Isolated cells were washed with PBS/0.1% BSA/5mM EDTA, filtered through 70µm mesh and resuspended in an appropriate volume of ice-cold PBS/0.1% BSA/5mM EDTA for subsequent analysis.

2.3.2 Isolation of leukocytes from the blood

Blood was collected via cardiac puncture or superficial tail bleed into a tube containing 100µL 0.5M EDTA. Red blood cells were lysed by incubation with 300µL ACK lysis buffer for 3 minutes at room temperature. Cells were washed with PBS/0.1% BSA/5mM EDTA and resuspended in the same buffer for subsequent analysis.

2.3.3 Isolation of leukocytes from the colonic lamina propria

Colon and caecum were harvested from the sacrificed mice and the luminal contents removed. Colons were cut open longitudinally, cleaned in ice-cold PBS/0.1% BSA, diced into small, 1cm long pieces, and placed in 10ml ice-cold PBS/0.1% BSA. The colon pieces were washed twice with 20mL of pre-warmed (37°C) RPMI1640 (Sigma- Aldrich)/10% FCS/5mM EDTA for 20min in a shaking incubator (200 rpm at 37°C) to remove intestinal epithelial cells. This was followed by a wash in RPMI/10% FCS/15mM Hepes (Sigma- Aldrich), for 10min in a shaking incubator (200 rpm and 37°C) to neutralise the activity of the EDTA. Supernatant was discarded and replaced with pre-warmed RPMI 1640/10% FCS containing 0.4mg/ml type VIII collagenase (Sigma Aldrich) and 40µg/ml DNase I (Roche). The samples were placed for 45 - 60 min at 37°C in a shaking incubator (180 rpm) for tissue digestion. Tissue pieces were further

disintegrated using a 10mL syringe and the digestion was terminated by addition of 5mM EDTA. Supernatants were filtered through 70µm nylon mesh, then centrifuged and resuspended in 3ml of 30% Percoll (GE Healthcare). A three-layer (30/40/70%) Percoll density-gradient was used to enrich lymphocytes. Gradients were centrifuged (1800 rpm, 10°C, minimal acceleration, 20 min, no brake) and the 40/70% Percoll interface was isolated and washed with PBS/0.1% BSA/5mM EDTA. The leukocyte enriched single-cell suspensions were resuspended in an appropriate volume of PBS/0.1% BSA/5mM EDTA for subsequent analysis.

2.3.4 Isolation of cells from fat tissue

The mouse was perfused with 20mL PBS immediately after being sacrificed and the epididymal fat tissue (eWAT) was isolated and placed in 'Fat media'. The epididymal fat was further minced with scissors or scalpels and incubated for 25minutes on a shaker at 37°C, in a 24 well plate containing 2mL 'Digestion media' per well. The fat tissue was further disrupted by forceful pipetting and washed in 'fat media' containing EDTA (1:4) to stop the digestion. After filtering through a 70µm mesh, the single cell suspension was resuspended in 400-500µL PBS/0.1% BSA/5mM EDTA for further analysis *(Han et al., 2017)*.

'Fat media' was made up of 500mL DMEM containing 5g low fatty acid BSA (Sigma, A7030-50G) and 25mL Hepes. 'Digestion media' contained 10mg Liberase TL (Roche, 230287) and 1:500 DNase (Sigma, DN25-5G) per 50mL Fat Medium.

2.3.5 T cell enrichment

Enrichment of naïve $CD4^+$ T cells or $CD4^+$ T cells was performed using the EasySep Mouse Naïve $CD4^+$T Cells Isolation (Catalog #19765) or EasySep Mouse $CD4^+$ T cells Isolation Kit (Catalog #19852) respectively, according to manufacturer's instructions (StemCell Technologies). Purity enrichment was checked by FACS, with an average of 95% purity for both kits (data not showed).

2.3.6 $CD3^+$ T cell depletion

Samples were incubated with anti-$CD3^+$ PE conjugated antibody for 30mins followed by incubation with Anti-PE MicroBeads (Miltenyi) as per the manufacturer's instructions. AutoMACS Pro Separator was used for purifying the PE negative fraction. Purity enrichment was checked by FACS, with an average of 90% purity (data not showed).

2.4 Flow cytometry and cell sorting

2.4.1 Flow cytometry antibodies

All antibodies used were specific for murine targets unless stated otherwise.

Table 4. Antibodies used for flow cytometry

Surface marker	Clone	Fluorochromes	Company
B220 / CD45R	RA3-6B2	AF700	BioLegend
CD11b	M1/70	PE-Cy5	BioLegend
CD3	145-2C11	BUV395, PE, BV785, FITC	ThermoFisher
CD4	GK1.5	B711, BV785	ThermoFisher
CD44	IM7	BUV395	ThermoFisher
CD45.1	A20	BV785, PB	BioLegend
CD45.2	104	eF450, FITC	ThermoFisher
CD62L	MEL14	PE-Cy7, BV605	ThermoFisher
CD8α	53.6.-7	AF700	BioLegend
Live/Dead Near-IR	-	Far red: 750⁄775	ThermoFisher
TCRβ	H57-597	FITC, PerCP-Cy5.5	ThermoFisher

Intracellular marker	Clone	Fluorochromes	Company
Foxp3	FJK-16s	FITC, APC, eFluor 450	ThermoFisher
Gata3	TWAJ	eFluor 660	ThermoFisher
IFNγ	XMG1.2	FITC, PE	ThermoFisher
IL-10	JES5-16E3	APC	ThermoFisher
IL-13	eBio13A	PE-Cy7	ThermoFisher
IL-17	17B7	FITC	ThermoFisher
IL-4	11B11	PE-Cy7	ThermoFisher
pS6	cupk43k	PE-Cy7	ThermoFisher

2.4.2 Re-stimulation of lymphocytes for intracellular cytokine staining

Single-cell suspensions of lymphocytes in RPMI-1640 medium supplemented with 10% FCS, 2mM L-glutamine (Life Technologies), 100U/ml Penicillin/Streptomycin and 0.05mM 2-mercaptoethanol (Life Technologies) were plated at 0.5-1x10^6 cells/well in 96 well U-bottom plates (Corning). For re-stimulation, 0.1µg/ml Phorbol 12-myristate 13- acetate (PMA), 1µg/ml Ionomycin and 10µg/ml Brefeldin A (all from Sigma Aldrich) and/or 10µg/ml Monensin (BioLegend) were added and cells were incubated for 3.5-4 hours at 37°C. Following the incubation, cells were centrifuged, the supernatant discarded and cells were washed twice in PBS/0.1% BSA/5mM EDTA.

2.4.3 Surface staining

Single-cell suspensions of lymphocytes, between 5x10^5 and 1x10^6 cells/well, were used for staining. All incubations were performed in PBS/0.1% BSA/5mM EDTA in V-bottom 96-well plates (Corning). All centrifugations were performed at 1500rpm for 3 minutes.

Cells were first stained with anti-CD16/CD32 (ThermoFisher) to prevent any non-specific antibody binding. Fixable Near-IR Viability Dye (ThermoFisher) was used at a concentration of 1:1000 for discriminating dead cells. The dye was incubated with cells for 10 minutes at 4°C in the dark. After washing once, cells were resuspended in PBS/0.1% BSA/5mM EDTA containing various combinations of fluorescently labelled antibodies (Table 4) and incubated for 30mins at 4°C in the dark. Cells were washed once in PBS/0.1% BSA/5mM EDTA to get rid of excess antibody and used for downstream analysis.

2.4.4 Intracellular staining for transcription factors and/or cytokines

Prior to the intracellular staining the surface staining protocol was performed as described in the section above. Cells were then fixed using 100µL of BD Cytofix fixation solution (BD Biosciences) for 1-2hrs at 4°C, followed by a wash in 1X permeabilisation buffer (from the Foxp3/Transcription Factor Staining Buffer Set, eBioscience). A cocktail of intracellular antibodies (Table 4) containing 1:100 rat serum was prepared in the 1X permeabilisation buffer and cells were incubated in this mixture overnight at room temperature (RT). Cells were washed once in 1X permeabilisation buffer and then once in PBS/0.1% BSA/5mM EDTA before being resuspended in 300µL PBS/0.1% BSA/5mM EDTA for flow cytometry analysis.

2.4.5 Flow cytometric analysis

Cells were acquired on BD LSRFortessa (BD Biosciences) using FACSDiva software (BD Biosciences). Compensation using single-coloured-stained CompBeads (BD Biosciences) or cells was always performed prior to the sample acquisition. The results were analysed using FlowJo 10 (Tree Star).

2.4.6 Fluorescence-activated cell sorting (FACS)

Single-cell suspensions of lymphocytes were obtained as described in section 2.3 and, when advisable, enriched using EasySep T Cell Enrichment Kits (StemCell Technologies) as described in section 2.3.5. Cells were surface stained with appropriate antibody mixes for 30 minutes at 4°C in the dark, washed with PBS and resuspended in PBS/0.1% BSA/5mM EDTA at approximately $5x10^7$ cells/mL prior to the sort. Based on the desired downstream procedure, cells were sorted into 15mL tubes containing PBS/10% FCS or directly into 0.2mL PCR tubes containing lysis buffer as described in section 2.7.2. Cells were sorted on FACS AriaIII (BD Biosciences) by Dr M. Maj or J. Webber.

2.5 In vivo experiments

2.5.1 Generation of bone marrow chimaeras

$Rag1^{-/-}$ or B6 mice were irradiated twice with 550 Rad y-irradiation from a ^{127}Cs source with a break of 180 minutes. Bone marrow cells were isolated from the tibia and femur of WT

(CD45.1$^+$) mice and Atg16l1$^{\Delta RosaCre\text{-}ERT2\text{-}tdTomato}$ (CD45.2$^+$) mice. Bones were briefly washed in 70% EtOH. Femurs and tibias were flushed with ice-cold PBS and the resulting bone marrow cells were filtered through 70µm cell strainers. Red blood cells were removed by incubation with ACK lysis buffer for 3 minutes at RT followed by a wash with PBS. After depletion of CD3$^+$ cells (as detailed in section 2.3.6), bone marrow cells were resuspended in ice-cold PBS and a total of 1x10^7 cells was injected i.v. into irradiated mice, at a 20:80 (CD45.1:CD45.2) or a 50:50 (CD45.1:CD45.2) ratio. Eight weeks later, mice were tested for reconstitution by sampling of blood from tail vein (see section 2.5.3) and tamoxifen was administered as detailed in section 2.5.2 to trigger excision of *Atg16l1*. Leukocyte chimerism was monitored for at least 8 weeks by peripheral tail bleeding before tissue harvesting.

2.5.2 Tamoxifen injection

To trigger excision of floxed *Atg16l1* alleles in cells with a tamoxifen-inducible Cre construct, mice were injected i.p. with a dose of 75mg/kg tamoxifen (Sigma, T5648) dissolved in corn oil, for 3 consecutive days (24 hours apart). Mice were aged more than 8 weeks and weighed at least 25 grams when tamoxifen was first administered.

2.5.3 Sampling blood from mouse tail vein

Mice were warmed under a lamp in order to dilate the tail blood vessel, after which mice were placed in a restrainer and a scalpel was used to make a superficial cut into the tail vein. A few drops of blood, no more than 0.2mL, were collected before blood flow was stopped by applying pressure.

2.5.4 Histological assessment

Tissue sections from mid small-intestine and mid colon were fixed in 4% formalin solution for at least 24 hours before being paraffin wax embedded. Transverse sections of 4µm thickness were cut using a microtome (Leica Biosystems) and mounted onto microscope slides with Haematoxylin and Eosin staining (Leica Biosystems). Crypt lengths were measured using FIJI software *(Schindelin et al., 2012)*.

2.6 In vitro experiments

2.6.1 Induced Treg (iTreg) cultures

Single-cell suspensions were isolated from spleens as described in *section 2.3.1*, enriched for naïve CD4$^+$ T cells as described in *section 2.3.5* and cultured (3x10^5 cells/well) in 96-well flat bottom plates that were pre-coated with anti-CD3 (5 µg/ml) and anti-CD28 mAb (1 µg/ml) overnight at 4°C. Cells were kept on the antibody coated plates for 48h in Treg or Th0 polarizing conditions in 200µL of T cell media per well. Next, cells were transferred to U-bottom plates and maintained in polarizing conditions for a further 5 days before FACS

analysis. For Th0 conditions IL-2 (100 U/ml) was included in the culture, whilst for Treg conditions cultures were supplemented with TGF-β1 (5 ng/ml), anti-IFN-γ, anti-IL-4 mAb and anti-IL-12 (all 10 µg/ml) plus IL-2 (100 U/ml), prepared in 200µL of T cell media per well. T cell media was prepared using IMDM Medium (ThermoFisher), supplemented with 10% FCS, 2mM L- glutamine (ThermoFisher), 0.05mM 2-mercaptoethanol (ThermoFisher), 100 U/ml each of penicillin and streptomycin (Sigma-Aldrich).

2.6.2 Colon explant cultures

A piece of about 0.5cm of mouse colon was cut longitudinally, the weight of the tissue was recorded, and the piece was incubated in 1ml RPMI-1640 medium supplemented with 10% FCS, 2mM L-glutamine (Life Technologies), 100U/ml Penicillin/Streptomycin and 0.05mM 2-mercaptoethanol (Life Technologies) for 24 hours at 37°C. Following incubation supernatants were collected and stored at -80°C for immunoglobulin and cytokine analysis.

2.6.3 Proteasomal activity measurement

Proteasomal chymotrypsin-like activity was measured with Abcam proteasomal activity kit (*ab107921*) according to the kit instructions. Briefly, in-vitro differentiated Treg cells obtained as detailed in *section 2.6.1*, were extracted using a 0.5% NP-40 (Sigma) lysis buffer and centrifuged at 4 °C , 16,000× G for 20 min. One sample contained the cell lysate from 2 million cells, tests were done in triplicate. 10µl of each cell lysate was incubated with the AMC-tagged proteasomal substrate, with or without the proteasomal inhibitor MG-132 (negative control). The resulting fluorescence, indicating proteasomal activity, was measured at excitation/emission wavelength of 360 nm/460 nm, respectively, with a microplate reader. The specific activity of only the proteasomes, excluding the activity of other proteases present in the sample, was calculated by subtracting the fluorescence value of the corresponding MG-132-treated sample from the total fluorescence value in the sample without MG-132 treatment, according to the manufacturer's instructions.

2.7 Analysis of gene expression

2.7.1 Droplet based single-cell RNA sequencing

$CD4^+$ T cells were isolated from pooled colonic lamina propria (cLP) cells of 5 $Atg16l1^{fl/fl}$ (WT) and 6 $Atg16l1^{\Delta CD4}$ (KO) male mice, using FACS sorting as detailed in *sections 2.3.3* and *2.4.6*. $CD4^+$ T cells were counted and loaded into a Chromium controller (10x Genomics), according to the standard protocol for the Chromium single cell 5' Kit (10x Genomics), in order to partition single cells into nanolitre-scale droplets, called GEMs (Gel Bead-in EMulsion) *(Zheng et al., 2017)*. Approximately 60% of cells loaded into the system can be captured into single cell GEMs and we aimed to recover between 3000-5000 good quality cells for each sample. Each GEM contains the necessary chemicals to break down the cell membranes and perform reverse transcription of the captured mRNA and amplification of the resulting cDNA. During

this process, the mRNA strands from each cell can be labelled with a droplet-specific 10-12 base pair long cellular barcode known as a unique molecular identifier (UMI). UMIs are used to distinguish between sequenced reads that originate from unique mRNA molecules vs PCR duplicates. The resulting libraries were sequenced across multiple Illumina HiSeq 4000 lanes to obtain a read depth of approximately 55,000 reads per cell for gene expression libraries and 45,000 reads per cell for V(D)J enriched T cell libraries. Sequencing was performed by core staff at the Wellcome Trust Centre for Human Genetics, Oxford in accordance with the manufacturer's protocol. FASTQ files from the WT and KO samples were processed and aligned to the mm10 mouse reference transcriptome using CellRanger v3.0.1, identifying a total of 11,218 cells (6,539 WT and 4,679 KO cells) (see Chapter 5 for further analysis). The resulting gene expression matrices for the WT and KO samples were integrated using RStudio R version 3.6.1 and analysed with Scater version 1.14.0 *(McCarthy et al., 2017)* and Seurat version 3.0.2 *(Stuart et al., 2019)* packages.

2.7.2 Real-time quantitative polymerase chain reaction (RT-qPCR) analysis

Total RNA from eWAT (epididymal white adipose tissue) and BAT (brown adipose tissue) tissue was isolated using the RNeasy Lipid Tissue Mini Kit (Qiagen), according to the manufacturer's instructions. Next, 2µg of RNA were reverse transcribed using SuperScript III Reverse Transcriptase Kit (Invitrogen) and oligo-dT primers (Sigma) according to the manufacturer's instructions. qPCR reactions of the samples were performed in duplicates with 4µL cDNA in a final reaction volume of 20µL. Amplification was done using TaqMan Gene Expression Assay probes (Applied Biosystems) and Eurogentec qPCR mix (RT-QP2X-03) with the cycling conditions recommended by the manufacturer for the Applied Biosystems StepOnePlus Real-Time PCR System. Expression levels were normalized to either HPRT or 18S rRNA and gene expression was calculated using the $2^{-\Delta Ct}$ method *(Pfaffl, 2004).* Taqman probe Mm01244861_m1 (ThermoFisher) was used to measure *UCP1* (uncoupling protein 1) gene expression.

2.8 Analysis of protein levels

2.8.1 Enzyme linked immunosorbent assays (ELISAs)

Immunoglobulin isotypes, except for IgE, were measured using the SBA Clonotyping ELISA System (Southern Biotech). IgE concentration was quantified using an anti-mouse IgE ELISA (BioLegend), according to the manufacturer's instructions. MCPT-1 concentrations were also measured by ELISA (eBioscience). 50µL of colon explant supernatant samples were prepared as described in sections 2.6.2 and quantified in duplicate. The absorbance was read at 450 nm by a spectrophotometric plate reader.

2.8.2 Western blot (WB)

A small piece of colon tissue was lysed in RIPA buffer (50mM Tris-HCl, 150mM NaCl, 1% NP-40, 0.5% sodium deoxycholate, 0.1% SDS) containing protease inhibitor cocktail (Roche). Protein levels (5-20 ug/sample) were normalized by BioRad DC protein assay (Bio-Rad Laboratories, Hercules, CA) and SDS-polyacrylamide gel electrophoresis (PAGE) (Bio-Rad Mini-PROTEAN TGX 4-20% gels) at 100 V. Protein transfer was carried out at 35 V for 1h onto a methanol-activated polyvinylidene difluoride (PVDF) membrane (GEHealthcare) at 4°C.

Following transfer onto the membrane, the sample was blotted with primary antibodies: anti-Atg16l1 antibody (AB1; Sigma-Aldrich), anti-tubulin antibody (sc5286, Santa Cruz Biotechnology), and incubated at 4°C overnight. The next day, the membrane was washed extensively (at least 4 times for 5 min) with PBS/0.2% Tween-20 before incubating with horseradish peroxidase (HRP)-conjugated secondary antibody for 1hr at RT. Five washes of 15 min each with PBS/0.2% Tween-20 were done to remove non-specifically bound secondary antibody, after which membranes were incubated with SuperSignal West Femto (Thermo Scientific) according to the manufacturers' instructions. Blots were developed using medical X-ray film (Fuji) and a RP X-OMAT developer (Kodak Limited, UK).

2.9 Statistical analysis

All statistical analysis was performed in Prism 8.0 (GraphPad).

For weight curves, p-values were determined by two-way ANOVA with Bonferroni post-hoc tests. We used two-way ANOVA in this context as we assume mouse weight data to be normally distributed. For weight curves the two-way ANOVA measured weight gain (quantitative dependent variables) based on time and mouse genotype (categorical independent variables).

ANOVA depends on 3 assumptions *(Festing et al., 2016)*:

1. The residuals (the difference between each observed value and the group mean) are normally distributed.
2. Variances within each group are approximately equal.
3. The observations are independent of one another.

For all other experiments, the nonparametric Mann–Whitney test was used to compare samples and determine significance as we assume this data to be non-normally distributed.

Differences were considered statistically significant when $p < 0.05$. Significance is indicated according to the following: * $p<0.05$, ** $p<0.01$, *** $p<0.001$. Experimenters were not 'blinded' in terms of allocation of animals to experimental groups.

2.10 Experimental design and power analysis

Estimates of sample sizes for *in vivo* experiments were derived from previous observations in the laboratory using well characterized models of intestinal inflammation *(Hue et al., 2006)*, in which we assume the incidence of intestinal pathology in the positive control groups will be 80%, and that impactful genetic or pharmacological intervention will reduce this to 30% in treated groups. With these baseline parameters, power analysis was performed using Power of Trial software (Dr. S. Cobbold, University of Oxford), which calculates a power value based on χ^2 test statistics:

- Frequency of disease in disease groups = 0.8;
- Frequency of disease in attenuated groups = 0.3;
- Power value = 0.95;
- Level of significance p=0.05
- Resultant number of mice required per experimental group = 19.

Therefore, we normally aim to perform 2-3 independent experiments with 6-7 mice per group, giving a total of 20-21 mice per experimental group, in accordance with the power analysis. However, when new mouse models or experimental conditions were being trialled (Chapter 2), we initially embarked on pilot experiments with smaller sample sizes in order to assess the potential of different lines of investigation. This approach is in accordance with the conditions attached to the project animal licence (30/3423). As most of these pilot experiments (Chapter 2) did not show any trends towards different disease incidences or severity, they were not repeated extensively. Although this means that they did not reach the sample size required by the power calculation, this approach is mandated by the 3Rs conditions in the project licence.

Chapter 3. Autophagy regulates intestinal Th2 cells through cell intrinsic and cell extrinsic mechanisms

3.1 Introduction and aims of chapter

$CD4^+$ $Foxp3^+$ regulatory T cells (Treg) are essential for maintaining immune homeostasis and self-tolerance *(Savage et al., 2020)*. Like conventional $CD4^+$ Th cells, Tregs are phenotypically and functionally diverse, and are broadly distributed in lymphoid and nonlymphoid tissue sites, even in the absence of any overt inflammation *(Campbell, 2015)*. *In vivo*, Treg cells can be broadly classified into two groups on the basis of their developmental origin: thymic Treg and peripheral Treg. Thymic Treg cells (tTreg), also known as natural Treg cells (nTreg), are generated during thymic T cell development, as a separate lineage at the stage of $CD4^+$ single-positive thymocytes from precursors that show high affinity for self-peptides *(Panduro et al., 2016)*. Peripheral Treg cells (pTreg) are differentiated *de novo* from naïve $CD4^+$ T cells at peripheral sites in the presence of IL-2 and TGF-β *(Panduro et al., 2016)*. In addition, Treg cells generated *in vitro* through TGF-β supplementation are known as induced Treg (iTreg) cells *(Panduro et al., 2016).*

Definitive markers differentiating tTregs and pTregs have not been identified, although, the transcription factor Helios and the cell surface receptor Neuropilin-1 have been proposed as putative tTreg markers *(Szurek et al., 2015; Thornton et al., 2010; Yadav et al., 2012).* Thus, in most cases, the relative contributions of tTregs and pTregs to the Treg pool in different tissues and inflammatory settings has not been determined.

The maintenance of local tissue homeostasis is of particular importance in the intestinal mucosa, where the immune system must be able to effectively discriminate between pathogens and innocuous antigens like dietary factors or the commensal flora. A link between defective Treg homeostasis and increased Th2 responses in the intestinal mucosa has previously been described *(Curotto de Lafaille et al., 2008; Josefowicz et al., 2012; Mucida et al., 2005; Ulges et al., 2015)*. While it is clear that a compromised Treg compartment can result in exacerbated Th2 responses, the mechanism through which Treg cells selectively inhibit mucosal Th2 cells is not well understood.

Mouse models where specific conserved noncoding sequences (CNSs) of the *Foxp3* locus were genetically deleted have provided some insight into the role of tTregs and pTregs in controlling allergic responses at mucosal surfaces. *CNS3* and *CNS1* have been shown to be of particular relevance for the development of tTreg and pTreg cells, respectively *(Zheng et al., 2010).* Using gene-targeted $Foxp3^{\Delta CNS1}$ mice, Rudensky and colleagues showed that T cells from these mice exhibit deficiencies in pTreg cell induction and develop aberrant type 2

immune responses in the lung and gastrointestinal tract *(Samstein et al., 2012; Zheng et al., 2010).* Moreover, *Foxp3*$^{\Delta CNS1}$ mice do not exhibit widespread organ-specific autoimmunity or immune activation throughout the body, suggesting that tTreg cells are sufficient to maintain most aspects of immune homeostasis *(Samstein et al., 2012; Zheng et al., 2010)*. These, studies provided key evidence that pTreg cells serve a critical, nonredundant modulatory function at anatomical sites that border with the external environment, however the precise mechanisms responsible remain unclear.

The Maloy lab has previously characterised the Atg16l1$^{\Delta CD4}$ mice and found that thymic development of Foxp3^{+} Treg cells was not diminished compared with Atg16l1$^{fl/fl}$ littermates *(Kabat et al., 2016a)*. In contrast, they observed a small decrease in frequencies and total numbers of Foxp3^{+} Treg cells in the spleen and mLN of Atg16l1$^{\Delta CD4}$ mice compared with Atg16l1$^{fl/fl}$ littermates *(Kabat et al., 2016a)*. However, the intestinal Treg compartment was severely affected by *Atg16l1* deficiency, as the frequencies of both colonic and SI LP Foxp3^{+} Treg cells were reduced by around two-fold relative to Atg16l1$^{fl/fl}$ littermates. This equated to a reduction in Treg cell numbers by around 10-fold in the colonic LP and 4-fold in SI LP of Atg16l1$^{\Delta CD4}$ mice *(Kabat et al., 2016a)*. Moreover, the intestinal inflammation observed in Atg16l1$^{\Delta CD4}$ mice was associated with the selective expansion of Th2 cells at the intestinal lamina propria. Furthermore, inflammation was preceded by the production of Th2-associated antibodies towards dietary and commensal antigens, the levels of which increased with age *(Kabat et al., 2016a)*.

Thus, it is possible that the dysregulated Th2 cell homeostasis seen the Atg16l1$^{\Delta CD4}$ mice could be a consequence of decreased levels of Treg cells at the intestinal mucosa. Therefore, to establish if expansion of Th2 cell frequencies in Atg16l1$^{\Delta CD4}$ mice were due to a cell-intrinsic defect or were a consequence of dysregulated Treg homeostasis, I combined a mixed bone marrow chimera approach with a tamoxifen-inducible system *(Ventura et al., 2007) t*o delete *Atg16l1* in T cells to be able to compare WT and *Atg16l1*-deficient T cells in the same homeostatic environment.

The two main objectives of this chapter were:

- To validate the excision efficiency of a mouse model in which tamoxifen administration triggers deletion of *Atg16l1* in leukocytes.
- To determine whether the expansion of Th2 cells in Atg16l1$^{\Delta CD4}$ mice is intrinsically or extrinsically regulated through generation of mixed BM chimeras in which WT and *Atg16l1*-deficient T cells are present in the same environment.

3.2 Experimental results

3.2.1 Validation of tamoxifen meditated *Atg16l1*-excision and tdTomato reporter expression

A mixed BM chimera experiment previously performed in the Maloy lab, in which $Rag1^{-/-}$ mice were reconstituted with a 1:1 mixture of BM cells from $Atg16l1^{\Delta CD4}$ mice and wild-type (WT) C57BL/6 CD45.1 congenic mice, showed that *Atg16l1*-deficient cells failed to reconstitute the peripheral lymphoid compartment under these conditions (data not shown). Therefore, it was not possible to examine whether the differential regulation of Treg and Th2 subsets seen in the $Atg16l1^{\Delta CD4}$ mice was primarily due to cell-intrinsic effects.

To circumvent the inability of *Atg16l1*-deficient BM cells to reconstitute lymphopenic hosts, I generated mice carrying a tamoxifen-inducible Cre-recombinase together with floxed *Atg16l1* and *tdTomato* reporter alleles, designated as $Atg16l1^{fl/fl}$ Rosa26-$tdTomato^{fl/fl}$ $Rosa26^{CreERT2}$ (Figure 5A), by crossing a series of transgenic mice as details in section 2.1. In this system Cre is sequestered in the cytosol by a mutant estrogen receptor (ERT) until the tamoxifen metabolite, 4-hydroxytamoxifen (4-OHT), releases Cre and allows it to travel to the nucleus and trigger the recombination of genomic *loxP* sites *(Ventura et al., 2007).* This is predicted to result in Cre recombinase expression in all cells, as well as tdTomato expression in all cells, following excision of the *loxP*-flanked "STOP" cassette (Figure 5A). Using mice in which Cre-ERT2 is expressed under the ubiquitous *ROSA26* locus, as donors in the BM chimera experiments, means that donor cells can be easily traced by tdTomato expression after tamoxifen injection in the host mice.

To confirm these mice were deficient in Atg16l1 protein after tamoxifen administration lysates from snap-frozen whole colonic tissues were subjected to western blotting with anti-tubulin and anti-Atg16l1. Colon lysates from mice treated with 75mg/kg tamoxifen i.p. for 3 consecutive days, showed a complete absence of Atg16l1 protein compared to control mice (Figure 5B), measured at 43 days after the first tamoxifen injection.

The excision efficacy of tamoxifen inducible Cre-drivers can vary. Therefore, a pilot experiment was performed in order to assess the excision efficacy of two tamoxifen-dosing regimens in $Atg16l1^{fl/fl}$ Rosa26-$tdTomato^{fl/fl}$ $Rosa26^{CreERT2}$ mice. Using a published protocol as a starting point *(Whitfield et al., 2015)*, a dose of 75mg/kg tamoxifen administered by intraperitoneal (IP) injection for either 3 or 5 consecutive days was trialled. Both dosing regimens yielded an excision efficacy of over 95% in $CD45^{+}$ peripheral blood leukocytes, as determined by tdTomato expression, 9 days after tamoxifen administration (Figure 6A). In the absence of tamoxifen recombination should be minimal, and in our system there was a Cre leakage of approximately 3%, as measured by tdTomato expression in $CD45^{+}$ cells (Figure 6A). Given that we observed equal effects of the two tamoxifen dosing regimens tested, for future experiments we administered tamoxifen IP for 3 consecutive days at 75mg/kg.

As Cre-ERT2 is under the control of the ubiquitously expressed ROSA26 promoter, *Atg16l1* is deleted across the mouse body after tamoxifen administration. This was noticeable with the naked eye as the skin along with other tissues from these mice had a pink colouring, most likely spill over into the visual spectrum from the tdTomato fluorescence (Fig. 4B). Although we did not observe any changes in body weight within the 40 days after tamoxifen administration (data not shown), the spleens and mesenteric lymph nodes (MLN) showed evidence of immune activation. Compared with Cre negative tamoxifen-treated littermates, the Cre +ve mice had significantly increased spleen weights, enlarged lymph nodes, as well as reduced frequencies and total numbers of $CD4^+$ T cells in the spleen and MLN (Figure 6C, D). This confirms that the reporter expression correlates with reduced T cell survival, indicating that Cre also drives functional deletion of *Atg16l1*.

Given the successful validation of Atg16l1 excision after 3-day tamoxifen administration in the $Atg16l1^{fl/fl}$ Rosa26-$tdTomato^{fl/fl}$ $Rosa26^{CreERT2}$ mice, I next used this strain to generate mixed BM chimeras in order to compare WT and autophagy-deficient $CD4^+$ T cells within the same environment (Figure 7A).

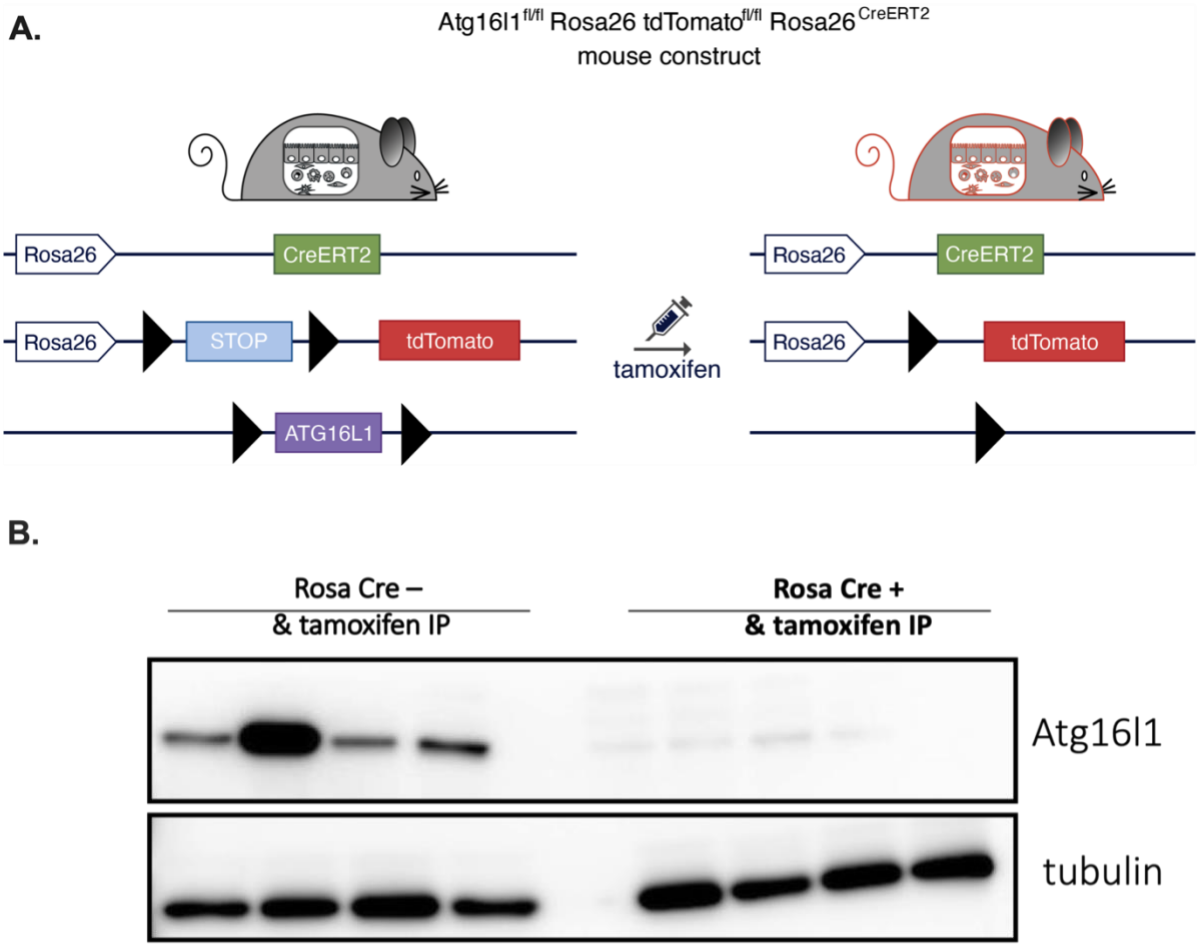


Figure 5. Validation of Atg16l1$^{fl/fl}$ Rosa26-tdTomato$^{fl/fl}$ Rosa26^{CreERT2} genetic construct.

(A) Schematic representation of the genetic constructs present in Atg16l1$^{fl/fl}$ Rosa26-tdTomato$^{fl/fl}$ Rosa26^{CreERT2} mice. After administration of tamoxifen, Cre excises the DNA sequences that lie between two *loxP* sites and re-joins the exposed ends. Thus, Cre activates the tdTomato reporter by excising the flanked STOP sequence and deletes the *Atg16l1* gene. Black triangles represent *lox*P-flanked alleles.

(B) Western blot of Atg16l1 protein expression from snap-frozen whole colonic tissue isolated from Atg16l1$^{fl/fl}$ Rosa26-tdTomato$^{fl/fl}$ Rosa26^{CreERT2} mice and Cre- littermate controls 43 days after the first tamoxifen injection. Tubulin was used as loading control. Each lane represents an individual mouse (n = 4 per group).

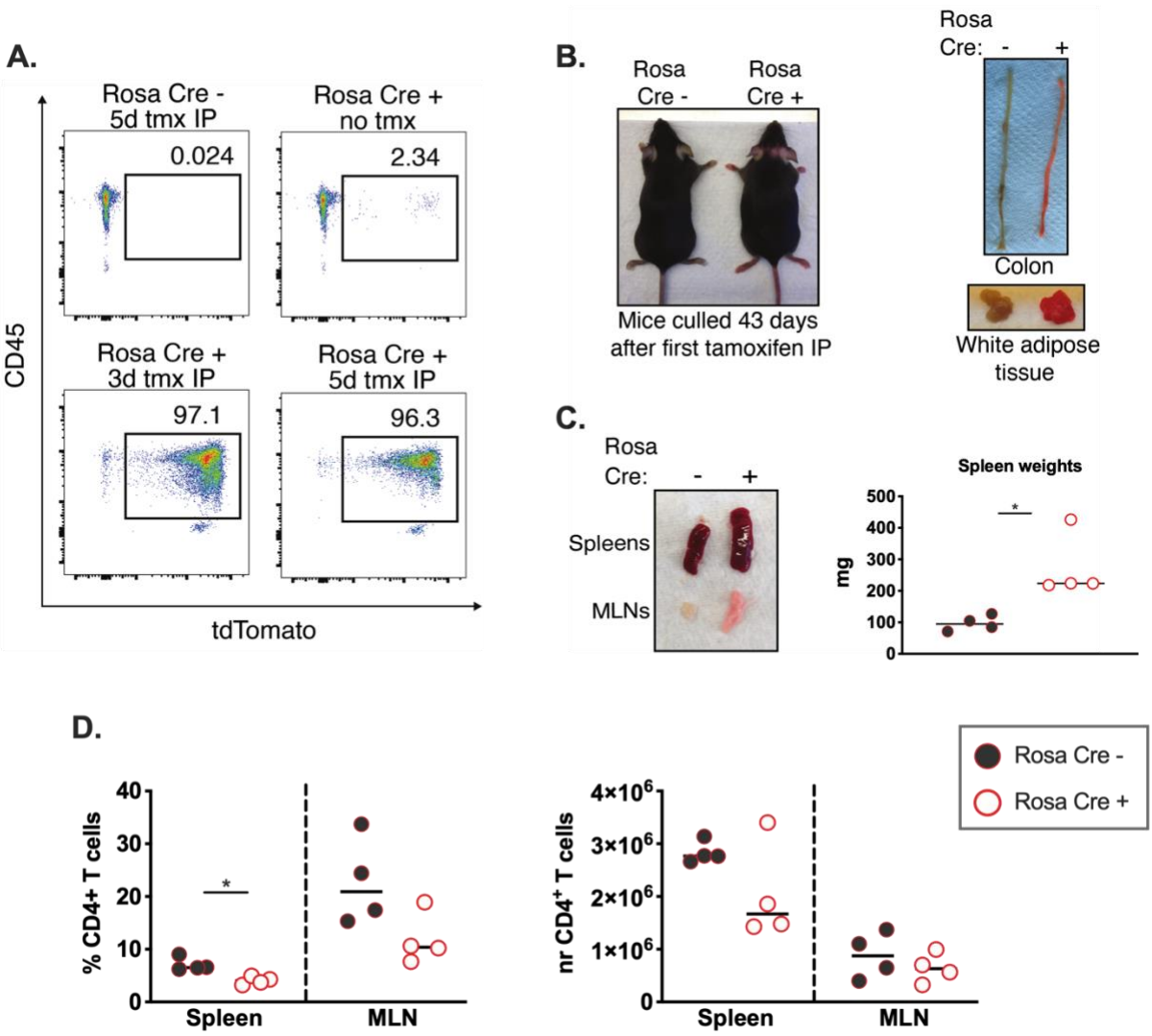


Figure 6. Validation of tamoxifen dosing regimen for triggering Atg16l1 deletion in the Atg16l1$^{fl/fl}$ Rosa26-tdTomato$^{fl/fl}$ Rosa26^{CreERT2} mouse model.

Sex-matched, 8-weeks old, RosaCre+ and RosaCre- littermates were injected IP with 75mg/kg tamoxifen for three or five consecutive days.

(A) Representative FACS plots of peripheral blood from control mice or mice treated with varying tamoxifen dosing regimens. Blood was obtained by superficial tail bleed 9 days after the initial tamoxifen injection.

(B) Representative images of mice and tissues 43 days after the first tamoxifen injection.

(C) Representative image of spleens and mesenteric lymph nodes (MLN) 43 days after the first tamoxifen injection and spleen weights of RosaCre+ and RosaCre- littermates.

(D) Frequencies and numbers of CD4 T cells as a proportion of live cells in the spleen and MLN of RosaCre+ and RosaCre- littermates.

Data is representative of one experiment with 4 mice per group. **(C, D)** Each symbol represents an individual mouse. Statistical significance was determined using the Mann-Whitney test, *p<0.05.

3.2.2 Autophagy-deficient Th2 cells compete well with WT counterparts whilst autophagy deficient Treg cells are outcompeted by WT counterparts in $Rag^{-/-}$ mixed BM chimeras

Mixed BM chimera experiments can be used in order to differentiate between cell intrinsic and cell extrinsic effects of a gene modification in hematopoietic cells. When cells of different genotypes develop under identical conditions within the same animal, any differences observed between them regarding proliferation and differentiation are cell-intrinsic.

To set up mixed BM chimeras, BM cells were isolated from the tibia and femur of congenic WT (C57BL/6, $CD45.1^+$) mice and the $Atg16l1^{fl/fl}$ Rosa26-$tdTomato^{fl/fl}$ $Rosa26^{CreERT2}$ (*Atg16l1*-inducible KO, $CD45.2^+$) mice described above. After depletion of $CD3^+$ cells, a 20% WT ($CD45.1^+$) and 80% *Atg16l1*-inducible KO ($CD45.2^+$) mixture of BM cells was injected i.v. (total of $1x10^7$cells per mouse) into irradiated $Rag^{-/-}$ recipients (Figure 7B). We posited that, following administration of tamoxifen and induction of autophagy deficiency, the number of autophagy-deficient T cells would fall. As such, we used a 20% WT : 80% *Atg16l1*-inducible ratio of BM cells to give us enough time to perform the necessary analysis before the autophagy-deficient T cells were replaced or out-competed by WT counterparts.

The BM chimera mice were allowed to reconstitute for 8 weeks before the proportions of donor cells (CD45.1 vs CD45.2) in the blood (chimerism) were checked. Before tamoxifen administration, all mice had roughly the desired proportion of 20:80 (WT:mutant) cells in the blood (Figure 8A). After the confirmation of reconstitution, tamoxifen was administered as previously described to trigger *Atg16l1* excision. Thereafter, tail vein blood samples were taken routinely (roughly every week) from the reconstituted $Rag1^{-/-}$mice to monitor chimerism (Figure 8A). These repeat measurements guided the scheduling of tissue analysis. Nine weeks after tamoxifen administration, the proportion of *Atg16l1*-deficient cells ($CD45.2^+$) in peripheral blood started to decrease (Figure 8A) and therefore the analysis of immune cells at tissue sites was performed at this time.

The proportion of $CD45.1^+$ $tdTomato^-$ cells and $CD45.2^+$ $tdTomato^+$ cells, referred to as "WT" and "*Atg16l1*-deficient" respectively amongst different subsets of $CD4^+$ T cells, was defined according to the gating strategy depicted in Figure 7C.

Additionally, we also assessed the frequencies of Treg ($Foxp3^+CD4^+$) and Th2 ($Gata3^+CD4^+$) subsets in the blood as proportion of WT and *Atg16l1*-deficient fractions. Before tamoxifen administration the relative frequencies of these subsets were almost perfectly comparable (Figure 8B, C). However, the proportion of *Atg16l1*-deficient Treg cells rapidly decreased after *Atg16l1* excision (Figure 8B). In contrast, the frequencies of *Atg16l1*-deficient Th2 cells continued to be similar to those observed for WT Th2 cells (Figure 8C).

Analysis of the immune compartment at tissue sites in the $Rag^{-/-}$ BM chimeras was performed 9 weeks post tamoxifen administration. The tissue chimerism was greatly different from the

chimerism observed in peripheral blood (Figure 9A). Additionally, the ratio of *Atg16l1*-deficient CD45.2$^+$Tomato$^+$ cells seemed to be decreased in the spleen and colonic lamina propria (cLP) in comparison to those observed in the blood (Figure 9A). This observation confirms the reliance of CD4$^+$ T cells on autophagy for survival at peripheral tissue sites.

Similar to what we observed in the blood, the frequencies of *Atg16l1*-deficient Treg cells were very low at tissues sites (Figure 9B). However, when we looked at other Th subsets, using lineage defining transcription factors (Gata3$^+$ for Th2; T-bet$^+$ for Th1; and RoRγT$^+$ for Th17 cells), we observed that *Atg16l1*-deficient Th2 cells performed the best in terms of survival alongside WT counterparts, across all tissues examined (Figure 10A, C, E). Similarly, the frequencies of *Atg16l1*-deficient cells expressing IFNγ$^+$ and IL-17$^+$ cells (cytokines associated with Th1 and Th17 cells, respectively) were decreased in the spleen and MLNs (Figure 10D, F), whereas the frequencies of *Atg16l1*-deficient cells expressing the Th2 cytokine IL-13 maintained levels comparable to those of WT counterparts (Figure 10B).

An intriguing observation within this set of results was the high frequency of WT Treg cells present in the spleen and MLNs in comparison to the cLP (Figure 9B). Usually the intestine harbours very high numbers of Treg cells as it requires heavy regulation to prevent intestinal inflammation *(Izcue et al., 2009)*. This expanded population of WT Treg cells could point to an effect of the Rag1$^{-/-}$ lymphopenic environment on driving donor Treg cell proliferation to fill up the lymphopenic niche. The increased frequencies of WT Treg cells could also be a consequence of the steep decrease in *Atg16l1*-deficient Treg cells following tamoxifen administration. From previous research we know that Treg cells rely on autophagy for survival in the periphery *(Kabat et al., 2016a)*. As such, since 80% of the donor cells were inducible *Atg16l1*-deficient, their sharp decline once tamoxifen was administered could have forced WT Treg cells to proliferative in order to maintain Treg homeostasis.

In order to counteract this potential bias in WT Treg expansion, I set up a second mixed BM chimera experiment, this time using sub-lethally irradiated C57BL/6 hosts reconstituted with a 50:50 mixture of WT (CD45.1$^+$) and *Atg16l1*-inducible KO (CD45.2$^+$) donor BM cells, as detailed in the next section.

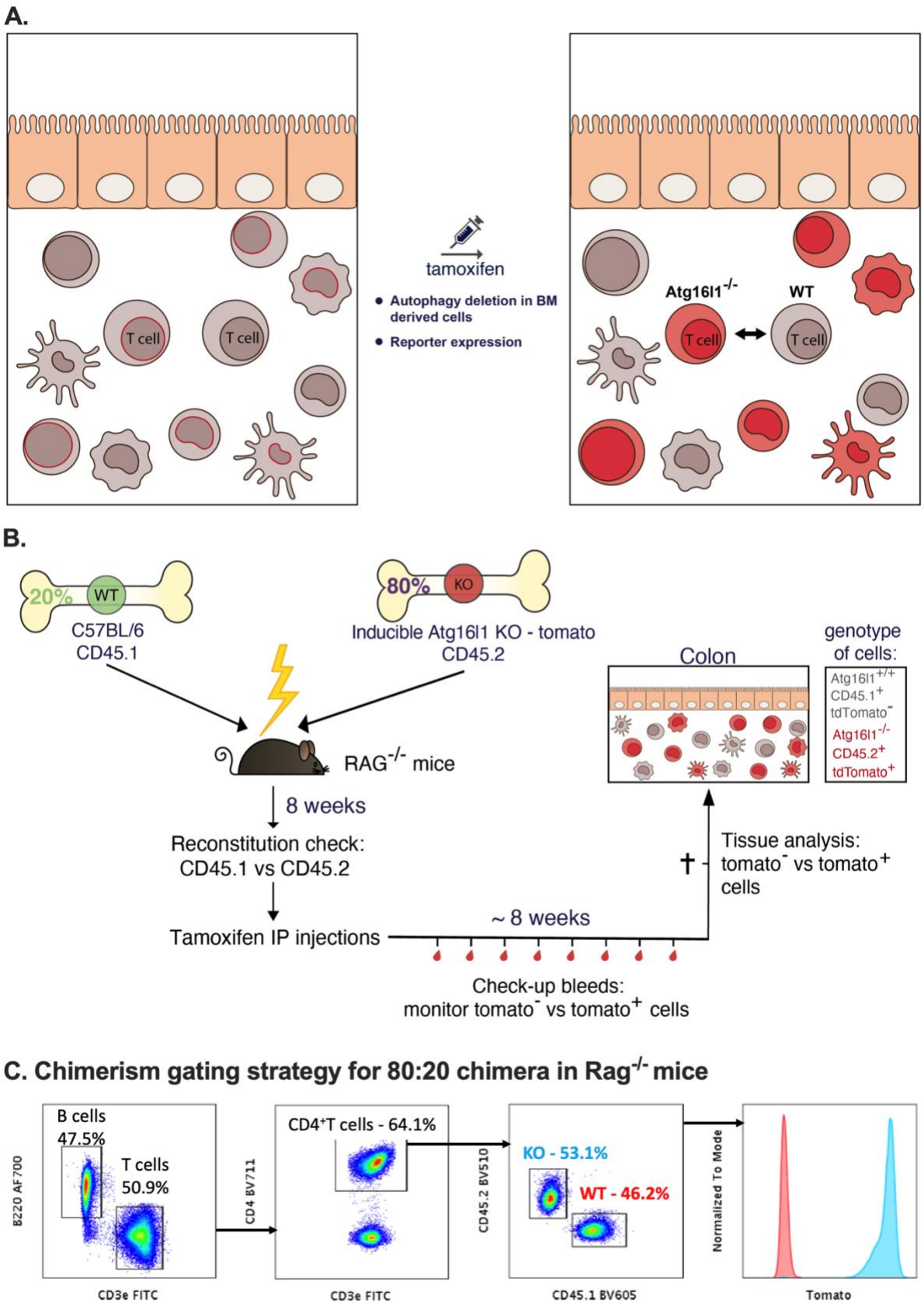


Figure 7. Setup of mixed BM chimeras in Rag$^{-/-}$ hosts.

$Rag^{-/-}$ mice were sub-lethally irradiated and then reconstituted with a mixture of 20% WT ($CD45.1^{+}$) and 80% *Atg16l1*-inducible KO ($CD45.2^{+}$) BM cells was injected i.v. (total of $1x10^{7}$cells per mouse).

(A) Schematic representation of the mixed BM chimeras using hematopoietic cells from WT and inducible autophagy-deficient mice. After the successful reconstitution of the host with a mix of BM donor cells, tamoxifen is administered to trigger deletion of autophagy in a subset of BM cells. This system allows comparison of autophagy-deficient and –competent leukocytes in the same environment.

(B) Schematic of mixed BM chimera experiment using $Rag^{-/-}$ hosts. Briefly, 20% WT and 80% inducible *Atg16l1* KO mixed BM chimeras were injected IP with 75mg of tamoxifen/kg for 3 days after successful reconstitution. Lymphocyte chimerism was subsequently measured in the blood to inform the timing for tissue analysis.

(C) FACS plots depicting the gating strategy used for the mixed BM chimeras. Th cells subsets, like Treg, Th2, etc are quantified as a proportion of $CD45.1^{+}Tomato^{-}$ or $CD45.2^{+}Tomato^{+}$ fractions.

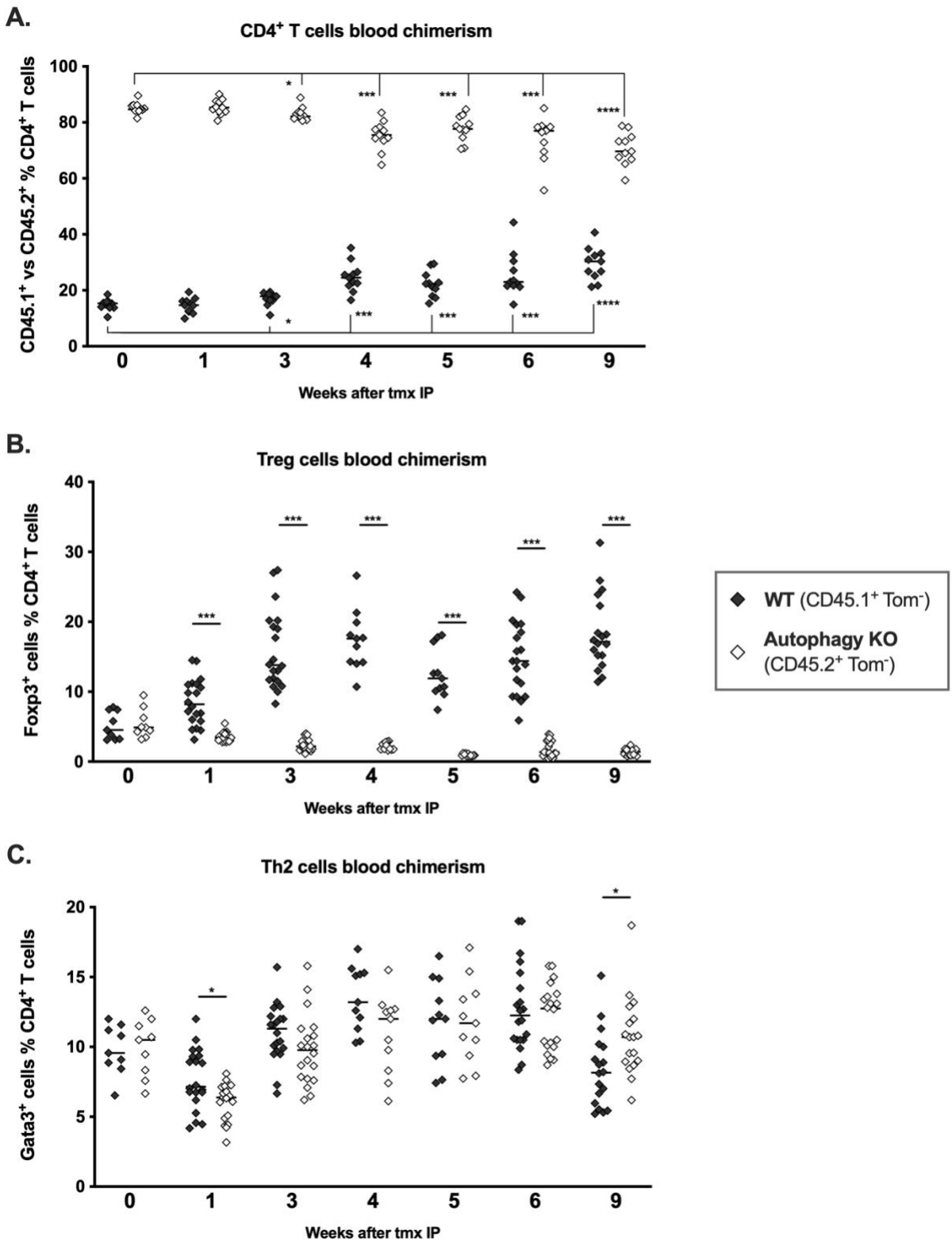


Figure 8. Analysis of Th cells in peripheral blood of $Rag^{-/-}$ mixed BM chimeras.
$Rag^{-/-}$ mice were sub-lethally irradiated and then reconstituted with a mixture of 20% WT ($CD45.1^+$) and 80% *Atg16l1*-inducible KO ($CD45.2^+$) BM cells was injected i.v. (total of $1x10^7$cells per mouse).

(A, B, C) At the indicated time points after IP tamoxifen administration, FACS analysis was used to assess the frequencies of WT ($CD45.1^+Tomato^-$) and *Atg16l1*-deficient ($CD45.2^+Tomato^+$) amongst Th cells subsets in peripheral blood. Samples were pre-gated on $B220^-CD3^+CD4^+$Live cells.

(B, C) Treg cell ($Foxp3^+CD4^+$ T cells) and Th2 cell ($Gata3^+CD4^+$ T cells) frequencies expressed as percentage of WT and *Atg16l1*-deficient $CD4^+$ T cells fractions, as indicated.

Data is combined from three repeat experiments, with at least 3 mice per group. One mouse is represented by a complementary pair of a white and a black diamond dot. Horizontal bars denote medians. Statistical significance was determined using the Mann-Whitney test * $p < 0.05$, *** $p < 0.001$, **** $p < 0.0001$.

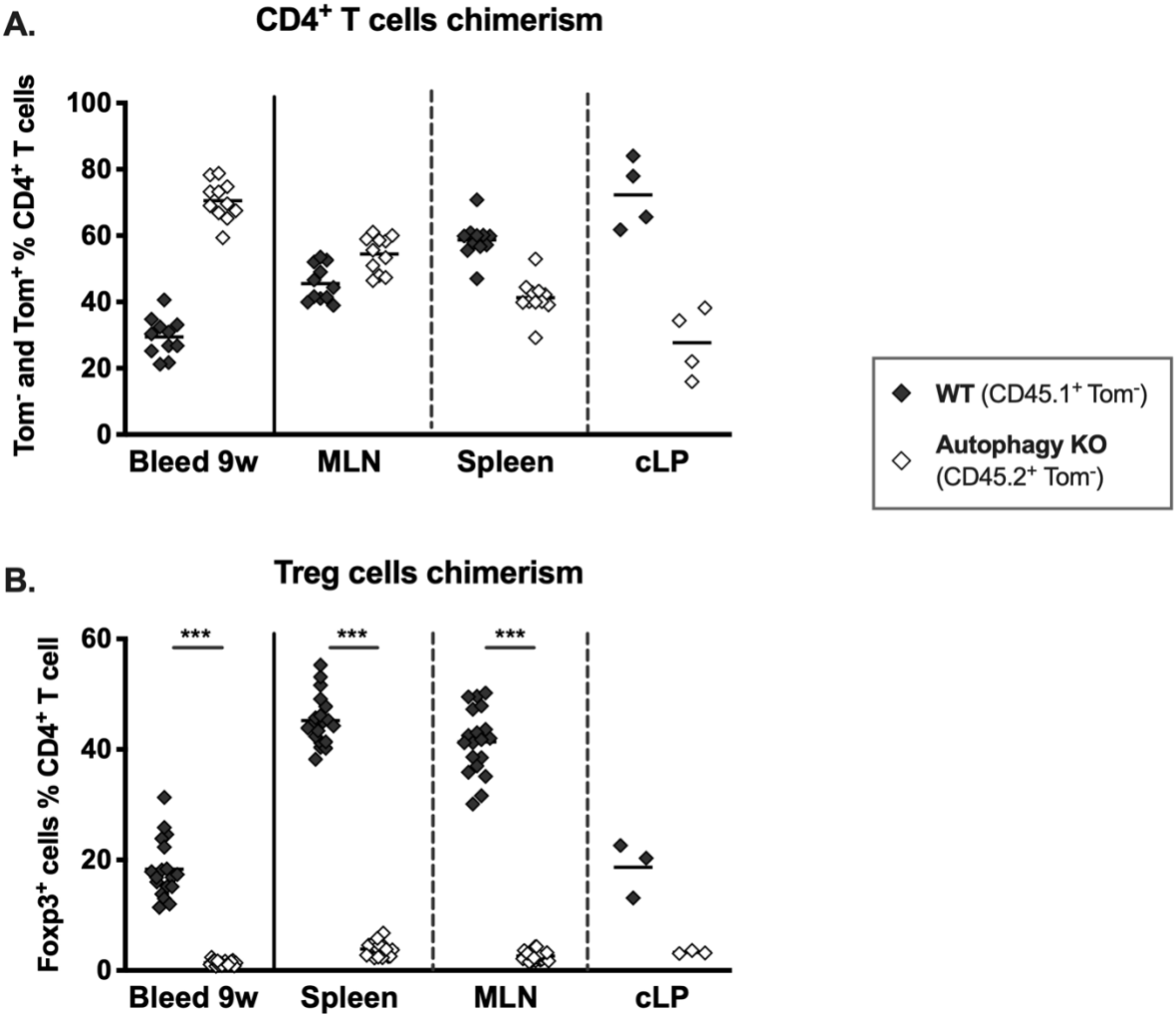


Figure 9. Analysis of Th cells in different tissues of $Rag^{-/-}$ mixed BM chimeras.

$Rag^{-/-}$ mice were sub-lethally irradiated and then reconstituted with a mixture of 20% WT ($CD45.1^+$) and 80% *Atg16l1*-inducible KO ($CD45.2^+$) BM cells was injected i.v. (total of $1x10^7$cells per mouse.

(A) Comparison of WT ($CD45.1^+Tomato^-$) and *Atg16l1*-deficient ($CD45.2^+Tomato^+$) fractions amongst $CD4^+$ T cells, at different tissue sites as indicated, 9 weeks after tamoxifen administration.

(B) Treg cell ($Foxp3^+CD4^+$ T cells) frequencies are expressed as percentage of WT and *Atg16l1*-deficient $CD4^+$ T cell fractions, as indicated.

Data is combined from three repeat experiments, with at least 3 mice per group. One mouse is represented by a complementary pair of a white and a black diamond dot. Horizontal bars denote medians. Statistical significance was determined using the Mann-Whitney test *** $p < 0.001$.

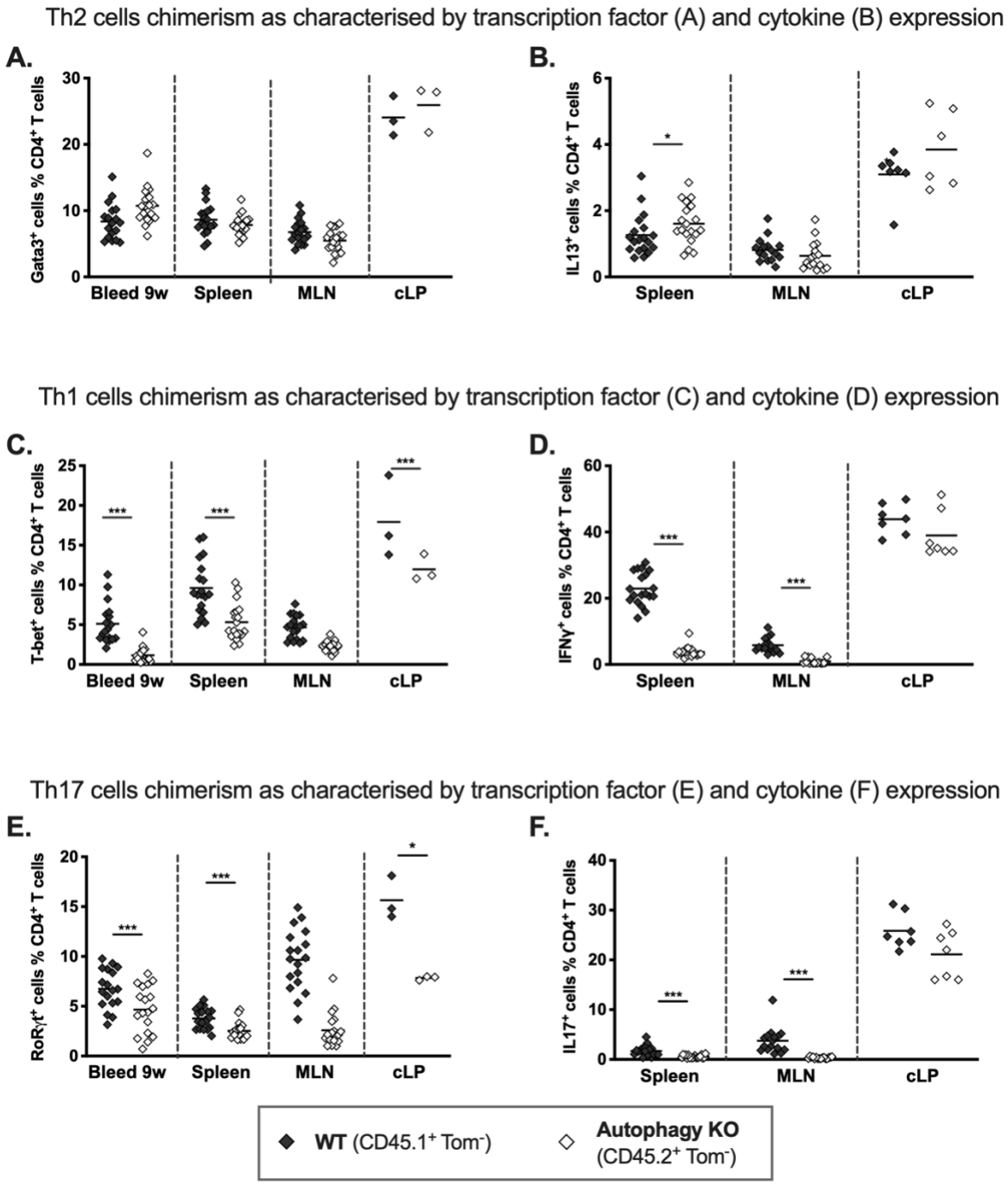


Figure 10. Analysis of Th cells at different tissues of Rag$^{-/-}$ mixed BM chimeras.
Rag$^{-/-}$ mice were sub-lethally irradiated and then reconstituted with a mixture of 20% WT (CD45.1^{+}) and 80% *Atg16l1*-inducible KO (CD45.2^{+}) BM cells was injected i.v. (total of 1x10^{7}cells per mouse).

(A-F) FACS analysis was used to assess the frequencies of WT (CD45.1^{+}Tomato^{-}) and *Atg16l1*-deficient (CD45.2^{+}Tomato^{+}) Th cell subsets in the spleen, MLN and cLP. Samples were pre-gated on B220^{-}CD3^{+}CD4^{+}Foxp3^{-}Live cells. Th2, Th1 and Th17 frequencies are expressed as percentage of WT and *Atg16l1*-deficient (Autophagy KO) within the CD4^{+} T cell fractions, as indicated.

Data is combined from three repeat experiments, with at least 3 mice per group. One mouse is represented by a complementary pair of a white and a black diamond dot. Horizontal bars denote medians. Statistical significance was determined using the Mann-Whitney test: * $p < 0.05$, *** $p < 0.001$.

3.2.2 C57BL/6 mixed BM chimeras corroborate the differential competitiveness of *Atg16l1*-deficient Th subsets

To address some of the potential limitations of the previous BM chimera experiment, a second mixed BM chimera experiment was performed. This followed broadly the same setup (Figure 11A) as the previous experiment with the exception of:

- the injected mixture which was made up of a 50:50 mix of donor cells (WT:*Atg16l1*-inducible KO). This was chosen in order to avoid a sharp decrease in the total pool of Treg cells following tamoxifen injection.
- the recipient mice which were C57BL/6 ($CD45.2^+$) rather than $Rag^{-/-}$ mice. This was to avoid any confounding effects of the $Rag^{-/-}$ lymphopenic environment on T cell reconstitution and proliferation.

The previous $Rag^{-/-}$ mixed BM chimera experiment relied on using WT and *Atg16l1*-deficient fractions as internal controls. Here, to have an external control for comparison I also set up control chimera mice as either;

- sub-lethally irradiated C57BL/6 hosts reconstituted 100% with WT (CD45.1) BM cells and receiving tamoxifen IP after successful reconstitution,

  or;

- sub-lethally irradiated C57BL/6 hosts reconstituted with the 50:50 mix of donor cells but receiving oil IP after successful reconstitution.

Before tamoxifen administration (week 0), mice had varying degrees of reconstitution with an average 40:60 ratio between WT and *Atg16l1*-inducible KO cells in peripheral blood (Figure 12A). After tamoxifen was administered, we observed that approximately 25% of the $CD4^+$ T cell population came from the immune system of the hosts ($CD45.2^+Tomato^-$), these cells were excluded from downstream analysis (Figure 11B) and the proportions of WT and *Atg16l1*-deficient T cells amongst donor cells were calculated. Six weeks after tamoxifen administration, the proportion of *Atg16l1*-deficient cells ($CD45.2^+$) in peripheral blood started to decrease (Figure 12A) and the analysis of immune cells at tissue sites was performed shortly after, i.e. at 8 weeks after tamoxifen administration.

The frequencies of Treg ($Foxp3^+CD4^+$) and Th2 ($Gata3^+CD4^+$) subsets in the blood, when compared between WT and *Atg16l1*-deficient fractions, corroborated the results of the previous BM chimera experiment. Before tamoxifen administration, the frequencies of Treg cells among both WT and *Atg16l1*-inducible KO $CD4^+$ T cells were comparable and were in line with the Treg frequencies seen in control mice (around 5% of $CD4^+$ T cells) (Figure 12B). However, after tamoxifen treatment, the WT Treg frequencies progressively increased, whereas the frequencies of *Atg16l1*-deficient Treg cells were significantly lower and showed a trend towards reduction at 6 weeks (Figure 12B). In contrast, the frequencies of *Atg16l1*-

deficient Th2 cells were comparable to those of WT Th2 cells for the first 3 weeks and even surpassed the WT Th2 cells 6 weeks after tamoxifen administration (Figure 12C).

Analysis of the immune compartment at tissue sites in the C57BL/6 BM chimera mice was performed 8 weeks post tamoxifen administration. Similar to what we observed in the $Rag^{-/-}$ mixed BM chimeras, the chimerism in the cLP was markedly different from that seen in other tissues, with *Atg16l1*-deficient $CD4^+$ T cells representing only around 20% of the cLP $CD4^+$ T cell population, compared to 40-50% in the blood, MLN and spleen. (Figure 13A). This further confirms the general reliance of $CD4^+$ T cells on autophagy to be able to adapt and survive in the intestine.

Similar to what we observed before, the frequencies of *Atg16l1*-deficient Treg cells were significantly lower than those of WT Treg cells at all tissue sites, with the latter being very similar to the levels seen in control mice (Figure 13B). In contrast, *Atg16l1*-deficient Th2 cells, assayed by Gata3 expression, competed well with WT counter parts, even exceeding WT or control Th2 frequencies in the MLNs (Figure 13C).

Looking at Th effector cells, we observed that *Atg16l1*-deficient Th2 cells performed the best in terms of competition with WT counterparts, across all tissues (Figure 14). Thus, we found that, compared to WT $CD4^+$ T cells, the frequencies of *Atg16l1*-deficient Th1 ($IFN\gamma^+$) and Th17 ($IL\text{-}17^+$) cells were greatly decreased in the spleen, MLN and cLP (Figure 14C-F), whereas the frequencies of *Atg16l1*-deficient Th2 ($IL\text{-}13^+$) cells were comparable to those of WT counterparts (Figure 14B).

Systemic measurements of the mixed BM chimeras did not reveal signs of systemic inflammation, as measured by spleen weight (Figure 15A), or signs of systemic Th2 cell activation, as measured by IgE serum concentration (Figure 15B), at 8 weeks post-tamoxifen treatment.

Overall, the results of the C57BL/6 chimeras corroborate the findings of the $Rag^{-/-}$ chimeras, indicating that these findings were robust and reproducible in different mouse models.

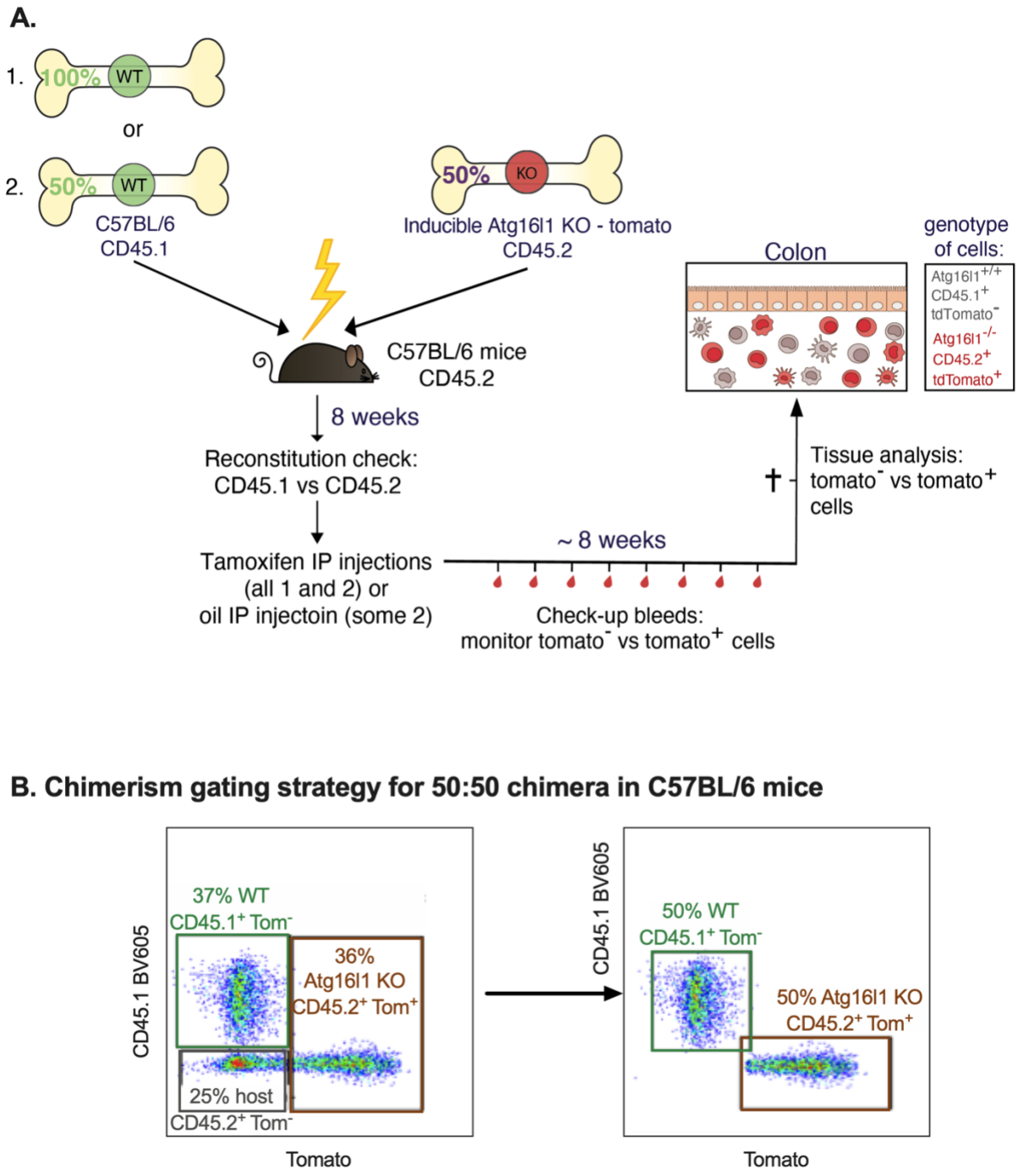


Figure 11. Set up of mixed BM chimeras with C57BL/6 hosts.
C57BL/6 mice were sub-lethally irradiated and then reconstituted with a mixture of 50% WT ($CD45.1^+$) and 50% Atg16l1-inducible KO ($CD45.2^+$) BM cells was injected i.v. (total of $1x10^7$cells per mouse).

(A) Schematic of mixed BM chimera experiment using C57BL/6 hosts. Briefly, host mice were irradiated twice with 550 Rad y-irradiation from a ^{127}Cs source with a break of 180 minutes. Then the hosts were reconstituted with a 50% WT ($CD45.1^+$) and 50% inducible *Atg16l1* KO mixture of BM cells. After successful reconstitution was confirmed, the mice were injected IP with 75mg of tamoxifen/kg for 3 days. Control chimera mice were also

setup as either hosts reconstituted with 100% WT ($CD45.1^+$) cells or hosts reconstituted with 50:50 donor cells mix and injected IP with oil.

(B) FACS plots depicting the relative proportions of donor vs host cells in reconstituted C57BL/6 hosts after tamoxifen administration. Hosts cells ($CD45.2^+Tom^-$) were excluded from further downstream analysis.

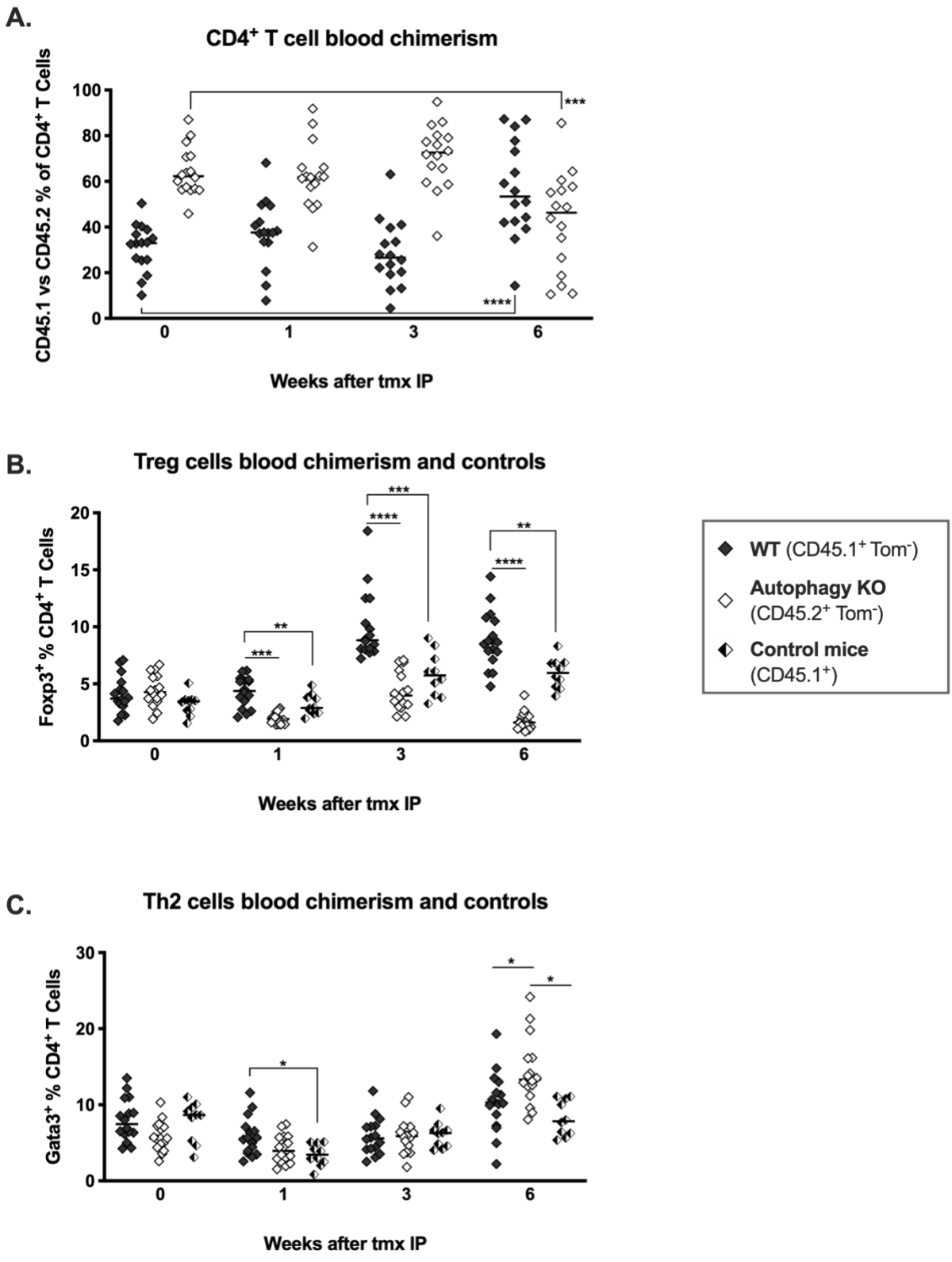


Figure 12. Analysis of Th cells in peripheral blood of mixed BM chimeras (C57BL/6 hosts). C57BL/6 mice were sub-lethally irradiated and then reconstituted with a mixture of 50% WT ($CD45.1^+$) and 50% *Atg16l1*-inducible KO ($CD45.2^+$) BM cells was injected i.v. (total of $1x10^7$cells per mouse).

(A) At the indicated time points after IP tamoxifen administration, FACS analysis was used to assess the relative proportions of WT ($CD45.1^+Tomato^-$) and *Atg16l1*-deficient ($CD45.2^+Tomato^+$) $CD4^+$ T cells in peripheral blood. Samples were pre-gated on $B220^-CD3^+CD4^+$Live cells. The host T cell population ($CD45.2^+Tomato^-$) was excluded from the analysis.

(B) Treg cell ($Foxp3^+CD4^+$ T cells) and (**C**) Th2 cell ($Gata3^+Foxp3^-CD4^+$ T cells) frequencies expressed as percentage of WT and *Atg16l1*-deficient $CD4^+$ T cells, or as percentage of $CD4^+$ T cells in the control mice, as indicated.

Data is combined from three repeat experiments, with at least 3 mice per group. One mouse is represented by a complementary pair of a white and a black diamond dot. The half-coloured diamonds represent one control mouse each. Horizontal bars denote medians. Statistical significance was determined using the Mann-Whitney test * $p < 0.05$, ** $p < 0.01$, *** $p < 0.001$, **** $p < 0.0001$.

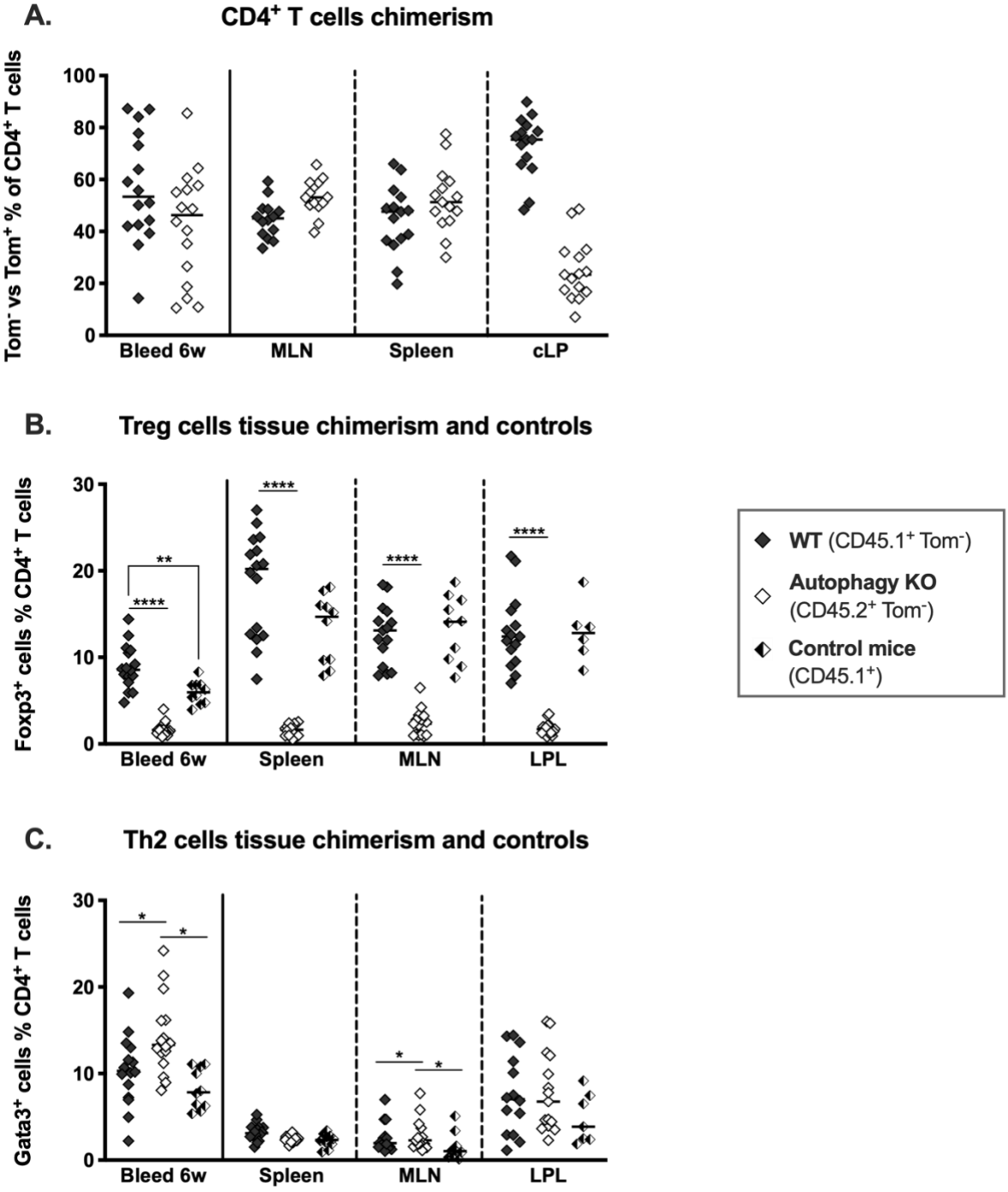


Figure 13. Analysis of Th cells intracellular markers across different tissues from mixed BM chimera (C57BL/6 hosts) mice.

C57BL/6 mice were sub-lethally irradiated and then reconstituted with a mixture of 50% WT ($CD45.1^+$) and 50% *Atg16l1*-inducible KO ($CD45.2^+$) BM cells was injected i.v. (total of $1x10^7$cells per mouse).

(A) Comparison of WT ($CD45.1^+Tomato^-$) and *Atg16l1*-deficient ($CD45.2^+Tomato^+$) fractions amongst $CD4^+$ T cells, at different tissue sites as indicated, 8 weeks after tamoxifen administration.

(B) Treg cell ($Foxp3^+CD4^+$ T cells) and (**C**) Th2 cell ($Gata3^+Foxp3^-CD4^+$ T cells) frequencies are expressed as percentage of WT and *Atg16l1*-deficient $CD4^+$ T cells, or as percentage of $CD4^+$ T cells in the control mice, as indicated.

Data is combined from three repeat experiments, with at least 3 mice per group. One mouse is represented by a complementary pair of a white and a black diamond dot. The half-coloured diamonds represent one control mouse each. Horizontal bars denote medians. Statistical significance was determined using the Mann-Whitney test: * $p < 0.05$, ** $p < 0.01$, **** $p < 0.0001$.

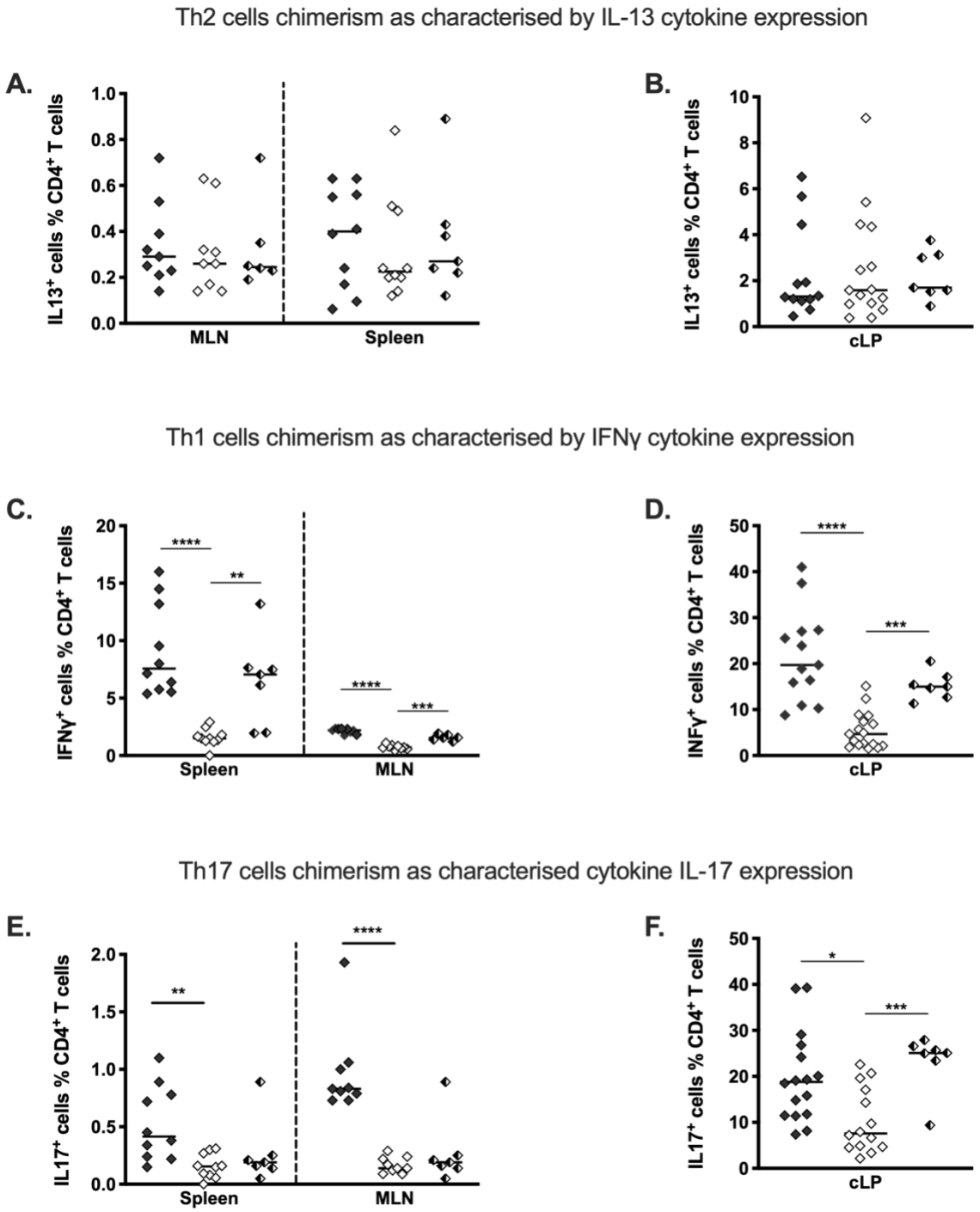


Figure 14. Analysis of Th cells cytokines expression across different tissues from mixed BM chimera (C57BL/6 hosts) mice.

C57BL/6 mice were sub-lethally irradiated and then reconstituted with a mixture of 50% WT (CD45.1$^+$) and 50% *Atg16l1*-inducible KO (CD45.2$^+$) BM cells was injected i.v. (total of 1x10^{7}cells per mouse).

(A) Comparison of WT (CD45.1$^+$Tomato$^-$) and *Atg16l1*-deficient (CD45.2$^+$Tomato$^+$) fractions amongst CD4$^+$ T cells, at different tissue sites as indicated, 8 weeks after tamoxifen administration.

(B) Treg cell ($Foxp3^+CD4^+$ T cells) and **(C)** Th2 cell ($Gata3^+Foxp3^-CD4^+$ T cells) frequencies are expressed as percentage of WT and *Atg16l1*-deficient $CD4^+$ T cells, or as percentage of $CD4^+$ T cells in the control mice, as indicated.

Data is combined from three repeat experiments, with at least 3 mice per group. One mouse is represented by a complementary pair of a white and a black diamond dot. The half-coloured diamonds represent one control mouse each. Horizontal bars denote medians. Statistical significance was determined using the Mann-Whitney test: * $p < 0.05$, ** $p < 0.01$, **** $p < 0.0001$.

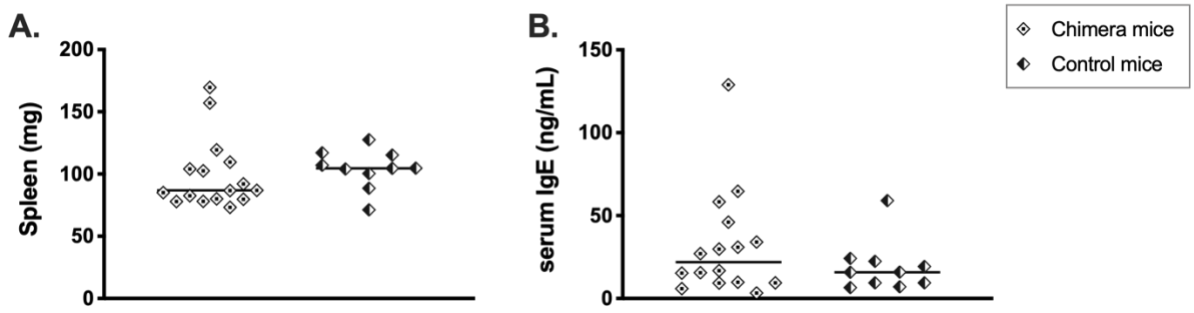


Figure 15. Systemic measurements of the C57BL/6 chimeras and control mice.

C57BL/6 mice were sub-lethally irradiated and then reconstituted with a mixture of 50% WT ($CD45.1^+$) and 50% *Atg16l1*-inducible KO ($CD45.2^+$) BM cells was injected i.v. (total of $1x10^7$cells per mouse). Control chimera mice were either hosts reconstituted with 100% WT ($CD45.1^+$) cells or hosts reconstituted with 50:50 donor cells mix and injected IP with oil.

(A) Spleen weights and **(B)** serum IgE levels of C57BL/6 mixed BM chimera and control mice.

Data is combined from three repeat experiments, with at least 3 mice per group. Each dot represents an individual mouse and horizontal bars denote medians.

3.2.5 Summary and conclusions

The characterisation of Atg16l1$^{\Delta CD4}$ mice revealed a selective expansion of Th2 cells in the colon and SI lamina propria *(Kabat et al., 2016a)*. This increase could have arisen due to a lack of cell extrinsic regulation from *Atg16l1*-deficient Treg cells and/or could have been a consequence of a cell intrinsic effect of *Atg16l1*-deficiency on Th2 cells. We have explored both hypotheses in the setting of inducible mixed bone marrow chimeras and found that *Atg16l1*-deficient Th2 cells show no cell-intrinsic disadvantage and are able to compete well with autophagy-sufficient counterparts.

The effects of *Atg16l1*-deletion on CD4$^+$ T cells in the peripheral blood took about 4 weeks to begin to become apparent, which is roughly in line with the accepted engraftment time for mouse bone marrow chimera models *(Passegue et al., 2005)*. However, another potential contributing factor is that autophagy deletion may have a cumulative effect over time. Evidence of the latter possibility comes from a study utilising a mouse model in which *Atg3* was selectively deleted in T cells, which reported that accumulation of cellular material over time caused the increased cell death observed in these T cells *(Jia and He, 2011)*. The late onset of autophagy-deficiency effects on CD4$^+$ T cells fits with the late onset of the pathology we found in Atg16l1$^{\Delta CD4}$ mice. The delayed disease onset could therefore reflect previous findings that thymic production of Treg cells was unimpaired in Atg16l1$^{\Delta CD4}$ mice *(Kabat et al., 2016a)*. As thymic involution occurs in older mice, the central output of Treg and conventional T cells is decreased, meaning that the peripheral Treg cell compartment cannot be fully replenished.

The results shown in this chapter also indicate that autophagy is crucial for the survival of not only Treg cells but also Th1 and Th17 cells within the gut environment, suggesting that autophagy is a part of the larger adaptation program needed for these cells to operate within peripheral tissues. Nevertheless, in the setup of mixed bone marrow chimera autophagy seems needed in order to restrain the expansion of Th2 cells in the periphery. The literature sustains the idea that autophagy modulates CD4$^+$ T cell function in a subset-specific manner, although there has been considerable variation in the effects reported between effector CD4$^+$ T cell subsets *(Clarke and Simon, 2019).*

From these findings we can hypothesise that the lack of sufficient Treg control over Th2 effector responses is a secondary event in the development of the immunopathology seen in Atg16l1$^{\Delta CD4}$ mice. The initial event is an increase in Th2 cells that arises as *Atg16l1*-deficient Th2 cells show no cell-intrinsic disadvantage compared to other autophagy-deficient Th subset. This is then further enhanced by the compromised suppression from autophagy-deficient Treg cells.

Chapter 4. Investigating the role of type 2 responses in the development of the pathology seen in Atg16l1$^{\Delta CD4}$ mice

4.1 Introduction and aims of chapter

The initial characterisation of Atg16l1$^{\Delta CD4}$ mice revealed a selective enhancement of Th2 responses in the intestinal mucosa, contrasted by a progressive loss of Treg cells. The immune phenotype was accompanied by intestinal inflammation and failure to gain weight as the mice aged *(Kabat et al., 2016a)*. This encouraged a line of investigation assessing the association between the elevated type 2 immune responses and the gut and weight pathology observed.

Type 2 immune responses play important roles in intestinal health by conferring protection against helminth infections, toxins and venoms (*Pulendran and Artis, 2012)*. Type 2 responses have even been considered a counterbalance for tissue-damaging inflammation initiated by type 1 immune response. For example, type 2 responses instigate tissue repair to mitigate the effects of worm migration through vital organs *(Lloyd and Snelgrove, 2018)*. This process of wound healing normally leads to efficient healing, however, in chronic inflammation it can results in exaggerated repair mechanisms which can ultimately lead to fibrosis and impaired organ function *(Lloyd and Snelgrove, 2018).*

Fibrosis, usually defined as an excessive accumulation of scar tissue, is a common complication in IBD patients *(Rieder and Fiocchi, 2009).* In CD fibrosis can involve the whole thickness of the bowel wall and can cause formation of strictures, whilst in UC fibrosis is limited to the mucosal and submucosal layers *(Rieder and Fiocchi, 2009)*. Several animal models of fibrosis that involve the intestine have identified the Th2 cytokine, IL-13 as a dominant, profibrotic mediator. IL-13 can act both directly on fibroblasts, or indirectly by inducing TGF-β1 release from macrophages *(Fichtner-Feigl et al., 2007; Kolodsick et al., 2004).* While the early stages of inflammation are characterized by elevated levels of Th1 cytokines, late inflammation is often accompanied by elevated levels of IL-13 together with increased production of TGF-β1 *(Rieder and Fiocchi, 2009)*. This pattern is also seen in murine models of chronic IBD, such as in IL-10-KO mice *(Bamias et al., 2005; Spencer et al., 2002).*

These observations suggest that Th2 responses involving IL-13 represent an important profibrotic driver in IBD, a notion consistent with the central role Th2 cytokines play in other fibrotic conditions. As such, we have crossed the Atg16l1$^{\Delta CD4}$ mouse line with mice that lack IL-13 to investigate the role of this cytokine in driving the intestinal pathology described in Atg16l1$^{\Delta CD4}$ mice.

Type 2 immune regulation has also emerged as a regulator of adipose tissue metabolism. Adipocytes, the major cell component of fat tissues, can be divided into three types: white

adipose tissue (WAT), beige adipose tissue, and brown adipose tissue (BAT) *(Pfeifer and Hoffmann, 2015)*. White and beige adipocytes descend from mesenchymal stem cells (AMSC) based on to the presence and absence of certain stimuli, like cold exposure. In contrast, BAT is derived from AMSC progenitors that express myogenic factor 5 (Myf5), a progenitor cell also shared with skeletal muscle. In terms of function, WAT is specialized to store energy as fat in lipid droplets, whereas BAT and beige adipocytes are dedicated to dissipate energy as heat through UCP1-dependent and independent thermogenesis *(Pfeifer and Hoffmann, 2015)*. UCP1 (uncoupling protein 1) belongs to a family of mitochondrial carriers that disrupt formation of adenosine triphosphate (ATP) favouring the conversion of energy into heat instead. Unlike white adipocytes which are unilocular and contain no mitochondria, brown adipocytes contain many mitochondria and multiple small lipid droplets, giving them a multilocular appearance and the ability to produce heat efficiently. *(Villarroya et al., 2018)*.

Research over the last decade has shed light on an immune-thermogenic circuit regulated by type 2 immunity that boost BAT and beige adipose tissue development and function. The circuit is composed of type 2 immune cells (ILC2s, eosinophils, AAM and Th2 cells) plus type 2 cytokines (IL-33, IL-5, IL-13 and IL-4) and it converges on AAM to secret norepinephrine and promote thermogenesis and 'browning' of adipose tissue *(Villarroya et al., 2018)*. The type 2 cytokine milieu also supports insulin responsiveness and other metabolic characteristics of healthy WAT as evidenced by the reduction in these parameters upon gene deletion of type 2 cytokines or disruption of cells that secrete them *(Cipolletta et al., 2012; Nussbaum et al., 2013; Odegaard et al., 2007)*.

In this chapter I further explore the pathologic effects of dysregulated type 2 immune responses in the Atg16l1$^{\Delta CD4}$ mice by interrogating the potential role of IL-13 in driving the pathology. Furthermore, I examine the systemic effects of enhanced type 2 cytokines in relation to adipocyte health and the ability of Atg16l1$^{\Delta CD4}$ mice to gain weight.

Kabat et al. established that Treg cells cannot survive in the gut without autophagy, and that this is associated with failure to switch their metabolic profile from glycolysis to fatty-acid oxidation *(Kabat et al., 2016a)*. The autophagy machinery can make a large amount of lipids available, through a process called lipophagy, that can be used to fuel cellular mitochondrial respiration in times of metabolic demand. As such, lipophagy could provide a link between autophagy, fatty-acid metabolism and Treg survival. In line with this idea, I attempt a rescue experiment of autophagy-deficient Treg cells through free-fatty supplementation.

In summary, the main objectives of this chapter are:

- To validate the Atg16l1$^{\Delta CD4}$ IL-13 reporter mouse lines.
- To assess the immune pathology developed in the Atg16l1$^{\Delta CD4}$ IL13-KO mouse model.
- To further characterise the systemic effects of dysregulated type 2 immune responses in the fat compartment of Atg16l1$^{\Delta CD4}$ mice.
- Assess the effects of high-fat diet supplementation in Atg16l1$^{\Delta CD4}$ mice.

4.2 Experimental results

4.2.1 Characterization and validation of Atg16l1$^{\Delta CD4}$ IL13 reporter mice

In order to investigate the cellular mechanism that uniquely allows Th2 cells to survive independent of autophagy, we required a system that would allow us to sort large numbers of autophagy-deficient Th2 cells with high-purity to then use in functional studies. *Ex vivo* isolation of Th2 cells is technically difficult as there is no known cell surface marker that would allow for the selective purification of Th2 cells. As such, we sourced two *Il13* transgenic reporter strains from Andrew McKenzie, Cambridge University. The fluorescent protein knock-in results in a functional knock-out of the *Il13* gene when mice are bred as homozygotes (IL-13$^{gfp/gfp}$ or IL-13$^{tomato/tomato}$), but allows tracking of IL-13 expressing cells in heterozygous mice (IL-13$^{gfp/+}$ or IL-13$^{tomato/+}$) (*Neill et al., 2010*). I subsequently crossed these strains onto the Atg16l1$^{\Delta CD4}$ background and further characterized the resulting reporters and IL-13 KO mice.

To verify the validity of the reporter strains, Atg16l1$^{\Delta CD4}$IL-13$^{gfp/+}$ and Atg16l1$^{\Delta CD4}$IL-13$^{tomato/+}$ mice were allowed to age, culled around 30 weeks of age and their immunophenotype and pathophysiology were assessed. As expected, the heterozygous reporter mice reproduced the pathophysiology of the Atg16l1$^{\Delta CD4}$ in terms of weight curves (Figure 16A), splenomegaly (Figure 16B) and small intestine lengthening (Figure 16C). Both fluorescent reporter strains slightly under-report IL-13 expressing Th2 cells when compared to IL-13 intracellular antibody staining (Figure 16D, 17A-D), nonetheless Atg16l1$^{\Delta CD4}$IL-13$^{tomato/+}$ was deemed a more reliable reporter strain as it gave a more distinct population staining when assessed by FACS, with less non-specific tomato expression (Figure 16D).

Thus, the Atg16l1$^{\Delta CD4}$IL-13$^{tomato/+}$ line was available for sort purifying Th2 cells for downstream experiments. The Atg16l1$^{\Delta CD4}$IL-13$^{gfp/+}$ mouse line was used to generate Atg16l1$^{\Delta CD4}$IL-13$^{gfp/gfp}$ homozygotes to assess the effects of knocking out IL-13 in the Atg16l1$^{\Delta CD4}$ mice.

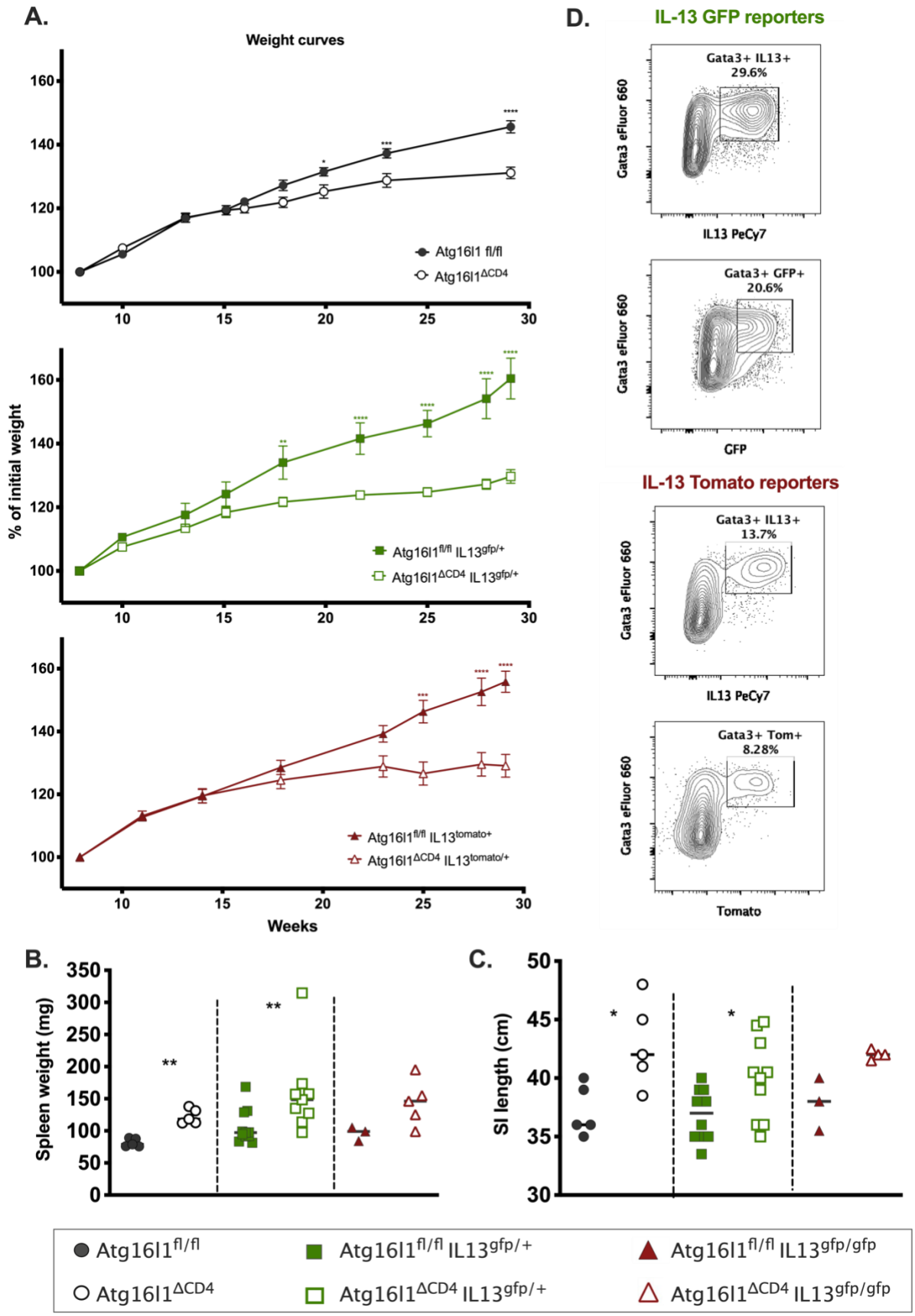

A.
Weight curves
% of initial weight
Weeks
Atg16l1 fl/fl
Atg16l1ΔCD4
Atg16l1fl/fl IL13gfp/+
Atg16l1ΔCD4 IL13gfp/+
Atg16l1fl/fl IL13tomato+
Atg16l1ΔCD4 IL13tomato/+
D.
IL-13 GFP reporters
Gata3+ IL13+
29.6%
Gata3 eFluor 660
IL13 PeCy7
Gata3+ GFP+
20.6%
GFP
IL-13 Tomato reporters
Gata3+ IL13+
13.7%
Gata3+ Tom+
8.28%
Tomato
B.
Spleen weight (mg)
C.
SI length (cm)
Atg16l1fl/fl
Atg16l1ΔCD4
Atg16l1fl/fl IL13gfp/+
Atg16l1ΔCD4 IL13gfp/+
Atg16l1fl/fl IL13gfp/gfp
Atg16l1ΔCD4 IL13gfp/gfp

Figure 16. Atg16l1$^{\Delta CD4}$IL-13 heterozygous reporter mice reproduce the immunopathology of Atg16l1$^{\Delta CD4}$ mice.

Atg16l1$^{\Delta CD4}$IL-13 heterozygous reporter mice were generated by crossing IL13 KO mice (IL-13$^{gfp/gfp}$ or IL-13$^{tomato/tomato}$) onto the Atg16l1$^{\Delta CD4}$ background. The mice were monitored for approximately 30 weeks before culling.

A) Body weight curves of Atg16l1$^{\Delta CD4}$, Atg16l1$^{\Delta CD4}$ IL-13$^{gfp/+}$ and Atg16l1$^{\Delta CD4}$IL13$^{tomato/+}$ mice.
B) Spleen weights and **(C)** small intestine lengths of cohorts of Atg16l1$^{\Delta CD4}$, Atg16l1$^{\Delta CD4}$ IL-13$^{gfp/+}$ and Atg16l1$^{\Delta CD4}$IL13$^{tomato/+}$ mice and Atg16l1$^{fl/fl}$ litter mates (>25 weeks old)
D) Representative FACS staining of IL-13 expression levels in Atg16l1$^{\Delta CD4}$ IL-13$^{gfp/+}$ and Atg16l1$^{\Delta CD4}$IL13$^{tomato/+}$ mice respectively. T cells were isolated from the cLP of aged mice (>25 weeks old) and *in vitro* re-stimulated with PMA, Ionomycin and Brefeldin for 3 hours prior to staining.

Data is combined from two independent experiments, with at least 3 mice per group. Data shown in (A) is representative of the mean weight ± s.e.m. (B, C) Each dot represents an individual mouse and horizontal bars denote medians. Statistical significance was determined using two-way analysis of variance (ANOVA) with Bonferroni's correction for multiple comparisons (A) or the Mann-Whitney test (B,C), * $p < 0.05$, ** $p < 0.01$, *** $p < 0.001$, *** $p < 0.0001$.

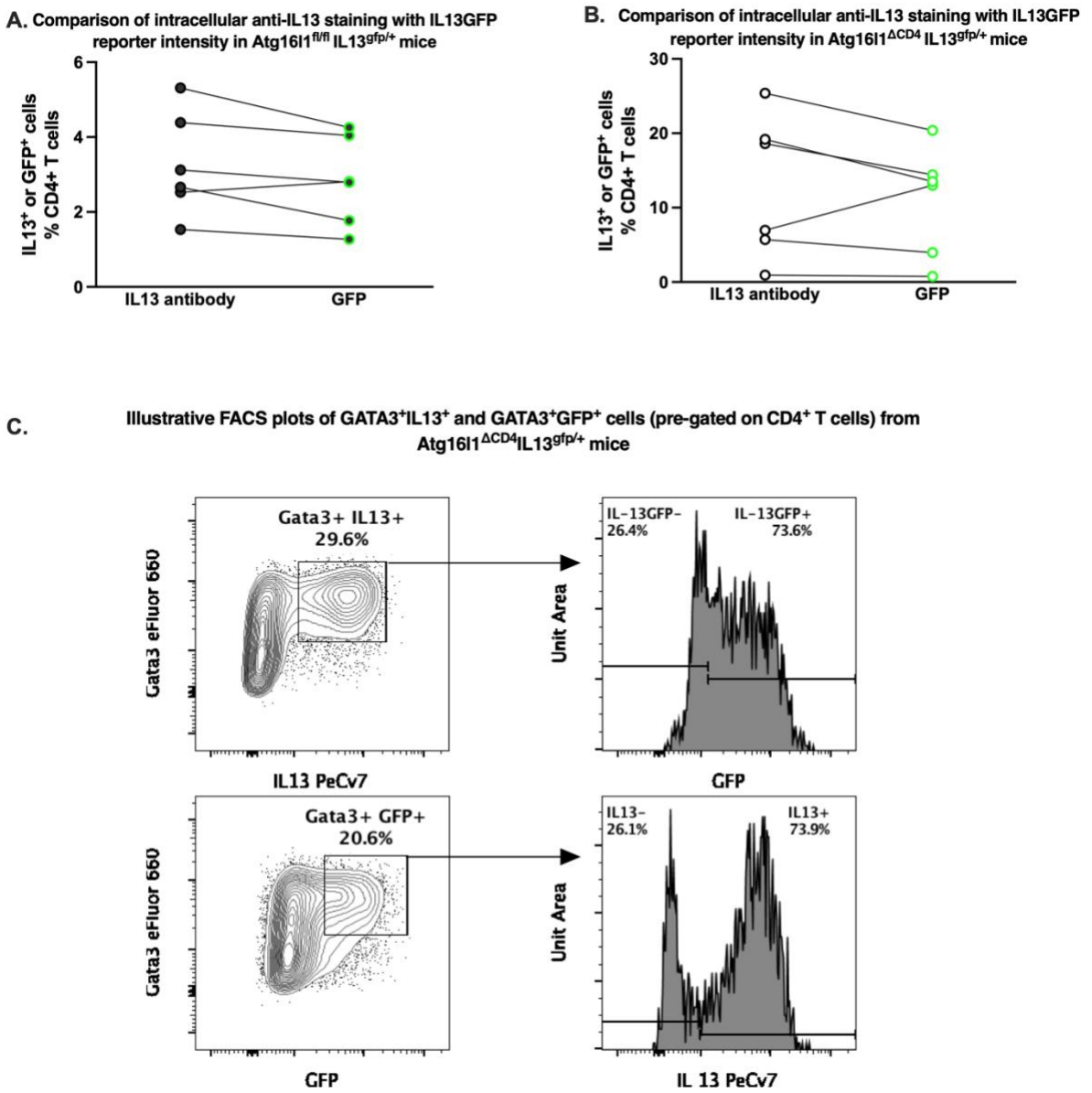


Figure 17. Atg16l1$^{\Delta CD4}$IL-13 heterozygous reporter mice provide a good equivalent to IL-13 antibody staining through GFP fluorescence.

Correlation of intracellular anti-IL13 staining with IL13-GFP reporter intensity in **(A)** Atg16l1$^{fl/fl}$IL13$^{gfp/+}$ mice and **(B)** Atg16L1$^{\Delta CD4}$IL13$^{gfp/+}$ mice. Two connected dots represent an individual mouse (n=6 per group), gated on CD4^{+} Foxp3^{-} live T cells.

C) Representative FACS staining of IL-13 expression levels in Th2 cells from Atg16l1$^{\Delta CD4}$ IL-13$^{gfp/+}$ mice, along with associated histograms. Gated on CD4^{+}Foxp3^{-}Gata3^{+} live T cells.

T cells were isolated from the cLP of aged, littermate control mice (>25 weeks old) and *in vitro* re-stimulated with PMA, Ionomycin and Brefeldin for 3 hours prior to staining.

4.2.2 Atg16l1$^{\Delta CD4}$ IL-13KO mice phenocopy the disease pathology and immune dysregulation seen in Atg16l1$^{\Delta CD4}$ mice

To test whether the prototypic Th2 cytokine IL-13 contributed to the pathology observed in Atg16l1$^{\Delta CD4}$ mice the pathophysiology and the immunophenotype of mice in which the *Atg16l1* gene is knocked out in T cells and *Il13* is knocked out in all cells (Atg16l1$^{\Delta CD4}$ IL-13$^{gfp/gfp}$) was assessed. IL-13, along with IL-4, is required to drive most of the key hallmarks associated with type 2 inflammation including IgE production *(Bao and Reinhardt, 2015)*. The frequency of GFP^{+} CD4^{+} T cells in the Atg16l1$^{\Delta CD4}$ IL-13$^{gfp/gfp}$ mice was comparable with the frequencies of IL-13^{+} CD4^{+} T cells present in Atg16l1$^{\Delta CD4}$ and Atg16l1$^{\Delta CD4}$ IL-13 reporters, providing a suitable surrogate for normal IL-13 expression (Figure 18B).

Atg16l1$^{\Delta CD4}$ IL-13$^{gfp/gfp}$ mice phenocopied the disease pathology and immune dysregulation seen in Atg16l1$^{\Delta CD4}$ mice, exhibiting a similar stunting in weight (Figure 18A), enteritis marked by lengthening of small intestinal crypts (Figure 18B), as well as splenomegaly (Figure 19C) and small intestine elongation (Figure 19D). Furthermore, serum IgE and IgG$_1$ (immunoglobulin isotypes associated with Th2 responses) in aged Atg16l1$^{\Delta CD4}$ IL-13$^{gfp/gfp}$ mice were significantly elevated relative to Atg16l1$^{fl/fl}$ littermates (Figure 19E,F). These results show that IL-13 is not required for the disease phenotype in Atg16l1$^{\Delta CD4}$ mice, or for the elevated type 2 responses.

The IL-13-independent disease phenotype might be explained by redundancy between Th2 cytokines *(Wynn, 2015).* ELISA measurements of the amount of IL-4 and IL-5 in colon explant culture supernatants obtained from aged Atg16l1$^{\Delta CD4}$ IL-13$^{gfp/gfp}$ mice showed that these mice have significantly increased levels of intestinal IL-5, but not IL-4, relative to Atg16l1$^{\Delta CD4}$ IL-13$^{gfp/+}$ mice (Figure 20).

To address the potential redundancy between Th2 cytokines it would be necessary to block IL-4, IL-5 and IL-13 at the same time in the Atg16l1$^{\Delta CD4}$ mice. However, due to the difficulty in sourcing enough IL-4 and IL-5 blocking antibodies to administer to the Atg16l1$^{\Delta CD4}$ IL-13$^{gfp/gfp}$ mice long term (3 months) I was not able to perform this experiment during the course of this thesis. In the future, this experiment could illuminate whether Th2 cytokines are driving the intestinal and systemic pathology seen in Atg16l1$^{\Delta CD4}$ mice.

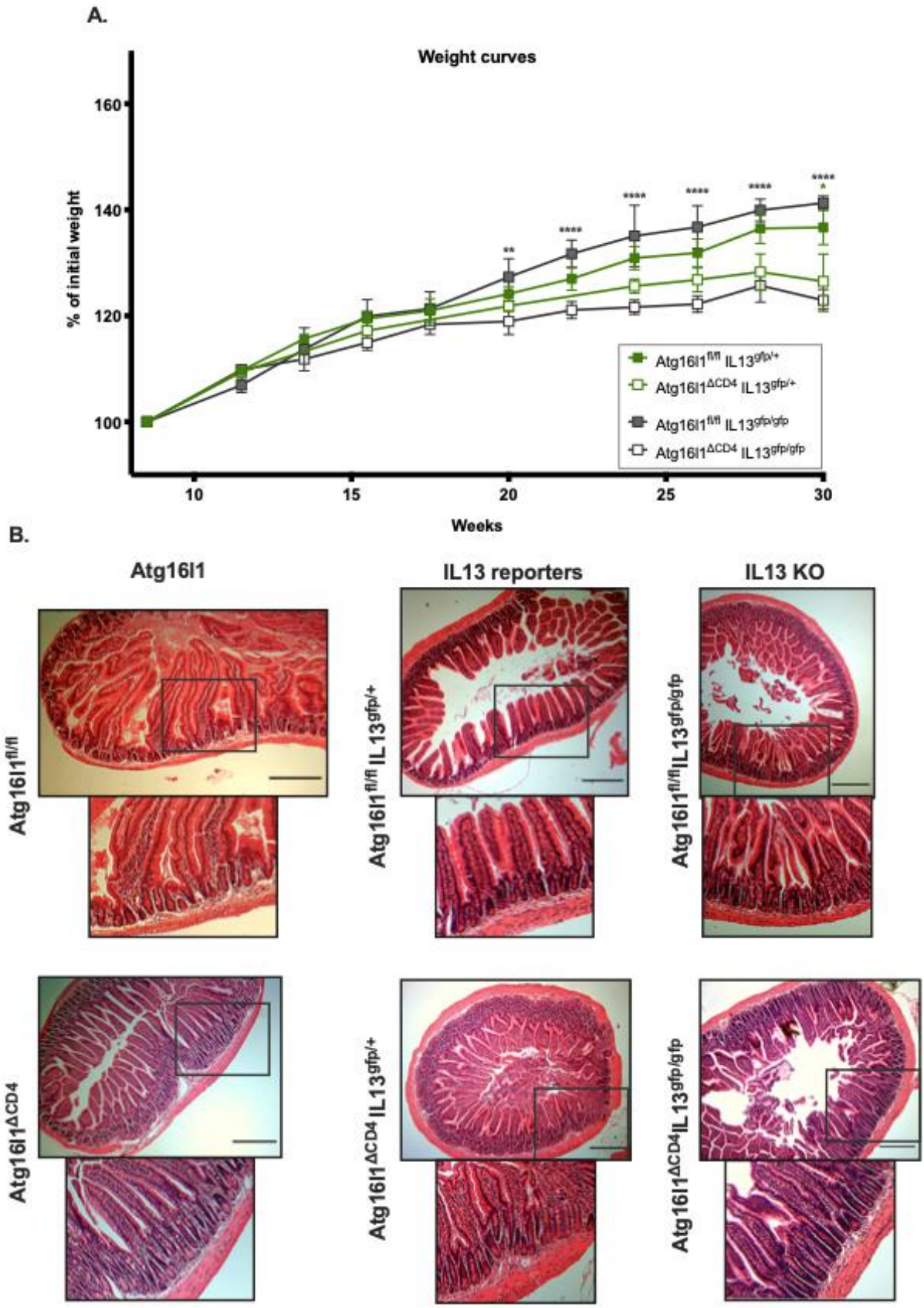


Figure 18. IL-13 is not required for the weight and intestinal pathology seen in Atg16l1$^{\Delta CD4}$ mice.

Atg16l1$^{\Delta CD4}$IL13$^{gfp/+}$, Atg16l1$^{fl/fl}$ IL-13$^{gfp/gfp}$ and littermate controls were monitored for 30 weeks, after which their intestinal pathology was assessed.

A) Body weight curves of Atg16l1$^{fl/fl}$ IL-13$^{gfp/+}$, Atg16l1$^{\Delta CD4}$IL13$^{gfp/+}$ and Atg16l1$^{fl/fl}$ IL-13$^{gfp/gfp}$, Atg16l1$^{\Delta CD4}$IL13$^{gfp/gfp}$ littermates mice.

B) Representative H&E stained sections of jejunum from aged (>25 weeks old) Atg16l1$^{\Delta CD4}$, Atg16l1$^{\Delta CD4}$ IL-13$^{gfp/+}$ and Atg16l1$^{\Delta CD4}$IL13$^{gfp/gfp}$ mice showing normal (top row) and abnormal (bottom row) crypt morphology.

Data is combined from two independent experiments, with at least 2 mice per group. Weight measurements are shown as means ± s.e.m (A). Statistical significance was determined using two-way analysis of variance (ANOVA) with Bonferroni's correction for multiple comparisons ** $p<0.01$, **** $p<0.0001$.

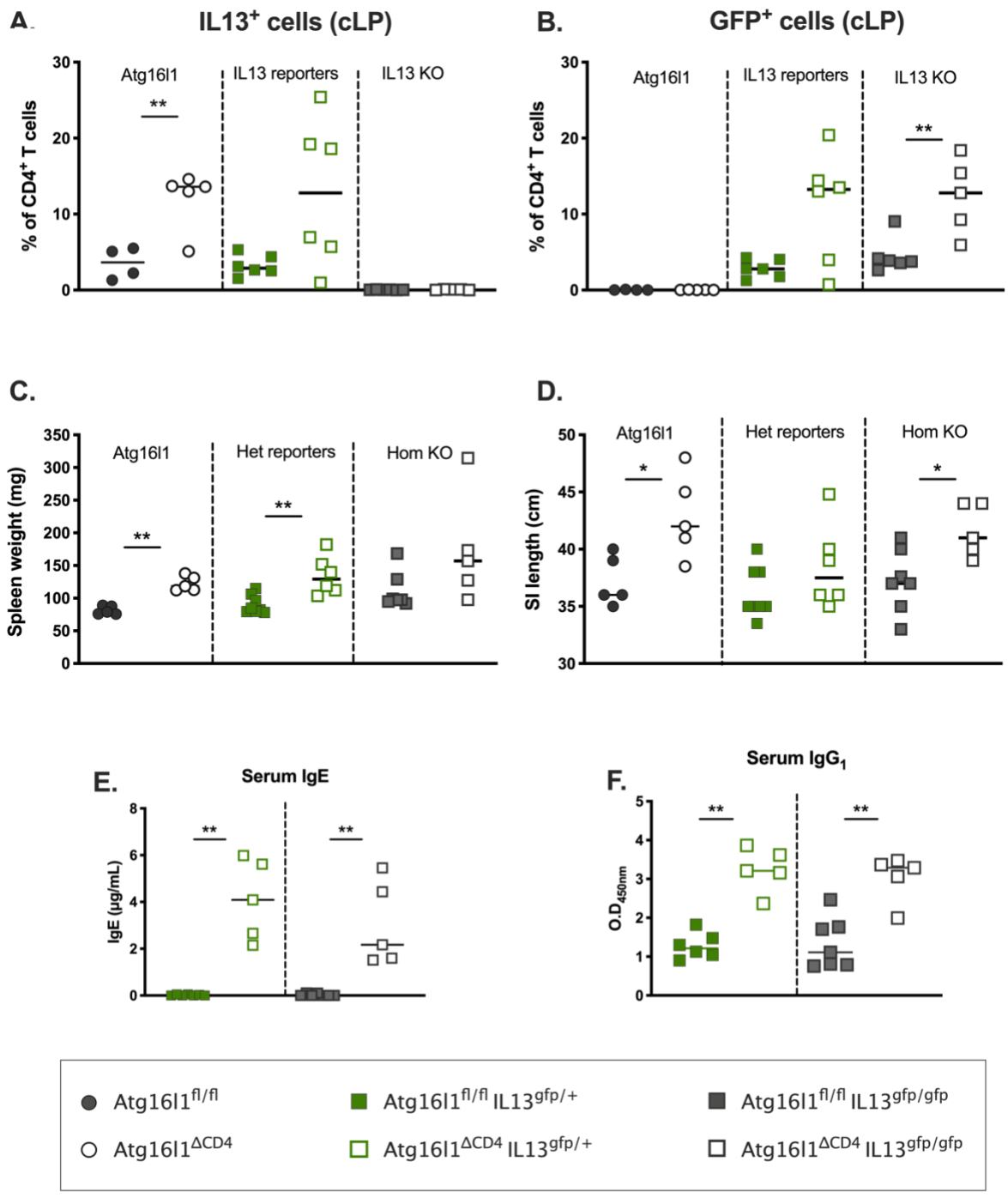


Figure 19. IL-13 is not required for the systemic pathology seen in Atg16l1$^{\Delta CD4}$ mice.

Aged (> 5 months old) Atg16l1$^{\Delta CD4}$, Atg16l1$^{\Delta CD4}$IL13$^{gfp/+}$, Atg16l1$^{fl/fl}$ IL-13$^{gfp/gfp}$ and littermate controls were assessed for signs of systemic disease.

A) and **B)** Validation of IL-13^{+} CD4^{+} T cells expression vs. GFP^{+} CD4^{+} T cells expression in aged (> 5 months old) Atg16l1$^{\Delta CD4}$ mice compared to Atg16l1$^{\Delta CD4}$ IL13$^{egfp/+}$ and Atg16l1$^{\Delta CD4}$ IL13$^{egfp/egfp}$ littermates mice. Lymphocytes were isolated from the cLP and re-stimulated *in vitro* for 3 hours prior to staining.

C) Spleen weights and (**D)** small intestine lengths in aged (> 5 months old) Atg16l1$^{\Delta CD4}$, Atg16l1$^{\Delta CD4}$ IL-13$^{gfp/+}$ and Atg16l1$^{\Delta CD4}$IL13$^{gfp/gfp}$ littermates.

Serum IgE **(E)** and IgG$_1$ **(F)** levels in aged (>5 months old) of Atg16l1$^{\Delta CD4}$, Atg16l1$^{\Delta CD4}$ IL-13$^{gfp/+}$ and Atg16l1$^{\Delta CD4}$ IL-13$^{gfp/gfp}$ littermates.

Data is combined from two independent experiments, with at least 2 mice per group. Each dot represents an individual mouse and horizontal bars denote medians (A, B, C, D, E). Serum IgG$_1$ levels are shown as means ± s.e.m at 10^5 dilution **(F)**. Statistical significance was determined using the Mann-Whitney test **(A-F)**, * $p<0.05$; ** $p<0.01$; *** $p<0.001$, **** $p<0.0001$.

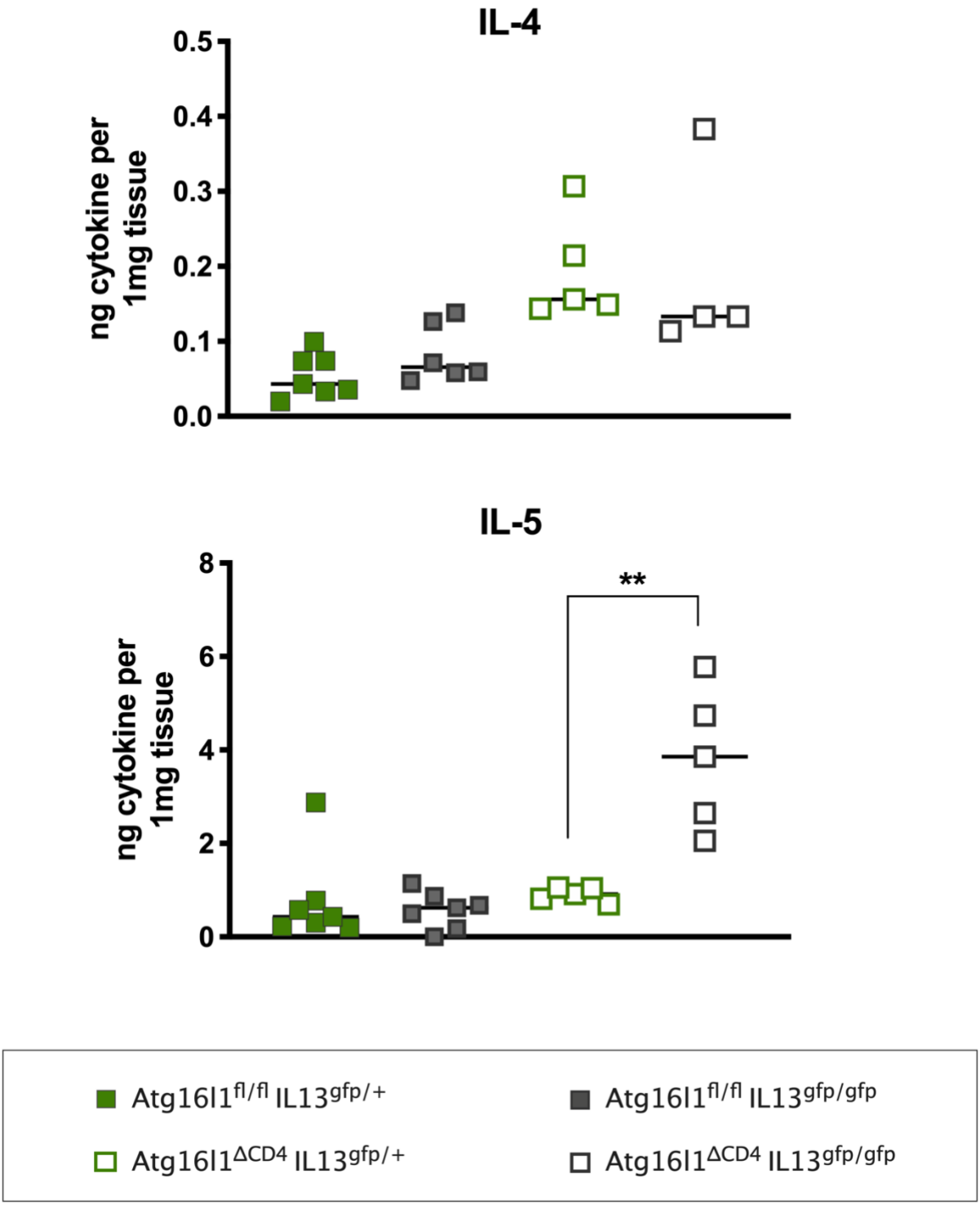


Figure 20. Elevated levels of IL-5, but not IL-4, in the colon of aged (> 5 months old) Atg16l1$^{\Delta CD4}$IL13$^{gfp/+}$, Atg16l1$^{fl/fl}$ IL-13$^{gfp/gfp}$ and littermate controls mice.

Protein quantification of IL-4 and L-5 by enzyme-linked immunosorbent assay in colon explant cultures incubated *ex vivo* for 24 hours. Graphs show amount of protein in ng per 1mg of incubated tissue.

Data is combined from two independent experiments, with at least 2 mice per group. Each dot represents an individual mouse and horizontal bars denote medians. Statistical significance was determined using the Mann-Whitney test ** $p<0.01$.

4.2.3 The exacerbated Th2 response in Atg16l1$^{\Delta CD4}$ mice does affect clearance of a helminth parasite

Heligmosomoides polygyrus (*H. polygyrus*), a natural intestinal parasite of mice, induces a strongly polarized Th2 response, which has been shown to be critical in control and expulsion of the worm *(Reynolds et al., 2012).*To see if the enhanced type 2 immune responses seen in Atg16l1$^{\Delta CD4}$ mice might confer an advantage in protective immunity to this helminth parasite, we collaborated with the group of Prof. Rick Maizels at Glasgow University.

Mice were infected with 200 L3 *H. polygyrus* larvae by oral gavage. Eggs in faces were counted at days 14 and 21 and mice were culled at day 28, when egg/worm counts were assessed and flow cytometry was performed on cells isolated from the MLNs (Figure 21A). Young Atg16l1$^{\Delta CD4}$ mice infected with *H. polygyrus* failed to reveal any difference in the rate of worm clearance when compared to Atg16l1$^{fl/fl}$ littermates (Figure 21B,C). The intensity of infection was determined by the amount of eggs per gram of faces (Figure 21B). At the end of the study, the intestinal adult worms were also counted to give the total worm burden of individual mice (Figure 21C).

Although having similar worm and egg burdens, it was found that infected Atg16l1$^{\Delta CD4}$ mice had a significantly reduced percentage of MLN CD4^{+} T cells compared to Atg16l1$^{fl/fl}$ littermates or naïve control C57BL/6 mice. However, a significantly larger proportion of CD4^{+} T cells in Atg16l1$^{\Delta CD4}$ MLNs were producing cytokines compared to those present in Atg16l1$^{fl/fl}$ littermates, and this was the case for both IL-13 and IFNγ (Figure 21D).

Thus, it seems that type 2 response to and clearance of a helminth parasite are not affected by a lack of autophagy in T cells. This study also shows that Atg16l1$^{\Delta CD4}$ mice can generate useful Th2 and Th1 responses towards intestinal pathogens.

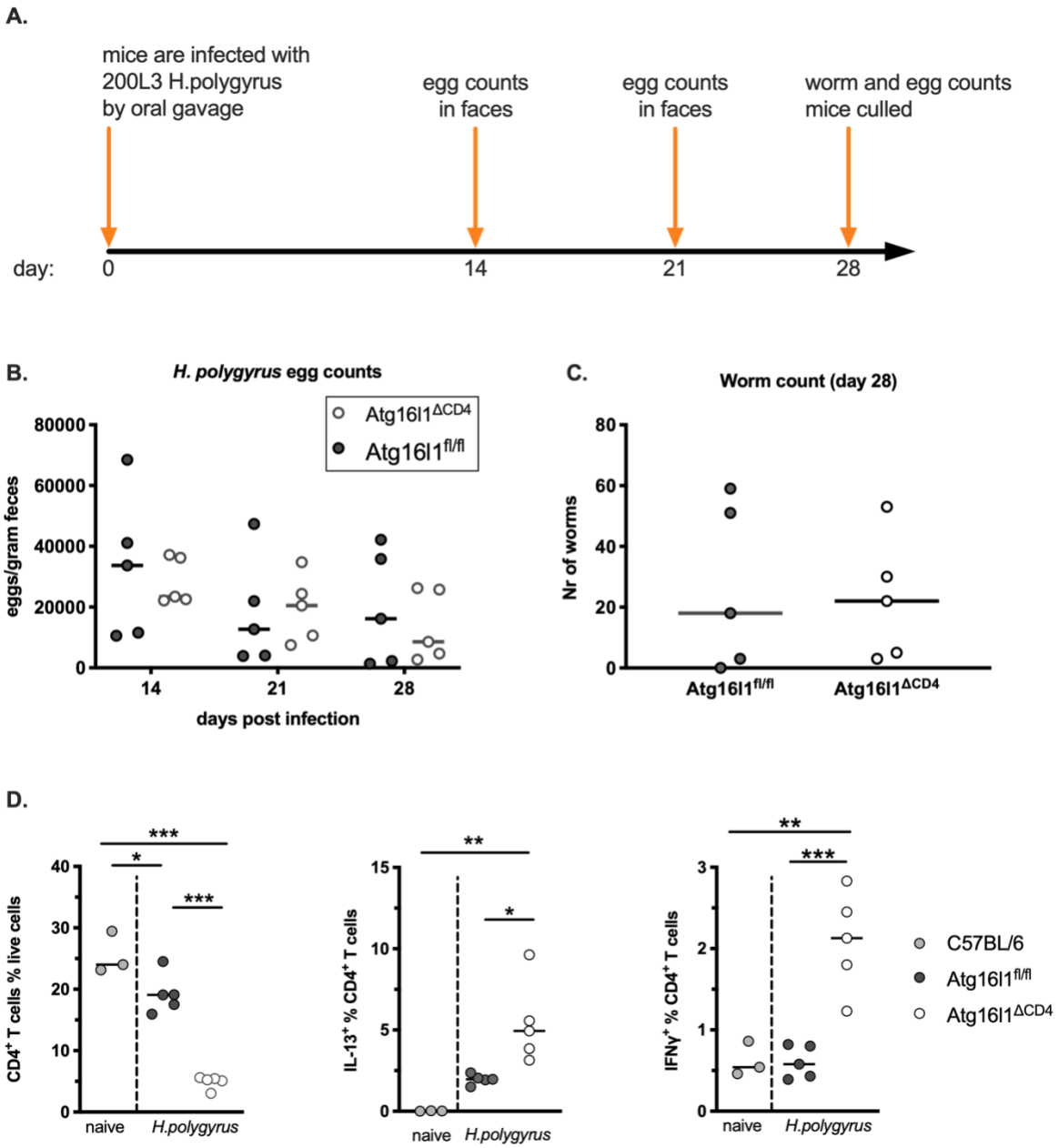


Figure 21. Atg16l1$^{\Delta CD4}$ mice show comparable clearance of the intestinal parasite, *H. polygyrus,* as littermate controls.

A) Experimental setup: mice were infected with 200 *H. polygyrus* L3 larvae by oral gavage. At day 14 and day 21 egg counts were performed followed by worm and egg counts on day 28, when the mice were culled.

B) *H.polygyrus* faecal egg counts at different days of the infection model.

C) Intestinal worm counts at 28 days post infection.

D) CD4$^+$ T cell responses to *H.polygyrus* infection in the MLNs of Atg16l1$^{\Delta CD4}$ mice and Atg16l1$^{fl/fl}$ littermate controls at 28 days post-infection.

Data represents results from a single experiment. Each dot denotes an individual mouse and horizontal bars represent medians. (B-D). Statistical significance was determined using the Mann-Whitney test: * $p<0.05$; ** $p<0.01$, *** $p<0.001$.

4.2.4 Investigating adipose tissues in Atg16l1$^{\Delta CD4}$ mice

Type 2 cytokines have been reported to influence adipocyte homeostasis *(Wu and Qiu, 2019).* Therefore, to examine whether this axis may account for the failure of Atg16l1$^{\Delta CD4}$ mice to gain weight as they age I investigated the morphology and the immune phenotype of adipose tissues in these mice.

Both the epididymal white adipose tissue (eWAT) and the brown adipose tissue (BAT) in aged Atg16l1$^{\Delta CD4}$ mice showed evidence of remodelling on visual inspection, with an increase in the total number of adipocytes per unit area, accompanied by a decrease in adipocyte size (Figure 22A). Further quantification of the eWAT H&E samples confirmed that aged Atg16l1$^{\Delta CD4}$ mice have a significantly smaller adipocyte surface area than Atg16l1$^{fl/fl}$ littermates (Figure 22B, C). It was not possible to quantify the BAT adipocyte surface area with this technique.

WAT has been described to undergo "beiging", a process through which white fat develops characteristics of BAT and upregulates *UCP1 (Pfeifer and Hoffmann, 2015).* eWAT and BAT tissue was isolated from young (~9 weeks old) Atg16l1$^{\Delta CD4}$ mice and littermates controls and assessed for UCP1 upregulation by RT-qPCR. eWAT tissue showed significantly increased expression of UCP1 when HPRT was used as housekeeping gene for RT-qPCR assessment, however, this increase was not observed when 18S rRNA was used as a housekeeping gene (Figure 22D). In BAT tissue, no significant difference was found in UCP1 expression between Atg16l1$^{\Delta CD4}$ mice and Atg16l1$^{fl/fl}$ littermate controls when using either HPRT or 18S rRNA as housekeeping gene (Figure 22E). It is generally accepted that 18S rRNA shows less variance in expression across tissues and experimental conditions than HPRT but because 18S rRNA is highly abundant, it amplifies rapidly during RT-qPCR, potentially exhausting the reaction reagents *(Kozera and Rapacz, 2013)*. Therefore, using 18S rRNA can make it difficult to detect products from rare messages while remaining in the exponential phase of amplification for 18S rRNA *(Kozera and Rapacz, 2013)*. Taken together, this may indicate a potential upregulation of *UCP1* in eWAT cells of Atg16l1$^{\Delta CD4}$ mice compared to littermates controls.

Thus, the reduction in adipocyte surface area and the potential increased expression of UCP1 in the eWAT compartment of Atg16l1$^{\Delta CD4}$ mice suggests that the weight stunting in these mice may be due to the systemic effects of dysregulated type 2 cytokine production on the adipose tissue compartment.

To examine the potential impact of the immune system on the adipose tissue remodelling described above, I characterised the presence of different T cell subsets in the eWAT compartment of young (8-12 weeks old) Atg16l1$^{\Delta CD4}$ mice, before the onset of inflammatory pathology or systemic symptoms. Although, there was no difference in the frequencies of CD3$^+$ T cells, CD4$^+$ T cells or CD8$^+$ T cells in the eWAT compartment of Atg16l1$^{\Delta CD4}$ mice and

Atg16l1$^{fl/fl}$ littermates, there was a significant decrease in the frequency of Foxp3^{+} Treg cells accompanied by an increased frequency of Gata3^{+} Th2 cells in eWAT from Atg16l1$^{\Delta CD4}$ mice (Figure 23 B, C, D). This shows that the phenotype seen in the colonic and small intestinal lamina propria in these mice, is also present in other peripheral tissues like the eWAT.

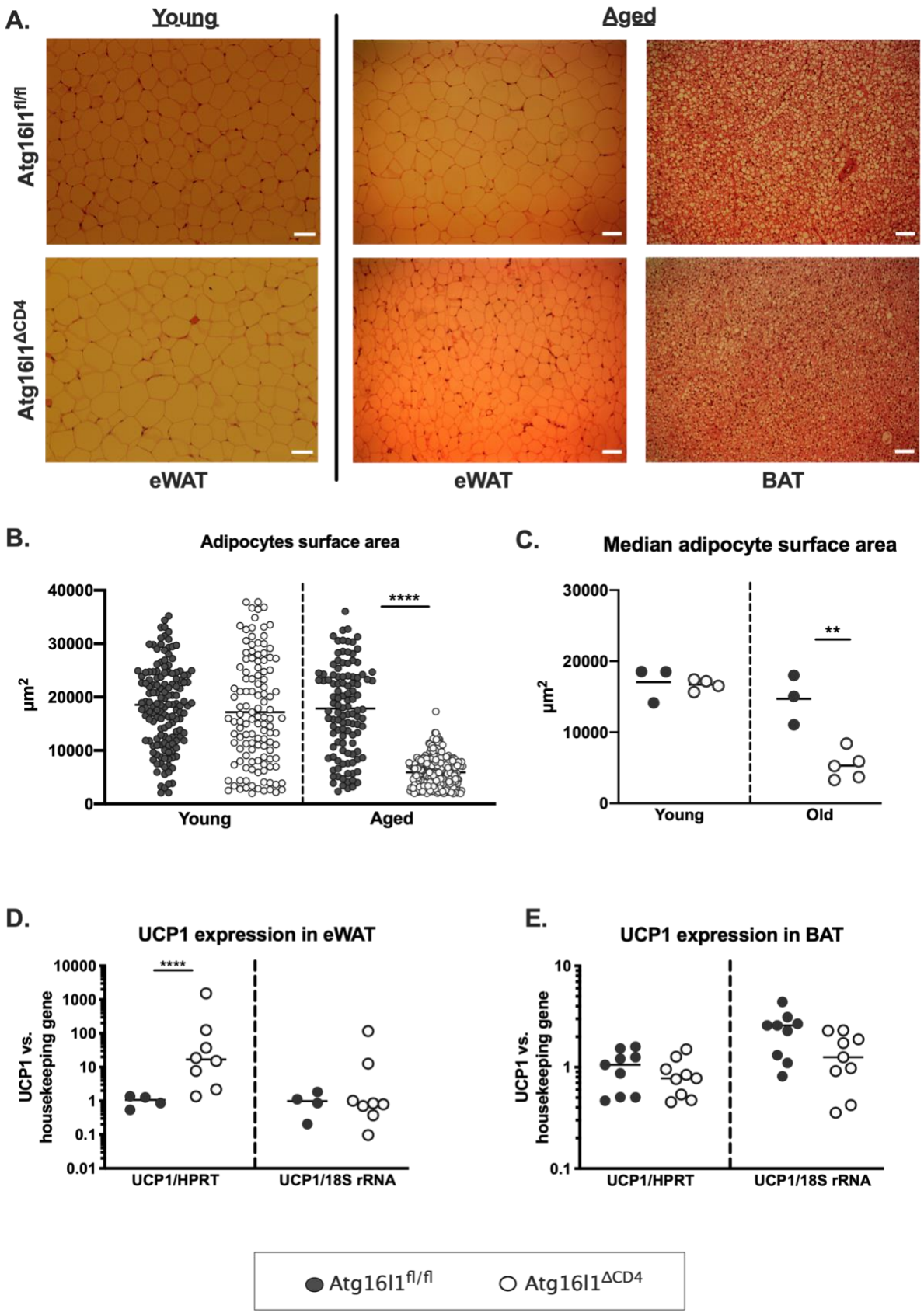


Figure 22. Aged Atg16l1$^{\Delta CD4}$ mice show evidence of fat remodelling as compared to littermate controls.

A) Representative H&E staining of epididymal white adipose tissue (eWAT) and brown adipose tissue (BAT, right column) isolated from Atg16l1$^{\Delta CD4}$ mice or Atg16l1$^{fl/fl}$ littermates as indicated. The histology sections were viewed at 20× magnification, the white scale bar represents 150µm.

B) Adipocyte surface area was quantified from the eWAT H&E images showed in (A) using AdipoSoft ImageJ plug-in. Horizontal bars represent median surface area.

C) The median value for the adipocyte surface area quantification plotted for several samples.

D) qPCR quantification of *Ucp1* expression in eWAT from Atg16l1$^{\Delta CD4}$ mice and Atg16l1$^{fl/fl}$ littermates. Relative expression levels were calculated using 2^(-ΔΔCT) method normalising to the housekeeper *Hprt* or *18S rRNA* and the average expression in the Atg16l1$^{fl/fl}$ samples.

Data are combined from two independent experiments with at least 2 mice per group. Each dot represents an adipocyte and horizontal bars denote medians (B). Each dot represents an individual adipocytye and horizontal bars denote medians (C). Each dot represents an individual mouse and horizontal bars denote means (B, C). Statistical significance was determined using two-way analysis of variance (ANOVA) ** $p<0.01$, **** $p<0.0001$ **(B.C)**. Statistical significance was determined using the Mann-Whitney test: **** $p<0.0001$ **(D)**.

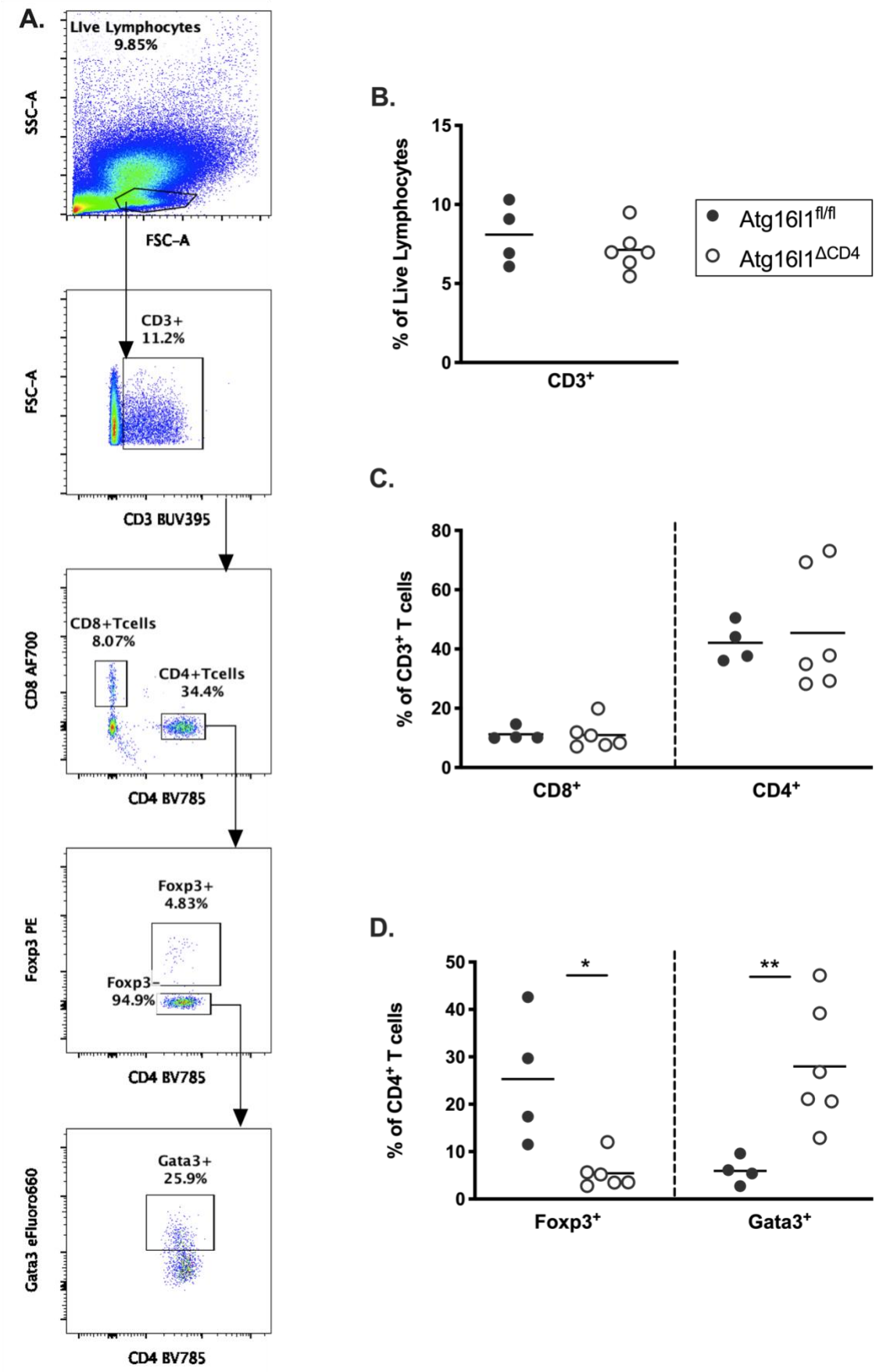


Figure 23. Young Atg16l1$^{\Delta CD4}$ mice (~9 weeks old) exhibit selective expansion of Th2 cells and loss of Treg cells in the epididymal WAT compartment.

The immune compartment was assessed in the WAT tissue of young Atg16l1$^{\Delta CD4}$ mice and littermate controls.

A) Schematic of FACS gating strategy for identifying Th2 and Treg subsets in epididymal WAT.

B, C) Frequencies of **(B)** CD3^{+} T cells and **(C)** CD4^{+} T cells and CD8^{+} T cells in epididymal WAT of Atg16l1$^{\Delta CD4}$ and Atg16l1$^{fl/fl}$ littermates.

D) Frequencies of Gata3^{+} CD4^{+} Foxp3^{-} T cells and Foxp3^{-} CD4^{+} T cells in the in epididymal WAT of Atg16l1$^{\Delta CD4}$ and Atg16l1$^{fl/fl}$ littermates.

Data represents results from a single experiment. Each dot denotes an individual mouse and horizontal bars represent medians. (B-D). Statistical significance was determined using the Mann-Whitney test: * $p<0.05$; ** $p<0.01$.

4.2.5 High fat diet does not rescue Treg cells in Atg16l1$^{\Delta CD4}$ mice

The altered adipocyte homeostasis, together with the reduced oxidative metabolic profile of peripheral Treg cells in Atg16l1$^{\Delta CD4}$ mice *(Kabat et al., 2016a),* led us to hypothesise that defective lipophagy may reduce β-oxidation of fatty acids leading to a maladaptive metabolic alterations in autophagy-deficient Treg cells. In addition, a previous study showed that provision of free fatty acids could restore the differentiation of autophagy deficient neutrophils *in vitro (Riffelmacher T. et al., 2017)*. Therefore, I attempted a rescue experiment to test whether transient provision of free fatty acids, through a 60% high-fat diet (HFD) (D12492, Research Diets) supplementation *in vivo,* would improve the survival of Treg cells in Atg16l1$^{\Delta CD4}$ mice.

Therefore, a high-fat diet (60% fat) was imposed on cohorts of young (6 weeks old) Atg16l1$^{\Delta CD4}$ mice and Atg16l1$^{fl/fl}$ littermate controls for a period of three weeks. The duration of the HFD supplementation was chosen in order to minimise any non-specific effects of the diet, like obesity or insulin-resistance *(Hotamisligil, 2017)*. The HFD regimen led to comparable weight gain in both Atg16l1$^{fl/fl}$ and Atg16l1$^{\Delta CD4}$-mice relative to cohorts maintained on standard chow (Figure 24A). Unexpectedly, provision of HFD rescued the splenomegaly phenotype in Atg16l1$^{\Delta CD4}$ mice, with spleen weights in the normal range (Figure 24B)

At the end of the HFD period, flow cytometric analysis was performed on T cells in spleen, MLN, cLP and eWAT. The results showed that HFD had little impact on the T cell compartments of Atg16l1$^{\Delta CD4}$ or Atg16l1$^{fl/fl}$ littermate controls (Figure 25). The proportions of CD4^{+} and CD8^{+} T cell were unchanged in all tissues following HFD treatment (Figure 25 A,B). Similarly, HFD treatment did not affect the balance of Treg and Th2 cells in the spleen and MLN of Atg16l1$^{\Delta CD4}$ or Atg16l1$^{fl/fl}$ littermate controls (Figure 25 C,D). However, exposure to a HFD significantly reduced the frequency of Treg cells in the cLP of Atg16l1$^{\Delta CD4}$ mice and there was similar trend in Atg16l1$^{fl/fl}$ littermate controls (Figure 25 C). In addition, there was a significant increase in Th2 frequencies in eWAT of Atg16l1$^{\Delta CD4}$ mice only following HFD treatment (Figure 25 D).

To evaluate whether the HFD had an impact on lipid acquisition by T cells in different tissues, I performed staining with BODIPY – a dye made up of a fluorescently labelled fatty-acids that provides a proxy for cellular uptake of lipids (BD Bioscience). BODIPY staining revealed that Tregs and Th2 cells isolated from the cLP of Atg16l1$^{fl/fl}$ littermate controls took up significantly more lipids following HFD exposure, whereas there was no increased lipid uptake by Atg16l1$^{\Delta CD4}$ Tregs or Th2 cLP cells (Figure 26 C, D).

Overall, these results indicate that transient exposure to a HFD did not rescue the Treg population in Atg16l1$^{\Delta CD4}$ mice and, conversely, may even have exacerbated the Treg/Th2 imbalance in peripheral tissues.

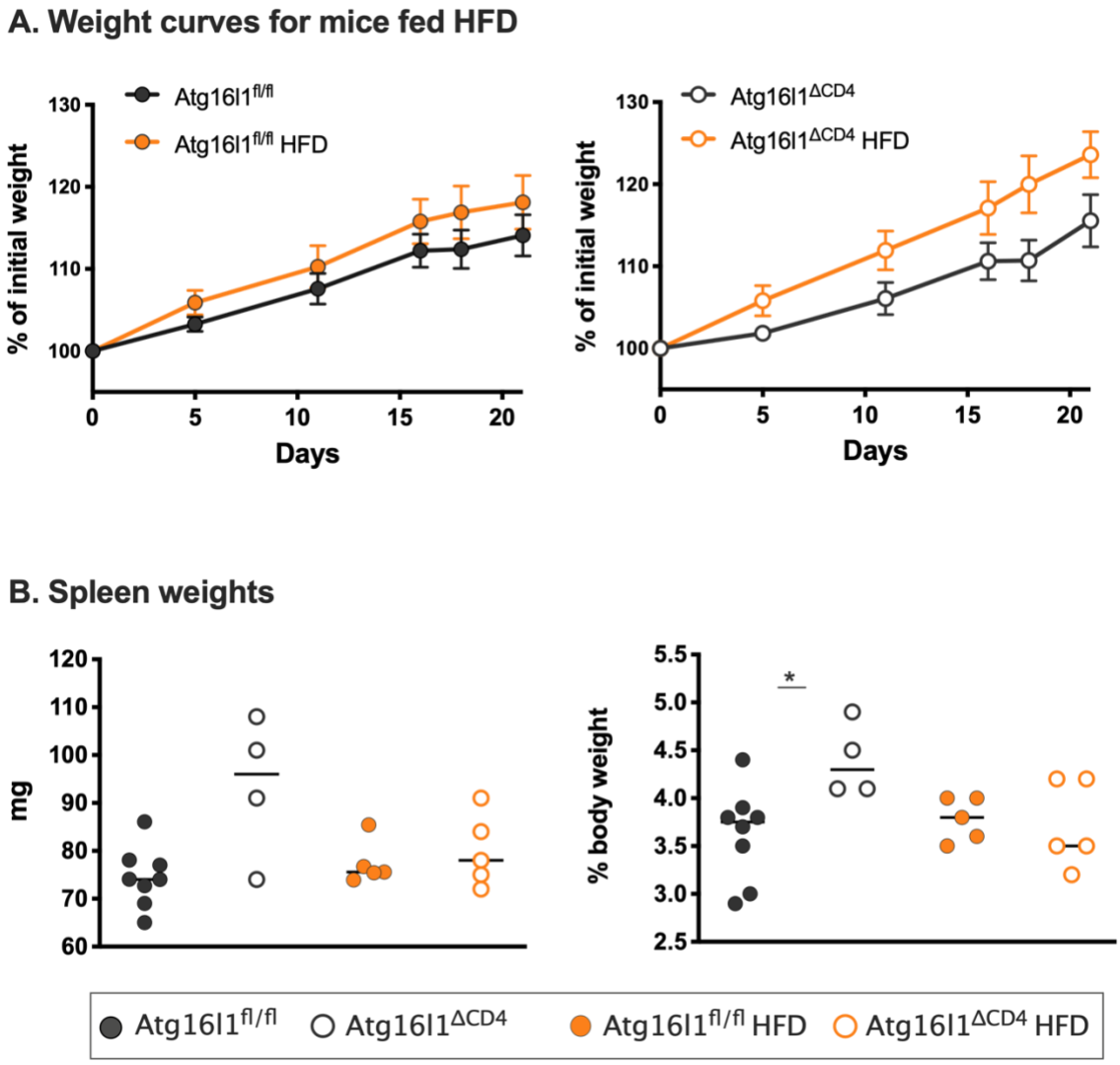


Figure 24. Systemic effects of HFD on Atg16l1$^{\Delta CD4}$ mice and littermate controls.

A high-fat diet (60% fat) was imposed on cohorts of young (6 weeks old) Atg16l1$^{\Delta CD4}$ mice and Atg16l1$^{fl/fl}$ littermate controls for a period of three weeks.

A) Weight curves and **(B)** spleen weights (shown as both actual and as a % of body weight) of young Atg16l1$^{\Delta CD4}$ and Atg161$^{fl/fl}$ littermates fed standard chow or HFD for 3 weeks.

Data are combined from two independent experiments with at least 2 mice per group. Each dot denotes an individual mouse and horizontal bars represent medians. Statistical significance was determined using the Mann Whitney test: * $p<0.05$.

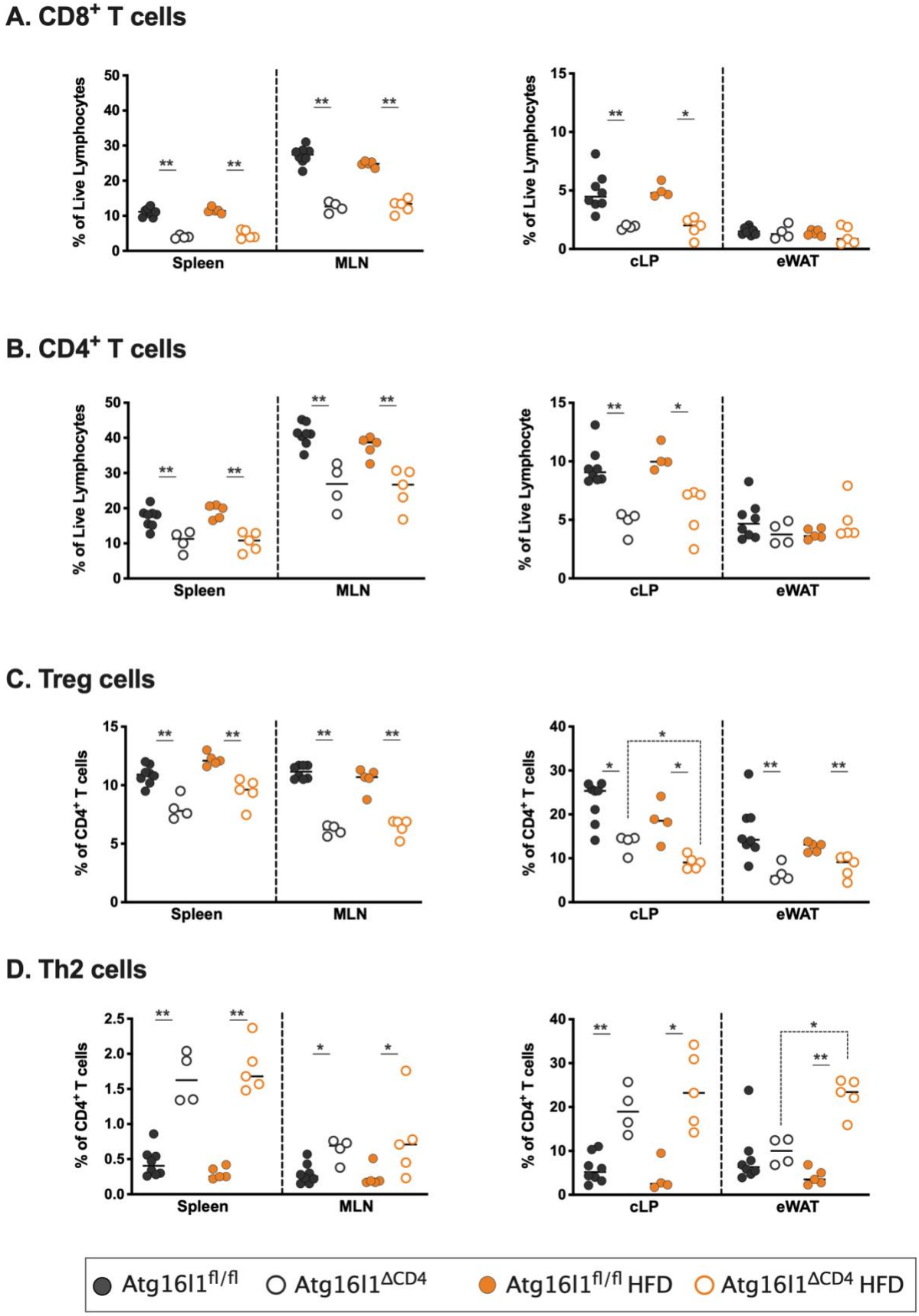


Figure 25. HFD treatment does not rescue autophagy deficient Treg cells.

A high-fat diet (60% fat) was imposed on cohorts of young (6 weeks old) Atg16l1$^{\Delta CD4}$ mice and Atg16l1$^{fl/fl}$ littermate controls for a period of three weeks.

(A-D) Frequencies of **(A)** CD8^{+}CD3^{+} T cells, **(B)** CD4^{+}CD3^{+} T cells, **(C)** Treg cells (Foxp3^{+}CD4^{+}CD3^{+}) and **(D)** Th2 cells (Gata3^{+}Foxp3^{-}CD4^{+}CD3^{+}) in spleen, MLN, cLP and eWAT were quantified using FACS. Samples were pre-gated on CD3^{+}B220^{-}Live cells.

Data are combined from two independent experiments with at least 2 mice per group. Each dot denotes an individual mouse and horizontal bars represent medians. Statistical significance was determined using the Mann Whitney test: * $p<0.05$; ** $p<0.01$

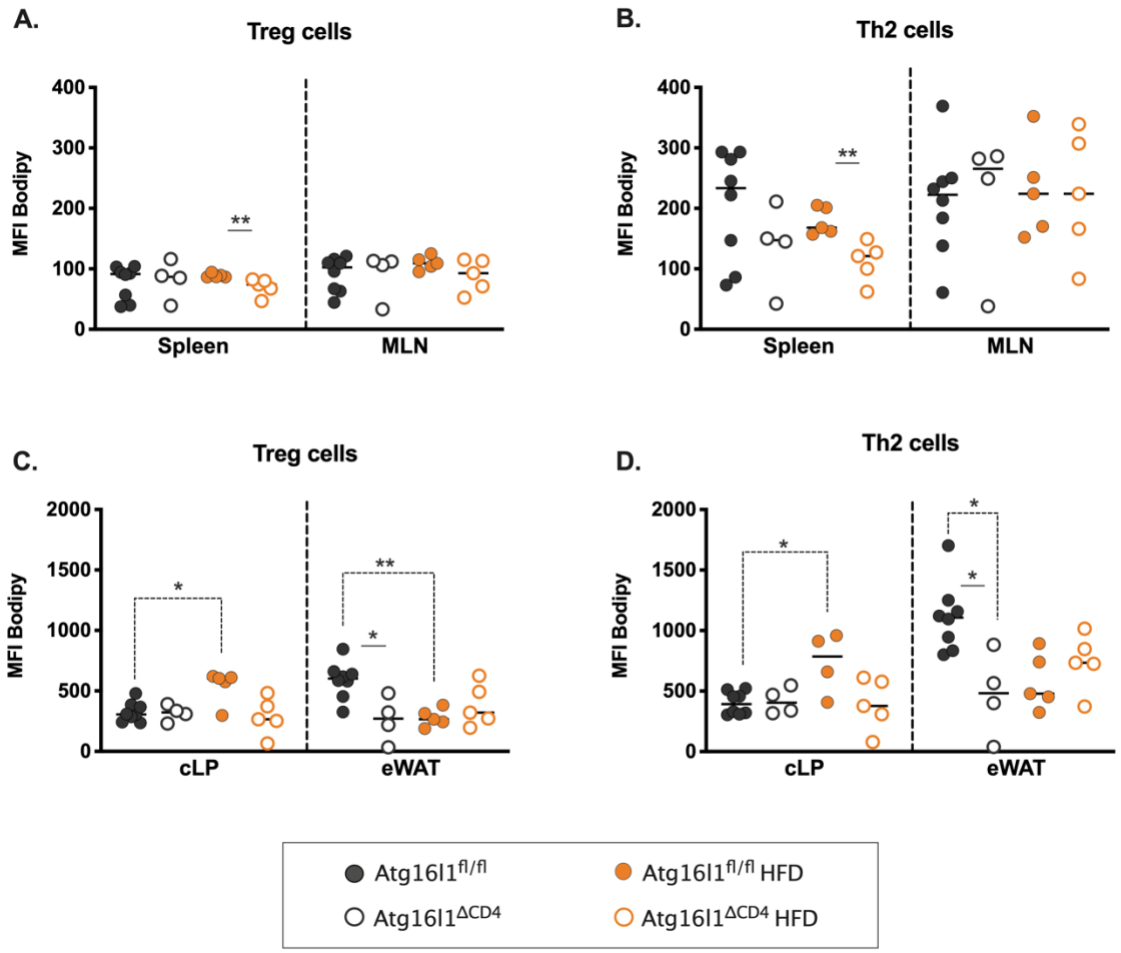


Figure 26. Autophagy-sufficient Treg and Th2 cells in the cLP show increased lipid uptake after HFD exposure, as measured by BODIPY staining.

A-D) BODIPY uptake in Treg (Foxp3^{+}CD4^{+} CD3^{+}) and Th2 (Gata3^{+}CD4^{+} CD3^{+}) cells isolated from **(A,B)** Spleen and MLN, or **(C,D)** cLP and eWAT, of Atg16l1$^{\Delta CD4}$ and Atg161$^{fl/fl}$ littermates fed standard chow or HFD, as indicated.

Data are combined from two independent experiments with at least 2 mice per group. Each dot represents an individual mouse and horizontal bars denote medians. Statistical significance was determined using the Mann Whitney test, * $p<0.05$; ** $p<0.01$.

4.3. Summary and conclusions

In this chapter I explored the potential link between type 2 immune responses and the intestinal pathology seen in Atg16l1$^{\Delta CD4}$ mice. I have successfully generated two Atg16l1$^{\Delta CD4}$ I L-13 reporter mouse lines (Atg16l1$^{\Delta CD4}$ IL-13$^{gfp/+}$ and Atg16l1$^{\Delta CD4}$IL-13$^{toamto/+}$) that recapitulate the immunophenotype and disease pathology of Atg16l1$^{\Delta CD4}$ mice and which can be used for isolating Th2 cells for further functional studies. The IL-13 fluorescent proteins in both lines slightly under-reports IL-13 levels when compared to IL-13 intracellular antibody staining (Figure 16D, 17). This may be due to slight quenching of the fluorescent proteins during the cell isolation and *in vitro* re-stimulation process, which could last up to 10hrs before the cells were analysed by flow cytometry.

Deleting IL-13, one of the key type 2 cytokines, through a genetic approach failed to rescue the immunopathology of the mice. Although functional redundancy between type 2 cytokines has been described *(Kelly-Welch et al., 2003),* there is substantial evidence that IL-13 functions as a primary disease-inducing cytokine, whereas IL-4 functions as an amplifier of type 2 responses by facilitating the expansion of the Th2 cells in secondary lymphoid organs *(Paul and Zhu, 2010)*. However, to definitively tease out a role for Th2 cytokines in the disease phenotype of Atg16l1$^{\Delta CD4}$ mice, it would be necessary to concomitantly block all three primary Th2 cytokines: IL-13, IL-4 and IL-5. This itself poses some technical challenges due to the extended period of time for which this treatment would need to be administered (~3 months) which means a large amount of blocking antibodies would be required. In addition, long-term administration of blocking antibodies could lead to immunogenicity and production of anti-drug antibodies which decreases treatment efficiency by neutralising the activity of the blocking antibodies.

Despite vast amounts of efforts to source the necessary reagents for the long term pharmacological blocked of IL-4 and IL-5 in Atg16l1$^{\Delta CD4}$IL-13KO mice, the COVID-19 pandemic has prevented this experiment from happening within the duration of this thesis. This experiment would have been done in collaboration with the group of Prof. Bart Lambrecht at the University of Ghent which developed a bi-specific neutralising antibody against IL-4 and IL-5, with a one-week half-life. This antibody would have been ideal for this setup as it combines two agents into one, thus minimises potential immunogenicity side-effects of the treatment.

The data presented in this chapter further establishes a crucial role for Atg16l1 in peripheral Treg cells maintenance. Previous results suggested that autophagy is crucial for the survival of Treg cells within the gut environment (Kabat et al., 2016a). I have extended this analysis to the fat compartment and found the frequency of Treg cells to be severelly depleted and the frequencies of Th2 cells to be selectively expanded in the eWAT of Atg16l1$^{\Delta CD4}$ mice, this preceded the eWAT remodelling described in aged mice. The delayed onset could therefore

reflect the previous finding that thymic production of Treg cells was unimpaired in Atg16l1$^{\Delta CD4}$ mice (Kabat et al., 2016a) . This may allow Treg cells to maintain some regulatory activity, even though their number in the periphery is compromised. As thymic involution occurs in older mice, the central output of Treg and conventional T cells is decreased, meaning that the peripheral Treg cell compartments cannot be fully replenished, suggesting that autophagy might be important for maintenance and self-renewal of Treg cells in the periphery *(Rubtsov et al., 2010).*

The reduction in adipocyte surface area and the potential increased expression of UCP1 in the eWAT compartment of Atg16l1$^{\Delta CD4}$ mice suggests that the weight stunting in these mice may be due to the systemic effects of dysregulated type 2 cytokine production on the adipose tissue compartment. Type 2 cytokines have been linked to the process of WAT "browning" which makes adipocytes more likely to dissipate energy as heat and therefore less likely to store it *(Wu and Qiu, 2019)*. However, further studies would be necessary in order to eliminate other causes of weight stunting. For example, we would need to verify whether Atg16l1$^{\Delta CD4}$ mice consume the same amount of food as littermate controls and check that their failure to thrive is not just a consequence of reduced food intake due to mild colitis.

It is striking that autophagy deficiency has a more detrimental effect on Treg cells in the periphery than those found in secondary lymphoid organs. It could be due to the fact that peripheral tissue sites often harbour more harsh metabolic conditions such as lower oxygen concentration, lower nutrient availability and lower temperatures than lymphoid organs *(Medzhitov, 2008)*. One limitation of this study is that we have not examined the T cell compartment in other peripheral tissues like the BAT or skin. It will be interesting to establish if these parallel the decrease in Treg cells and expansion in Th2 cells seen in the colon, small intestine and WAT. If this phenotype is not found in all peripheral tissues but only in certain microenvironments it may provide a hint towards the type of metabolic adaptation that autophagy provides for CD4^{+} T cell.

An experiment using HFD supplementation failed to rescue colonic autophagy-deficient Treg cells. On the contrary, HFD supplementation of Atg16l1$^{\Delta CD4}$ mice negatively affected the survival of *Atg16l1*-deficient Treg cells in the colonic lamina propria, suggesting that these cells poorly adapted to a new fuel source. One limitation of this study is that we did not measure fatty acids levels, across lipid classes at tissue sites, to establish whether administration of HFD had the intended purpose of increasing free fatty acids availability *in vivo*. A previous study of rats that were fed for 3 weeks with the same D12492, 60% HFD fat diet that was used in this thesis, showed that the HFD altered serum fatty acid composition of free fatty acids from predominantly mono-unsaturated fatty acids to predominantly polyunsaturated *(Liu et al., 2015b)*. The D12492, 60% HFD is comprised of 31% saturated fatty acids (SFA), 37% mono-unsaturated fatty acids (MUFA) and 32% polyunsaturated (PUFA) *(Liu et al., 2015b)*. *In vitro* studies often use palmitic acid (16:0) and oleic acid (18:1) as they are the dominant SFA and MUFA in circulation and in most tissues (*Firl et al., 2013)*. Other types of fatty acids have also

been used for *in vitro* studies. For example, PUFA linoleic acid (18:2) has been shown to improve mature neutrophil function and restore the differentiation of autophagy deficient neutrophils *in vitro* *(Riffelmacher T. et al., 2017; Rodrigues et al., 2010).*

Unexpectedly, provision of HFD rescued the splenomegaly phenotype in Atg16l1$^{\Delta CD4}$ mice, with spleen weights in the normal range (Figure 24B). To our knowledge, this has not been previously described in the literature. Although the experiment was preformed twice, overall the experiment did not utilise enough mice per group to meet the power calculation requirements specified in *section 2.10*. It is possible that the observed beneficial effect of HFD on splenomegaly could be the result of small batch differences that could be negated by a third repeat experiment. However, given the high incidence with which we observed splenomegaly in aged Atg16l1$^{\Delta CD4}$ mice in previous experiments, we are confident the HFD rescue of the splenomegaly phenotype is a valid finding. For now, we can only speculate on the potential mechanism behind this finding. The enlarged spleen in Atg16l1$^{\Delta CD4}$ mice is likely a consequence of extramedullary erythropoiesis due to prolonged systemic inflammation driven by T effector cell skewing. An enlarged spleen in the context of systemic inflammation has been previously described in mice with autophagy-deficiency in myeloid precursors *(Mortensen et al., 2011; Watson et al., 2015)* and *Atg7*-deficient T cells *(Wei et al., 2016)*. A recent paper has also found that mice with a mitochondrial defect in T cells initiate an inflammatory program driven by TNFα which induces inflammation in several tissues, including the spleen *(Desdin-Mico et al., 2020).* In addition, autophagy-deficient T cells are known to have an increased mitochondrial mass due to inappropriate organelle turn over *(Parekh et al., 2013; Pua et al., 2009).* Thus, we can hypothesize that *Atg16l1*-deficient T cells accumulate defective mitochondria and may produce excessive TNFα which ultimately contributes to the systemic inflammation and spleen enlargement. Perhaps, in the context of HFD, the extra FFA could preferentially induce M2 macrophages, which have been described to be more reliant on FAO than M1 macrophages *(Van den Bossche et al., 2017)*. These M2 macrophages could thus contribute to better control of type-1 systemic inflammation in the HFD fed Atg16l1$^{\Delta CD4}$ mice resulting in the rescue of the enlarged spleen phenotype.

One limitation of the HFD supplementation experiment was that the young Atg16l1$^{\Delta CD4}$ mice fed standard chow failed to show a significant increase in Th2 frequencies in eWAT when compared Atg16l1$^{fl/fl}$ littermate controls, although there was a trend in this direction (Figure 25D). This may have happened due to inadequate perfusion of the fat before harvesting, leaving a higher proportion than desirable of blood immune cells. The selective expansion of autophagy-deficient Th2 cells found in peripheral tissue is not present in systemic blood (data not shown). Thus, having a large proportion of blood immune cells would mask the difference seen in periphery with adequate perfusion.

The observations in this chapter provide further evidence that autophagy enables tissue-specific adaptation of Tregs which has critical consequences for controlling dysregulated immune response and disease pathology in peripheral tissues.

Chapter 5. Characterisation of the transcriptional changes in autophagy deficient CD4$^+$ T cells

5.1 Introduction and aims of chapter

In *chapter 3*, I have described how the increase in Th2 cells in Atg16l1$^{\Delta CD4}$ mice arises predominantly due to a cell-intrinsic effect of autophagy deficiency. Moreover, given the apparent opposing effects of *Atg16l1* deficiency on Th2 and Treg cell survival in the cLP, we have harnessed the power of scRNA-seq to identify molecular changes in autophagy deficient CD4$^+$ T cells compared to normal CD4$^+$ T cells. This analysis would not have been possible with traditional bulk gene expression methods as these are contingent on being able to selectively isolate the population of interest and on doing so in sufficient numbers. These requirements would have made bulk gene profiling of Th2 cells, which do not express a unique cell surface marker, and of autophagy deficient Treg cells, which are severally depleted in our model, very difficult from a technical perspective.

Named method of the year in 2013 by Nature *(Nature Methods, 2014)*, single-cell RNA sequencing (scRNA-seq) is a rapidly growing collection of methods and protocols designed to measure gene expression at single-cell level. The first scRNA-seq experiment was published in 2009 where the transcriptome of eight cells was profiled *(Tang et al., 2009)*. Advances in microfluidics and cellular barcoding, along with improvements in RNA isolation and amplification, has significantly increased the throughput of scRNA-seq experiments and it is now possible to profile the transcriptome of millions of individual cells *(10x Genomics, 2020)*. Previous methods of sequencing the mRNA expression of a sample were performed in "bulk" with the data representing an averaged gene expression pattern across thousands to millions of cells, which could mask or even misrepresent signals of interest. scRNA-seq overcomes this problem by capturing and obtaining transcriptome-wide data from individual cells.

A major application for scRNA-seq studies has been the assessment of cellular heterogeneity across tissues in health, disease or at various stages of development. Traditionally, cells of the same phenotype are viewed as identical, however RNA sequencing from single cells suggests a more complex picture, revealing previously unappreciated levels of heterogeneity *(Papatheodorou et al., 2020)*. Moreover, scRNA-seq methods are based on unbiased assessment, allowing for *de novo* reconstruction and classification of cellular features away from customary taxonomy. This offers a great opportunity for the scientific community and as such, 'The Human Cell Atlas', a global collaborative initiative has been setup with the aim of describing and defining all cells in the human body in both health and disease *(Human Cell Atlas, 2017)*.

Single-cell approaches are also shedding light on previously unappreciated heterogeneity within immune cells. Studying the immune system has long relied on single-cell techniques such as flow cytometry and microscopy in order to explore and define the plasticity and extreme heterogeneity of immune cells responses during inflammation, autoimmunity, and infection. Applying scRNA-seq techniques to the field of immunology has allowed for deeper profiling of immune cell phenotypes through transcriptome analysis rather than just surface markers.

For example, single-cell transcriptomics has been used to delineate the heterogeneity of Treg cells and to identify genes modulating their adaption to tissue environments *(Miragaia et al., 2019; Zemmour et al., 2018)*. scRNA-seq has also revealed heterogeneity among Th2 cells and has helped to identify a novel Th2 subpopulation with immunosuppressive activity via production of the steroid hormone pregnenolone in a helminth infection model *(Mahata et al., 2014).* Another scRNA-seq study identified a sequence of three cell states in the path to Th2 differentiation in a helminth infection model and also in the differentiation trajectory of Th1 cells in a malaria model *(Proserpio et al., 2016)*. The authors hypothesize that these intermediate states in the differentiation pathway reduce heterogeneity in the final effector population by introducing checkpoints to ensure maximal proliferation of the cell types responsible for effective pathogen clearance.

To generate a better appreciation of the complex cellular networks underlying chronic inflammatory diseases, a number of studies have performed scRNA-seq on cells from diseased and healthy tissues. *Smillie* et *al.* compared the transcription profile of 366,650 cells from intestinal biopsies from healthy individuals as well as biopsies from UC patients in various disease states. Their investigation yielded a number of discoveries that may help to better understand the mechanisms that lead to this complex, heterogeneous disease, by linking genetic risk alleles with observed changes in pathophysiology *(Smillie et al., 2019)*. Another study used scRNA-seq to look at biopsies from asthmatic lungs versus healthy lung tissue, revealing a dominating pathogenic Th2 cell state in the asthma samples. Moreover, network analysis of the two cohorts showed a shift from normal cell communications in healthy lungs to a Th2-dominated interactome in asthmatic lungs *(Mould et al., 2019)*.

A recent study has also utilised scRNA-seq for profiling the immune system in ageing by using blood from humans older than 110 years, called supercentenarians. This has revealed that cytotoxic $CD4^+$ T cells are clonally expanded in the supercentenarians tested, a possible adaptation of the immune system to old life, so as to maintain the ability to eliminate abnormal or infected cells *(Hashimoto et al., 2019)*.

Single-cell RNA-seq studies have been conducted mainly by specialist labs with expertise in bioinformatics and computation, however, with the increasing commercialisation of scRNA-seq platforms this technique is becoming more widely disseminated. In the near future, it is entirely feasible that scRNA-seq will become a routine method in any immunology research

lab, much like flow cytometry today. Despite this rising popularity, analysing single-cell transcriptomic data remains a challenging task. There are several steps involved in the computational analysis of scRNA-seq data, including mapping, quality control, quantification, normalisation, clustering, finding trajectories and identifying differentially expressed genes (DEG) *(Andrews and Hemberg, 2018).* However, there is no strong consensus on best practices and steps upstream of clustering may have a substantial impact on the outcomes yielded by the analysis. Additionally, current algorithms used for analyses are likely to change or be superseded by different techniques in the coming years. Thus, one must carefully consider the results obtained from the computational analysis and validate the findings with additional studies and/or techniques especially as changes in transcript levels may not necessarily correspond to similar changes in protein levels.

I have utilised scRNA-seq to evaluate the transcriptomic changes triggered by autophagy-deficiency in the $CD4^+$ T cell compartment from the cLP of $Atg16l1^{\Delta CD4}$ mice. For this experiment I have analysed two pooled samples (N=1 vs N=1), namely $Atg16l1^{fl/fl}$ (WT) and $Atg16l1^{\Delta CD4}$ (KO), obtained from 5-6 mice. Samples were pooled before FACS -purifying $CD4^+$ T cells, thus pre-RNA isolation and library preparation. A limitation of this approach is that it effectively creates two experimental batches (by genotype) and therefore relies on the assumption that technical and biological variation between pools is small compared to genotype effect. We have taken several steps to minimise technical variation between the two pooled samples used for scRNA-seq: both $Atg16l1^{fl/fl}$ (WT) and $Atg16l1^{\Delta CD4}$ (KO) samples were obtained from mouse tissues and FACS-purified on the same day, by the same people, using the same reagents. RNA isolation and library preparation were also performed on the same day, by one person, using the same reagents for both samples. Nevertheless, it is important to acknowledge the potential for confounding effects derived from technical variation, which necessitates validation of differentially expressed molecules/pathways using independent samples.

I have performed scRNA-seq analysis of FACS purified $CD4^+$ T cells isolated from pooled cLP samples from male $Atg16l1^{fl/fl}$ and $Atg16l1^{\Delta CD4}$ littermate controls mice as described in *chapter 2.3.3* and sequenced as described in *chapter 2.7.1*. Briefly, $CD4^+$ T cells were isolated from pooled colonic lamina propria (cLP) cells of 5 $Atg16l1^{fl/fl}$ (WT) and 6 $Atg16l1^{\Delta CD4}$ (KO) male mice, using FACS sorting as detailed in *sections 2.3.3* and *2.4.6*. $CD4^+$ T cells were counted and loaded into a Chromium controller (10x Genomics), in order to create single cell partitions. The resulting libraries were sequenced across multiple Illumina HiSeq 4000 lanes to obtain a read depth of approximately 55,000 reads per cell. We have taken several steps to minimise technical variation between the two pooled samples used for scRNA-seq: both $Atg16l1^{fl/fl}$ (WT) and $Atg16l1^{\Delta CD4}$ (KO) samples were obtained from mouse tissues and FACS-purified on the same day, by the same people, using the same reagents. RNA isolation and library preparation were also performed on the same day, by one person, using the same reagents for both samples. The resulting dataset contained the gene expression profile of almost 9,000

intestinal $CD4^+$ T cells. In this chapter I explore the computational analysis of this dataset and present the main transcriptomic differences between autophagy-deficient and sufficient $CD4^+$ T subpopulations, as well as preliminary *in vitro* and *in vivo* validation of these findings.

The main objectives of this chapter are:

- To characterise the changes induced by autophagy deficiency in the intestinal $CD4^+$ T cells population in an unbiased manner based on their transcriptional profile.
- To evaluate whether and how autophagy-deficiency affects the transcriptional program of different T cell subsets, particularly in relation to Th2 and Treg cell populations.
- To validate the scRNA-seq computational findings with *in vitro* and *in vivo* methods.

5.2 Experimental results

5.2.1 Filtering cells by quality control metrics

Once the gene expression for the WT and KO samples was quantified (CellRanger software as described in *section 2.7.1*), it was summarised as an expression matrix where each row corresponds to a gene and each column corresponds to a single cell. This matrix was examined for various quality metrics in order to identify and remove cells of low quality from the analysis. The following thresholds were chosen, based on both accepted quality standards for single cell data *(Andrews and Hemberg, 2018; Satija, 2020b)* and on outlier values with respect to this particular dataset:

- UMI counts (transcripts) per cell was limited to cells with more than 500 nUMI and less than 25000 nUMI (Figure 27A) *(Satija, 2020b)*.
- The number of unique genes detected in each cell (nGenes) was used to filter out cells with less than 500 and more than 3500 genes. Low-quality cells or empty droplets will often have very few genes whilst droplets with two or multiple cells may exhibit an aberrantly high gene count *(Satija, 2020b)*.
- Cells with more than 10% mitochondrial genes were removed from the analysis, as dying cells often exhibit high number of mitochondrial genes (Figure 27C)*(Satija, 2020b)*.
- Cells were further filtered to remove cells expressing an excessive diversity of TCR chains, defined as cells with greater than 1 beta chain or 2 alpha chains, in order to exclude potential cell doublets or multiples (Figure 27F) *(Miragaia et al., 2019).*
- After filtering out poor quality cells, genes considered 'undetectable', defined as genes that were expressed in fewer than 10 cells, were removed from the analysis *(Satija, 2020b)*.

As shown in Figure 27D the majority of cells have a high ribosomal gene content (40-45%), this is in line with guidelines published by 10x Genomics on T cells sequencing (*https://kb.10xgenomics.com/hc/en-us/articles/218169723-What-fraction-of-reads-map-to-ribosomal-proteins-*). Moreover, the top 50 most highly expressed genes across cells contain mostly ribosomal protein genes (Rps, Rpl) and non-protein coding genes (Gm42418, Malat1) (Figure 28). These genes are often uninteresting when the aim is to characterise population heterogeneity and to detect meaningful biological differences. As such, ribosomal genes and non-protein coding genes were removed from the expression matrix. The downstream analysis was also performed with these genes included in the expression matrix with similar findings (data not shown).

To assess the potential effects of the cell-cycle stage in the interpretation of the scRNA-seq data set, a rough normalisation was performed by dividing by total counts per cells and taking the natural log, to ensure that counts are comparable between cells. Each cell was then assigned a 'cell cycle score' using the 'CellCycleScoring' function in Seurat. The scoring is done

based on the expression of G2/M and S phase markers with cells expressing neither likely not cycling *(Satija, 2020a).* Figure 27E shows there are no large differences in the cell cycle phase of the cells at the time of sequencing. As such, the variation due to cell cycle was not regressed out but instead outlier cells (falling outside -0.15 < S.Score < 0.20 and -0.30 < G2M.Score < 0.20) were eliminated from the analysis (Figure 27E).

From the QC graphs presented in Figure 27 it is apparent that the dataset, particularly WT cells, tend to exhibit a binomial distribution. This has been attributed to the presence of biologically distinct populations of cells, with different transcriptomic complexities, specifically Treg cells were found to display fewer transcriptomes than other $CD4^+$ T cells (data not shown). This has also been described in a recent paper from the Teichmann lab *(Miragaia et al., 2019)*.

The "SCTransform" Seurat method was used to normalise raw counts, to account for differences in sequencing depth, and to identify highly variable genes. "SCTransform" was shown to reveal sharper biological distinctions in single-cell data compare to other normalisation methods *(Hafemeister and Satija, 2019)*. Several iterations of different analysis parameters revealed that regressing out variation due to mitochondrial expressions with "SCTransform" helps to better distinguish between cell clusters.

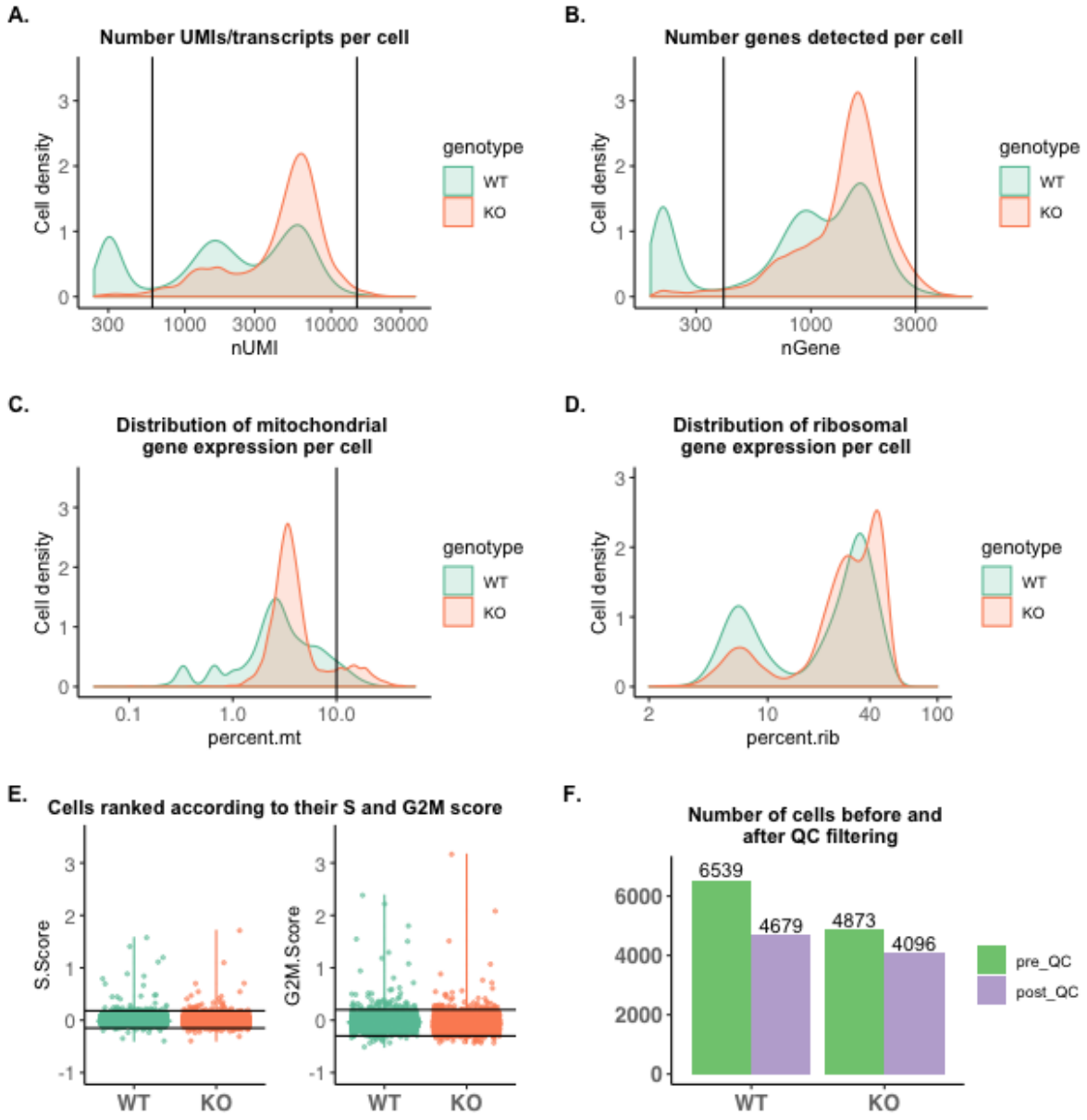


Figure 27. Quality control summary metrics of dataset comprising single-cell transcriptome analysis of $CD4^{+}$ T cells isolated from the colonic lamina propria of $Atg16l1^{\Delta CD4}$ mice (KO) and $Atg16l1^{fl/fl}$ littermate (WT) controls.

(A) Histogram of nUMI counts per cell. Vertical bars denote the cell cut-off threshold of more than 500 nUMI and less than 25000 nUMI.

(B) Histogram of number of genes detected per cells. Vertical bars denote the cell cut-off threshold of more than 500 and less than 3500 genes.

(C) Histogram of mitochondrial genes % of total reads per cell. Cells which surpassed the 10.0 mitochondrial percentage were eliminate from further analysis.

(D) Histogram of ribosomal genes % of total reads per cell.

(E) Dot plot ranking cells based on their cell cycle score. Horizontal bars denote the cell cut-off threshold of -0.15 < S.Score < 0.20 for the first graph and -0.30 < G2M.Score < 0.20 for the second graph.

(F) Number of cells before and after the QC filters mentioned above were applied.

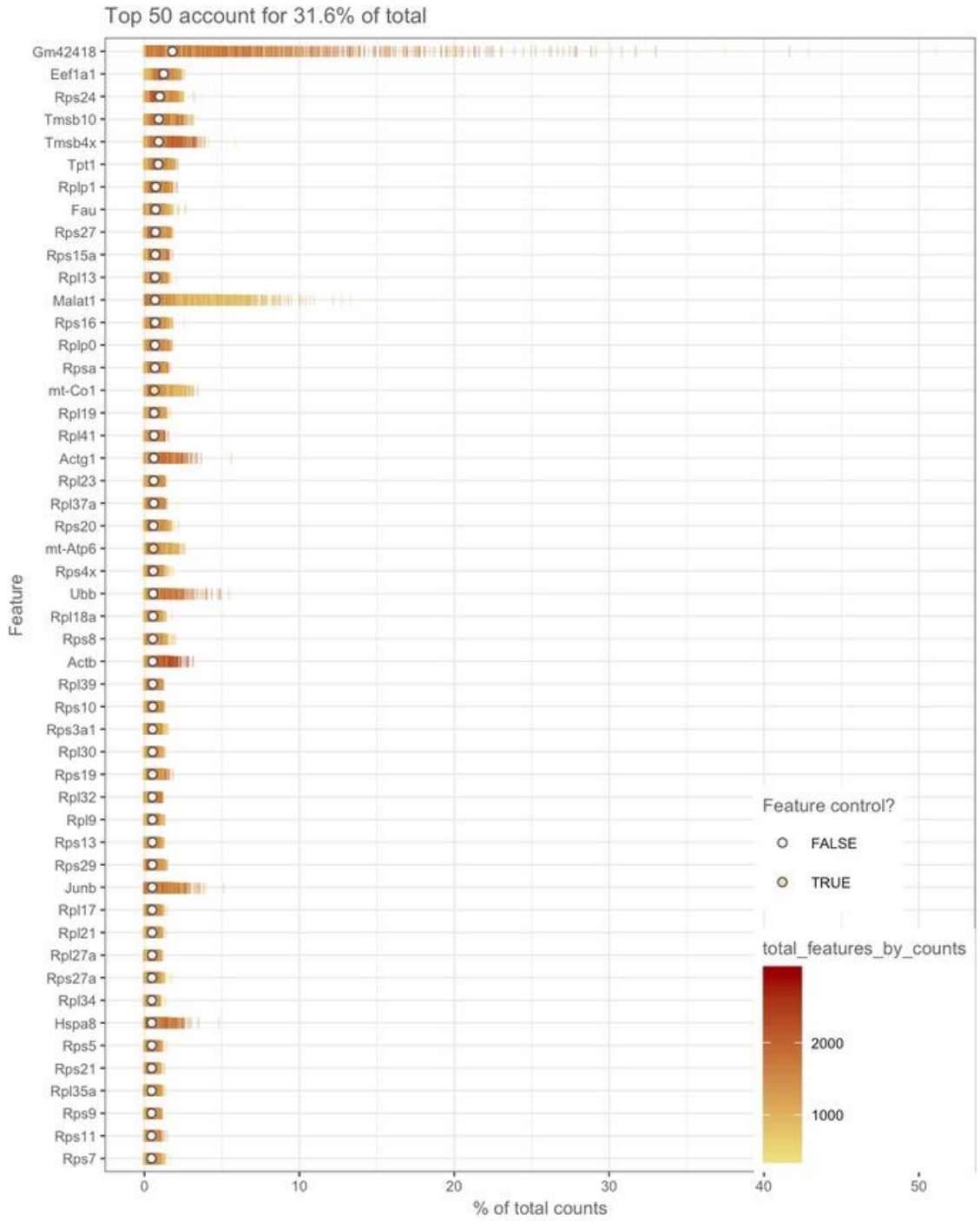


Figure 28. Percentage of counts accounted for by the top 50 most highly expressed genes of dataset comprising single-cell transcriptome analysis of $CD4^+$ T cells isolated from the colonic lamina propria of $Atg16l1^{\Delta CD4}$ mice (KO) and $Atg16l1^{fl/fl}$ littermate (WT) controls.

Each row corresponds to a gene, and each bar corresponds to the expression of a gene in a single cell. The circle indicates the median expression of each gene. Graph generated with "Scater" R package.

5.2.2 Dimensionality reduction and feature selection

One of the most useful features of scRNA-seq analysis is that it provides information on nearly all genes transcribed by cells at the time of sequencing. However, trying to simultaneously analyse thousands of genes introduces computational challenges. The total number of genes measured in a dataset is known as dimensionality. For mammalian samples there are often around 10^4 dimensions/genes *(Andrews and Hemberg, 2018)*. When comparing cells in a high dimensional gene expression space, distances between cells become homogenous, making it difficult to distinguish differences between populations from variability within a population, this is known as "curse of dimensionality" *(Andrews and Hemberg, 2018)*.

Two main approaches, adapted from the machine learning field, are commonly used to deal with highly dimensional data. Firstly, since not all genes are informative to classify cells into meaningful clusters, uninformative genes can be removed in order to reduce the number of dimensions used in the analysis, referred to as "feature selection" *(Andrews and Hemberg, 2018; Satija, 2020b)*. Reducing the number of genes not only facilitates visualisation, but it may also reduce noise and speed up calculations. Secondly, data can be projected onto a lower dimensional space (referred to as "dimensionality reduction") *(Andrews and Hemberg, 2018; Satija, 2020b)*. The lower dimensional space is defined by an algorithm trying to optimally preserve the main characteristics of the original data. The limitations of these methods are that they contain parameters that require manual input defined by the user. As the guidelines for choosing the parameters are vague and largely based on individual datasets, the possibility of achieving a wide range of outcomes remains open *(Andrews and Hemberg, 2018; Satija, 2020b)*.

For this dataset, feature selection was performed with the "SCTransform" Seurat method which identified the top 3000 highly variable genes (HVG) to be used for downstream analysis. HVG selection assumes that genes with high variance relative to their mean expression are representative of biological effects rather than technical noise. Subsequently, Principal Component Analysis (PCA) dimensionality reduction was performed on the SCT normalised expression data. Seurat assigns cells to clusters based on their PCA, with each principal component (PC) representing a "metagene" that combines information across a correlated gene set *(Satija, 2020b).* Determining how many PCs to select for further downstream analyses is important to ensure that the majority of the cell variation is captured. In Figure 29, the top 15 HVGs from each end of the PC scores spectrum are plotted for a random sample of 500 cells of both WT and KO cells combined. By visually inspecting the heatmaps the PC after the first few PCs appear to have clear-cut expression differences for the top genes. The distinction becomes less clear for more distant principal components (PCs 12 to 15). Several iterative trials of data analysis revealed that 13 PCs provides the best clustering profile for the cells in the data.

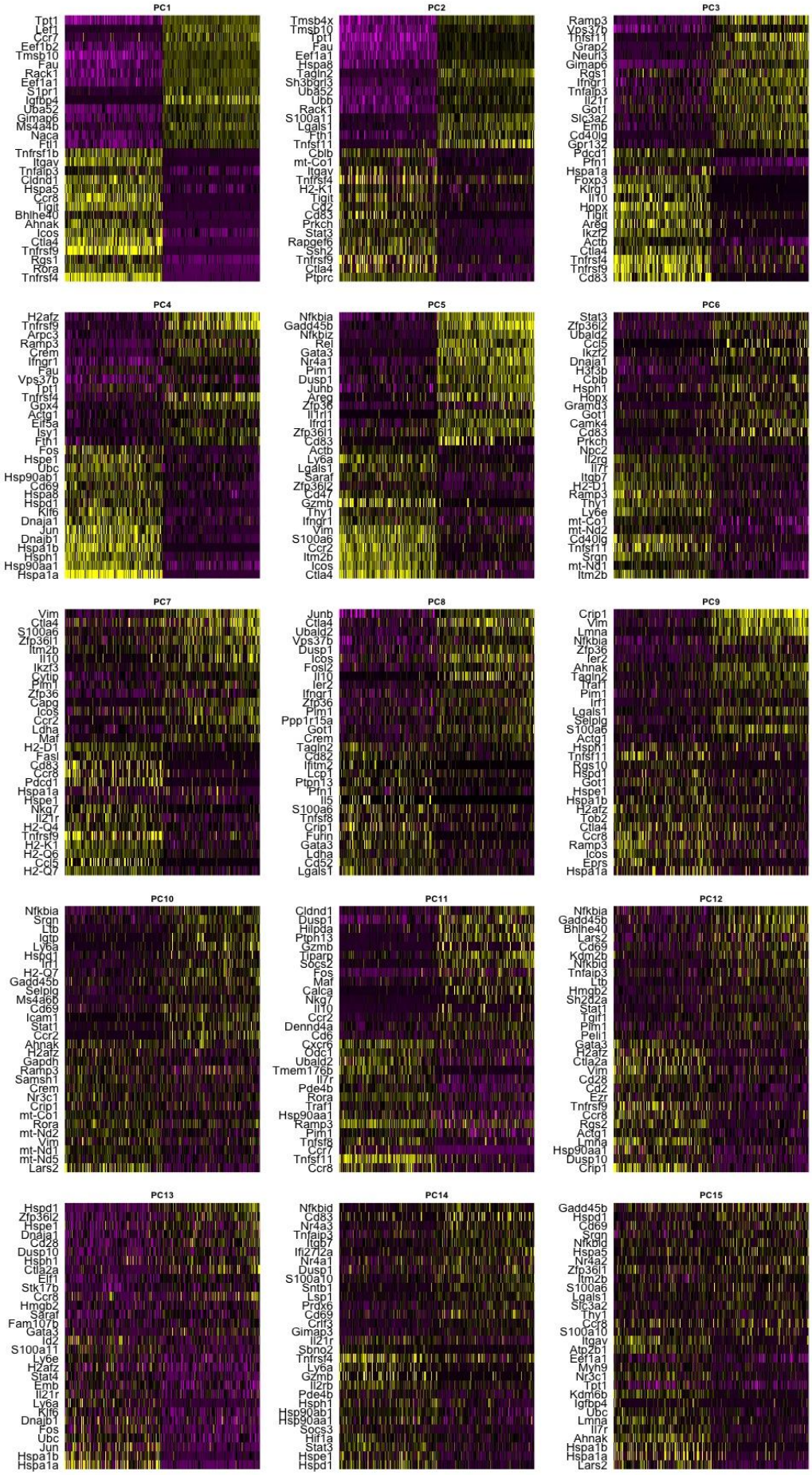

PC1
Tpt1 Lef1 Ccr7 Eef1b2 Tmsb10 Fau Rack1 Eef1a1 S1pr1 Igfbp4 Uba52 Gimap6 Ms4a4b Naca Ftl1 Tnfrsf1b Itgav Tnfaip3 Cldnd1 Hspa5 Ccr8 Tigit Bhlhe40 Ahnak Icos Ctla4 Tnfrsf9 Rgs1 Rora Tnfrsf4
PC2
Tmsb4x Tmsb10 Tpt1 Fau Eef1a1 Hspa8 Tagln2 Sh3bgrl3 Uba52 Ubb Rack1 S100a11 Lgals1 Fth1 Tnfsf11 Cblb mt-Co1 Itgav Tnfrsf4 H2-K1 Tigit Cd7 Cd83 Prkch Stat3 Rapgef6 Ssh2 Tnfrsf9 Ctla4 Ptprc
PC3
Ramp3 Vps37b Tnfsf11 Grap2 Neurl3 Gimap6 Rgs1 Ifngr1 Tnfaip3 Il21r Got1 Slc3a2 Emb Cd40lg Gpr132 Pdcd1 Pfn1 Hspa1a Foxp3 Klrg1 Il10 Hpgx Tigit Areg Ikzf2 Actb Ctla4 Tnfrsf4 Tnfrsf9 Cd83
PC4
H2afz Tnfrsf9 Arpc3 Ramp3 Crem Ifngr1 Fau Vps37b Tpt1 Tnfrsf4 Gpx4 Actg1 Eif5a Isy1 Fth1 Fos Hspe1 Ubc Hsp90ab1 Cd69 Hspa8 Hspd1 Klf6 Dnaja1 Jun Dnajb1 Hspa1b Hsph1 Hsp90aa1 Hspa1a
PC5
Nfkbia Gadd45b Nfkbiz Rel Gata3 Nr4a1 Pim1 Dusp1 Juhb Areg Zfp36 Il1r1 Ifrd1 Zfp36l1 Cd83 Actb Ly6a Lgals1 Saraf Zfp36l2 Cd47 Gzmb Thy1 Ifngr1 Vim S100a6 Ccr2 Itm2b Icos Ctla4
PC6
Stat3 Zfp36l2 Ubald2 Ccl5 Ikzf2 Dnaja1 H3f3b Cblb Hsph1 Hopx Gramd3 Got1 Camk4 Cd83 Prkch Npc2 Il2rg Il7r Itgb7 H2-D1 Ramp3 Thy1 Ly6e mt-Co1 mt-Nd2 Cd40lg Tnfsf11 Srgn mt-Nd1 Itm2b
PC7
Vim Ctla4 S100a6 Zfp36l1 Itm2b Il10 Ikzf3 Cytip Pim1 Zfp36 Capg Icos Ccr2 Ldha Maf H2-D1 Fasl Cd83 Ccr8 Pdcd1 Hspa1a Hspe1 Nkg7 Il21r H2-Q4 Tnfrsf9 H2-K1 H2-Q6 Ccl5 H2-Q7
PC8
Junb Ctla4 Ubald2 Vps37b Dusp1 Icos Fosl2 Il10 Ier2 Ifngr1 Zfp36 Pim1 Ppp1r15a Got1 Crem Tagln2 Cd82 Ifitm2 Lcp1 Ptpn13 Pfn1 Il6 S100a6 Tnfsf8 Crip1 Fuhn Gata3 Ldha Cd52 Lgals1
PC9
Crip1 Vim Lmna Nfkbia Zfp36 Ier2 Ahnak Tagln2 Ifi27l2a Pim1 Irf1 Lgals1 Selplg S100a6 Actg1 Hsph1 Tnfsf11 Rgs10 Hspd1 Got1 Hspe1 Hspa1b H2afz Tob2 Ctla4 Ccr8 Ramp3 Icos Eprs Hspa1a
PC10
Nfkbia Srgn Ltb Igtp Ly6a Hspd1 Irf1 H2-Q7 Gadd45b Selplg Ms4a6b Cd69 Icam1 Stat1 Ccr2 Ahnak H2afz Gapdh Ramp3 Samsn1 Crem Nr3c1 Crip1 mt-Co1 Rora mt-Nd2 Vim mt-Nd1 mt-Nd5 Lars2
PC11
Cldnd1 Dusp1 Hilpda Ptpn13 Gzmb Tiparp Socs2 Fos Maf Calca Nkg7 Il10 Ccr2 Dennd4a Cd6 Cxcr6 Odc1 Ubald2 Tmem176b Il7r Pde4b Rora Traf1 Hsp90aa1 Ramp3 Pim1 Tnfsf8 Ccr7 Tnfsf11 Ccr8
PC12
Nfkbia Gadd45b Bhlhe40 Lars2 Cd69 Kdm2b Nfkbid Tnfaip3 Ltb Hmgb2 Sh2d2a Stat1 Tgif1 Pim1 Peli1 Gata3 H2afz Ctla2a Vim Cd28 Cd2 Ezr Tnfrsf9 Ccr8 Rgs2 Actg1 Lmna Hsp90aa1 Dusp10 Crip1
PC13
Hspd1 Zfp36l2 Hspe1 Dnaja1 Cd28 Dusp10 Hsph1 Ctla2a Elf1 Stk17b Ccr8 Hmgb2 Saraf Fam107b Gata3 Id2 S100a11 Ly6e H2afz Stat4 Emb Il21r Ly6a Klf6 Dnajb1 Fos Ubc Jun Hspa1b Hspa1a
PC14
Nfkbid Cd83 Nr4a3 Tnfaip3 Itgb7 Ifi27l2a Nr4a1 Dusp1 S100a10 Sntb1 Lsp1 Prdx6 Cd69 Crlf3 Gimap3 Il21r Sbno2 Tnfrsf4 Ly6a Gzmb Il2rb Pde4b Hsph1 Hsp90ab1 Hsp90aa1 Socs3 Hif1a Stat3 Hspe1 Hspd1
PC15
Gadd45b Hspd1 Cd69 Srgn Nfkbid Hspa5 Nr4a2 Zfp36l1 Itm2b S100a6 Lgals1 Slc3a2 Thy1 Ccr8 S100a10 Itgav Atp2b1 Eef1a1 Myh9 Nr3c1 Tpt1 Kdm6b Igfbp4 Ubc Lmna Il7r Ahnak Hspa1b Hspa1a Lars2

Figure 29. Principal Components selection of dataset comprising single-cell transcriptome analysis $CD4^+$ T cells isolated from the colonic lamina propria of $Atg16l1^{\Delta CD4}$ mice (KO) and $Atg16l1^{fl/fl}$ littermate (WT) controls.

The 15 HVG with the highest and 15 genes with the lowest PC loadings are displayed for each PC for a random sample of 500 cells of both WT and KO cells combined. 13PCs were chosen for further downstream analysis. Columns represent individual cells and rows represent individual genes. The gene expression level is color-coded using a diverging scale from -2.5 (purple) to 2.5 (yellow) and the midpoint (black) is at 0.

5.2.3 Samples integration using shared HVG

Integration is a method implemented in Seurat v3 that uses shared sources of greatest variation across samples in order to identify subpopulations that have a common set of biological features and to overlay these between groups *(Stuart et al., 2019)*. Groups can be represented by different conditions (e.g. WT and KO), different datasets (e.g. scRNA-seq data generated using different library preparation methods) or different modalities (e.g. scRNA-seq and scATAC-seq). In the case of this dataset, good alignment of the WT and KO cells was observed using both integrated and non-integrated methods. Several iterative trials of data analysis revealed that performing the integration step ensures that all cells of the same type cluster together.

5.2.4 Cell clustering and identification by known cell type markers

One of the most powerful applications of scRNA-seq is the ability to define cells through unsupervised clustering on the basis of their transcriptome profile. The goal of unsupervised clustering is to discover the natural grouping(s) of a set of unlabelled objects based on quantitative comparisons of multiple characteristics *(Jain, 2010)*. Afterwards, by looking for specific markers from known biology or by using differential expression tools to identify unique cluster characteristics, a phenotype can be attributed to each cluster. This is a useful approach to uncover new biology both in terms of characterising different cell types (macrophages, T cells, B cell) and different states of identical cell-types (stimulated and unstimulated T-cells). However, there are many algorithms for performing clustering with no strong consensus on the best approach for scRNA-seq data *(Freytag et al., 2018).* The number of clusters identified can also significantly change based on user inputted values.

The data was clustered using the “FindClusters” function of Seurat which performs graph-based clustering using a K-nearest neighbours (KNN) algorithm *(Butler et al., 2018)*. The previously identified PCs drive the clustering analysis. The resolution parameter of “FindClusters” sets the granularity of downstream clusters, with high resolution values resulting in a greater number of clusters. This parameter needs to be optimised for individual datasets. To help visualises the relationships between a range of resolutions a clustering tree was built using the “Clustree” R package as shown in Figure 30 *(Zappia and Oshlack, 2018)*. Each cluster forms a node in the tree and branches are constructed by considering the way cells move between clusters when increasing the “resolution” parameter. “Resolution” 0.7 was chosen for downstream analysis as it resulted in 11 (0 to 10) distinct, stable clusters with meaningful biological interpretation on further downstream analysis.

To visualize the cell clusters, a nonlinear dimensionality reduction technique called Uniform Manifold Approximation and Projection (UMAP) was used (Figure 31. A-C). UMAP aims to place cells with similar local neighbourhoods in high-dimensional space together in low-dimensional space *(McInnes et al., 2018)*. One advantage of UMAP in comparison to other

dimensionality reduction visualisation techniques is that it can provide outcomes that are more aesthetically pleasing and easier to interpret by visual inspection *(McInnes et al., 2018)*. The same PCs as inputted for FindClusters (13PCs - Figure 29) were inputted for the UMAP visualisation.

Figure 31 (A - C) illustrates the UMAP distribution of the 11 identified clusters. Both, *a priori* knowledge of known canonical biological markers (Figure 31D) and unsupervised output of the top marker genes expressed by for each cluster (Figure 32) were used in assigning identities to the putative $CD4^+$ T cell subpopulations, as detailed below.

Canonical markers for naïve and effector $CD4^+$ T cells correlate well with the unbiased clustering results, with 3 out of 11 clusters expressing high levels of *Sell* (CD62L) and low levels of *Cd44* (Figure 31D). In addition, the *CCR7* gene encoding for the C-chemokine receptor 7 involved in T cell homing to secondary lymphoid tissues is also expressed by these 3 'naïve' clusters (Figure 31D). Furthermore, the Treg canonical transcription factor, Foxp3, is expressed by 3 clusters that can be assigned an identity based on their expression of other Treg population markers, such as *Il10* (IL-10), *Ikzf2* (Helios) and *Il1rl1* (ST2). In terms of effector populations, Th1 cells were identified by expression of the T-bet transcription factor and IFNγ, whereas Th17 cells were identified by expression of the RoRγT transcription factor and IL-17. Finally, Th2 cells were distinguished as the cluster expressing the Gata3 transcription factor along with the Th2 cytokines IL-4 and IL-5.

To summarise the information above, the following identities were assigned to clusters, also shown in Figure 33A as UMAP visualisation:

- Clusters 0, 5, 9 – naïve $CD4^+$ T cells, designated as clusters "naïve0", "naive1" and "naive2" respectively. The cells that make up cluster "naive2" do not express a known immunological gene signature and appear to occupy a different space on the UMAP projection. It is possible that this cluster represents an artefact of poor-quality cells (low transcripts and high % of mitochondrial genes relative to other clusters– data not shown) that were not eliminated at the QC stage and thus will not be examined in more detail during subsequent downstream analysis.
- Cluster 2, 3, 8 – $Foxp3^+$ Treg cells subclassified as:
    - Cluster 2 – $IL10^+$ Treg cells
    - Cluster 3 – tTreg ($Helios^+$) cells
    - Cluster 8 – $ST2^+$ tTreg ($Helios^+$) cells
- Cluster 1 – Th1 cells
- Cluster 4 – Th2 cells
- Cluster 6 – Th17 cells

- Cluster 10 – express both markers of Th1 and Th2 cells and probably represent an intermediate state – designated as "Th1/Th2". This mixed cell phenotype has been previously described in the literature *(Hegazy et al., 2010; Peine et al., 2013)*.
- Cluster 7 – does not express a clear gene signature, instead it expressed low levels of multiple markers (*Cd44, Cd69*) (Figure 31D). This cluster was designated as "memory?" and was not examined in more detail during subsequent analysis.

Colonic Treg cells are well known for their heterogeneity and mixed origin *(Lui et al., 2020)*. This corroborates the dataset presented here which identified, through unsupervised clustering, 3 distinct population for Treg cells (Figure 31D). In the WT Treg population circa 50% of Treg cells are positive for *Helios*, implying a thymic origin *(Thornton et al., 2010)*. *Nrp-1* (neuropilin-1) was not detected in the sequencing data. The transcription factor Helios and the cell surface receptor Neuropilin-1 have been proposed as putative tTreg markers *(Szurek et al., 2015; Thornton et al., 2010; Yadav et al., 2012)*. In contrast, the other half of WT Treg cells express *Il10* and minimal levels of *Helios* and have therefore been assigned as of peripheral origin (Figure 31B). A subset of the *Helios*$^{+}$ *Foxp3*$^{+}$ Treg cells also express *Ilrl1* (ST2 - suppression of tumorigenicity 2 receptor). ST2 is the receptor for IL-33, which is a pleiotropic cytokine that has commonly been associated with type 2 immunity and is often expressed alongside *Gata3* by Treg cells *(Lui et al., 2020)*. Expression of ST2 has been reported on Treg cells found preferentially in non-lymphoid tissues such as WAT, muscle and colon *(Lui et al., 2020)*. The functional relevance of ST2^{+} Treg cells is still under investigation but they are thought to play key suppressive roles in maintaining gut, lung, and adipose tissue homeostasis *(Alvarez et al., 2019; Han et al., 2015; Schiering et al., 2014).*

Parallel analyses of the *Atg16l1*-deficient cLP CD4^{+} T cells indicated that all three clusters of Treg cells are severely depleted, both in terms of absolute numbers and relative frequencies (Figure 33B). Conversely, among the autophagy-KO cLP CD4^{+} T cells, Th2 cells are enriched in terms of absolute number and relative frequencies (Figure 33B). This is also the case for the naive0 and naive1 clusters, which are over-represented among *Atg16l1*-deficient cLP CD4^{+} T cells. In contrast to these differences, the Th1 and Th17 clusters show an almost 50/50 composition between WT and autophagy-KO cells, in terms of numbers and relative frequencies (Figure 33B).

Taken together, these findings corroborate and extend the altered immunophenotype we have previously described in the colonic CD4^{+} T cell compartment of Atg16l1$^{\Delta CD4}$ mice *(Kabat et al., 2016a),* and provide a reassuring early validation check for the sc-RNAseq dataset.

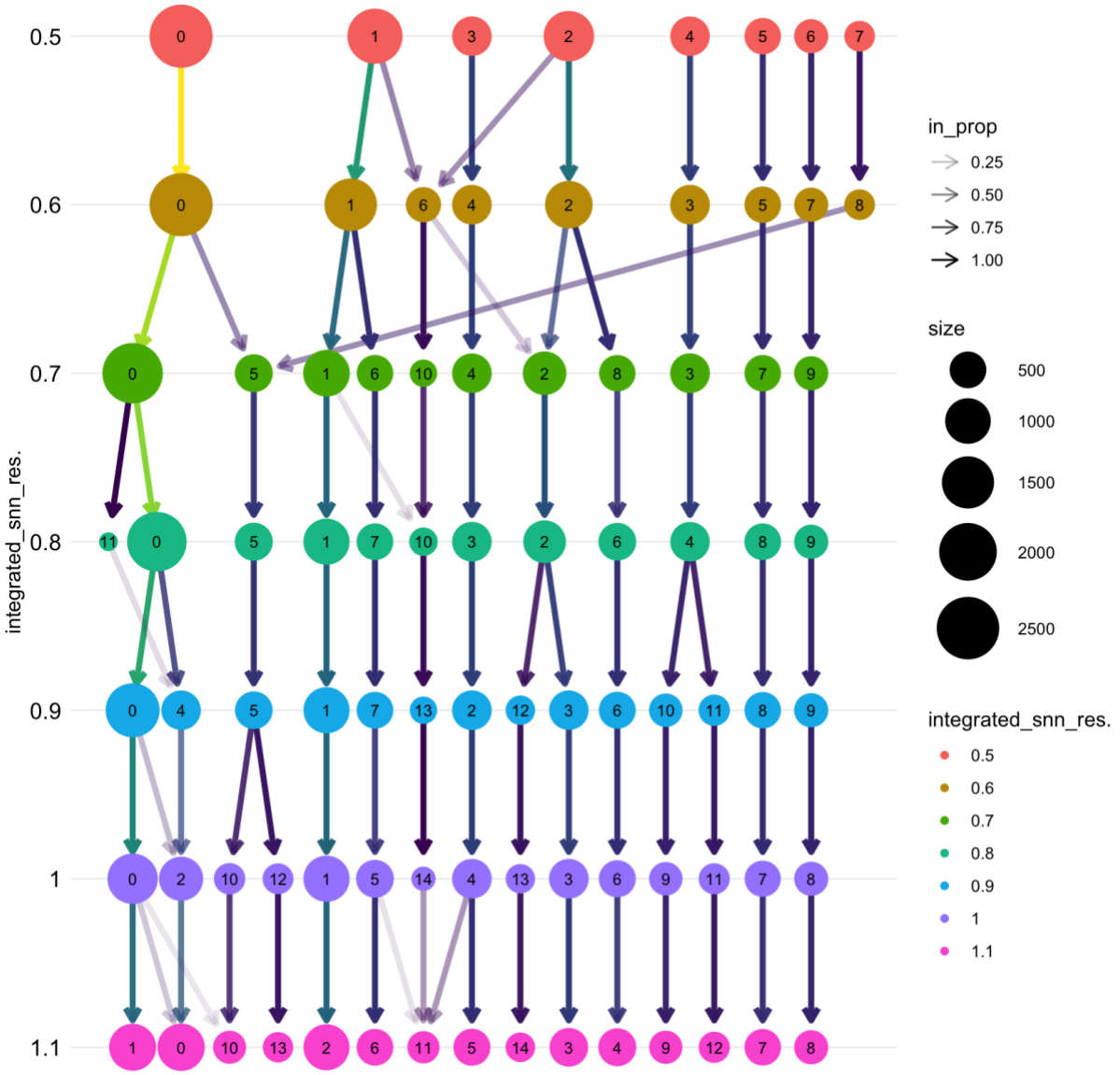


Figure 30. Clustering tree of dataset comprising single-cell transcriptome analysis CD4^{+} T cells isolated from the colonic lamina propria of Atg16l1$^{\Delta CD4}$ mice (KO) and Atg16l1$^{fl/fl}$ littermate (WT) controls.

Consistency of clustering was assessed at different resolution levels for all cells from the WT and KO groups combined. Nodes are coloured according to the resolution value and sized according to the number of cells they represent. The transparency of branches is adjusted according to the proportion of cells coming into a new cluster, with more solid lines showing edges that are more important to cluster makeup. Cluster numbers are randomly assigned by the algorithm. Graph generated with the "Clustree" R package.

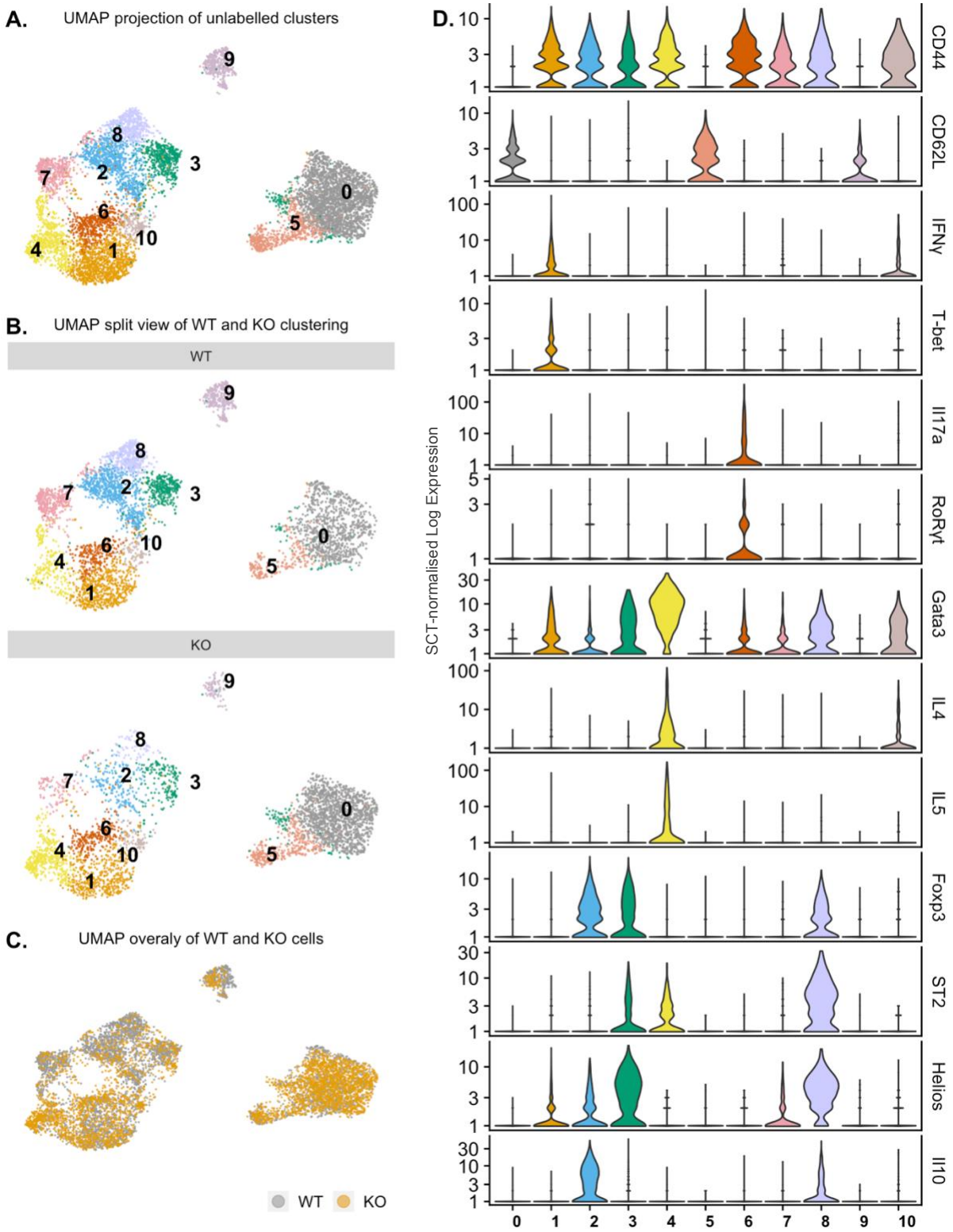


Figure 31. UMAP visualisation of clustering analysis and identification of cell populations of dataset comprising single-cell transcriptome analysis $CD4^+$ T cells isolated from the colonic lamina propria of $Atg16l1^{\Delta CD4}$ mice (KO) and $Atg16l1^{fl/fl}$ littermate (WT) controls.

(A, B, C) Different UMAP visualisations of the unsupervised clustering analysis of WT and KO cells combined. 11 different clusters were identified. **(D)** Violin plots of normalized log-expression values of known biological markers across the 11 identified clusters.

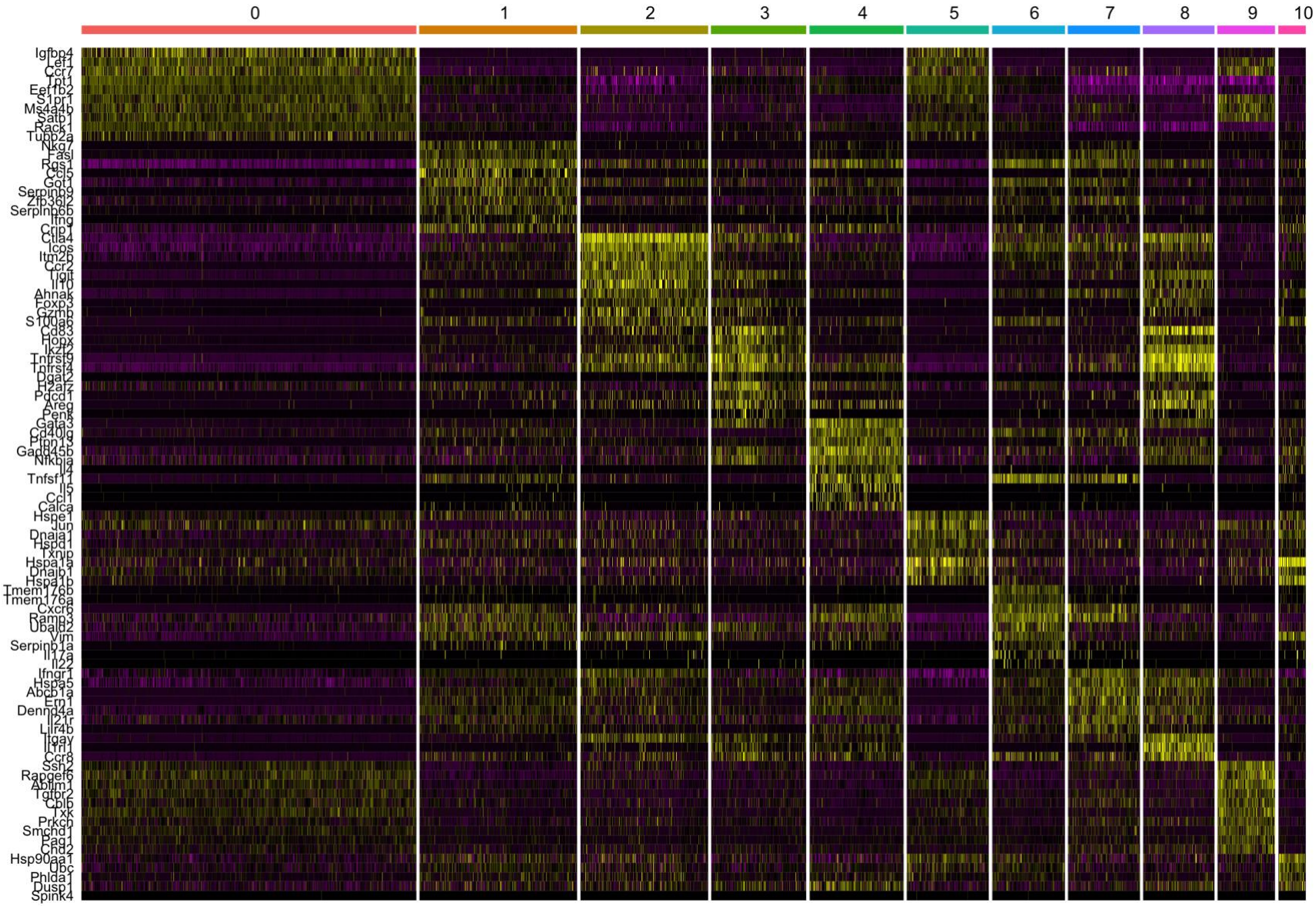

0
1
2
3
4
5
6
7
8
9
10
Igfbp4
Lef1
Ccr7
Tpt1
Eef1b2
S1pr1
Ms4a4b
Satb1
Rack1
Tubb2a
Nkg7
Fasl
Rgs1
Ccl5
Gpt1
Serpinb9
Zfp36l2
Serpinb6b
Ifng
Crip1
Ctla4
Icos
Itm2b
Ccr2
Tigit
Il10
Ahnak
Foxp3
Gzmb
S100a6
Cd83
Hopx
Ikzf2
Tnfrsf9
Tnfrsf4
Dgat2
H2afz
Pdcd1
Areg
Penk
Gata3
Cd40lg
Fbln7
Gadd45b
Nfkbia
Il4
Tnfsf11
Il5
Ccl1
Calca
Hspe1
Jun
Dnaja1
Hspd1
Txnip
Hspa1a
Dnajb1
Hspa1b
Tmem176b
Tmem176a
Cxcr6
Ramp3
Ubald2
Vim
Serpinb1a
Il17a
Il2
Ifngr1
Hspa5
Abcb1a
Emp1
Dennd4a
Il2rb
Lilrb4b
Itgay
Ifitm1
Ccr8
Sshl1
Rapgef6
Abhd17b
Tgfbr2
Cblb
Txk
Prkch
Smchd1
Pag1
Cnot2
Hsp90aa1
Ubc
Phlda1
Dusp1
Spink4

Figure 32. Heatmap displaying the expression patters of the top 10 marker genes across all cells with the 11 clusters resulting from clustering analysis.

Dataset comprises single-cell transcriptome analysis $CD4^+$ T cells isolated from the colonic lamina propria of $Atg16l1^{\Delta CD4}$ mice (KO) and $Atg16l1^{fl/fl}$ littermate (WT) controls.

A random sample of 500 cells from WT and KO groups combined. Columns represent individual cells and rows represent individual genes. The gene expression level is color-coded using a diverging scale from -2.5 (purple – high expression) to -2.5 (yellow – low expression) and the midpoint (black) is at 0.

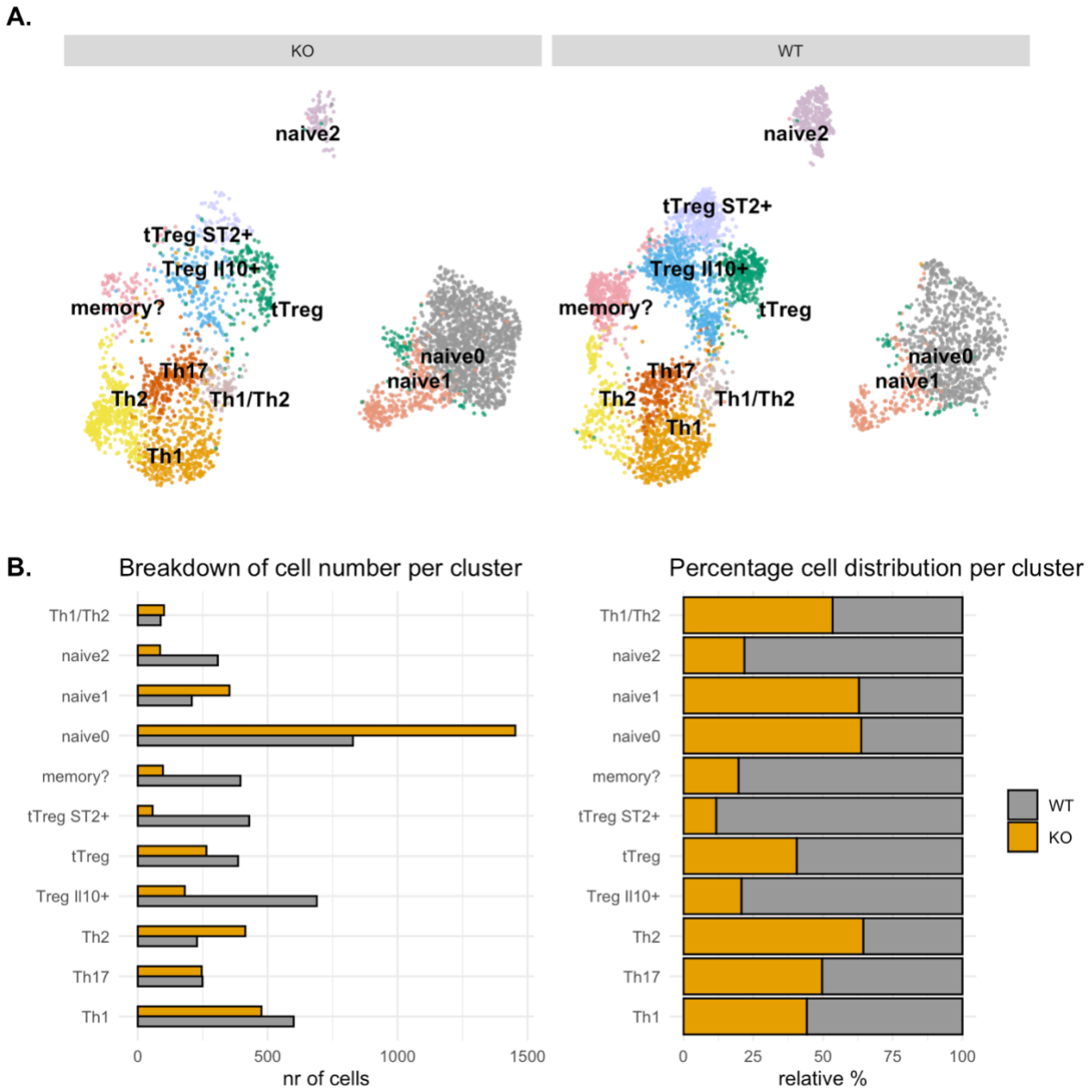


Figure 33. Clustering composition breakdown of dataset comprising single-cell transcriptome analysis of CD4⁺ T cells isolated from the colonic lamina propria of Atg16l1$^{\Delta CD4}$ mice (KO) and Atg16l1$^{fl/fl}$ littermate (WT) controls.

(A) UMAP clustering visualisation of all cells from each genotype with renamed cluster identities.
(B) Absolute numbers and proportions breakdown of the designated clusters as derived from WT and KO cells.

5.2.5 Differential expression and over-representation analysis

Once the clusters were identified, differential gene expression analysis was performed between the WT and KO cells within clusters using Seurat's 'FindMarkers' function along with the non-parameteric Wilcoxon rank sum test. Benjamini-Hochberg (BH) correction was used for p-value adjustment for multiple testing based on the total number of genes in the dataset. The number of cells tested for differential expression analysis was randomly equalised between the WT and KO group. Significantly differentially expressed genes were those with a |fold change| > 1.5 and BH–adjusted p-value < 0.05.

Volcano plots were generated in order to visualise broad differences in gene expression between autophagy-sufficient and -deficient T cell subsets (Figure 34). Significantly downregulated or upregulated genes after multiple testing corrections between WT and Atg16l1 KO cLP $CD4^+$ T cells are indicated in red or blue dots respectively (Figure 34). For readability the top upregulated and downregulated genes from each cluster are also listed in Tablets 5 and 6 respectively. Moreover, Figure 35 summarises the number of differentially expressed genes (DEG) between WT and *Atg16l1*-deficient $CD4^+$ T cells in each cluster.

Overall, $CD4^+$ T cells deficient in *Atg16l1* show a higher number of upregulated than downregulated genes. Figure 35 summarises the number of differentially expressed genes (DEG) for each cluster of *Atg16l1*-deficient $CD4^+$ T cells when compared to WT $CD4^+$ T cells. The Naïve 0 cluster shows 122 upregulated genes in autophagy deficiency and only 31 downregulated genes, whilst Naïve 1 cluster shows 27 upregulated genes and only 15 downregulated genes. The *Atg16l1*-deficient Treg $IL10^+$ cell cluster exhibits the highest number of DEG (822 genes upregulated), followed by the tTreg cluster with 336 upregulated genes. Due to the small number of cells (57) used for the differential expression analysis of tTreg ST2+ autophagy-deficient cells against WT cells, only 15 genes were identified as upregulated and 2 genes identified as downregulated. The *Atg16l1*-deficient Th17 cluster stands out as the only cluster having more downregulated genes (70) than upregulated genes (20) when compared to WT counterparts (Figure 35). In the Th1 cluster 142 genes were identified as upregulated whilst 71 genes were downregulated. Autophagy-deficient Th2 cells displayed 113 upregulated genes and 15 downregulated genes.

A shared upregulated gene signature across clusters were genes relating to the mitochondrial electron transport chain (ETC). This includes the *mt-Co1*, *mt-Co2, mt-Co3* genes, also known as *Cox1, Cox2, Cox3* respectively (part of respiratory complex IV) and the *mt-Atp6* gene (part of the ATP-synthase complex - the last step in the ETC) (Figure 34, Table 5). The gene coding for the CD4 receptor (*Cd4*) was also significantly upregulated across autophagy deficient clusters.

Several genes were found to be selectively upregulated only in some autophagy-deficient $CD4^+$ T cell clusters but not others. For example, the *Fth1* (Ferritin heavy chain 1) gene

involved in metabolic processes relating to iron storage in the cytosol was upregulated by autophagy-deficient Naive0, Naive1, Treg IL10$^+$, tTreg, tTreg ST2+ and Th2 cells. Similarly, genes relating to glucose metabolism like *Gapdh* (Glyceraldehyde 3-phosphate dehydrogenase), *Ldha* (Lactate dehydrogenase A), *Aldoa* (Aldolase, Fructose-Bisphosphate A) and *Gpi1* (glycolytic enzyme glucose phosphate isomerase) were selectively upregulated by autophagy-deficient Treg IL10$^+$, tTreg and Th2 cells.

Autophagy-deficient pTreg IL10$^+$ cells selectively upregulate genes which positively regulate mTOR signalling, such as *Gator2, Rheb*, and *Lamtor1,2,3* (Ragulator complex), as well as downstream targets of mTOR like *Rho*, *Eif4e* and *Eif4b*. In addition, autophagy-deficient Treg IL10$^+$ also showed a striking upregulation of proteasome genes, including genes relating to the 20S core proteasome particle (*Psma2, Psma3, Psmb1, Psmb4, Psmb5, Psmb6, Psmb7, Psma1, Psma4, Psma5, Psma6, Psma7, Psmb2, Psmb3*), genes relating to the PA700 regulatory particle (*Psmc2, Psmc3, Psmc5, Psmd4, Psme1, Sem1, Psmc4, Psmd13, Adrm1, Psmd8, Psmd11*), as well as immunoproteasome genes (*Psmb8, Psmb9, Psmb10)*. The "Pathview" R package (*Luo and Brouwer, 2013)* was used to visualise the upregulation of the genes relating to the mTOR and proteasome pathways (Figure 36 A,B).

In terms of downregulated genes, we note no common signature of downregulate genes across clusters. The gene for the IL-7 receptor (*Il7r*) was selectively downregulated in autophagy-deficient cells part of the Th1, Th17 and tTreg clusters. Other interesting downregulated genes included the *Il21r* within the Th17 cluster and the *Il10* gene within the pTreg IL10+ clusters (Figure 34).

As previously mentioned, CD4$^+$ T cells tended to preferentially upregulate genes in autophagy-deficiency and further analysis focused on these genes. The "gsfisher" R package (*https://github.com/sansomlab/gsfisher/*) was used to perform over-representation analysis of upregulated genes on a per cluster basis, using the GO (Gene Ontology) and KEGG (Kyoto Encyclopedia of Genes and Genomes) databases. Only genes found in a minimum of 10% of cluster cells and that showed at least a log fold change of 0.25 were tested for over-representation. Semi-redundant GO categories were subsequently filtered out manually. The *Appendix* contains two tables of the upregulated genes which are part of the identified enriched GO categories and KEGG pathways for each cluster.

GO analysis indicated in *Atg16l1*-deficiciency has a consistent effect across most CD4$^+$ T cells clusters in terms of upregulated mitochondrial metabolism, which was most evidently in Treg subsets. The GO categories associated with mitochondrial cell metabolism included "oxidative phosphorylation" and "electric transport chain" which were enriched across Th2, pTreg IL10$^+$, tTreg and Naive0 clusters (Figure 37A). The upregulation of mitochondrial metabolism was also evidenced in KEGG analysis with enriched pathways such as "oxidative

phosphorylation" and "thermogenesis" enriched in Th1. Th2, pTreg IL10^{+}, tTreg, Naïve 0, Naïve 1 (Figure 37B).

KEGG analysis also revealed that pathways associated with glycolytic metabolism ("Glycolysis / Gluconeogenesis") are enriched in autophagy-deficient CD4^{+} T cells effector clusters (Th1 and Th2) and most prominently in Treg clusters (pTreg lL10+ and tTreg) (Figure 37B). GO analysis only picked up glycolytic metabolism related category enrichened ("glycolytic process") in autophagy-deficient cells part of the tTreg cluster.

A few enriched pathways were identified only in the *Atg16l1*-deficient IL10^{+} Treg and to a smaller extend tTreg clusters. These pathways relate to cellular metabolism ("carbon metabolism", "biosynthesis of amino acids") and with the proteasome degradation pathway ("proteasome core complex", "proteasome complex", "proteasome regulatory particle"). A summary of the main enriched pathways across clusters is presented in Figure 37.

Overall, the results of the differential expression analysis and over-representation analysis confirmed our previous findings relating to the metabolic shift occurring in autophagy deficient CD4^{+} T cells and highlighted previously unappreciated transcriptomic changes in autophagy-deficient Treg cells, namely decreased *Il10* expression and increased expression of proteasomal genes.

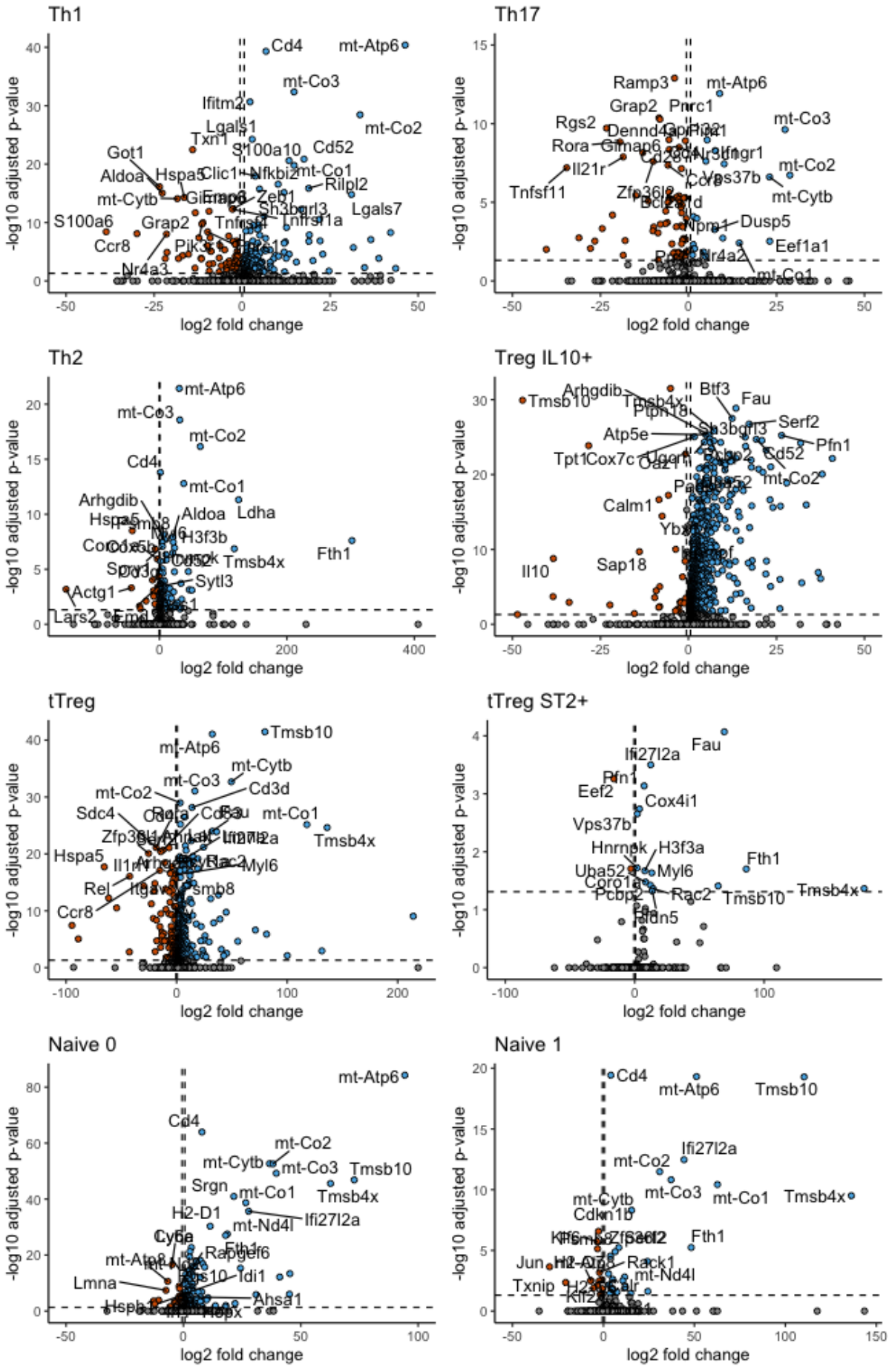

Th1
Th17
Th2
Treg IL10+
tTreg
tTreg ST2+
Naive 0
Naive 1
-log10 adjusted p-value
log2 fold change
Cd4
mt-Atp6
mt-Co3
mt-Co2
Ifitm2
Lgals1
Txn1
S100a10
Cd52
Got1
Aldoa
Hspa5
Clic1
Nfkbi2
mt-Co1
Rilpl2
mt-Cytb
Emp3
Zeb1
Sh3bgrl3
Lgals7
S100a6
Grap2
Tnfrsf1a
Ccr8
Pik3r1
Ppp1r1
Nr4a3
Ramp3
Grap2
Pnrc1
Rgs2
Dennd4a
Rora
Gimap6
Il21r
Tnfsf11
Zfp36l2
Vps37b
Npm1
Dusp5
Eef1a1
Nr4a2
mt-Co1
Arhgdib
Ldha
Aldoa
H3f3b
Fth1
Tmsb4x
Sytl3
Actg1
Lars2
Tmsb10
Btf3
Fau
Ptpn18
Serf2
Atp5e
Sh3bgrl3
Pfn1
Tpt1
Cox7c
Cd52
Calm1
Ybx1
Il10
Sap18
Cd3d
Sdc4
Cox4i1
Vps37b
Hnrnpk
H3f3a
Uba52
Myl6
Coro1a
Pcbp2
Rac2
Tmsb10
Tmsb4x
Hspa5
Il1r
Rel
Itgav
Ccr8
Ifi27l2a
Eef2
Pfn1
Fau
Fth1
Srgn
H2-D1
Cyba
Rap1gap
Rap1gap2
Lmna
Idi1
Ahsa1
Hspb1
Hspa8
Ifi27l2a
mt-Nd4l
Cdkn1b
Fth1
Jun
Rack1
Txnip
Klf2

Figure 34. Volcano plots of differentially expressed (DE) genes across clusters.

Dataset comprises single-cell transcriptome analysis of $CD4^+$ T cells isolated from the colonic lamina propria of $Atg16l1^{\Delta CD4}$ mice (KO) and $Atg16l1^{fl/fl}$ littermate (WT) controls.

Differential gene expression analysis was performed by comparing the KO cells against the WT cells within each identified cluster using Seurat's 'FindMarkers' function. Significantly upregulated genes in $Atg16l1^{\Delta CD4}$ $CD4^+$ T cells are indicated with blue dots. Significantly downregulated genes in $Atg16l1^{\Delta CD4}$ $CD4^+$ T cells are indicated in red dots. Grey dots represent non-significant genes. The horizontal line indicates the cut-off value for significance ($p = 0.05$). Significance was defined as Benjamini-Hochberg adjusted p-value of less than 0.05. The two dashed vertical lines indicate a 1.5-fold downregulation ($\log_2FC = -0.58$) left-side line, and upregulation ($\log_2FC = 0.58$) right-side line in each plot.

Cluster	Top Upregulatd Genes	Cluster	Top Upregulatd Genes	Cluster	Top Upregulatd Genes
Th1	mt-Atp6	**Th17**	mt-Atp6	**Th2**	mt-Atp6
	Cd4		mt-Co3		mt-Co3
	mt-Co3		Gpr132		mt-Co2
	Ifitm2		Ifngr1		Cd4
	mt-Co2		Cd4		mt-Co1
	Lgals1		Vps37b		Ldha
	Cd52		mt-Co2		Psmb8
	S100a10		mt-Cytb		Aldoa
	mt-Co1		Bcl2a1d		Arhgdib
	Clic1		Npm1		Fth1
	Nfkbiz		Dusp5		H3f3b
	Rilpl2		Nr4a2		Cox5b
	Emp3		Eef1a1		Cd3g
	Sh3bgrl3		mt-Co1		Cd52
	Lgals7		Prr7		Tmsb4x
Treg IL10+	Fau	**tTreg**	Tmsb10	**tTreg ST2+**	Cox4i1
	mt-Atp6		mt-Atp6		Fau
	Btf3		mt-Cytb		Fth1
	Serf2		mt-Co3		H3f3a
	Ptpn18		mt-Co2		Hnrnpk
	Atp5e		Cd3d		Ifi27l2a
	Arhgdib		Cd4		Myl6
	Pfn1		Serf2		Pcbp2
	Cox7c		mt-Co1		Pfdn5
	Sh3bgrl3		Tmsb4x		Pfn1
	Uba52		Fau		Rac2
	mt-Co2		Ifi27l2a		Tmsb10
	Cd52		Lat		Tmsb4x
	Pcbp2		Arhgdib		Uba52
	Uqcrh		Rac2		Vps37b
Naïve 0	mt-Atp6	**Naïve 1**	Cd4		
	Cd4		mt-Atp6		
	mt-Cytb		Tmsb10		
	mt-Co2		Ifi27l2a		
	mt-Co3		mt-Co2		
	Tmsb10		mt-Co3		
	Tmsb4x		mt-Co1		
	Srgn		Tmsb4x		
	mt-Co1		mt-Cytb		
	Ifi27l2a		Fth1		
	H2-D1		Serf2		
	mt-Nd4l		Psmb8		
	Fth1		H2-Q7		
	Cyba		H2-Q7		
	mt-Nd2		mt-Nd4l		

Table 5. Top upregulated genes from each cluster.

Differential gene expression analysis was performed by comparing the KO cells against the WT cells within each identified cluster using Seurat's 'FindMarkers' function.

Cluster	Top Downregulated Genes	Cluster	Top Downregulated Genes	Cluster	Top Downregulated Genes
Th1	Txn1	**Th17**	Hspa5	**Th2**	Hspa5
	Got1		Ramp3		Myl6
	Aldoa		Grap2		Coro1a
	Hspa5		Pnrc1		Hnrnpk
	mt-Cytb		Rgs2		Spry1
	Zeb1		Dennd4a		Sytl3
	Tnfrsf1a		Pim1		Actg1
	Gimap6		Rora		Lars2
	Grap2		Nr3c1		Emd
	Tnfrsf4		Cd28		Ass1
	Pik3r1		Gimap6		Cotl1
	S100a6		Il21r		Ifi27l2a
	Pnrc1		Zfp36l2		Mif
	Ccr8		Ccr8		Eif1
	Nr4a3		Tnfsf11		Tnfsf11
Treg IL10+	Tmsb4x	**tTreg**	Rora	**tTreg ST2+**	Eef2
	Tmsb10		Ahnak		Coro1a
	Tpt1		Cd83		
	Oaz1		Sdc4		
	Pabpc1		Zfp36l1		
	Calm1		Il1rl1		
	Ybx1		Lmna		
	Hnrnpf		Hspa5		
	Sap18		Ccr8		
	Il10		Pcyt1a		
	Tomm20		Itgav		
	Ptpn1		Myl6		
	Junb		Rel		
	Fgl2		Psmb8		
	Srgn		Ky		
Naïve 0	Ly6e	**Naïve 1**	Cdkn1b		
	mt-Atp8		Klf6		
	Rapgef6		Zfp36l2		
	Rgs10		Jun		
	Lmna		Rack1		
	Idi1		Calr		
	Hsph1		mt-Atp8		
	Ahsa1		Klf2		
	Irf1		Pnrc1		
	Hopx		Txnip		
	Gclm		Rgs2		
	Cdkn1b				
	Rack1				
	Hspa8				
	Gpx1				

Table 6. Top downregulated genes from each cluster.

Differential gene expression analysis was performed by comparing the KO cells against the WT cells within each identified cluster using Seurat's 'FindMarkers' function.

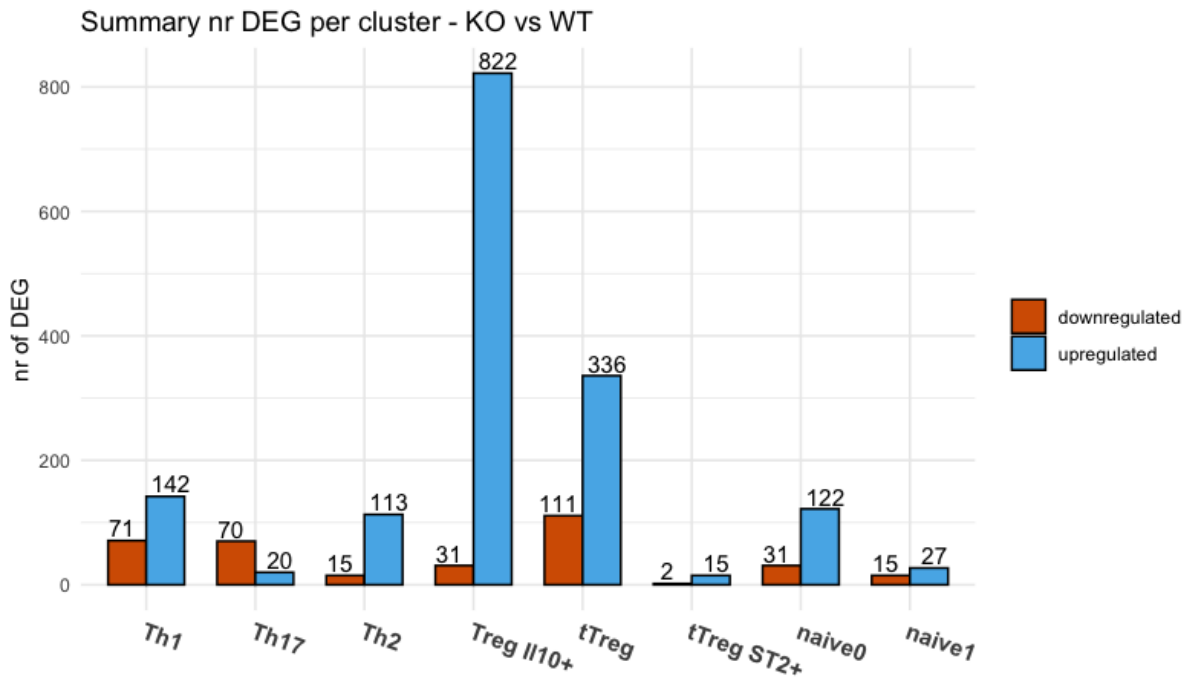
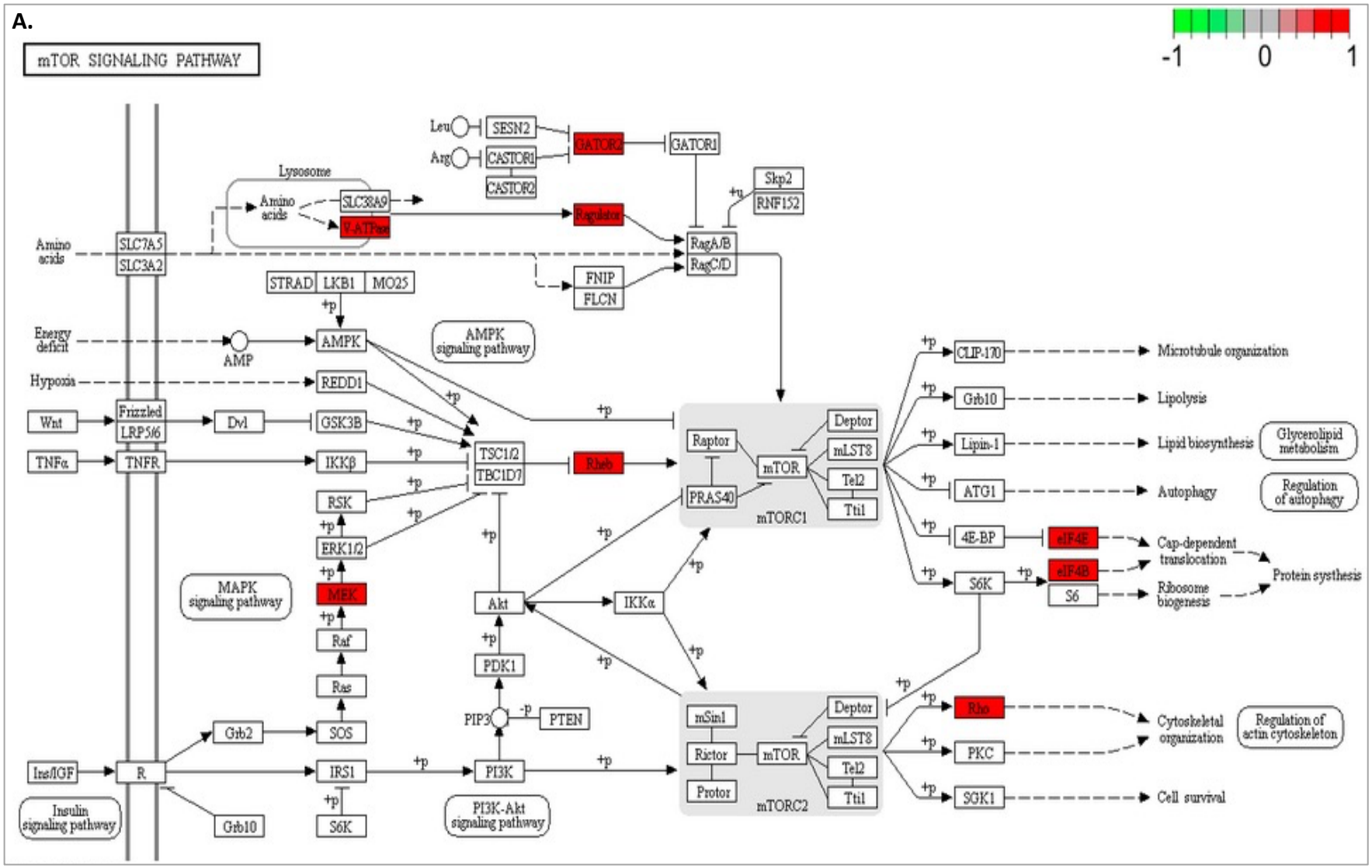


Figure 35. Summary of the number of differentially expressed genes (DEG) per cluster.

Dataset comprising single-cell transcriptome analysis of $CD4^+$ T cells isolated from the colonic lamina propria of $Atg16l1^{\Delta CD4}$ mice (KO) and $Atg16l1^{fl/fl}$ littermate (WT) controls. cells within each identified cluster using Seurat's 'FindMarkers' function. Differential gene expression analysis was performed by comparing the KO cells against the WT cells using Seurat's 'FindMarkers' function within the clusters named along the x axis.DEG were those with a Benjamini-Hochberg adjusted p-value of less than 0.05 and a |fold change| greater than 1.5 (cut-offs as: log2FC = -0.58 for downregulated genes and log2FC = 0.58 for upregulated genes)


A.
mTOR SIGNALING PATHWAY
-1
0
1
Leu
Arg
SESN2
CASTOR1
CASTOR2
GATOR2
GATOR1
Lysosome
Amino acids
SLC38A9
v-ATPase
Regulator
Skp2
RNF152
Amino acids
SLC7A5
SLC3A2
RagA/B
RagC/D
FNIP
FLCN
STRAD
LKB1
MO25
Energy deficit
AMP
AMPK
AMPK signaling pathway
Hypoxia
REDD1
Wnt
Frizzled
LRP5/6
Dvl
GSK3B
TNFα
TNFR
IKKβ
TSC1/2
TBC1D7
Rheb
RSK
ERK1/2
MAPK signaling pathway
MEK
Raf
Ras
SOS
Grb2
Ins/IGF
R
IRS1
Grb10
Insulin signaling pathway
S6K
PDK1
PIP3
PTEN
PI3K
PI3K-Akt signaling pathway
Akt
IKKα
Raptor
PRAS40
mTOR
Deptor
mLST8
Tel2
Tti1
mTORC1
mSin1
Rictor
Protor
mTOR
Deptor
mLST8
Tel2
Tti1
mTORC2
CLIP-170
Microtubule organization
Grb10
Lipolysis
Lipin-1
Lipid biosynthesis
Glycerolipid metabolism
ATG1
Autophagy
Regulation of autophagy
4E-BP
eIF4E
Cap-dependent translocation
S6K
eIF4B
S6
Ribosome biogenesis
Protein synthesis
Rho
Cytoskeletal organization
Regulation of actin cytoskeleton
PKC
SGK1
Cell survival

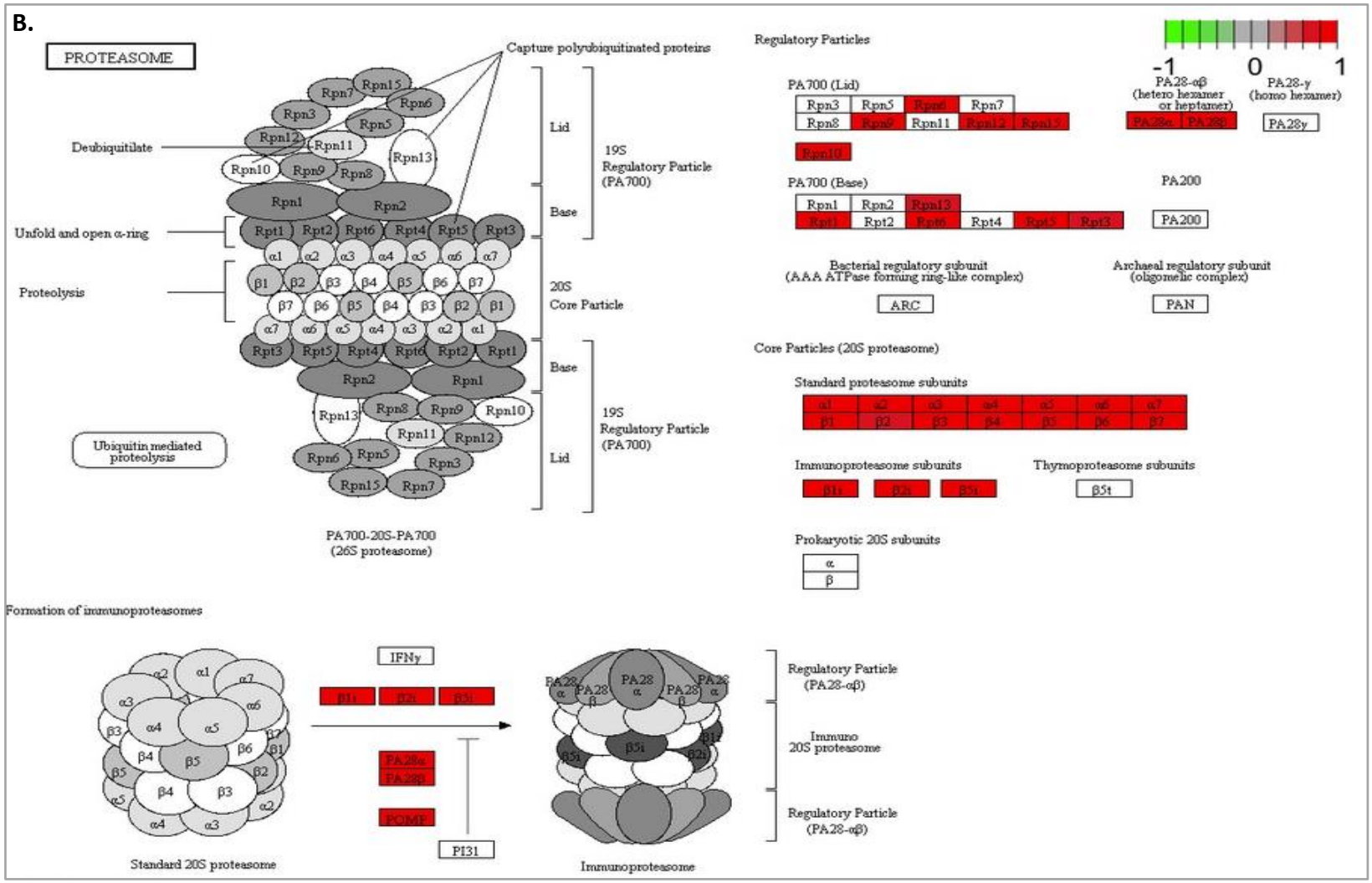


Figure 36. Visualisation of upregulated genes relating to the mTOR **(A)** and proteasome **(B)** pathways by autophagy-deficient pTreg IL10^{+} cells using "Pathview" R package.

Differential gene expression analysis was performed by comparing the KO cells against the WT cells, within the pTreg IL10+ cluster, using Seurat's 'FindMarkers' function. Subunits encoded by upregulated genes are coloured in red.

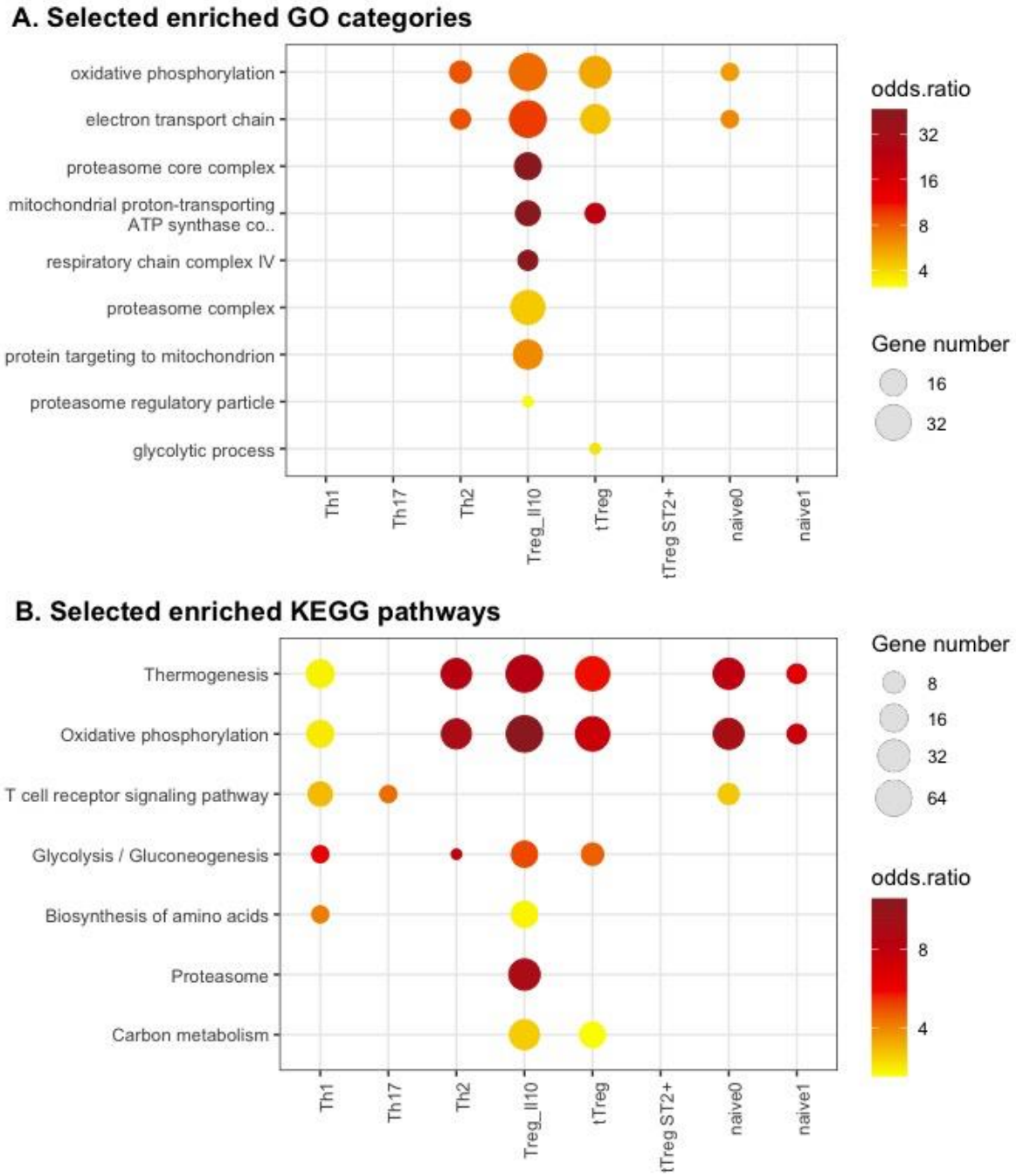


Figure 37. Summary of enriched GO categories **(A)** and KEGG pathways **(B)** following over-representation analysis.

Dataset comprising single-cell transcriptome analysis of $CD4^+$ T cells isolated from the colonic lamina propria of $Atg16l1^{\Delta CD4\ mice}$ (KO) and $Atg16l1^{fl/fl}$ littermate (WT) controls. Over-representation analysis of differentially expressed genes was performed using one-sided Fisher's exact tests, as implemented in the "gsfisher" R package *https://github.com/sansomlab/gsfisher/*. Differential gene expression analysis was performed by comparing the KO cells against the WT cells using Seurat's 'FindMarkers' function within the clusters named along the x axis. The Appendix contains the upregulated genes which are part of the identified enriched GO categories and KEGG pathways for the named clusters.

5.2.6 Successful validation of some of the sc-RNAseq findings

Validation of the genes and pathways suggested by differential expression and by over-representation analysis was severely impacted by the facilities lockdown triggered by the COVID-19 pandemic.

In order to test whether the transcriptomic downregulation of the *Il10* gene identified in autophagy-deficient Treg cells through the scRNA-seq analysis described above, translates into functional differences, I have performed a FACS *ex-vivo* staining for $IL10^{+}$ cytokine expression on re-stimulated lymphocytes isolated from the cLP of $Atg16l1^{\Delta CD4}$ mice and $Atg16l1^{fl/fl}$ littermate controls (Figure 38). This experiment confirmed that autophagy-deficient $Foxp3^{+}$ Treg show significantly lower expression of IL-10^{+} than WT counterparts (Figure 38), providing a first validation for the scRNA-seq data.

Similarly, in order to test whether the transcriptomic upregulation of genes involved in the mTOR pathway (*Gator2, Rheb*, *Lamtor1,2,3*, *Rho*, *Eif4e* and *Eif4b)*, which were identified in autophagy-deficient Treg cells through the scRNA-seq analysis described in the previous section, translates into increased functional mTOR activity, I have performed a FACS *ex-vivo* staining for p-S6 protein on lymphocytes isolated from the cLP, MLN and spleens of $Atg16l1^{\Delta CD4}$ mice and $Atg16l1^{fl/fl}$ littermate controls (Figure 39). This experiment confirmed that autophagy-deficient $Foxp3^{+}$ Treg cells show enhanced mTOR activation as measured by p-S6 intracellular FACS staining. This difference was confined to the periphery as autophagy-deficient $Foxp3^{+}$ Treg showed comparable levels of p-S6 to WT counterparts in the spleen and MLN (Figure 39).

Lastly, in order to test whether the upregulation of proteasome genes which were identified in autophagy-deficient Treg cells through the scRNA-seq analysis described in the previous section, translates into increased cellular proteasome activity, I have measured the proteasome activity of *in vitro* differentiated Treg cells isolated from the spleens of $Atg16l1^{\Delta CD4}$ mice and $Atg16l1^{fl/fl}$ littermate controls (Figure 40). Lymphocytes were *in vitro* differentiated towards Treg cells as described in *section 2.6.1*. This experiment confirmed that *in vitro* differentiated autophagy-deficient Treg cells show higher proteasome activity, when measured using a fluorometric proteasome activity assay kit as detailed in *section 2.6.3* (Figure 40).

Given these promising results, I attempted to test the functional consequences of enhanced proteasome activity in autophagy-deficient peripheral Treg cells by blocking the proteasome pathway of *in-vitro* differentiated Treg cells with a low dose of the proteasome inhibitor MG-132 (Sigma-Aldrich, M8699-1MG) to test the hypothesis that increased proteasomal transcription is mal-adaptive (Figure 41). Previous experiments done in the lab established a

system that allows us to compare the survival of *in vitro* differentiated *Atg16l1*-deficient Treg cells with autophagy-sufficient Treg cells. Briefly, naïve $CD4^+$ T cells isolated from the spleen of $Atg16l1^{\Delta CD4}$ mice or $Atg16l1^{fl/fl}$ littermate controls are cultured in Th0 or Treg polarizing conditions for prolonged periods of time (as described in *section 2.6.1*). When compared on day 7 of culture (day 5 after 2 days of TCR co-stimulation) autophagy-deficient Treg cells showed a marked decrease in their survival as compared to WT controls. Using this experimental set-up, I tested the effects of a short, 2hrs long treatment of 1μM MG-132 proteasome inhibitor on the survival ratios of *in vitro* differentiated $CD4^+$ T cells and Treg cells. The proteasome treatment was done on day 6 of culture and T cell survival was measure either at 7.5hrs or 24hrs after proteasome treatment. In this experimental set-up the proteasome inhibitor treatment had no significant effect on the *in vitro* survival of autophagy-deficient $CD4^+$ T cells and Treg cells when survival was measure at 7.5hrs post proteasome treatment (Figure 41 B,C). Some positive and significant trends towards an improved survival of autophagy-deficient Treg cells where seen after proteasome treatment, when survival was measured after 24hrs in Treg differentiating conditions (Figure 41C). Unfortunately, further optimisation of this system was not possible for the duration of this thesis due to the impact of the COVID-19 pandemic on experimental work.

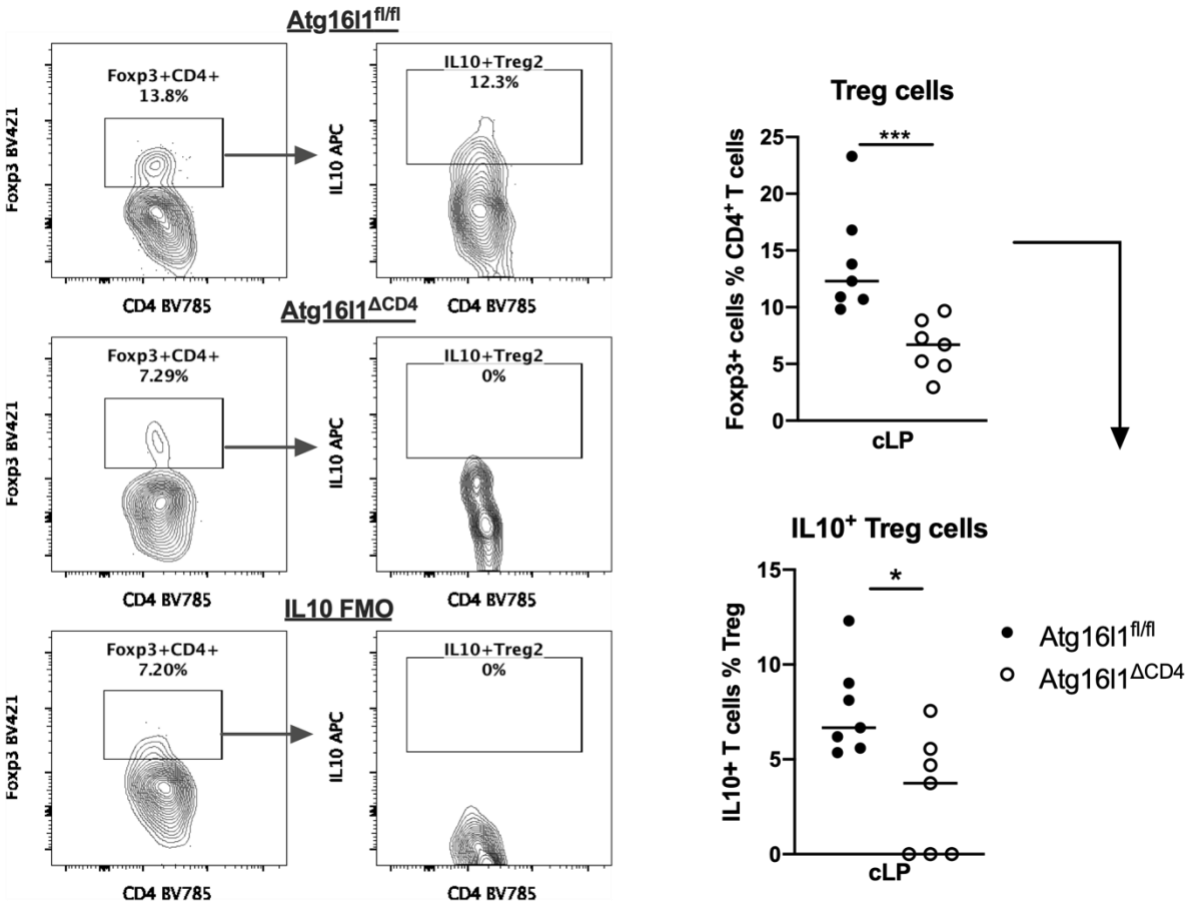


Figure 38. Validation of IL-10^{+} expression by Treg cells in Atg16l1$^{\Delta CD4}$ mice and Atg16l1$^{fl/fl}$ littermate controls.

Cells were re-stimulated *ex-vivo* with PMA, Ionomycin, Brefeldin and Monesin for 4hrs at 37°C as described in *section 2.4.2*. Representative FACS plots of IL10^{+} staining in pre-gated Treg (Foxp3^{+}CD4^{+}TCRβ^{+} T cells) and corresponding graphs quantifying the ratio of IL10^{+} cells as percentage of Treg cells.

Data is combined from two independent experiments, with at least 2 mice per group. Each dot represents and individual mouse. Statistical significance was determined using the Mann-Whitney test: * $p<0.05$, *** $p<0.001$.

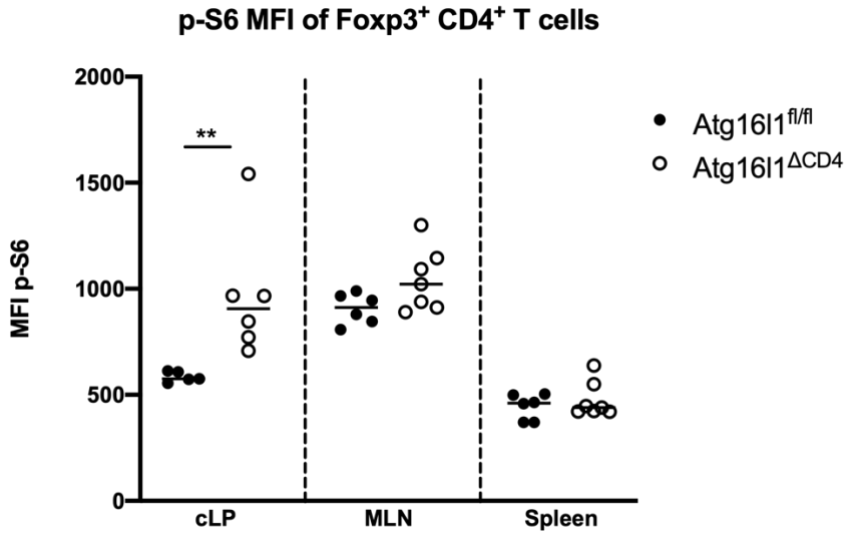


Figure 39. Validation of mTOR and activity expression by Treg cells in Atg16l1$^{\Delta CD4}$ mice and Atg16l1$^{fl/fl}$ littermate controls.

MFI of phosphorylated-S6 (p-S6) in Foxp3^{+}Treg cells isolated from the cLP, MLN and spleen of Atg16l $^{\Delta CD4}$ mice and Atg16l1$^{fl/fl}$ littermate controls. Intracellular FACS staining of p-S6 on *ex-vivo* cells was performed as described in *section 2.4.4*. Cells were pre-gated on live Foxp3^{+}CD4^{+}TCRβ^{+} T cells.

Data is combined from two independent experiments, with at least 2 mice per group. Each dot represents and individual mouse. Statistical significance was determined using the Mann-Whitney test: ** $p<0.01$.

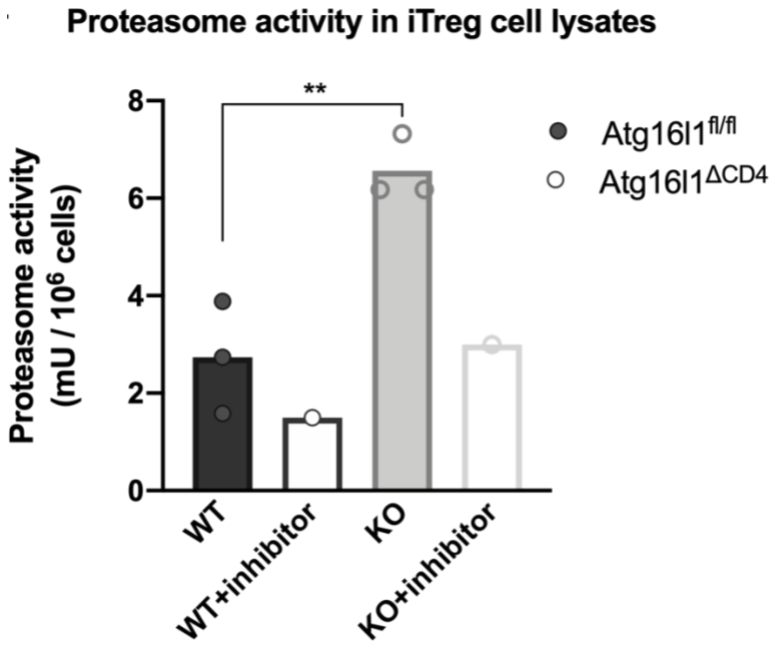


Figure 40. Validation of proteasome activity in *in-vitro* differentiated Treg cells derived from Atg16l1$^{\Delta CD4}$ mice and Atg16l1$^{fl/fl}$ littermate controls.

Proteasome activity as measured in cell lysates (2mil cells per sample) of *in-vitro* differentiated Treg cells. Determined using a proteasome activity assay as described in *section 2.6.3*, three technical replicates were performed for the WT and KO samples. 10mM MG-132 was used as proteasome inhibitor. Lymphocytes were isolated from spleens of Atg16l $^{\Delta CD4}$ mice and Atg16l1$^{fl/fl}$ littermate controls, enriched for naïve CD4^{+} T cells as described in *section 2.3.5*, followed by *in vitro* differentiation towards Treg cells as described in *section 2.6.1*. Each dot represents an individual culture. Statistical significance was determined by unpaired t-test ** $p < 0.01$.

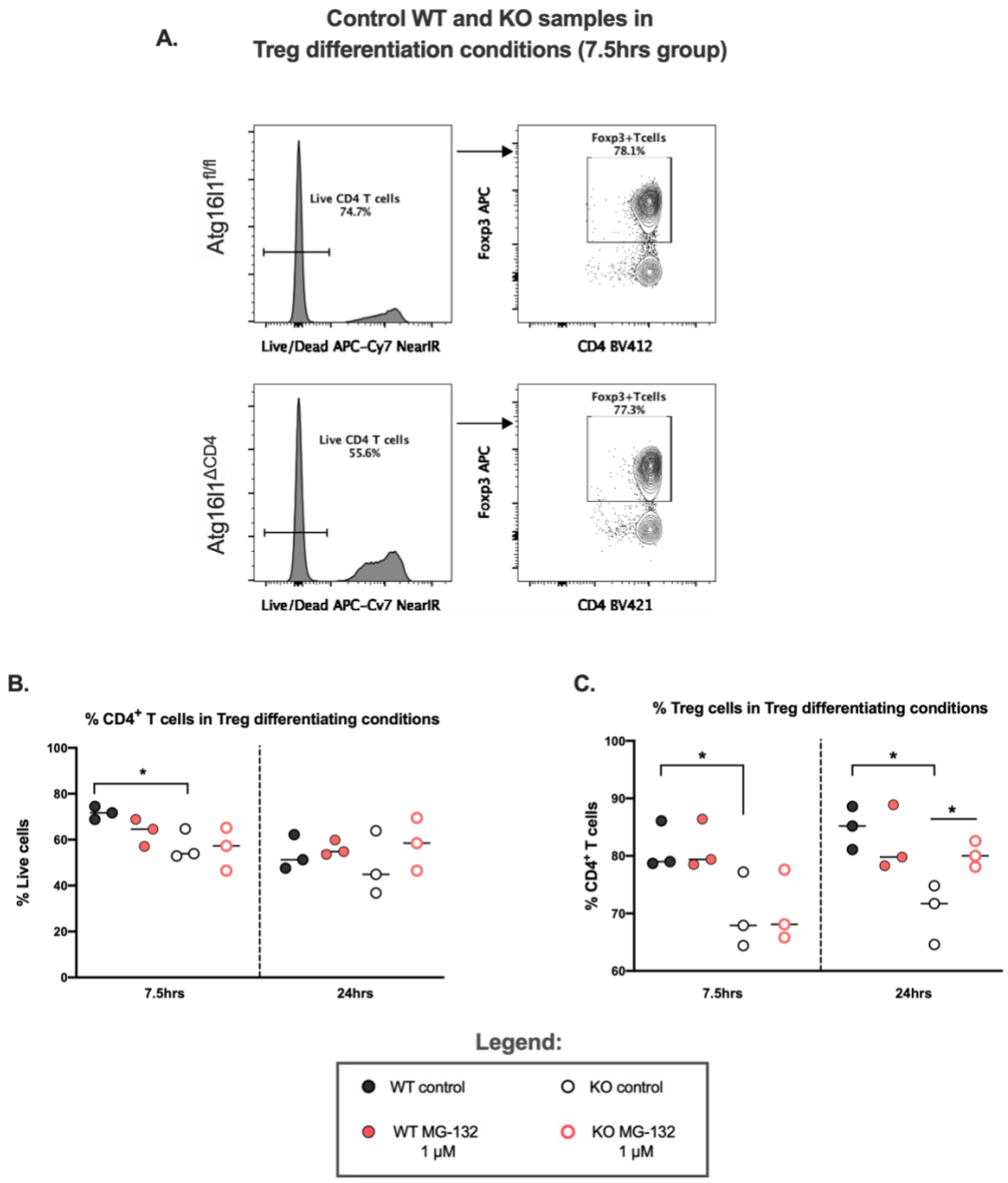


Figure 41. Proteasome inhibitor treatment of *in vitro* differentiated Treg cells, isolated from splenocytes of Atg16l1$^{\Delta CD4}$ or Atg16l1$^{fl/fl}$ mice.

(A,B,C) Naïve CD4$^+$ T cells isolated from Atg16l1$^{\Delta CD4}$ or Atg16l1$^{fl/fl}$ mice were cultured in the presence of plate bound anti-CD3 (5μg/ml) plus soluble anti-CD28 (1μg/ml) for 48hrs in Treg polarizing conditions, then maintained in polarizing conditions for a further 5 days before analysed by FACS (day 7 of *in vitro* culture). Treg conditions: TGF-β1 (5 ng/ml), anti-IFN-γ, anti-IL-4 mAb and anti-IL-12 (all 10 μg/ml) plus IL-2 (100 U/ml)

(A) Representative FACS staining. Histograms show gates and frequencies of live CD4$^+$T cells (gated on CD4$^+$ TCRβ$^+$ live cells).

Frequencies of live $CD4^+$ T cells **(B)** and live Treg cells **(C)** in Treg polarizing conditions. Naïve $CD4^+$ T cells isolated from $Atg16l1^{\Delta CD4}$ or $Atg16l1^{fl/fl}$ were differentiated as described in (A,B,C). A 2hrs pulse treatment with 1µM of MG-132 proteasome inhibitor was administered on day 6 of *in vitro* culture. Frequencies of live $CD4^+$ T cells were assessed 7.5hrs or 24hrs after MG-132 treatment, as indicated.

(B,C) Data is representative of one experiment with three technical replicates. Cells from 4 mice were pooled per group. Each dot represents an individual culture. Statistical significance was determined by unpaired t-test, *p<0.05, ***p<0.001.

5.3 Summary and conclusions

By employing an unbiased approach that uses sc-RNAseq I have characterised the changes induced by autophagy deficiency in intestinal $CD4^+$ T cells. This approach has recapitulated the previous findings made by the Maloy lab, including the selective expansion of Th2 cells and the reduction in $Foxp3^+$Treg cells in the intestinal lamina propria, both in terms of relative proportions and absolute numbers.

To combat the experimental limitation described in section 5.1, created by pooling $Atg16l1^{fl/fl}$ (WT) and $Atg16l1^{\Delta CD4}$ (KO) mice into two samples (N=1 vs N=1), an improved replicate experiment could be performed utilising cell-multiplexing. This would involve labelling cells obtained from individual mice with a molecular tag/barcode and subsequently mixing together all such labelled samples. The multiplexed samples can be combined before FACS purification, eliminating batch effects. Following RNA isolation, library preparation and sequencing, the molecular tag information can be bioinformatically assigned to cells originating from individual mice. Thus, this approach would address any potential technical variation created by batching WT and KO samples separately. At the time when the sc-RNA-seq experiment described in the thesis was performed (Aug 2018), commercially available sample barcoding approaches were not readily available, although specialist labs were trialling in-house versions of this method. At the time of writing of the thesis the multiplexed sample scRNA-seq approach is more common place, partly due to the launch of the CellPlex kit from 10x Genomics in the first part of 2020. Several papers validating cell-multiplexing approaches have also been published in the meantime *(Gehring et al., 2020; Ranu et al., 2019).*

The scRNA-seq data was used to generate hypotheses about the pathways that autophagy may regulate in intestinal $CD4^+$ T cells. The IL-10, mTOR and proteasome analyses give proof-of-principle that some of the differences identified can be validated at the protein level in independent cohorts using independent methods. This gives confidence that further analyses may yield additional functional insights. Thus, the scRNA-seq data set represents a resource for further investigation and validation, rather than a definitive means to conclude differences about WT and KO T cells.

Previous findings indicated that the discrepancy in T cell survival could be partly attributed to an altered metabolic programme, characterised by dysfunctional mitochondrial metabolism and enhanced glycolytic metabolism, employed by *Atg16l1*-deficient Treg cells when compared to WT counterparts. In contrast, WT Th2 cells seemed to have a constitutive high level of glycolytic metabolism that is comparable to *Atg16l1*-deficient Th2 cells *(Kabat et al., 2016a)*. Analysis of the data generated through sc-RNAseq analysis further corroborates this hypothesis. I found systemic upregulation across T effector clusters, and most evidently across Treg clusters, of genes essential for mitochondrial metabolism and genes relating to glucose metabolism. Moreover, autophagy-deficient Th2 cells when compared to WT counterparts, did not reveal as many DEG as autophagy-deficient Treg clusters compared to WT

counterparts, implying that autophagy deficiency may have a smaller transcriptomic effect on Th2 cells than on Treg cells. These findings are even more striking when accounting for the smaller number of cells used for differential expression analysis in the pTreg IL10+ cluster after equalising the numbers between WT and KO groups (c180 cells each) when compared to number of cells used for analysis with the Th2 cluster (c250 cells each), as it is more difficult to detect differences across a smaller number of cells than a larger number of cells. Many studies have already shown that metabolism of some T cell subsets is highly depended on functional autophagy *(Kabat et al., 2016a; Simon et al., 2019; Wei et al., 2016)*. Thus, we have not explored these findings further but rather used them as an indirect proxy for validating the sc-RNAseq data with previous findings.

The scRNA-seq analysis also provided new insights into the effects of autophagy deficiency on Treg cells, such as reduced *Il10* gene expression. I have validated this finding with *ex-vivo* FACS staining, showing that autophagy-deficient Treg cells in the colonic lamina propria express less IL-10^{+} cytokine than autophagy-sufficient Treg cells from littermate control. IL-10 is produced by a wide range of immune cell types, however, IL-10 secreted by Foxp3^{+} Treg cells appears to be particularly important in regulating immune responses at the body's environmental interfaces *(Ng et al., 2013; Rubtsov et al., 2008)*. Indeed, mice with selective knockout of IL-10 in Foxp3^{+} Treg cells are known to develop spontaneous colitis *(Rubtsov et al., 2008)*. Many studies unequivocally identify Foxp3^{+} Treg cell derived IL-10 as a key mediator of intestinal immune homeostasis but the exact mechanisms of IL-10 induction in the these cells in the intestine remain elusive *(Saraiva and O'Garra, 2010)*. IL-10 was described to inhibit autophagy by activating the PI3K/Akt/mTORC1 pathways in dendritic cells *(Santarelli et al., 2014)*. Our study may provide a further insight into the overlap between the autophagy and the IL-10 pathway in Foxp3+ Treg cell. Unfortunately, further investigation of the cross-overs between these two pathways was not possible during the timeline of this thesis. A follow up experiment could involve using *in vitro* methods to generate IL-10^{+} Foxp3+ Treg cells and study the impact of autophagy inhibitors and inducers on IL10^{+} secretion.

The finding we found most interesting from the sc-RNAseq analysis was the selective upregulation of proteasomal pathways in autophagy-deficient IL-10^{+} Treg cells. Although I have validated this finding using a proteasome activity kit on *in-vitro* differentiated Treg cells, I could not thoroughly determine the functional consequences of this upregulation. We hypothesise that the upregulation of the proteasomal pathway by autophagy-deficient Treg cells could either be an adaptation mechanism that allows these cells to survive in the colon in the absence of autophagy, or a maladaptive mechanism that has detrimental consequences for Treg cells. A preliminary *in-vitro* experiment to assess the functional consequences of proteasome upregulation in autophagy-deficient Treg cells found that inhibition of the proteasome activity could be beneficial for boosting the survival of autophagy-deficient Treg cells. Further validation of this finding was not possible for the duration of this thesis due to the facilities lockdown triggered by the COVID-19 pandemic.

Nevertheless, if the upregulation of the proteasome in autophagy-deficient Treg cells represents a maladaptive mechanism that compounds their survival defect, it is interesting to speculate on the mechanism behind this. The sc-RNAseq analysis has also indicated that the mTOR pathway is over-represented in autophagy-deficient Treg IL-10$^+$ cells and I have validated this finding through p-S6 *ex-vivo* FACS staining of colonic Treg cells. Thus, we can hypothesise that over-activation of the proteasome in these cells could lead to increase generation of amino-acids, which in turn could lead to over-activation of the mTOR pathway. Moreover, the sc-RNAseq analysis also showed that genes involved in the formation of the Ragulator complex (*Lamtor1-3*) are upregulated in autophagy-deficient IL10$^+$ Treg cells. Ragulator is an essential component of the docking complex that recruits mTORC1 to the lysosome in response to amino-acids and mTOR translocation to lysosomes is impaired in the absence of Ragulator *(Sancak et al., 2010)*. Aberrant mTOR activity in Atg7-deficient Treg cells was associated with heightened glycolytic metabolism *(Wei et al., 2016).* Given that Treg cells are known to rely on OXPHOS and FAO metabolism to perform suppressor functions *(Buck et al., 2015)*, a potential feedback loop begins to emerge, connecting the overactivation of the proteasome pathway with amino-acids generation and over-activation of mTOR which could ultimately lead to a dysfunctional, glycolytic Treg cells metabolism affecting Treg functioning (Figure 42).

The sc-RNAseq data described in this chapter provides a rich source of candidate genes for follow-up studies to better understand the multiple roles of the autophagy pathway in CD4$^+$ T cells. For example, autophagy-deficient in CD4$^+$ T cells seems to trigger downregulation of the the IL-7 receptor gene (*Il7r*) in Th1, Th17 and tTreg cells. IL-7 receptor is thought to regulate T cell homeostasis, proliferation, and survival and several genome-wide association studies have linked polymorphisms in *Il7r* with susceptibility to multiple diseases including inflammatory bowel diseases *(Schluns et al., 2000)*. Conventional mature T cells are known to express high levels of the IL-7 receptor, whilst Treg cells express lower levels of IL-7 receptor *(Schluns et al., 2000)*. Thus, this could be an interesting target for further study to understand the different effects of autophagy on individual T cell subsets

In this chapter I have used single-cell transcriptomic analysis to characterise the perturbations induced by autophagy deficiency in intestinal CD4$^+$ T cells. This approach corroborated previous finings made using traditional immunology methods, as well as provided new insight into the diverse functions of autophagy in intestinal CD4$^+$ T cell. The functional importance of these new findings for Treg cells survival and functioning in the periphery remain to be fully validated.

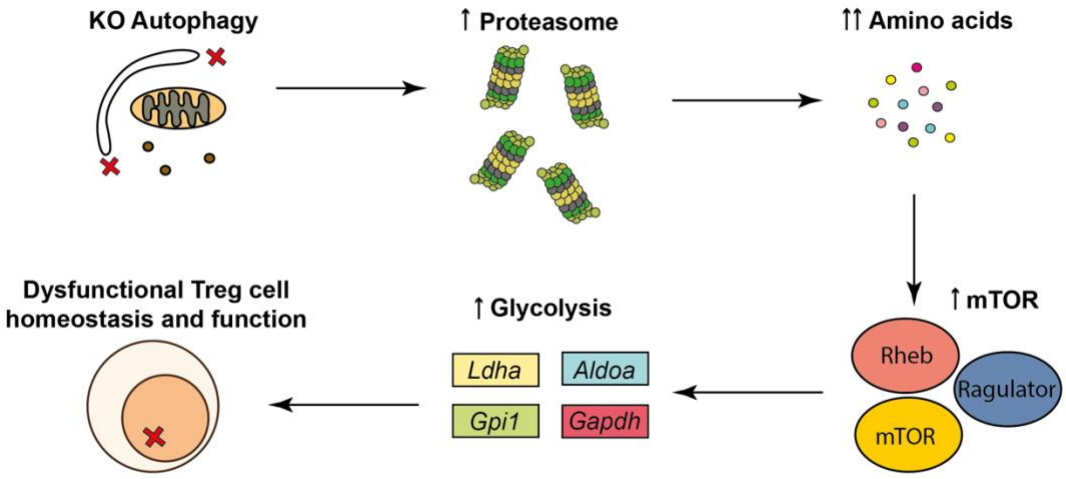


Figure 42. Potential mechanistic implications of autophagy deficiency in Treg cells.

The sc-RNAseq analysis of $CD4^+$ T cells isolated from the cLP of $Atg16l1^{fl/fl}$ and $Atg16l1^{\Delta CD4}$ littermates, as well as follow-up functional validation, suggest that autophagy deficient Treg cells upregulate the proteasome pathway, display increases mTOR activity and glycolytic metabolism. Thus, a potential feedback loop begins to emerge, connecting the over-activation of the proteasome pathway with amino-acids generation and over-activation of mTOR. This could ultimately lead to a dysfunctional, glycolytic Treg cells metabolism affecting Treg homeostasis and functioning.

Chapter 6. General discussion

The role of the microenvironment in number, function and metabolism of Treg cells

The immune system is an extraordinarily diverse inventory of specialised cells and molecules that continuously patrol the blood and tissues for invaders and protect body surfaces which are under constant assault from infectious agents. These invading agents vary by anatomic location and are constantly evolving to evade detection; thus, the immune system has evolved to customise its defences accordingly.

We have gained most of our information about the immune system by analysing cells from the blood, spleen and lymph nodes, due to convenience in sampling these cells. In recent years, it has become increasingly appreciated that the phenotype, function, metabolism and regulatory mechanisms of immune cells are drastically different and significantly customised to the anatomical location in which they reside *(Hu and Pasare, 2013).* For example, the composition of Treg cells varies by organ type. Typically, Treg cells represent about 5-15% of the $CD4^+$ T cell population in spleen and lymph nodes (Panduro et al., 2016). By comparison, of the $CD4^+$ T cell population present in the intestine of adult mice, 10-20% are Treg cells. Treg cells are highly enriched in the visceral adipose tissue compartment, reaching a peak of 40-80% of $CD4^+$ T cells in mice around 10-15 weeks of age *(Panduro et al., 2016*. Mouse skin also has an unusually high Treg representation, with 20-60% of $CD4^+$ T cells *(Pao et al., 2018).* These differences in Treg cell proportions may be partially explained through the different origin of these cells. For examples, the majority of Treg cells found in the intestine are peripheral Treg cells, induced by commensal microbes, whilst Treg in mouse skin are thought to be thymus-derived and accumulate in the skin during a specific window of neonatal development *(Pao et al., 2018).*

This thesis has shown that cell-intrinsic autophagy is indispensable for Treg cell maintenance in the periphery and thus control of effector T cells responses and other immune cell types in the periphery. Autophagy deficiency did not affect thymic generation of Treg cells or their numbers and phenotype in the systemic immune system *(Kabat et al., 2016a).* Although precisely how autophagy deficiency in Treg cell impairs their survival still remains to be elucidated, this study adds to the body of evidence that suggests autophagy is important for Treg adaptations in peripheral tissues.

It is striking that autophagy-deficiency has a more detrimental effect on Treg cells in the intestine and adipose tissues than on those found in the systemic immune system. Recent evidence suggests that Treg cells undergo tissue-specific adaptations and metabolic changes are emerging as an important part of such tissue specific reprogramming *(Buck et al., 2015)*. To date, it is not well understood how peripheral tissues control the development and

education of $CD4^+$ T cells. We can hypothesise that the local microenvironment may impact the functioning and metabolism of these cells. Although each site will have unique characteristic, some shared features could include low oxygen and low nutrient levels (like glucose and glutamine). Thus, T cells traveling from nutrient-rich secondary lymphoid tissues to peripheral sites will experience a dramatic shift in microenvironment conditions and will need to adopt their metabolism accordingly.

Several other studies on mouse T cells also revealed the function and composition of T cells to be closely linked to their anatomical location. Treg cells, in particular, seed to various tissues early in development where they acquire highly specialised programs that are tailored to the tissue in which they reside *(Panduro et al., 2016).* For example, Treg cells in adipose tissues uniquely express peroxisome proliferator-activated receptor γ (PPARγ), a transcription factor normally restricted to adipocytes *(Lui et al., 2020).* A mouse model with a conditional knockout of PPARγ in Treg cells resulted in a 70% reduction in the abundance of Treg cells in adipose tissues *(Cipolletta et al., 2012).*
More recently, the Teichmann lab used sc-RNAseq to determine the trajectories of tissue adaptation for skin and colonic Treg cells and showed that the acquisition of tissue-specific transcriptional programmes proceeds through discrete transitional states *(Miragaia et al., 2019).* Thus, we can hypothesise that autophagy may provide Treg cells with the means to bridge these distinctive transitional states and facilitate adaptation to tissues in the periphery.

An important avenue of future investigation would be to connect the mouse findings of this thesis on the functional consequences of *Atg16l1*-deletion in T cells, with further improving our understanding on how the *ATG16L1* T300A polymorphism could result in increased susceptibility to CD in humans. The role of the autophagy polymorphism *ATG16L1* T300A in intestinal homeostasis has been explored by a number of studies, mainly assessing its function in intestinal epithelial cells and myeloid cells. These studies showed that the polymorphism, in the presence of additional triggering factors, can drive several abnormalities, like Paneth cell defects or increased cytokine release and decreased intracellular bacterial clearance by myeloid cells *(Cadwell et al., 2008; Cadwell et al., 2010; Cooney et al., 2010; Lassen et al., 2014; Matsuzawa-Ishimoto et al., 2017)*. However, the impact of the *ATG16L1* T300A polymorphism in human Treg cells has not been explored. The TGU Biobank/Oxford IBD patient cohort is an ongoing archive established at the John Radcliffe Hospital in Oxford from which PBMC samples of patients could be requested. These samples would need to be genotyped to identify the *ATG16L1* T300A polymorphism and exclude other risk-associated genetic polymorphisms. Moreover, given that the *ATG16L1* T300A variant is common in the human population, approximately 55% of alleles in the European population and 20% to 40% of alleles in other populations *(Hampe et al., 2007; Rioux et al., 2007)*, we would need to study 4 experimental groups: healthy donors with and without the SNP and CD patients with and without the SNP. Naïve $CD4^+$ T cells could be purified from the PBMC samples from these 4 experiment groups, and cultured under Treg polarising conditions.

Expression of the key genes identified by this thesis as affected by autophagy-deficiency (*Il10*, proteasome subunits) could be assessed in the polarised Treg cells, using both molecular (qPCR) and protein-detecting methods (FACS, proteasome activity assay). As mentioned above, the *ATG16L1* T300A hypomorphic phenotype seems to emerge under stress conditions, so the functional responses of the polarised Treg cells could be assessed in the presence of additional triggering factors, like inflammatory cytokines (TNF), that could activate caspase-3 which would degrade the T300A protein. Additionally, the Human Cell Atlas project is generating a comprehensive database of human cells in health and disease. For example, the Regev group released a paper in which they generated an atlas of cells from the cLP of 7 UC and 10 healthy individuals *(Smillie et al., 2019)*. Thus, datasets like these, but from CD patients with the *ATG16L1* T300A mutation, could be used for an *in silico* experiment that would attempt to identify altered Treg gene signatures like the ones described in this thesis (eg. upregulation of proteasomal genes).

The complementary roles of the proteasome and autophagy pathways

The data presented in this thesis also identifies a previously unrecognized compensatory mechanism between the autophagy and the proteasome pathways within intestinal Treg cells. This is somewhat unexpected as the two pathways differ significantly with respect to their mechanistic details. For example, whilst autophagy is a vesicular trafficking pathway, the enzymatic reactions of the proteasome system occur directly in the cytosol. Moreover, the activity of proteasome system is restricted to soluble proteins, but autophagy is practically unrestricted in the type of substrate degraded. These differences meant that for a long time the autophagy and the proteasomal machineries were considered two separate degradative systems *(Korolchuk et al., 2010).* However, increasing evidence document an induction of autophagy when the proteasome is inhibited or overloaded *(Ding et al., 2007; Korolchuk et al., 2010).* In contrast, evidence for a reverse, autophagy to proteasome shift, upon impairment of autophagy is currently weak, and mostly explored in cultured and transformed cells. In starved colon cancer cells inhibition of autophagy was shown to induce the proteasome pathway by increasing the expression of proteasomal subunits and proteolytic activity *(Wang et al., 2013)*. However, other reports did not detect an upregulation of proteasomal activity upon autophagy inhibition *(Korolchuk et al., 2009; Qiao and Zhang, 2009).* This may be because the autophagy to proteasome shift only occurs in specific circumstances like nutritional stress. In this case, starvation coupled with autophagy deficiency may cause a substantial impairment in cellular metabolism that triggers a certain threshold at which the proteasomal system kicks in. This may not happen in nutrient-replete conditions when this critical threshold is not met. Nevertheless, there are some autophagy functions that cannot be handled by the proteasome. For example, autophagy is the only currently known mechanism to degrade mitochondria *(Goldman et al., 2010).*

Why is it important to prove this seemingly reciprocal compensatory link between autophagy and the proteasome? Understanding the fine molecular details of how the autophagy and proteasomal systems are integrated may be important when we want to manipulate one of these pathways for therapeutic goals. Autophagy has been implicated in many diseases, including cancer, autoimmunity and neurodegeneration *(Levine et al., 2011).* Autophagy is thus an attractive therapeutic target and several autophagy modulating compounds are have been trialled for the treatment of various disorders *(Jiang and Mizushima, 2014).* Similarly, the proteasomal degradation system contributes to the pathobiology of a myriad of malignancies. Inhibitors of the 20S proteasome have been important advancements in the treatment of patients with the haematological malignancy multiple myeloma *(Manasanch and Orlowski, 2017).* Treatment with both proteasome and autophagy inhibitors may be beneficial to those patients that do not respond to proteasome inhibitor alone, an area which is currently researched intensely. Challenges still remain in identifying the disease phenotypes that would benefit most from these treatments whilst also minimise drug-resistance and preventing toxicity. Thus, understanding the reciprocal regulation of these two cellular degradative systems could have a significant impact for the development of future drugs or drug combination therapies.

All living organisms require cellular degradation mechanism in order to remove cellular components that are no longer required and eliminate their harmful effects in a timely manner. Autophagy and the proteasomal system are two cornerstones of cellular catabolism that are involved in most processes of normal physiology and development and also degrade dysfunctional or damaged cellular components, ranging from soluble proteins to whole organelles. Thus, these systems are critical for maintaining cellular homeostasis, suggesting that their activities need to be carefully orchestrated. Our findings may raise the possibility of a compensatory effect of the proteasome system when autophagy is impaired in intestinal Treg cells. However, the functional consequences of this compensatory effect remain to be confirmed *in vivo*. This opens an exciting avenue to further explore the role of degradative systems in the functioning of $CD4^+$ T cells.

Appendix

GO category (ontology)	Cluster	Genes
Proteasome complex (CC)	Treg_Il10	Psmb9, Psmb8, Psma2, Psma3, Psmb1, Psmb10, Psmb4, Psmb5, Psmb6, Psmb7, Psmc2, Psmc3, Psmc5, Psmd4, Psme1, Sem1, Psmc4, Psmd13,
Proteasome core complex (CC)	Treg_Il10	Psmb9, Psmb8, Psma2, Psma3, Psmb1, Psmb10, Psmb4, Psmb5, Psmb6, Psmb7, Psma1, Psma4, Psma5, Psma6, Psma7, Psmb2, Psmb3
Proteasome regulatory particle (CC)	Treg_Il10	Psmc2, Psmc3, Psmc5, Psmd4, Sem1, Psmc4, Psmd13, Adrm1, Psmd8, Psmd11
Oxidative phosphorylation(BP)	Th2	Cox5a, Cox5b, Cox7a2, Cox7c, Cycs, Cox1, Cox2 ,Cox3, Cytb, Nd4l, Uqcrq, Park7, Uqcrh
	Treg_Il10	Rhoa, Atp5b, Cox4i1, Cox5a, Cox5b, Cox6a1, Cox7a2, Cox7c, Cycs, Cox1, Cox2, Cox3, Cytb, Nd4, Nd4l, Ndufv1, Pgk1, Cox7a2l, Uqcrq, Uqcrc1, Park7, Uqcr10, Ndufb9, Iscu, Ndufa12, Ndufa7, Cyc1, Uqcrh, Uqcrfs1, Ndufb8, Uqcrb, Ndufc2, Ndufa8, Ndufv2, Ndufv3, Ndufs8, Ndufs2, Ndufb6, Vcp, Ndufs6
	tTreg	Rhoa, Cox5a, Cox5b, Cox7a2, Cox7c, Cox1, Cox2, Cox3, Cytb, Nd2, Nd4, Nd4l, Myc, Pgk1, Cox7a2l, Uqcrq, Uqcr10, Ndufb9, Uqcrh, Uqcrfs1, Ndufb8, Ndufa8, Ndufs2, Ndufb6
	naive0	Cox4i1, Cox7c,Cox1, Cox2, Cox3, Cytb, Nd2, Nd4, Nd4l, Uqcrh, Uqcrb
Electron transport chain (BP)	Th2	Cox5a, Cox5b, Cox7c, Cycs, Cox1, Cox2, Cox3, Cytb, Nd4l, Uqcrq, Park7, Uqcrh
	Treg_Il10	Cox4i1, Cox5a, Cox5b, Cox6a1, Cox7c, Cycs, Cox1, Cox2, Cox3, Cytb, Nd4, Nd4l, Ndufs4, Ndufv1, Sod2, Uqcrq, Uqcrc1, Park7, Uqcr10, Ndufb9, Iscu, Ndufa12, Ndufa7, Cyc1, Ndufb3, Uqcrh, Uqcrfs1, Ndufb8, Uqcrb, Sdhb, Ndufc2, Ndufa5, Ndufa8, Ndufv2, Ndufv3, Ndufs8, Ndufs2, Ndufb6, Ndufs6
	tTreg	Cox5a, Cox5b, Cox7c, Cox1, Cox2, Cox3, Cytb, Nd2, Nd4, Nd4l, Uqcrq, Uqcr10, Ndufb9, Uqcrh, Uqcrfs1, Ndufb8, Sdhb, Ndufa8, Ndufs2, Ndufb6
	naive0	Cox4i1, Cox7c, Cox1, Cox2, Cox3, Cytb, Nd2, Nd4, Nd4l, Uqcrh, Uqcrb
Respiratory chain complex IV (CC)	Treg_Il10	Cox4i1, Cox5a, Cox6a1, Cox8a, Cox1, Cox2, Cox3, Ndufa4, Cox7b, Uqcrfs1, Uqcrc2, Cox6b1
Glycolytic process (BP)	tTreg	Aldoa, Gapdh, Gpi1, Hif1a, Mi , Myc, Pgk1, Pkm, Tpi1, Eno1b
Mitochondrial proton-transporting ATP synthase complex (CC)	Treg_Il10	Atp5a1, Atp5b, Atp5c1, Atp5pb, Atp5g1, Atp5j, Atp5k, Atp6, Atp5l, Atp5j2, Atp5d, Atp5e, Atp5g2, Atp5h, Atp5g3
	tTreg	Atp5c1, Atp5pb, Atp5j, Atp5k, Atp6, Atp5l, Atp5j2, Atp5d, Atp5e, Atp5g2, Atp5h, Atp5g3
Protein targeting to mitochondrion	Treg_Il10	Atpif1, Bnip3l, Hspa4, Grpel1, Timm17b, Ywhaz, Timm13, Timm23, Pdcd5, Tomm7, Fis1, Uqcrc2, Romo1, Tomm34, Ndufa13, Dnajc19, Tomm20,

Table 7. Upregulated genes part of an enriched GO categories for the named clusters.
See Figure 37 for experimental details. CC – Cellular Component, BP – Biological processes

KEGG pathway	Cluster	Genes
Biosynthesis of amino acids	Th1	Aldoa, Got1, Idh3b, Pgk1, Pkm, Tpi1
	Treg_Il10	Aldoa, Ass1, Cs, Eno1, Gapdh, Got2, Idh3b, Pgam1, Pgk1, Pkm, Taldo1, Tkt, Tpi1, Eno1b
Carbon metabolism	Treg_Il10	Acads, Adh5, Aldoa, Cat, Cs, Eno1, Esd, Gapdh, Got2, Gpi1, Idh3b, Mdh2, Mdh1, Pdha1, Pgam1, Pgk1, Pkm, Taldo1, Tkt, Tpi1, Eno1b, Pgls, Sdhb, Pdhb
	tTreg	Aldoa, Eno1, Gapdh, Gpi1, Mdh2, Pgk1, Pkm, Tkt, Tpi1, Eno1b, Pgls, Sdhb, Echs1
Glycolysis / Gluconeogenesis	Th1	Aldoa, Gpi1, Ldha, Pgk1, Pkm, Tpi1
	Th2	Aldoa, Gapdh, Gpi1, Ldha, Akr1a1
	Treg_Il10	Adh5, Aldoa, Eno1, Gapdh, Gpi1, Ldha, Pdha1, Pgam1, Pgk1, Pkm, Tpi1, Eno1b, Akr1a1, Pdhb
	tTreg	Aldoa, Eno1, Gapdh, Gpi1, Ldha, Pgk1, Pkm, Tpi1, Eno1b
Oxidative phosphorylation	Th1	Cox6b1, Atp5c1, Atp5pb, Cox5a, Cox6c, Atp6, Cox1, Cox2, Cox3, Cytb, Nd4l, Atp5l, Atp5e, Ndufa6, Atp5g2
	Th2	Cox6b1, Atp5j, Cox17, Cox5a, Cox5b, Cox7a2, Cox7c, Cox8a, Atp6, Cox1, Cox2, Cox3, Cytb, Nd4l, Uqcrq, Atp5g3, Atp5j2, Ndufa3, Uqcrh, Atp5e, Ndufa6, Ndufa13, Atp5g2, Atp5h
	Treg_Il10	Ndufb4c, Ndufb4b, Ndufb11, Cox6b1, Atp5a1, Atp5b, Atp5c1, Atp5pb, Atp5g1, Atp5j, Atp5k, Atp6v0e, Cox17, Cox4i1, Cox5a, Cox5b, Cox6a1, Cox6c, Cox7a2, Cox7c, Cox8a, Atp6, Cox1, Cox2, Cox3, Cytb, Nd4, Nd4l, Ndufa2, Ndufa4, Ndufs4, Ndufv1, Cox7a2l, Uqcrq, Uqcrc1, Ndufs8, Ndufs2, Atp5g3, Ndufb6, Atp5l, Ndufs6, Ndufa1, Atp5j2, Ndufs5, Atp5d, Ndufb5, Ndufa3, Cox7b, Atp6v1f, Uqcr10, Ndufb9, Atp6v1g1, Ndufc1, Ndufa12, Ndufa7, Cyc1, Ndufb3, Uqcrh, Uqcr11, Uqcrfs1, Ndufb7, Uqcrc2, Atp5e, Ndufa6, Ndufa13, Ndufb8, Uqcrb, Sdhb, Atp5g2, Ndufb4, Ndufc2, Ndufb2, Ndufa5, Ndufb10, Ndufs3, Ndufa8, Ndufa11, Atp5h, Ndufv2, Atp6v1d, Ndufs7, Ndufv3
	tTreg	Ndufb11, Cox6b1, Atp5c1, Atp5pb, Atp5j, Atp5k, Cox17, Cox5a, Cox5b, Cox6c, Cox7a2, Cox7c, Cox8a, Atp6, Cox1, Cox2, Cox3, Cytb, Nd1, Nd2, Nd3, Nd4, Nd4l, Cox7a2l, Uqcrq, Ndufs2, Atp5g3, Ndufb6, Atp5l, Ndufa1, Atp5j2, Atp5d, Ndufb5, Ndufa3, Cox7b, Uqcr10, Ndufb9, Atp6v1g1, Uqcrh, Uqcr11, Uqcrfs1, Atp5e, Ndufa6, Ndufa13, Ndufb8, Sdhb, Atp5g2, Ndufb10, Ndufa8, Atp5h, Atp6v1d
	naive0	Ndufb11,Cox6b1,Cox4i1,Cox6c,Cox7c,Atp6,Atp8,Cox1,Cox2,Cox3,Cytb,Nd1,Nd2,Nd3,Nd4,Nd4l,Ndufa2,Ndufa4,Atp5l,Atp5j2,Atp5d,Ndufa3,Uqcrh,Atp5e,Ndufa6,Ndufa13,Uqcrb,Atp5h
	naive1	Atp6, Atp8, Cox1, Cox2, Cox3, Cytb, Nd4l
Proteasome	Treg_Il10	Psmb9, Psmb8, Psma2, Psma3, Psmb1, Psmb10, Psmb4, Psmb5, Psmb6, Psmb7, Psmc2, Psmc3, Psmc5, Psmd4, Psme1, Psme2, Sem1, Psmc4, Psmd13, Psma1, Psma4, Psma5, Psma6, Psma7, Psmb2, Psmb3, Adrm1, Psmd8, Pomp, Psmd11
T cell receptor signaling pathway	Th1	Cd3d, Cd4, Cdc42 ,Lat, Lck, Lcp2, Grap2, Nfkbia, Pdcd1, Pik3r1, Cblb
	Th17	Cd28, Cd4, Itk, Grap2, Pik3r1, Icos
	naive0	Cd3d, Cd3e, Cd3g, Cd4, Jun, Lat, Cblb, Pak2
Thermogenesis	Th1	Cox6b1, Actb, Actg1, Atp5c1, Atp5pb, Cox5a, Cox6c, Atp6, Cox1, Cox2, Cox3, Cytb, Nd4l, Atp5l, Atp5e, Ndufa6, Atp5g2
	Th2	Cox6b1, Actg1, Atp5j, Cox17, Cox5a, Cox5b, Cox7a2, Cox7c, Cox8a, Atp6, Cox1, Cox2, Cox3, Cytb, Nd4l, Uqcrq, Atp5g3, Atp5j2, Ndufa3, Cox14, Uqcrh, Atp5e, Ndufa6, Ndufa13, Atp5g2, Atp5h
	Treg_Il10	Ndufb4c, Ndufb4b, Ndufb11, Cox6b1, Actb, Actg1, Atp5a1, Atp5b, Atp5c1, Atp5pb, Atp5g1, Atp5j, Atp5k, Cox17, Cox4i1, Cox5a, Cox5b, Cox6a1, Cox6c, Cox7a2, Cox7c, Cox8a, Gnas, Atp6, Cox1, Cox2, Cox3, Cytb, Nd4, Nd4l, Ndufa2, Ndufa4, Ndufs4, Ndufv1, Rheb, Cox7a2l, Uqcrq, Uqcrc1, Ndufs8, Ndufs2, Atp5g3, Ndufb6, Atp5l, Ndufs6, Coa3, Ndufa1, Smarce1, Atp5j2, Ndufs5, Atp5d, Ndufb5, Ndufa3, Cox7b, Uqcr10, Ndufb9, Cox16, Cox20, Ndufc1, Cox14, Ndufa12, Ndufa7, Cyc1, Ndufb3, Uqcrh, Uqcr11, Uqcrfs1, Ndufb7, Uqcrc2, Atp5e, Ndufa6, Ndufa13, Ndufb8, Uqcrb, Sdhb, Atp5g2, Ndufb4, Ndufc2, Ndufb2, Ndufa5, Ndufb10, Ndufs3, Ndufa8, Ndufa11, Atp5h, Ndufv2, Ndufs7, Coa5, Ndufv3
	tTreg	Ndufb11, Cox6b1, Actb, Actg1, Atp5c1, Atp5pb, Atp5j, Atp5k, Cox17, Cox5a, Cox5b, Cox6c, Cox7a2, Cox7c, Cox8a, Atp6, Cox1, Cox2, Cox3, Cytb, Nd1, Nd2, Nd3, Nd4, Nd4l, Cox7a2l, Uqcrq, Ndufs2, Atp5g3, Ndufb6, Atp5l, Ndufa1, Atp5j2, Atp5d, Ndufb5, Ndufa3, Cox7b, Uqcr10, Ndufb9, Uqcrh, Uqcr11, Uqcrfs1, Atp5e, Ndufa6, Ndufa13, Ndufb8, Sdhb, Atp5g2, Ndufb10, Ndufa8, Atp5h
	naive0	Ndufb11, Cox6b1, Actg1, Cox4i1, Cox6c, Cox7c, Atp6, Atp8, Cox1, Cox2, Cox3, Cytb, Nd1, Nd2, Nd3, Nd4, Nd4l, Ndufa2, Ndufa4, Atp5l, Atp5j2, Atp5d, Ndufa3, Uqcrh, Atp5e, Ndufa6, Ndufa13, Uqcrb, Atp5h
	naive1	Atp6, Atp8, Cox1, Cox2, Cox3, Cytb, Nd4l

Table 8. Upregulated genes part of an enriched KEGG pathway for the named clusters.
See Figure 37 for experimental details.

References

10x Genomics (2020). Single cell gene expression datasets, *https://support.10xgenomics.com/single-cell-gene-expression/datasets*.
Allen, J.E., and Wynn, T.A. (2011). Evolution of Th2 immunity: a rapid repair response to tissue destructive pathogens. PLoS Pathog *7*, e1002003.
Alvarez, F., Istomine, R., Shourian, M., Pavey, N., Al-Aubodah, T.A., Qureshi, S., Fritz, J.H., and Piccirillo, C.A. (2019). The alarmins IL-1 and IL-33 differentially regulate the functional specialisation of Foxp3(+) regulatory T cells during mucosal inflammation. Mucosal Immunol *12*, 746-760.
Anderson, M.S., Venanzi, E.S., Klein, L., Chen, Z., Berzins, S.P., Turley, S.J., von Boehmer, H., Bronson, R., Dierich, A., Benoist, C., et al. (2002). Projection of an immunological self shadow within the thymus by the aire protein. Science *298*, 1395-1401.
Andrews, T.S., and Hemberg, M. (2018). Identifying cell populations with scRNASeq. Mol Aspects Med *59*, 114-122.
Andris, F., and Leo, O. (2015). AMPK in lymphocyte metabolism and function. International Reviews of Immunology *34*, 67-81.
Bakula, D., Mueller, A.J., and Proikas-Cezanne, T. (2018). WIPI beta-propellers function as scaffolds for STK11/LKB1-AMPK and AMPK-related kinase signaling in autophagy. Autophagy *14*, 1082-1083.
Bamias, G., Martin, C., Mishina, M., Ross, W.G., Rivera-Nieves, J., Marini, M., and Cominelli, F. (2005). Proinflammatory effects of TH2 cytokines in a murine model of chronic small intestinal inflammation. Gastroenterology *128*, 654-666.
Bao, K., and Reinhardt, R.L. (2015). The differential expression of IL-4 and IL-13 and its impact on type-2 immunity. Cytokine *75*, 25-37.
Basler, M., Kirk, C.J., and Groettrup, M. (2013). The immunoproteasome in antigen processing and other immunological functions. Curr Opin Immunol *25*, 74-80.
Basler, M., Moebius, J., Elenich, L., Groettrup, M., and Monaco, J.J. (2006). An altered T cell repertoire in MECL-1-deficient mice. J Immunol *176*, 6665-6672.
Baumgart, D.C., and Sandborn, W.J. (2007). Inflammatory bowel disease: clinical aspects and established and evolving therapies. Lancet *369*, 1641-1657.
Berod, L., Friedrich, C., Nandan, A., Freitag, J., Hagemann, S., Harmrolfs, K., Sandouk, A., Hesse, C., Castro, C.N., Bahres, H., et al. (2014). De novo fatty acid synthesis controls the fate between regulatory T and T helper 17 cells. Nature Medicine *20*, 1327-1333.
Blagih, J., Coulombe, F., Vincent, E.E., Dupuy, F., Galicia-Vazquez, G., Yurchenko, E., Raissi, T.C., van der Windt, G.J.W., Viollet, B., Pearce, E.L., et al. (2015). The Energy Sensor AMPK Regulates T Cell Metabolic Adaptation and Effector Responses In Vivo. Immunity *42*, 41-54.
Buck, M.D., O'Sullivan, D., and Pearce, E.L. (2015). T cell metabolism drives immunity. The Journal of Experimental Medicine *212*, 1345.
Burger, E., Araujo, A., Lopez-Yglesias, A., Rajala, M.W., Geng, L., Levine, B., Hooper, L.V., Burstein, E., and Yarovinsky, F. (2018). Loss of Paneth Cell Autophagy Causes Acute Susceptibility to Toxoplasma gondii-Mediated Inflammation. Cell Host Microbe *23*, 177-190 e174.
Butler, A., Hoffman, P., Smibert, P., Papalexi, E., and Satija, R. (2018). Integrating single-cell transcriptomic data across different conditions, technologies, and species. Nat Biotechnol *36*, 411-420.
Cadwell, K., Liu, J.Y., Brown, S.L., Miyoshi, H., Loh, J., Lennerz, J.K., Kishi, C., Kc, W., Carrero, J.A., Hunt, S., et al. (2008). A key role for autophagy and the autophagy gene Atg16l1 in mouse and human intestinal Paneth cells. Nature *456*, 259-263.

Cadwell, K., Patel, K.K., Maloney, N.S., Liu, T.C., Ng, A.C., Storer, C.E., Head, R.D., Xavier, R., Stappenbeck, T.S., and Virgin, H.W. (2010). Virus-plus-susceptibility gene interaction determines Crohn's disease gene Atg16L1 phenotypes in intestine. Cell *141*, 1135-1145.
Campbell, D.J. (2015). Control of Regulatory T Cell Migration, Function, and Homeostasis. The Journal of Immunology *195*, 2507-2513.
Chaudhry, A., Rudra, D., Treuting, P., Samstein, R.M., Liang, Y., Kas, A., and Rudensky, A.Y. (2009). CD4+ regulatory T cells control TH17 responses in a Stat3-dependent manner. Science *326*, 986-991.
Chen, L., and Flies, D.B. (2013). Molecular mechanisms of T cell co-stimulation and co-inhibition. Nat Rev Immunol *13*, 227-242.
Chen, W., Norbury, C.C., Cho, Y., Yewdell, J.W., and Bennink, J.R. (2001). Immunoproteasomes shape immunodominance hierarchies of antiviral CD8(+) T cells at the levels of T cell repertoire and presentation of viral antigens. J Exp Med *193*, 1319-1326.
Ciofani, M., Madar, A., Galan, C., Sellars, M., Mace, K., Pauli, F., Agarwal, A., Huang, W., Parkhurst, C.N., Muratet, M., et al. (2012). A validated regulatory network for Th17 cell specification. Cell *151*, 289-303.
Cipolletta, D., Feuerer, M., Li, A., Kamei, N., Lee, J., Shoelson, S.E., Benoist, C., and Mathis, D. (2012). PPAR-gamma is a major driver of the accumulation and phenotype of adipose tissue Treg cells. Nature *486*, 549-553.
Clarke, A.J., and Simon, A.K. (2019). Autophagy in the renewal, differentiation and homeostasis of immune cells. Nat Rev Immunol *19*, 170-183.
Cooney, R., Baker, J., Brain, O., Danis, B., Pichulik, T., Allan, P., Ferguson, D.J., Campbell, B.J., Jewell, D., and Simmons, A. (2010). NOD2 stimulation induces autophagy in dendritic cells influencing bacterial handling and antigen presentation. Nat Med *16*, 90-97.
Crotty, S. (2011). Follicular helper CD4 T cells (TFH). Annu Rev Immunol *29*, 621-663.
Cuervo, A.M., and Wong, E. (2014). Chaperone-mediated autophagy: roles in disease and aging. Cell Res *24*, 92-104.
Curotto de Lafaille, M.A., Kutchukhidze, N., Shen, S., Ding, Y., Yee, H., and Lafaille, J.J. (2008). Adaptive Foxp3+ regulatory T cell-dependent and -independent control of allergic inflammation. Immunity *29*, 114-126.
Dang, E.V., Barbi, J., Yang, H.Y., Jinasena, D., Yu, H., Zheng, Y., Bordman, Z., Fu, J., Kim, Y., Yen, H.R., et al. (2011). Control of T(H)17/T(reg) balance by hypoxia-inducible factor 1. Cell *146*, 772-784.
de Lange, K.M., and Barrett, J.C. (2015). Understanding inflammatory bowel disease via immunogenetics. J Autoimmun *64*, 91-100.
DeFranco, A.L., Locksley, R.M., and Robertson, M. (2007). Immunity : the immune response in infectious and inflammatory disease. (London: New Science Press in association with Oxford University Press and Sinauer Associates).
Delgoffe, G.M., Pollizzi, K.N., Waickman, A.T., Heikamp, E., Meyers, D.J., Horton, M.R., Xiao, B., Worley, P.F., and Powell, J.D. (2011). The kinase mTOR regulates the differentiation of helper T cells through the selective activation of signaling by mTORC1 and mTORC2. Nat Immunol *12*, 295-303.
Derbinski, J., Schulte, A., Kyewski, B., and Klein, L. (2001). Promiscuous gene expression in medullary thymic epithelial cells mirrors the peripheral self. Nat Immunol *2*, 1032-1039.
Desdin-Mico, G., Soto-Heredero, G., Aranda, J.F., Oller, J., Carrasco, E., Gabande-Rodriguez, E., Blanco, E.M., Alfranca, A., Cusso, L., Desco, M., et al. (2020). T cells with dysfunctional mitochondria induce multimorbidity and premature senescence. Science *368*, 1371-1376.

Dikic, I. (2017). Proteasomal and Autophagic Degradation Systems. Annu Rev Biochem *86*, 193-224.
Dikic, I., and Elazar, Z. (2018). Mechanism and medical implications of mammalian autophagy. Nat Rev Mol Cell Biol *19*, 349-364.
Ding, W.X., Ni, H.M., Gao, W., Yoshimori, T., Stolz, D.B., Ron, D., and Yin, X.M. (2007). Linking of autophagy to ubiquitin-proteasome system is important for the regulation of endoplasmic reticulum stress and cell viability. Am J Pathol *171*, 513-524.
Duerr, R.H., Taylor, K.D., Brant, S.R., Rioux, J.D., Silverberg, M.S., Daly, M.J., Steinhart, A.H., Abraham, C., Regueiro, M., Griffiths, A., et al. (2006). A genome-wide association study identifies IL23R as an inflammatory bowel disease gene. Science *314*, 1461-1463.
Dumitru, C., Kabat, A.M., and Maloy, K.J. (2018). Metabolic Adaptations of CD4(+) T Cells in Inflammatory Disease. Front Immunol *9*, 540.
DuPage, M., and Bluestone, J.A. (2016). Harnessing the plasticity of CD4(+) T cells to treat immune-mediated disease. Nat Rev Immunol *16*, 149-163.
Fahlen, L., Read, S., Gorelik, L., Hurst, S.D., Coffman, R.L., Flavell, R.A., and Powrie, F. (2005). T cells that cannot respond to TGF-beta escape control by CD4(+)CD25(+) regulatory T cells. J Exp Med *201*, 737-746.
Ferrington, D.A., and Gregerson, D.S. (2012). Immunoproteasomes: structure, function, and antigen presentation. Prog Mol Biol Transl Sci *109*, 75-112.
Festing, M.F.W., Overend, P., Borja, M.C., and Berdoy, M. (2016). The design of animal experiments : reducing the use of animals in research through better experimental design. (Los Angeles: SAGE).
Fichtner-Feigl, S., Fuss, I.J., Young, C.A., Watanabe, T., Geissler, E.K., Schlitt, H.J., Kitani, A., and Strober, W. (2007). Induction of IL-13 triggers TGF-beta1-dependent tissue fibrosis in chronic 2,4,6-trinitrobenzene sulfonic acid colitis. J Immunol *178*, 5859-5870.
Finlay, D., and Cantrell, D.A. (2011). Metabolism, migration and memory in cytotoxic T cells. Nat Rev Immunol *11*, 109-117.
Finley, D. (2009). Recognition and processing of ubiquitin-protein conjugates by the proteasome. Annu Rev Biochem *78*, 477-513.
Finnish-German, A.C. (1997). An autoimmune disease, APECED, caused by mutations in a novel gene featuring two PHD-type zinc-finger domains. Nat Genet *17*, 399-403.
Finotto, S., Neurath, M.F., Glickman, J.N., Qin, S., Lehr, H.A., Green, F.H., Ackerman, K., Haley, K., Galle, P.R., Szabo, S.J., et al. (2002). Development of spontaneous airway changes consistent with human asthma in mice lacking T-bet. Science *295*, 336-338.
Fracchia, K.M., and Walsh, C.M. (2015). Metabolic Mysteries of the Inflammatory Response: T Cell Polarization and Plasticity. International Reviews of Immunology *34*, 3-18.
Frauwirth, K.A., Riley, J.L., Harris, M.H., Parry, R.V., Rathmell, J.C., Plas, D.R., Elstrom, R.L., June, C.H., and Thompson, C.B. (2002). The CD28 signaling pathway regulates glucose metabolism. Immunity *16*, 769-777.
Freytag, S., Tian, L., Lonnstedt, I., Ng, M., and Bahlo, M. (2018). Comparison of clustering tools in R for medium-sized 10x Genomics single-cell RNA-sequencing data. F1000Res *7*, 1297.
Fullgrabe, J., Klionsky, D.J., and Joseph, B. (2014). The return of the nucleus: transcriptional and epigenetic control of autophagy. Nat Rev Mol Cell Biol *15*, 65-74.
Gaffen, S.L., Jain, R., Garg, A.V., and Cua, D.J. (2014). The IL-23-IL-17 immune axis: from mechanisms to therapeutic testing. Nat Rev Immunol *14*, 585-600.
Gaublomme, J.T., Yosef, N., Lee, Y., Gertner, R.S., Yang, L.V., Wu, C., Pandolfi, P.P., Mak, T., Satija, R., Shalek, A.K., et al. (2015). Single-Cell Genomics Unveils Critical Regulators of Th17 Cell Pathogenicity. Cell *163*, 1400-1412.

Gause, W.C., and Artis, D. (2016). The Th2 type immune response in health and disease : from host defense and allergy to metabolic homeostasis and beyond. (Berlin: Springer).
Gause, W.C., Wynn, T.A., and Allen, J.E. (2013). Type 2 immunity and wound healing: evolutionary refinement of adaptive immunity by helminths. Nat Rev Immunol *13*, 607-614.
Gehring, J., Hwee Park, J., Chen, S., Thomson, M., and Pachter, L. (2020). Highly multiplexed single-cell RNA-seq by DNA oligonucleotide tagging of cellular proteins. Nat Biotechnol *38*, 35-38.
Geng, J., and Klionsky, D.J. (2008). The Atg8 and Atg12 ubiquitin-like conjugation systems in macroautophagy. 'Protein modifications: beyond the usual suspects' review series. EMBO Rep *9*, 859-864.
Geremia, A., Biancheri, P., Allan, P., Corazza, G.R., and Di Sabatino, A. (2014). Innate and adaptive immunity in inflammatory bowel disease. Autoimmun Rev *13*, 3-10.
Gerriets, V.A., and Rathmell, J.C. (2012). Metabolic pathways in T cell fate and function. Trends Immunol *33*, 168-173.
Ghoreschi, K., Laurence, A., Yang, X.P., Tato, C.M., McGeachy, M.J., Konkel, J.E., Ramos, H.L., Wei, L., Davidson, T.S., Bouladoux, N., et al. (2010). Generation of pathogenic T(H)17 cells in the absence of TGF-beta signalling. Nature *467*, 967-971.
Glocker, E., Kotlarz, D., Boztug, K., Gertz, E., Schaffer, A., Koletzko, S., Shah, N., Segal, A., Snapper, S., Grimbacher, B., et al. (2009). Early-onset inflammatory bowel disease caused by loss-of-function mutations in the IL10-receptor genes. Inflamm Bowel Dis *15*, S56-S56.
Goldman, S.J., Taylor, R., Zhang, Y., and Jin, S. (2010). Autophagy and the degradation of mitochondria. Mitochondrion *10*, 309-315.
Gonzalez, A., and Hall, M.N. (2017). Nutrient sensing and TOR signaling in yeast and mammals. EMBO J *36*, 397-408.
Hafemeister, C., and Satija, R. (2019). Normalization and variance stabilization of single-cell RNA-seq data using regularized negative binomial regression. Genome Biol *20*, 296.
Hampe, J., Franke, A., Rosenstiel, P., Till, A., Teuber, M., Huse, K., Albrecht, M., Mayr, G., De La Vega, F.M., Briggs, J., et al. (2007). A genome-wide association scan of nonsynonymous SNPs identifies a susceptibility variant for Crohn disease in ATG16L1. Nat Genet *39*, 207-211.
Han, J.M., Wu, D., Denroche, H.C., Yao, Y., Verchere, C.B., and Levings, M.K. (2015). IL-33 Reverses an Obesity-Induced Deficit in Visceral Adipose Tissue ST2+ T Regulatory Cells and Ameliorates Adipose Tissue Inflammation and Insulin Resistance. J Immunol *194*, 4777-4783.
Han, S.J., Glatman Zaretsky, A., Andrade-Oliveira, V., Collins, N., Dzutsev, A., Shaik, J., Morais da Fonseca, D., Harrison, O.J., Tamoutounour, S., Byrd, A.L., et al. (2017). White Adipose Tissue Is a Reservoir for Memory T Cells and Promotes Protective Memory Responses to Infection. Immunity *47*, 1154-1168 e1156.
Hashimoto, K., Kouno, T., Ikawa, T., Hayatsu, N., Miyajima, Y., Yabukami, H., Terooatea, T., Sasaki, T., Suzuki, T., Valentine, M., et al. (2019). Single-cell transcriptomics reveals expansion of cytotoxic CD4 T cells in supercentenarians. Proc Natl Acad Sci U S A *116*, 24242-24251.
Hegazy, A.N., Peine, M., Helmstetter, C., Panse, I., Frohlich, A., Bergthaler, A., Flatz, L., Pinschewer, D.D., Radbruch, A., and Lohning, M. (2010). Interferons direct Th2 cell reprogramming to generate a stable GATA-3(+)T-bet(+) cell subset with combined Th2 and Th1 cell functions. Immunity *32*, 116-128.
Hotamisligil, G.S. (2017). Inflammation, metaflammation and immunometabolic disorders. Nature *542*, 177-185.

Howie, D., Cobbold, S.P., Adams, E., Ten Bokum, A., Necula, A.S., Zhang, W., Huang, H., Roberts, D.J., Thomas, B., Hester, S.S., et al. (2017). Foxp3 drives oxidative phosphorylation and protection from lipotoxicity. JCI Insight *2*.
Hu, W., and Pasare, C. (2013). Location, location, location: tissue-specific regulation of immune responses. J Leukoc Biol *94*, 409-421.
Hue, S., Ahern, P., Buonocore, S., Kullberg, M.C., Cua, D.J., McKenzie, B.S., Powrie, F., and Maloy, K.J. (2006). Interleukin-23 drives innate and T cell-mediated intestinal inflammation. J Exp Med *203*, 2473-2483.
Human Cell Atlas (2017). About Human Cell Atlas, *https://www.humancellatlas.org/*.
Hwang, S., Maloney, N.S., Bruinsma, M.W., Goel, G., Duan, E., Zhang, L., Shrestha, B., Diamond, M.S., Dani, A., Sosnovtsev, S.V., et al. (2012). Nondegradative role of Atg5-Atg12/ Atg16L1 autophagy protein complex in antiviral activity of interferon gamma. Cell Host Microbe *11*, 397-409.
Ishigame, H., Kakuta, S., Nagai, T., Kadoki, M., Nambu, A., Komiyama, Y., Fujikado, N., Tanahashi, Y., Akitsu, A., Kotaki, H., et al. (2009). Differential roles of interleukin-17A and -17F in host defense against mucoepithelial bacterial infection and allergic responses. Immunity *30*, 108-119.
Ivanov, II, Frutos Rde, L., Manel, N., Yoshinaga, K., Rifkin, D.B., Sartor, R.B., Finlay, B.B., and Littman, D.R. (2008). Specific microbiota direct the differentiation of IL-17-producing T-helper cells in the mucosa of the small intestine. Cell Host Microbe *4*, 337-349.
Izcue, A., Coombes, J.L., and Powrie, F. (2009). Regulatory Lymphocytes and Intestinal Inflammation. Annual Review of Immunology *27*, 313-338.
Jacobs, S.R., Herman, C.E., MacIver, N.J., Wofford, J.A., Wieman, H.L., Hammen, J.J., and Rathmell, J.C. (2008). Glucose Uptake Is Limiting in T Cell Activation and Requires CD28-Mediated Akt-Dependent and Independent Pathways. Journal of immunology (Baltimore, Md. : 1950) *180*, 4476-4486.
Jain, A.K. (2010). Data clustering: 50 years beyond K-means. Pattern Recogn Lett *31*, 651-666.
Jairath, V., and Feagan, B.G. (2020). Global burden of inflammatory bowel disease. Lancet Gastroenterol Hepatol *5*, 2-3.
Jia, W., and He, Y.W. (2011). Temporal regulation of intracellular organelle homeostasis in T lymphocytes by autophagy. J Immunol *186*, 5313-5322.
Jia, W., Pua, H.H., Li, Q.J., and He, Y.W. (2011). Autophagy regulates endoplasmic reticulum homeostasis and calcium mobilization in T lymphocytes. J Immunol *186*, 1564-1574.
Jiang, P., and Mizushima, N. (2014). Autophagy and human diseases. Cell Res *24*, 69-79.
Josefowicz, S.Z., Niec, R.E., Kim, H.Y., Treuting, P., Chinen, T., Zheng, Y., Umetsu, D.T., and Rudensky, A.Y. (2012). Extrathymically generated regulatory T cells control mucosal TH2 inflammation. Nature *482*, 395-399.
Jostins, L., Ripke, S., Weersma, R.K., Duerr, R.H., McGovern, D.P., Hui, K.Y., Lee, J.C., Philip Schumm, L., Sharma, Y., and Anderson, C.A. (2012). Host-microbe interactions have shaped the genetic architecture of inflammatory bowel disease. Nature *491*.
Kabat, A.M., Harrison, O.J., Riffelmacher, T., Moghaddam, A.E., Pearson, C.F., Laing, A., Abeler-Dorner, L., Forman, S.P., Grencis, R.K., Sattentau, Q., et al. (2016a). The autophagy gene Atg16l1 differentially regulates Treg and TH2 cells to control intestinal inflammation. Elife *5*, e12444.
Kabat, A.M., Pott, J., and Maloy, K.J. (2016b). The Mucosal Immune System and Its Regulation by Autophagy. Front Immunol *7*, 240.

Kalim, K.W., Basler, M., Kirk, C.J., and Groettrup, M. (2012). Immunoproteasome subunit LMP7 deficiency and inhibition suppresses Th1 and Th17 but enhances regulatory T cell differentiation. J Immunol *189*, 4182-4193.
Kano, S., Sato, K., Morishita, Y., Vollstedt, S., Kim, S., Bishop, K., Honda, K., Kubo, M., and Taniguchi, T. (2008). The contribution of transcription factor IRF1 to the interferon-gamma-interleukin 12 signaling axis and TH1 versus TH-17 differentiation of CD4+ T cells. Nat Immunol *9*, 34-41.
Kaplan, M.H., Hufford, M.M., and Olson, M.R. (2015). The development and in vivo function of T helper 9 cells. Nat Rev Immunol *15*, 295-307.
Kaser, A., Zeissig, S., and Blumberg, R.S. (2010). Genes and Environment: How Will Our Concepts on the Pathophysiology of IBD Develop in the Future? Digest Dis *28*, 395-405.
Kelly-Welch, A.E., Hanson, E.M., Boothby, M.R., and Keegan, A.D. (2003). Interleukin-4 and interleukin-13 signaling connections maps. Science *300*, 1527-1528.
Kirkin, V., and Rogov, V.V. (2019). A Diversity of Selective Autophagy Receptors Determines the Specificity of the Autophagy Pathway. Mol Cell *76*, 268-285.
Kitajima, M., Lee, H.C., Nakayama, T., and Ziegler, S.F. (2011). TSLP enhances the function of helper type 2 cells. Eur J Immunol *41*, 1862-1871.
Koch, M.A., Tucker-Heard, G., Perdue, N.R., Killebrew, J.R., Urdahl, K.B., and Campbell, D.J. (2009). The transcription factor T-bet controls regulatory T cell homeostasis and function during type 1 inflammation. Nat Immunol *10*, 595-602.
Koch, U., and Radtke, F. (2011). Mechanisms of T cell development and transformation. Annu Rev Cell Dev Biol *27*, 539-562.
Kolodsick, J.E., Toews, G.B., Jakubzick, C., Hogaboam, C., Moore, T.A., McKenzie, A., Wilke, C.A., Chrisman, C.J., and Moore, B.B. (2004). Protection from fluorescein isothiocyanate-induced fibrosis in IL-13-deficient, but not IL-4-deficient, mice results from impaired collagen synthesis by fibroblasts. J Immunol *172*, 4068-4076.
Korn, T., Bettelli, E., Oukka, M., and Kuchroo, V.K. (2009). IL-17 and Th17 Cells. Annu Rev Immunol *27*, 485-517.
Korolchuk, V.I., Mansilla, A., Menzies, F.M., and Rubinsztein, D.C. (2009). Autophagy inhibition compromises degradation of ubiquitin-proteasome pathway substrates. Mol Cell *33*, 517-527.
Korolchuk, V.I., Menzies, F.M., and Rubinsztein, D.C. (2010). Mechanisms of cross-talk between the ubiquitin-proteasome and autophagy-lysosome systems. FEBS Lett *584*, 1393-1398.
Kovacs, J.R., Li, C., Yang, Q., Li, G., Garcia, I.G., Ju, S., Roodman, D.G., Windle, J.J., Zhang, X., and Lu, B. (2012). Autophagy promotes T-cell survival through degradation of proteins of the cell death machinery. Cell Death Differ *19*, 144-152.
Kozera, B., and Rapacz, M. (2013). Reference genes in real-time PCR. J Appl Genet *54*, 391-406.
Kuma, A., Hatano, M., Matsui, M., Yamamoto, A., Nakaya, H., Yoshimori, T., Ohsumi, Y., Tokuhisa, T., and Mizushima, N. (2004). The role of autophagy during the early neonatal starvation period. Nature *432*, 1032-1036.
Kwak, M.K., Wakabayashi, N., Greenlaw, J.L., Yamamoto, M., and Kensler, T.W. (2003). Antioxidants enhance mammalian proteasome expression through the Keap1-Nrf2 signaling pathway. Mol Cell Biol *23*, 8786-8794.
Lassen, K.G., Kuballa, P., Conway, K.L., Patel, K.K., Becker, C.E., Peloquin, J.M., Villablanca, E.J., Norman, J.M., Liu, T.C., Heath, R.J., et al. (2014). Atg16L1 T300A variant decreases selective autophagy resulting in altered cytokine signaling and decreased antibacterial defense. Proc Natl Acad Sci U S A *111*, 7741-7746.

Levine, B., Mizushima, N., and Virgin, H.W. (2011). Autophagy in immunity and inflammation. Nature *469*, 323-335.
Li, W.W., Li, J., and Bao, J.K. (2012). Microautophagy: lesser-known self-eating. Cell Mol Life Sci *69*, 1125-1136.
Lighvani, A.A., Frucht, D.M., Jankovic, D., Yamane, H., Aliberti, J., Hissong, B.D., Nguyen, B.V., Gadina, M., Sher, A., Paul, W.E., et al. (2001). T-bet is rapidly induced by interferon-gamma in lymphoid and myeloid cells. Proc Natl Acad Sci U S A *98*, 15137-15142.
Linterman, M.A., Rigby, R.J., Wong, R.K., Yu, D., Brink, R., Cannons, J.L., Schwartzberg, P.L., Cook, M.C., Walters, G.D., and Vinuesa, C.G. (2009). Follicular helper T cells are required for systemic autoimmunity. J Exp Med *206*, 561-576.
Liu, J.Z., van Sommeren, S., Huang, H.L., Ng, S.C., Alberts, R., Takahashi, A., Ripke, S., Lee, J.C., Jostins, L., Shah, T., et al. (2015a). Association analyses identify 38 susceptibility loci for inflammatory bowel disease and highlight shared genetic risk across populations. Nature Genetics *47*, 979-+.
Liu, T.W., Heden, T.D., Matthew Morris, E., Fritsche, K.L., Vieira-Potter, V.J., and Thyfault, J.P. (2015b). High-Fat Diet Alters Serum Fatty Acid Profiles in Obesity Prone Rats: Implications for In Vitro Studies. Lipids *50*, 997-1008.
Lloyd, C.M., and Snelgrove, R.J. (2018). Type 2 immunity: Expanding our view. Sci Immunol *3*.
Lochner, M., Berod, L., and Sparwasser, T. (2015). Fatty acid metabolism in the regulation of T cell function. Trends Immunol *36*, 81-91.
Lui, P.P., Cho, I., and Ali, N. (2020). Tissue regulatory T cells. Immunology *161*, 4-17.
Lundh, M., Bugliani, M., Dahlby, T., Chou, D.H., Wagner, B., Ghiasi, S.M., De Tata, V., Chen, Z., Lund, M.N., Davies, M.J., et al. (2017). The immunoproteasome is induced by cytokines and regulates apoptosis in human islets. J Endocrinol *233*, 369-379.
Luo, W.J., and Brouwer, C. (2013). Pathview: an R/Bioconductor package for pathway-based data integration and visualization. Bioinformatics *29*, 1830-1831.
MacIver, N.J., Michalek, R.D., and Rathmell, J.C. (2013). Metabolic regulation of T lymphocytes. Annu Rev Immunol *31*, 259-283.
Mahata, B., Zhang, X., Kolodziejczyk, A.A., Proserpio, V., Haim-Vilmovsky, L., Taylor, A.E., Hebenstreit, D., Dingler, F.A., Moignard, V., Gottgens, B., et al. (2014). Single-cell RNA sequencing reveals T helper cells synthesizing steroids de novo to contribute to immune homeostasis. Cell Rep *7*, 1130-1142.
Maloy, K.J., and Powrie, F. (2011). Intestinal homeostasis and its breakdown in inflammatory bowel disease. Nature *474*, 298-306.
Manasanch, E.E., and Orlowski, R.Z. (2017). Proteasome inhibitors in cancer therapy. Nat Rev Clin Oncol *14*, 417-433.
Marshall, R.S., Li, F., Gemperline, D.C., Book, A.J., and Vierstra, R.D. (2015). Autophagic Degradation of the 26S Proteasome Is Mediated by the Dual ATG8/Ubiquitin Receptor RPN10 in Arabidopsis. Mol Cell *58*, 1053-1066.
Matsuzawa-Ishimoto, Y., Shono, Y., Gomez, L.E., Hubbard-Lucey, V.M., Cammer, M., Neil, J., Dewan, M.Z., Lieberman, S.R., Lazrak, A., Marinis, J.M., et al. (2017). Autophagy protein ATG16L1 prevents necroptosis in the intestinal epithelium. Journal of Experimental Medicine *214*, 3687-3705.
McCarthy, D.J., Campbell, K.R., Lun, A.T., and Wills, Q.F. (2017). Scater: pre-processing, quality control, normalization and visualization of single-cell RNA-seq data in R. Bioinformatics *33*, 1179-1186.
McGeachy, M.J., Bak-Jensen, K.S., Chen, Y., Tato, C.M., Blumenschein, W., McClanahan, T., and Cua, D.J. (2007). TGF-beta and IL-6 drive the production of IL-17 and IL-10 by T cells and restrain T(H)-17 cell-mediated pathology. Nat Immunol *8*, 1390-1397.

McInnes, L., Healy, J., Saul, N., and Grossberger, L. (2018). UMAP: Uniform Manifold Approximation and Projection. Journal of Open Source Software *3*, 861.
Medzhitov, R. (2008). Origin and physiological roles of inflammation. Nature *454*, 428-435.
Mehrpour, M., Esclatine, A., Beau, I., and Codogno, P. (2010). Autophagy in health and disease. 1. Regulation and significance of autophagy: an overview. Am J Physiol Cell Physiol *298*, C776-785.
Mihaylova, M.M., and Shaw, R.J. (2011). The AMPK signalling pathway coordinates cell growth, autophagy and metabolism. Nat Cell Biol *13*, 1016-1023.
Miragaia, R.J., Gomes, T., Chomka, A., Jardine, L., Riedel, A., Hegazy, A.N., Whibley, N., Tucci, A., Chen, X., Lindeman, I., et al. (2019). Single-Cell Transcriptomics of Regulatory T Cells Reveals Trajectories of Tissue Adaptation. Immunity *50*, 493-504 e497.
Mitsiades, N., Mitsiades, C.S., Poulaki, V., Chauhan, D., Fanourakis, G., Gu, X., Bailey, C., Joseph, M., Libermann, T.A., Treon, S.P., et al. (2002). Molecular sequelae of proteasome inhibition in human multiple myeloma cells. Proc Natl Acad Sci U S A *99*, 14374-14379.
Mizushima, N., Noda, T., Yoshimori, T., Tanaka, Y., Ishii, T., George, M.D., Klionsky, D.J., Ohsumi, M., and Ohsumi, Y. (1998). A protein conjugation system essential for autophagy. Nature *395*, 395-398.
Mombaerts, P., Iacomini, J., Johnson, R.S., Herrup, K., Tonegawa, S., and Papaioannou, V.E. (1992). RAG-1-deficient mice have no mature B and T lymphocytes. Cell *68*, 869-877.
Mortensen, M., Watson, A.S., and Simon, A.K. (2011). Lack of autophagy in the hematopoietic system leads to loss of hematopoietic stem cell function and dysregulated myeloid proliferation. Autophagy *7*, 1069-1070.
Mosmann, T.R., Cherwinski, H., Bond, M.W., Giedlin, M.A., and Coffman, R.L. (1986). Two types of murine helper T cell clone. I. Definition according to profiles of lymphokine activities and secreted proteins. J Immunol *136*, 2348-2357.
Mould, K.J., Jackson, N.D., Henson, P.M., Seibold, M., and Janssen, W.J. (2019). Single cell RNA sequencing identifies unique inflammatory airspace macrophage subsets. JCI Insight *4*.
Muchamuel, T., Basler, M., Aujay, M.A., Suzuki, E., Kalim, K.W., Lauer, C., Sylvain, C., Ring, E.R., Shields, J., Jiang, J., et al. (2009). A selective inhibitor of the immunoproteasome subunit LMP7 blocks cytokine production and attenuates progression of experimental arthritis. Nat Med *15*, 781-787.
Mucida, D., Kutchukhidze, N., Erazo, A., Russo, M., Lafaille, J.J., and Curotto de Lafaille, M.A. (2005). Oral tolerance in the absence of naturally occurring Tregs. J Clin Invest *115*, 1923-1933.
Mullen, A.C., High, F.A., Hutchins, A.S., Lee, H.W., Villarino, A.V., Livingston, D.M., Kung, A.L., Cereb, N., Yao, T.P., Yang, S.Y., et al. (2001). Role of T-bet in commitment of TH1 cells before IL-12-dependent selection. Science *292*, 1907-1910.
Murata, S., Yashiroda, H., and Tanaka, K. (2009). Molecular mechanisms of proteasome assembly. Nat Rev Mol Cell Biol *10*, 104-115.
Murthy, A., Li, Y., Peng, I., Reichelt, M., Katakam, A.K., Noubade, R., Roose-Girma, M., DeVoss, J., Diehl, L., Graham, R.R., et al. (2014). A Crohn's disease variant in Atg16l1 enhances its degradation by caspase 3. Nature *506*, 456-462.
Nature Methods (2014). Method of the year 2013. Nat Methods *11*, 1.
Neill, D.R., Wong, S.H., Bellosi, A., Flynn, R.J., Daly, M., Langford, T.K., Bucks, C., Kane, C.M., Fallon, P.G., Pannell, R., et al. (2010). Nuocytes represent a new innate effector leukocyte that mediates type-2 immunity. Nature *464*, 1367-1370.
Nelson, D.L., Lehninger, A.L., and Cox, M.M. (2013). Lehninger Principles of biochemistry. (New York: W.H. Freeman).
Newton, R., Priyadharshini, B., and Turka, L.A. (2016). Immunometabolism of regulatory T cells. Nature Immunology *17*, 618-625.

Ng, T.H., Britton, G.J., Hill, E.V., Verhagen, J., Burton, B.R., and Wraith, D.C. (2013). Regulation of adaptive immunity; the role of interleukin-10. Front Immunol *4*, 129.
Nurieva, R.I., Chung, Y., Martinez, G.J., Yang, X.O., Tanaka, S., Matskevitch, T.D., Wang, Y.-H., and Dong, C. (2009). Bcl6 Mediates the Development of T Follicular Helper Cells. Science *325*, 1001.
Nussbaum, J.C., Van Dyken, S.J., von Moltke, J., Cheng, L.E., Mohapatra, A., Molofsky, A.B., Thornton, E.E., Krummel, M.F., Chawla, A., Liang, H.E., et al. (2013). Type 2 innate lymphoid cells control eosinophil homeostasis. Nature *502*, 245-248.
Odegaard, J.I., Ricardo-Gonzalez, R.R., Goforth, M.H., Morel, C.R., Subramanian, V., Mukundan, L., Red Eagle, A., Vats, D., Brombacher, F., Ferrante, A.W., et al. (2007). Macrophage-specific PPARgamma controls alternative activation and improves insulin resistance. Nature *447*, 1116-1120.
Pai, S.Y., Truitt, M.L., and Ho, I.C. (2004). GATA-3 deficiency abrogates the development and maintenance of T helper type 2 cells. Proc Natl Acad Sci U S A *101*, 1993-1998.
Panduro, M., Benoist, C., and Mathis, D. (2016). Tissue Tregs. Annu Rev Immunol *34*, 609-633.
Pao, W., Ooi, C.H., Birzele, F., Ruefli-Brasse, A., Cannarile, M.A., Reis, B., Scharf, S.H., Schubert, D.A., Hatje, K., Pelletier, N., et al. (2018). Tissue-Specific Immunoregulation: A Call for Better Understanding of the "Immunostat" in the Context of Cancer. Cancer Discov *8*, 395-402.
Papatheodorou, I., Moreno, P., Manning, J., Fuentes, A.M., George, N., Fexova, S., Fonseca, N.A., Fullgrabe, A., Green, M., Huang, N., et al. (2020). Expression Atlas update: from tissues to single cells. Nucleic Acids Res *48*, D77-D83.
Parekh, V.V., Wu, L., Boyd, K.L., Williams, J.A., Gaddy, J.A., Olivares-Villagomez, D., Cover, T.L., Zong, W.X., Zhang, J., and Van Kaer, L. (2013). Impaired autophagy, defective T cell homeostasis, and a wasting syndrome in mice with a T cell-specific deletion of Vps34. J Immunol *190*, 5086-5101.
Park, H., Li, Z., Yang, X.O., Chang, S.H., Nurieva, R., Wang, Y.H., Wang, Y., Hood, L., Zhu, Z., Tian, Q., et al. (2005). A distinct lineage of CD4 T cells regulates tissue inflammation by producing interleukin 17. Nat Immunol *6*, 1133-1141.
Passegue, E., Wagers, A.J., Giuriato, S., Anderson, W.C., and Weissman, I.L. (2005). Global analysis of proliferation and cell cycle gene expression in the regulation of hematopoietic stem and progenitor cell fates. J Exp Med *202*, 1599-1611.
Patel, N., Wu, W., Mishra, P.K., Chen, F., Millman, A., Csoka, B., Koscso, B., Eltzschig, H.K., Hasko, G., and Gause, W.C. (2014). A2B adenosine receptor induces protective antihelminth type 2 immune responses. Cell Host Microbe *15*, 339-350.
Paul, W.E., and Zhu, J. (2010). How are TH2-type immune responses initiated and amplified? Nature Reviews Immunology *10*, 225-235.
Peine, M., Rausch, S., Helmstetter, C., Frohlich, A., Hegazy, A.N., Kuhl, A.A., Grevelding, C.G., Hofer, T., Hartmann, S., and Lohning, M. (2013). Stable T-bet(+)GATA-3(+) Th1/Th2 hybrid cells arise in vivo, can develop directly from naive precursors, and limit immunopathologic inflammation. PLoS Biol *11*, e1001633.
Peng, M., Yin, N., Chhangawala, S., Xu, K., Leslie, C.S., and Li, M.O. (2016). Aerobic glycolysis promotes T helper 1 cell differentiation through an epigenetic mechanism. Science *354*, 481-484.
Peyrin-Biroulet, L. (2010). Anti-TNF therapy in inflammatory bowel diseases: a huge review. Minerva Gastroenterol Dietol *56*, 233-243.
Pfaffl (2004). Quantification Strategies in real-time PCR. In The Real-Time PCR Encyclopedia A–Z of Quantitative PCR. S.A. Bustin, ed., pp. pp. 87-120.

Pfeifer, A., and Hoffmann, L.S. (2015). Brown, beige, and white: the new color code of fat and its pharmacological implications. Annu Rev Pharmacol Toxicol *55*, 207-227.
Pott, J., and Hornef, M. (2012). Innate immune signalling at the intestinal epithelium in homeostasis and disease. EMBO Rep *13*, 684-698.
Pott, J., Kabat, A.M., and Maloy, K.J. (2018). Intestinal Epithelial Cell Autophagy Is Required to Protect against TNF-Induced Apoptosis during Chronic Colitis in Mice. Cell Host & Microbe *23*, 191-+.
Proserpio, V., Piccolo, A., Haim-Vilmovsky, L., Kar, G., Lonnberg, T., Svensson, V., Pramanik, J., Natarajan, K.N., Zhai, W., Zhang, X., et al. (2016). Single-cell analysis of CD4+ T-cell differentiation reveals three major cell states and progressive acceleration of proliferation. Genome Biol *17*, 103.
Pua, H.H., Dzhagalov, I., Chuck, M., Mizushima, N., and He, Y.W. (2007). A critical role for the autophagy gene Atg5 in T cell survival and proliferation. J Exp Med *204*, 25-31.
Pua, H.H., Guo, J., Komatsu, M., and He, Y.W. (2009). Autophagy is essential for mitochondrial clearance in mature T lymphocytes. J Immunol *182*, 4046-4055.
Pulendran, B., and Artis, D. (2012). New paradigms in type 2 immunity. Science *337*, 431-435.
Puleston, D.J., Zhang, H., Powell, T.J., Lipina, E., Sims, S., Panse, I., Watson, A.S., Cerundolo, V., Townsend, A.R., Klenerman, P., et al. (2014). Autophagy is a critical regulator of memory CD8(+) T cell formation. Elife *3*.
Qiao, L., and Zhang, J. (2009). Inhibition of lysosomal functions reduces proteasomal activity. Neurosci Lett *456*, 15-19.
Ranu, N., Villani, A.C., Hacohen, N., and Blainey, P.C. (2019). Targeting individual cells by barcode in pooled sequence libraries. Nucleic Acids Res *47*, e4.
Ray, J.P., Staron, M.M., Shyer, J.A., Ho, P.C., Marshall, H.D., Gray, S.M., Laidlaw, B.J., Araki, K., Ahmed, R., Kaech, S.M., et al. (2015). The Interleukin-2-mTORc1 Kinase Axis Defines the Signaling, Differentiation, and Metabolism of T Helper 1 and Follicular B Helper T Cells. Immunity *43*, 690-702.
Reynolds, L.A., Filbey, K.J., and Maizels, R.M. (2012). Immunity to the model intestinal helminth parasite Heligmosomoides polygyrus. Semin Immunopathol *34*, 829-846.
Rich, R.R. (2013). Clinical immunology : principles and practice. (London: Elsevier Saunders,), pp. 1 online resource (xxvii, 1295 pages).
Rieder, F., and Fiocchi, C. (2009). Intestinal fibrosis in IBD--a dynamic, multifactorial process. Nat Rev Gastroenterol Hepatol *6*, 228-235.
Riffelmacher, T., Richter, F.C., and Simon, A.K. (2018). Autophagy dictates metabolism and differentiation of inflammatory immune cells. Autophagy *14*, 199-206.
Riffelmacher T., Clarke A., Richter FC., Stranks A., Pandey S., Danielli S., Hublitz P., Yu Z., Johnson E., Schwerd T., et al. (2017). Autophagy-Dependent Generation of Free Fatty Acids Is Critical for Normal Neutrophil Differentiation. Immunity *47*, P466-480.
Rioux, J.D., Xavier, R.J., Taylor, K.D., Silverberg, M.S., Goyette, P., Huett, A., Green, T., Kuballa, P., Barmada, M.M., Datta, L.W., et al. (2007). Genome-wide association study identifies new susceptibility loci for Crohn disease and implicates autophagy in disease pathogenesis. Nat Genet *39*, 596-604.
Rousseau, A., and Bertolotti, A. (2018). Regulation of proteasome assembly and activity in health and disease. Nat Rev Mol Cell Biol *19*, 697-712.
Rubin, G.P., Hungin, A.P.S., Kelly, P.J., and Ling, J. (2000). Inflammatory bowel disease: epidemiology and management in an English general practice population. Aliment Pharm Ther *14*, 1553-1559.

Rubtsov, Y.P., Niec, R.E., Josefowicz, S., Li, L., Darce, J., Mathis, D., Benoist, C., and Rudensky, A.Y. (2010). Stability of the regulatory T cell lineage in vivo. Science *329*, 1667-1671.
Rubtsov, Y.P., Rasmussen, J.P., Chi, E.Y., Fontenot, J., Castelli, L., Ye, X., Treuting, P., Siewe, L., Roers, A., Henderson, W.R., Jr., et al. (2008). Regulatory T cell-derived interleukin-10 limits inflammation at environmental interfaces. Immunity *28*, 546-558.
Saitoh, T., Fujita, N., Jang, M.H., Uematsu, S., Yang, B.G., Satoh, T., Omori, H., Noda, T., Yamamoto, N., Komatsu, M., et al. (2008). Loss of the autophagy protein Atg16L1 enhances endotoxin-induced IL-1beta production. Nature *456*, 264-268.
Samstein, R.M., Josefowicz, S.Z., Arvey, A., Treuting, P.M., and Rudensky, A.Y. (2012). Extrathymic generation of regulatory T cells in placental mammals mitigates maternal-fetal conflict. Cell *150*, 29-38.
Sancak, Y., Bar-Peled, L., Zoncu, R., Markhard, A.L., Nada, S., and Sabatini, D.M. (2010). Ragulator-Rag complex targets mTORC1 to the lysosomal surface and is necessary for its activation by amino acids. Cell *141*, 290-303.
Santarelli, R., Gonnella, R., Di Giovenale, G., Cuomo, L., Capobianchi, A., Granato, M., Gentile, G., Faggioni, A., and Cirone, M. (2014). STAT3 activation by KSHV correlates with IL-10, IL-6 and IL-23 release and an autophagic block in dendritic cells. Sci Rep *4*, 4241.
Saraiva, M., and O'Garra, A. (2010). The regulation of IL-10 production by immune cells. Nat Rev Immunol *10*, 170-181.
Sasaki, C.Y., Chen, G., Munk, R., Eitan, E., Martindale, J., Longo, D.L., and Ghosh, P. (2016). p(70S6K1) in the TORC1 pathway is essential for the differentiation of Th17 Cells, but not Th1, Th2, or Treg cells in mice. European Journal of Immunology *46*, 212-222.
Satija, R. (2020a). Cell-Cycle Scoring and Regression, *https://satijalab.org/seurat/v3.2/cell_cycle_vignette.html*.
Satija, R. (2020b). Seurat - Guided Clustering Tutorial, *https://satijalab.org/seurat/v3.2/pbmc3k_tutorial.html*.
Savage, P.A., Klawon, D.E.J., and Miller, C.H. (2020). Regulatory T Cell Development. Annu Rev Immunol *38*, 421-453.
Saxton, R.A., and Sabatini, D.M. (2017). mTOR Signaling in Growth, Metabolism, and Disease. Cell *169*, 361-371.
Schatz, D.G., and Swanson, P.C. (2011). V(D)J recombination: mechanisms of initiation. Annu Rev Genet *45*, 167-202.
Schiering, C., Krausgruber, T., Chomka, A., Frohlich, A., Adelmann, K., Wohlfert, E.A., Pott, J., Griseri, T., Bollrath, J., Hegazy, A.N., et al. (2014). The alarmin IL-33 promotes regulatory T-cell function in the intestine. Nature *513*, 564-568.
Schindelin, J., Arganda-Carreras, I., Frise, E., Kaynig, V., Longair, M., Pietzsch, T., Preibisch, S., Rueden, C., Saalfeld, S., Schmid, B., et al. (2012). Fiji: an open-source platform for biological-image analysis. Nat Methods *9*, 676-682.
Schlie, K., Westerback, A., DeVorkin, L., Hughson, L.R., Brandon, J.M., MacPherson, S., Gadawski, I., Townsend, K.N., Poon, V.I., Elrick, M.A., et al. (2015). Survival of effector CD8+ T cells during influenza infection is dependent on autophagy. J Immunol *194*, 4277-4286.
Schluns, K.S., Kieper, W.C., Jameson, S.C., and Lefrancois, L. (2000). Interleukin-7 mediates the homeostasis of naive and memory CD8 T cells in vivo. Nat Immunol *1*, 426-432.
Schulz, E.G., Mariani, L., Radbruch, A., and Hofer, T. (2009). Sequential polarization and imprinting of type 1 T helper lymphocytes by interferon-gamma and interleukin-12. Immunity *30*, 673-683.

Shaid, S., Brandts, C.H., Serve, H., and Dikic, I. (2013). Ubiquitination and selective autophagy. Cell Death Differ *20*, 21-30.
Shi, L.Z., Wang, R., Huang, G., Vogel, P., Neale, G., Green, D.R., and Chi, H. (2011). HIF1alpha-dependent glycolytic pathway orchestrates a metabolic checkpoint for the differentiation of TH17 and Treg cells. J Exp Med *208*, 1367-1376.
Shimobayashi, M., and Hall, M.N. (2014). Making new contacts: the mTOR network in metabolism and signalling crosstalk. Nat Rev Mol Cell Biol *15*, 155-162.
Shinkai, Y., Koyasu, S., Nakayama, K., Murphy, K.M., Loh, D.Y., Reinherz, E.L., and Alt, F.W. (1993). Restoration of T cell development in RAG-2-deficient mice by functional TCR transgenes. Science *259*, 822-825.
Shull, M.M., Ormsby, I., Kier, A.B., Pawlowski, S., Diebold, R.J., Yin, M., Allen, R., Sidman, C., Proetzel, G., Calvin, D., et al. (1992). Targeted disruption of the mouse transforming growth factor-beta 1 gene results in multifocal inflammatory disease. Nature *359*, 693-699.
Simon, A.K., Obba, S., Zhang, H.L., and Riffelmacher, T. (2019). Autophagy in the Hematopoietic System. Blood *134*.
Smillie, C.S., Biton, M., Ordovas-Montanes, J., Sullivan, K.M., Burgin, G., Graham, D.B., Herbst, R.H., Rogel, N., Slyper, M., Waldman, J., et al. (2019). Intra- and Inter-cellular Rewiring of the Human Colon during Ulcerative Colitis. Cell *178*, 714-730 e722.
Smith-Garvin, J.E., Koretzky, G.A., and Jordan, M.S. (2009). T Cell Activation. Annual Review of Immunology *27*, 591-619.
Sonnenberg, G.F., Fouser, L.A., and Artis, D. (2011). Border patrol: regulation of immunity, inflammation and tissue homeostasis at barrier surfaces by IL-22. Nat Immunol *12*, 383-390.
Spencer, D.M., Veldman, G.M., Banerjee, S., Willis, J., and Levine, A.D. (2002). Distinct inflammatory mechanisms mediate early versus late colitis in mice. Gastroenterology *122*, 94-105.
Steed, H., Walsh, S., and Reynolds, N. (2010). Crohn's Disease Incidence in NHS Tayside. Scot Med J *55*, 22-25.
Stritesky, G.L., Jameson, S.C., and Hogquist, K.A. (2012). Selection of self-reactive T cells in the thymus. Annu Rev Immunol *30*, 95-114.
Stuart, T., Butler, A., Hoffman, P., Hafemeister, C., Papalexi, E., Mauck, W.M., 3rd, Hao, Y., Stoeckius, M., Smibert, P., and Satija, R. (2019). Comprehensive Integration of Single-Cell Data. Cell *177*, 1888-1902 e1821.
Suraweera, A., Munch, C., Hanssum, A., and Bertolotti, A. (2012). Failure of amino acid homeostasis causes cell death following proteasome inhibition. Mol Cell *48*, 242-253.
Szabo, S.J., Sullivan, B.M., Peng, S.L., and Glimcher, L.H. (2003). Molecular mechanisms regulating Th1 immune responses. Annu Rev Immunol *21*, 713-758.
Szurek, E., Cebula, A., Wojciech, L., Pietrzak, M., Rempala, G., Kisielow, P., and Ignatowicz, L. (2015). Differences in Expression Level of Helios and Neuropilin-1 Do Not Distinguish Thymus-Derived from Extrathymically-Induced CD4+Foxp3+ Regulatory T Cells. PLoS One *10*, e0141161.
Takeda, A., Hamano, S., Yamanaka, A., Hanada, T., Ishibashi, T., Mak, T.W., Yoshimura, A., and Yoshida, H. (2003). Cutting edge: role of IL-27/WSX-1 signaling for induction of T-bet through activation of STAT1 during initial Th1 commitment. J Immunol *170*, 4886-4890.
Tanaka, K., and Matsuda, N. (2014). Proteostasis and neurodegeneration: the roles of proteasomal degradation and autophagy. Biochim Biophys Acta *1843*, 197-204.
Tang, F., Barbacioru, C., Wang, Y., Nordman, E., Lee, C., Xu, N., Wang, X., Bodeau, J., Tuch, B.B., Siddiqui, A., et al. (2009). mRNA-Seq whole-transcriptome analysis of a single cell. Nat Methods *6*, 377-382.

Tao, X., Constant, S., Jorritsma, P., and Bottomly, K. (1997). Strength of TCR signal determines the costimulatory requirements for Th1 and Th2 CD4+ T cell differentiation. J Immunol *159*, 5956-5963.
Targan, S.R., Hanauer, S.B., van Deventer, S.J., Mayer, L., Present, D.H., Braakman, T., DeWoody, K.L., Schaible, T.F., and Rutgeerts, P.J. (1997). A short-term study of chimeric monoclonal antibody cA2 to tumor necrosis factor alpha for Crohn's disease. Crohn's Disease cA2 Study Group. N Engl J Med *337*, 1029-1035.
Thornton, A.M., Korty, P.E., Tran, D.Q., Wohlfert, E.A., Murray, P.E., Belkaid, Y., and Shevach, E.M. (2010). Expression of Helios, an Ikaros transcription factor family member, differentiates thymic-derived from peripherally induced Foxp3+ T regulatory cells. J Immunol *184*, 3433-3441.
Travassos, L.H., Carneiro, L.A., Ramjeet, M., Hussey, S., Kim, Y.G., Magalhaes, J.G., Yuan, L., Soares, F., Chea, E., Le Bourhis, L., et al. (2010). Nod1 and Nod2 direct autophagy by recruiting ATG16L1 to the plasma membrane at the site of bacterial entry. Nat Immunol *11*, 55-62.
Tripathi, D.N., Chowdhury, R., Trudel, L.J., Tee, A.R., Slack, R.S., Walker, C.L., and Wogan, G.N. (2013). Reactive nitrogen species regulate autophagy through ATM-AMPK-TSC2-mediated suppression of mTORC1. Proc Natl Acad Sci U S A *110*, E2950-2957.
Truett, G.E., Heeger, P., Mynatt, R.L., Truett, A.A., Walker, J.A., and Warman, M.L. (2000). Preparation of PCR-quality mouse genomic DNA with hot sodium hydroxide and tris (HotSHOT). Biotechniques *29*, 52, 54.
Tsai, M., Starkl, P., Marichal, T., and Galli, S.J. (2015). Testing the 'toxin hypothesis of allergy': mast cells, IgE, and innate and acquired immune responses to venoms. Curr Opin Immunol *36*, 80-87.
Ulges, A., Klein, M., Reuter, S., Gerlitzki, B., Hoffmann, M., Grebe, N., Staudt, V., Stergiou, N., Bohn, T., Bruhl, T.J., et al. (2015). Protein kinase CK2 enables regulatory T cells to suppress excessive TH2 responses in vivo. Nat Immunol *16*, 267-275.
Usui, T., Nishikomori, R., Kitani, A., and Strober, W. (2003). GATA-3 suppresses Th1 development by downregulation of Stat4 and not through effects on IL-12Rbeta2 chain or T-bet. Immunity *18*, 415-428.
Van den Bossche, J., O'Neill, L.A., and Menon, D. (2017). Macrophage Immunometabolism: Where Are We (Going)? Trends Immunol *38*, 395-406.
Van Limbergen, J., Radford-Smith, G., and Satsangi, J. (2014). Advances in IBD genetics. Nat Rev Gastroenterol Hepatol *11*, 372-385.
Veldhoen, M., Uyttenhove, C., van Snick, J., Helmby, H., Westendorf, A., Buer, J., Martin, B., Wilhelm, C., and Stockinger, B. (2008). Transforming growth factor-beta 'reprograms' the differentiation of T helper 2 cells and promotes an interleukin 9-producing subset. Nat Immunol *9*, 1341-1346.
Ventura, A., Kirsch, D.G., McLaughlin, M.E., Tuveson, D.A., Grimm, J., Lintault, L., Newman, J., Reczek, E.E., Weissleder, R., and Jacks, T. (2007). Restoration of p53 function leads to tumour regression in vivo. Nature *445*, 661-665.
Villarroya, F., Cereijo, R., Villarroya, J., Gavalda-Navarro, A., and Giralt, M. (2018). Toward an Understanding of How Immune Cells Control Brown and Beige Adipobiology. Cell Metab *27*, 954-961.
Wagner, L.K., Gilling, K.E., Schormann, E., Kloetzel, P.M., Heppner, F.L., Kruger, E., and Prokop, S. (2017). Immunoproteasome deficiency alters microglial cytokine response and improves cognitive deficits in Alzheimer's disease-like APPPS1 mice. Acta Neuropathol Commun *5*, 52.

Waite, K.A., De-La Mota-Peynado, A., Vontz, G., and Roelofs, J. (2016). Starvation Induces Proteasome Autophagy with Different Pathways for Core and Regulatory Particles. J Biol Chem *291*, 3239-3253.
Wang, C., Yosef, N., Gaublomme, J., Wu, C., Lee, Y., Clish, Clary B., Kaminski, J., Xiao, S., Zu Horste, Gerd M., Pawlak, M., et al. (2015). CD5L/AIM Regulates Lipid Biosynthesis and Restrains Th17 Cell Pathogenicity. Cell *163*, 1413-1427.
Wang, R., and Green, D.R. (2012). Metabolic checkpoints in activated T cells. Nat Immunol *13*, 907-915.
Wang, X.J., Yu, J., Wong, S.H., Cheng, A.S., Chan, F.K., Ng, S.S., Cho, C.H., Sung, J.J., and Wu, W.K. (2013). A novel crosstalk between two major protein degradation systems: regulation of proteasomal activity by autophagy. Autophagy *9*, 1500-1508.
Warburg, O., Wind, F., and Negelein, E. (1927). The Metabolism of Tumors in the Body. J Gen Physiol *8*, 519-530.
Watson, A.S., Riffelmacher, T., Stranks, A., Williams, O., De Boer, J., Cain, K., MacFarlane, M., McGouran, J., Kessler, B., Khandwala, S., et al. (2015). Autophagy limits proliferation and glycolytic metabolism in acute myeloid leukemia. Cell Death Discov *1*.
Wei, J., Long, L., Yang, K., Guy, C., Shrestha, S., Chen, Z., Wu, C., Vogel, P., Neale, G., Green, D.R., et al. (2016). Autophagy enforces functional integrity of regulatory T cells by coupling environmental cues and metabolic homeostasis. Nat Immunol *17*, 277-285.
Whitfield, J., Littlewood, T., and Soucek, L. (2015). Tamoxifen administration to mice. Cold Spring Harb Protoc *2015*, 269-271.
Widjaja, C.E., Olvera, J.G., Metz, P.J., Phan, A.T., Savas, J.N., de Bruin, G., Leestemaker, Y., Berkers, C.R., de Jong, A., Florea, B.I., et al. (2017). Proteasome activity regulates CD8+ T lymphocyte metabolism and fate specification. J Clin Invest *127*, 3609-3623.
Wildin, R.S., Ramsdell, F., Peake, J., Faravelli, F., Casanova, J.L., Buist, N., Levy-Lahad, E., Mazzella, M., Goulet, O., Perroni, L., et al. (2001). X-linked neonatal diabetes mellitus, enteropathy and endocrinopathy syndrome is the human equivalent of mouse scurfy. Nat Genet *27*, 18-20.
Willinger, T., and Flavell, R.A. (2012). Canonical autophagy dependent on the class III phosphoinositide-3 kinase Vps34 is required for naive T-cell homeostasis. Proc Natl Acad Sci U S A *109*, 8670-8675.
Wills-Karp, M., Rani, R., Dienger, K., Lewkowich, I., Fox, J.G., Perkins, C., Lewis, L., Finkelman, F.D., Smith, D.E., Bryce, P.J., et al. (2012). Trefoil factor 2 rapidly induces interleukin 33 to promote type 2 immunity during allergic asthma and hookworm infection. J Exp Med *209*, 607-622.
Wohlfert, E.A., Grainger, J.R., Bouladoux, N., Konkel, J.E., Oldenhove, G., Ribeiro, C.H., Hall, J.A., Yagi, R., Naik, S., Bhairavabhotla, R., et al. (2011). GATA3 controls Foxp3(+) regulatory T cell fate during inflammation in mice. J Clin Invest *121*, 4503-4515.
Wu, D.M., and Qiu, Y.F. (2019). Type 2 immune regulation of adipose tissue homeostasis. Curr Opin Physiol *12*, 20-25.
Wynn, T.A. (2015). Type 2 cytokines: mechanisms and therapeutic strategies. Nat Rev Immunol *15*, 271-282.
Xing, Y., and Hogquist, K.A. (2012). T-cell tolerance: central and peripheral. Cold Spring Harb Perspect Biol *4*.
Yadav, M., Louvet, C., Davini, D., Gardner, J.M., Martinez-Llordella, M., Bailey-Bucktrout, S., Anthony, B.A., Sverdrup, F.M., Head, R., Kuster, D.J., et al. (2012). Neuropilin-1 distinguishes natural and inducible regulatory T cells among regulatory T cell subsets in vivo. J Exp Med *209*, 1713-1722, S1711-1719.

Yagi, R., Junttila, I.S., Wei, G., Urban, J.F., Jr., Zhao, K., Paul, W.E., and Zhu, J. (2010). The transcription factor GATA3 actively represses RUNX3 protein-regulated production of interferon-gamma. Immunity *32*, 507-517.
Yang, K., and Chi, H.B. (2012). mTOR and metabolic pathways in T cell quiescence and functional activation. Semin Immunol *24*, 421-428.
Yoshimoto, T., Takeda, K., Tanaka, T., Ohkusu, K., Kashiwamura, S., Okamura, H., Akira, S., and Nakanishi, K. (1998). IL-12 up-regulates IL-18 receptor expression on T cells, Th1 cells, and B cells: synergism with IL-18 for IFN-gamma production. J Immunol *161*, 3400-3407.
Zappia, L., and Oshlack, A. (2018). Clustering trees: a visualization for evaluating clusterings at multiple resolutions. Gigascience *7*.
Zemmour, D., Zilionis, R., Kiner, E., Klein, A.M., Mathis, D., and Benoist, C. (2018). Single-cell gene expression reveals a landscape of regulatory T cell phenotypes shaped by the TCR. Nat Immunol *19*, 291-301.
Zhang, H., Zheng, L., McGovern, D.P., Hamill, A.M., Ichikawa, R., Kanazawa, Y., Luu, J., Kumagai, K., Cilluffo, M., Fukata, M., et al. (2017). Myeloid ATG16L1 Facilitates Host-Bacteria Interactions in Maintaining Intestinal Homeostasis. J Immunol *198*, 2133-2146.
Zhang, Y.N., Nicholatos, J., Dreier, J.R., Ricoult, S.J.H., Widenmaier, S.B., Hotamisligil, G.S., Kwiatkowski, D.J., and Manning, B.D. (2014). Coordinated regulation of protein synthesis and degradation by mTORC1. Nature *513*, 440-+.
Zheng, G.X., Terry, J.M., Belgrader, P., Ryvkin, P., Bent, Z.W., Wilson, R., Ziraldo, S.B., Wheeler, T.D., McDermott, G.P., Zhu, J., et al. (2017). Massively parallel digital transcriptional profiling of single cells. Nat Commun *8*, 14049.
Zheng, W., and Flavell, R.A. (1997). The transcription factor GATA-3 is necessary and sufficient for Th2 cytokine gene expression in CD4 T cells. Cell *89*, 587-596.
Zheng, Y., Josefowicz, S., Chaudhry, A., Peng, X.P., Forbush, K., and Rudensky, A.Y. (2010). Role of conserved non-coding DNA elements in the Foxp3 gene in regulatory T-cell fate. Nature *463*, 808-812.
Zhu, J., Min, B., Hu-Li, J., Watson, C.J., Grinberg, A., Wang, Q., Killeen, N., Urban, J.F., Jr., Guo, L., and Paul, W.E. (2004). Conditional deletion of Gata3 shows its essential function in T(H)1-T(H)2 responses. Nat Immunol *5*, 1157-1165.
Zielinski, C.E., Mele, F., Aschenbrenner, D., Jarrossay, D., Ronchi, F., Gattorno, M., Monticelli, S., Lanzavecchia, A., and Sallusto, F. (2012). Pathogen-induced human TH17 cells produce IFN-gamma or IL-10 and are regulated by IL-1beta. Nature *484*, 514-518.